Microstructural Development During Processing of Rapidly Solidified Al-Fe-(V, Si) Alloys

By

Ruangdaj Tongsri

A Thesis Submitted For The Degree
Doctor Of Philosophy Of The University Of London And The
Diploma Of The Imperial College

November 1999

Materials Processing Group
Department Of Materials
Imperial College Of Science, Technology And Medicine
University Of London

1
BIBL
LONDON
UNIV.

Abstract

Microstructural development during extrusion processing of rapidly solidified Al-6.5Fe-1.5V and Al-6.5Fe-1.5V-1.7Si powders has been investigated using characterisation techniques such as XRD, SEM, TEM, EDS, and DSC. Three different types of microstructure, namely zone A, zone B and zone C, have been observed in powder particles. Zone A consisted of micro-quasicrystalline icosahedral (MI) particles engulfed in the α-Al matrix. Zone B consisted of microcellular structures with MI particles entrapped in the intercellular regions. Zone C consisted of globular clusters of micro-quasicrystalline icosahedral (GCMI) and/or globular icosahedral (I) particles entrapped in coarse cellular structures. Zone A was the predominant microstructure of the fine powder particles. A mixture of zone A and zone B was the main morphology of the medium sized powder particles, whereas a mixture of zone B and zone C was the predominant microstructure of the coarse powder particles.

During extrusion consolidation, zone A and zone B transformed to the microstructure designated as band I for Al-6.5Fe-1.5V alloy and band I′ for Al-6.5Fe-1.5V-1.7Si alloy, consisting of fine intermetallics {Al_6Fe + $Al_{13}Fe_4$ + $Al_{45}(V, Fe)_7$ for Al-6.5Fe-1.5V alloy and $Al_{13}(Fe, V)_3Si$ for Al-6.5Fe-1.5V-1.7Si alloy} distributed homogeneously in the matrix. Zone C transformed to the microstructure designated as band II for Al-6.5Fe-1.5V alloy and band II′ for Al-6.5Fe-1.5V-1.7Si alloy, consisting of coarse intermetallics {I particles for Al-6.5Fe-1.5V alloy and coarse $Al_{13}(Fe, V)_3Si$ particles for Al-6.5Fe-1.5V-1.7Si alloy}. The as-extruded alloy consisting of band I or I′ exhibited superior strength to that consisting of band II or II′, except for the case of the Al-6.5Fe-1.5V alloy consisting of band I microstructure, which exhibited poorer strength at elevated temperatures due to coarsening of $Al_{13}Fe_4$ + $Al_{45}(V, Fe)_7$.

During heat-treatment, an icosahedral phase transformed to a hexagonal phase. The hexagonal phase further decomposed to form $Al_{13}Fe_4$ + $Al_{45}(V, Fe)_7$ upon heating for longer times.

To My Family (The Tongsris)

Acknowledgements

I would like to express my sincere gratitude to my supervisors, Dr. H. B. McShane and Dr. R. J. Dashwood. Without their encouragement and helpful advice throughout the period of this research, this thesis would never been possible.

The funding for this thesis was provided by the Royal Thai Government. The hardship funding, during the period of Thai economic crisis, was also provided by the European Commission via the Brite Euram project. I would like to thank to them.

My thanks goes to the National Metal and Materials Technology Centre (MTEC), Bangkok, Thailand, for allowing me to continue writing up in UK and for providing financial support.

I would like to thank the following people for providing me some useful articles: Dr. P. D. Lee, and Dr. L. Christodoulou. My thanks also goes to the following: R. P. Thackray, E. J. Minay, D. Middleton, I. Haurie, and all friends in the Materials Processing Group (MPG).

The technical staff have been valuable with help and assistance they have given me over the period of my study and I would like to thank the following: M. Andrews, R. Sweeney, N. Salpadoru, N. Royall, and G. Briers.

I would like to thank my Thai friends (Thai students in London, Sheffield, and Durham) for their support during the preparation of this thesis.

Finally, I would like to thank all members of my family for their constant love, attention, and support. This thesis is dedicated to them.

Contents

	Page
Abstract	2
Acknowledgements	4
Contents	5
List of Figures	7
List of Tables	11
Chapter 1 Introduction	12
Chapter 2 Microstructural Development in Rapidly Solidified Alloy Powders and Evolution during Extrusion Consolidation	15
Introduction	15
2.1 Undercooling	17
2.2 Nucleation after Undercooling	19
2.3 Growth by Movement of the Solid/liquid Interface	21
2.4 Solid Solubility Extension	25
2.5 Formation of Metastable Phases	27
2.6 Microstructures of Atomised Powders	29
2.7 Phase Transformation in Rapidly solidified Alloys	33
2.8 Coarsening of Second Phase Particles	36
2.9 Microstructural Development in Powder Extrusion	38
2.10 Restoration Processes Operating during Extrusion of Metals	40
2.11 Microstructures of Extruded Aluminium Alloys	46
2.12 Transformation and Coarsening of Second Phase Particles in Extruded Aluminium Alloys	48
2.13 Microstructural Inhomogeneity in Extruded Aluminium Alloys	49
Chapter 3 Development of Rapidly Solidified Al-Fe-(V, Si) Alloys	50
3.1 Binary Al-Fe Alloys	50
3.2 Binary Al-V Alloys	56
3.3 Ternary Al-Fe-V Alloys	58
3.4 Quaternary Al-Fe-V-Si Alloys	59

	Page
Chapter 4 Experimental Procedure	63
4.1 Characterisation of the As-atomised Powders	63
4.2 Powder Consolidation	65
4.3 Mechanical Testing	66
4.4 Heat-treatment	67
4.5 Phase Identification and Microstructural Investigation of Bulk Materials (Consolidated Alloys, Mechanically Tested Specimens and Heat-treated Specimens	67
Chapter 5 Results and Discussion	68
5.1 Characterisation of the As-atomised Powders	68
5.2 Phase Transformation during Heating of the As-atomised Powders	97
5.3 Microstructures of the As-extruded Alloys	104
5.4 Phase Transformation during Extrusion of Powders	123
5.5 Mechanical Properties of the As-extruded Alloys	126
5.6 Microstructures of Tested Specimens	133
5.7 Coarsening and Phase Transformation during Heat-treatment of the As-extruded Alloys	140
Chapter 6 Conclusions	163
Chapter 7 Suggestions for Further Work	166
References	168
Appendix	190

List of Figures

	Page
2.1 Concepts of undercooling and extended solid solubility	18
2.2 Free energy of a solid particle formed in the melt by fluctuations	20
2.3 Time-temperature-nucleation (TTN) curves	21
2.4 Hypothetical diagram of free energy at temperature *T* against concentration for (major) phase α and (minor) phases β and β′ for a binary system A-B	26
2.5 Schematic representation of solidification of initially undercooled liquid droplets for nucleation on the surface when the initial interface is: (a) dendritic, (b) smooth, and (c) cellular	30
2.6 A sketch showing shear zones in a metal billet during extrusion at a steady flow pattern of a load/displacement curve	39
2.7 Stress-strain curves for dynamic recovery	42
2.8 Stress-strain curves for dynamic recrystallization	44
3.1 Approximate cooling rate regimes for formation of the different intermetallic phases in hypoeutectic Al-Fe alloys	52
3.2 Solidification microstructure selection diagram for Al-rich Al-Fe alloys	54
3.3 Al-rich portion of the Al-Fe phase diagram showing stable (Al-Al_3Fe) diagram and metastable (Al-Al_6Fe) diagram	55
3.4 Equilibrium phase diagram of Al-(0-40) at. % V	57
5.1.2.1 Examples of microstructures and SADPs of zone A exhibited by fine RS-Al-Fe-V and RS-Al-Fe-V-Si powder particles	73
5.1.2.2 Schematic diagram showing interaction between second phase particles and planar (a) and cellular (b) solidification fronts	74
5.1.2.3 Examples of microstructures exhibited by fine to medium RS-Al-Fe-V and RS-Al-Fe-V-Si powders	79
5.1.2.4 SEM micrographs of coarse RS-Al-Fe-V powders	80
5.1.2.5 Examples of the RS-Al-Fe-V and RS-Al-Fe-V-Si powders showing more than one nucleation site	81

	Page
5.1.2.6 Showing a fine satellite particle acting as the nucleation site for solidification of coarse powder particle	82
5.1.2.7 Irregular-shaped powder particles of (a) RS-Al-Fe-V and (b) RS-Al-Fe-V-Si alloys	82
5.1.3.1 Bright field TEM image of GCMI phase particles in coarse cellular microstructures (zone C) of coarse RS-Al-Fe-V powders (a) and SADP (b)	88
5.1.3.2 Bright field TEM image (a) and SADP (b) of microcellular structures (zone B) of fine RS-Al-Fe-V powders	89
5.1.4.1 Bright field TEM image of I-(Al, Si)x(Fe, V) particles in coarse cellular structures of coarse RS-Al-Fe-V-Si powders (a) and SADPs showing fivefold (b), threefold (c), twofold (d), and pseudo twofold (e) symmetries, respectively	92
5.1.4.2 Bright field TEM image (a) and SADP (b) of microcellular structures (zone B) of RS-Al-Fe-V-Si powders	93
5.1.4.3 Coarse cellular microstructures (zone C) of coarse RS-Al-Fe-V-Si powders consisting of fine dispersoids	94
5.1.5 Plot of lattice parameters against powder particle sizes of (a) RS-Al-Fe-V alloy and (b) RS-Al-Fe-V-Si alloy	96
5.2.1.1 Schematic diagram showing powder microstructures and corresponding DSC curves of RS-Al-Fe-V powders	99
5.2.1.2 Bright field TEM images of a RS-Al-Fe-V powder particle heated at 500 °C for 10 minutes	101
5.2.2 Schematic diagram showing powder microstructures and corresponding DSC curves of Al-Fe-V-Si powders	103
5.3.1 Bright field TEM images of the as-extruded products of RS-Al-Fe-V powders	106-107
5.3.2 Bright field TEM images of the as-extruded products of RS-Al-Fe-V-Si powders	109
5.3.3.2.1 Identification of the Al_6Fe phase: (a) EDS spectrum, (b) a bright field TEM image and SADPs	114

	Page
5.3.3.2.2 Showing a bright field TEM image (a) and EDS spectrum of the unknown Al-Fe-V phase	116
5.3.3.2.3 Identification of the I phase: (a) a bright field TEM image of the I phase particle with SADPs, (b) EDS spectrum	117
5.3.4.1 Plot of apparent lattice parameters against the N-R function for the as-extruded products produced from different RS-Al-Fe-V-Si powder size fractions	119
5.3.4.2 Electron diffraction patterns of intermetallic phases in the as-extruded RS-Al-Fe-V-Si alloy	122
5.4.1 Schematic diagram showing phase transformation reactions during extrusion of RS-Al-Fe-V powders	124
5.4.2 Schematic diagram representing phase transformations during extrusion of RS-Al-Fe-V-Si powders	125
5.5.1.1 Plot of 0.2 % CS as a function of powder particle size and test temperature of the as-extruded RS-Al-Fe-V alloys	128
5.5.1.2 Plot of maximum extrusion pressure as a function of powder particle size of RS-Al-Fe-V powders	128
5.5.1.3 Plot of 0.2 % CS of the IPC and NIPC alloys as a function of test temperature	129
5.5.2.1 Plot of 0.2 % CS as a function of powder particle size and test temperature of the as-extruded RS-Al-Fe-V-Si alloys	130
5.5.2.2 Plot of maximum extrusion pressure as a function of powder particle size of RS-Al-Fe-V-Si powders	130
5.6.1.1 Schematic diagram showing compression of an alloy specimen, a compressed specimen and sectioning of a compressed specimen	133
5.6.1.2 Bright field TEM images of compressed RS-Al-Fe-V alloy specimens	136
5.6.1.3 Bright field TEM images of compressed RS-Al-Fe-V-Si alloy specimens	137
5.6.2 Fracture surfaces of the as-extruded RS-Al-Fe-V and RS-Al-Fe-V-Si alloys	139

	Page
5.7.1.1 TEM bright field image and electron diffraction patterns of the equilibrium $Al_{13}Fe_4$ phase	141
5.7.1.2 Schematic solutions ((a) and (c)) and electron diffraction pattern (b) with a $<1\bar{1}4>$ beam direction for the $Al_{13}Fe_4$ phase	143
5.7.1.3 Identification of a plate-like $Al_{13}Fe_4$ particle exhibiting a tenfold SADP: (a) bright field TEM image, (b) tenfold SADP, and (c) EDS spectrum	145
5.7.1.4 Identification of a H-Al_x(Fe, V) particle	151
5.7.1.5 Selected area electron diffraction patterns and convergent beam electron diffraction patterns (whole pattern) of the H-Al_x(Fe, V) phase	152
5.7.1.6 Bright field TEM image and electron diffraction pattern of H-Al_x(Fe, V) and I-Al_x(Fe, V) phases	153
5.7.1.7 Identification of the $Al_{45}(V, Fe)_7$ phase	155
5.7.2.1 Microstructures of the heated RS-Al-Fe-V-Si alloy	157
5.7.2.2 Identification of the $Al_{13}(Fe, V)_3Si$ particle	158
5.7.2.3 Electron diffraction patterns of the $Al_{13}(Fe, V)_3Si$ phase	159
5.7.2.4 Identification of the $(Al, Si)_{45}(V, Fe)_7$ phase	161

List of Tables

	Page
2.1 Descriptions of precipitation from solid solution in rapidly solidified aluminium alloys	35
5.1.1 Particle diameters of RS-Al-Fe-V and RS-Al-Fe-V-Si powders	69
5.1.3.1 XRD data and possible phases in RS-Al-Fe-V powders	84
5.1.3.2 Showing the measured *d*-values and relative intensities of a GCMI-Al_x(Fe, V) phase particle (Fig. 5.1.3.1 (b)) and intercellular phases (Fig. 5.1.3.2 (b)) in the as-atomised RS-Al-Fe-V powders, compared to those values of the I-Al_4Mn phase	87
5.1.4.1 XRD data and possible phases in RS-Al-Fe-V-Si powders	90
5.1.4.2 Showing the measured *d*-values and relative intensities of intercellular phases in the as-atomised RS-Al-Fe-V-Si powders (Fig. 5.1.4.2 B)), compared to those of the I-Al_4Mn phase	94
5.1.5 Estimated (Fe + V) content in solid solution for each powder size fraction of RS-Al-Fe-V and RS-Al-Fe-V-Si alloys	97
5.2.1.1 XRD data and possible phases of heated RS-Al-Fe-V powders (excluding Al peaks)	101
5.3.1 XRD data and possible phases in the as-extruded RS-Al-Fe-V alloys produced from different powder size fractions	111
5.3.4 XRD data and possible phase in the as-extruded RS-Al-Fe-V-Si alloys produced from different powder size fractions	120
5.5.3 Fracture toughness of the as-extruded RS-Al-Fe-V and RS-Al-Fe-V-Si alloys	131
5.7.1 All possible crystal point groups corresponding to the CBED whole patterns shown in Fig. 5.7.1.5	147
5.7.2 Hexagonal phases in aluminium alloys	150

CHAPTER 1

INTRODUCTION

Rapid solidification processing (RSP) is one of the materials processing methods developed for producing high strength and elevated temperature alloys. In RSP, the alloy microstructures and hence the alloy properties are controlled by quenching treatments. RSP has an important role in the production of novel alloys as it circumvents limitations associated with conventional solidification processing (CSP). The superiority of RSP over CSP includes extension of solid solubility, refinement of microstructures, improved chemical uniformity, and formation of metastable phases.

The equilibrium solid solubility of transition and rare earth elements in aluminium is very low so attempts to introduce larger amounts of them into the aluminium matrix by using CSP may lead to formation of coarse second phase particles. The coarse or segregated second phases have detrimental effects on mechanical properties of the materials. RSP can maintain solute concentration in solid solution above the equilibrium level of solid solubility. It can also minimise segregation of solute in the as-cast materials. Because of these advantages of RSP, the microstructures of rapidly solidified alloys or their products, following thermomechanical processing are usually superior to those of CSP materials.

RSP is usually associated with high cooling rates of the melt before, during and after solidification. These can be achieved by making at least one dimension of the specimen thin enough to allow faster heat removal, for example in atomisation, splat-quenching, and planar flow casting. However, rapid solidification can also be achieved under conditions that involve low cooling rates, so long as the heterogeneous nucleation at low undercooling is suppressed. In such cases, high undercooling of melts can be achieved, for example, in emulsification [1.1] and fluxing [1.2] of liquid metal droplets, and containerless processing [1.3-1.4]. In highly undercooled alloy droplets, solidification velocities or growth rates of the solid/liquid interface are high.

The solid/liquid velocity is the important factor that governs microstructural development in alloys (§ Chapter 2).

RSP techniques may be classified into two categories [1.5], namely, atomisation methods (gas, water, and centrifugal atomisation), and non-atomisation methods (melt spinning, surface melting, and fibre drawing). Amongst these methods, atomisation is the most common and most economic way of producing rapidly solidified alloys in commercial quantity [1.6]. There are several atomisation techniques used for making alloy powders [1.7-1.10]. The term 'powder metallurgy/rapid solidification or PM/RS' may represent the alloy production processes consisting of powder production and powder consolidation. The powder production usually employs atomisation techniques. The powder consolidation may start with powder compaction followed by metal forming processes such as extrusion, forging, sintering, or rolling.

PM/RS has been widely used for development of high performance or novel materials, in heavy alloys [1.11] (ferrous-based, nickel-based, copper-based, and iron-rare earth-based) and light alloys [1.11, 1.12] (aluminium-based, titanium-based, and magnesium-based). Aluminium-based alloys have been developed for applications in land vehicles [1.13, 1.14], and in aircraft [1.14-1.16]. Most of the research and development activities have been directed towards aircraft and aerospace applications.

PM/RS aluminium-based alloys may be classified into three groups, namely high strength/corrosion resistant, low-density/high-modulus, and elevated temperature alloys. One of the most attractive potential developments of RS/PM aluminium alloys is to improve substantially their elevated temperature performances. The basic idea is to introduce stable second phase forming elements into the aluminium matrix. Dispersion of the stable second phases in the matrix may be achieved during solidification and/or during the consolidation processing.

Most elevated temperature aluminium alloys [1.16-1.18] are dispersion-strengthened Al-Fe based alloys, such as Allied-Signal's alloy 8009 (Al-Fe-V-Si), Alcoa's alloy 8019 (Al-Fe-Ce), and Pratt & Whitney's alloy (Al-Fe-Mo). The Al-Fe based alloys have been considered promising candidates for development for elevated temperature applications owing to their lower cost of production compared to Ti-based alloys, the thermal stability of their microstructures, and excellent mechanical properties at both room and elevated temperatures. Most investigations on the rapidly

solidified Al-Fe based alloys have been carried out on microstructures and mechanical properties of either the as-solidified or the as-consolidated materials.

The rapidly solidified Al-Fe-(V, Si) alloys have been recently developed for use as replacements for more expensive titanium alloys in parts of aircraft. In this study, microstructural development in the as-solidified powders, the as-extruded products and the heated specimens of rapidly solidified Al-Fe based alloys, namely Al-6.5Fe-1.5V and Al-6.5Fe-1.5V-1.7Si alloys, have been investigated. Understanding of the microstructural development of the as-solidified Al-Fe powders during solidification, consolidation, and heating is necessarily required for comprehension of microstructure-process-property relationships in the materials.

Note that since the monoclinic Al-Fe phase has been frequently referred to in this thesis, it is useful to mention it here. The same monoclinic Al-Fe phase can be represented by Al_3Fe or $Al_{13}Fe_4$. The designation 'Al_3Fe' has been used frequently in the section of literature review (in accordance to the designation used in reference papers) of this thesis, while the correct designation '$Al_{13}Fe_4$' has been used in the section of results and discussion and conclusions.

CHAPTER 2

MICROSTRUCTURAL DEVELOPMENT IN RAPIDLY SOLIDIFIED ALLOY POWDERS AND EVOLUTION DURING EXTRUSION CONSOLIDATION

Introduction

RSP techniques can be classified into three main groups that show distinct and important differences in processing parameters [2.1]. These parameters include interface growth (solidification) velocity (V), temperature gradient in the liquid ahead of the solid/liquid interface (G), ratio G/V, and cooling rate ($\dot{T} = dT/dt$). Note that G/V is also a parameter that controls planar interface stability at low solidification rates (constitutional undercooling). In directional solidification, the cooling rate is equal to GV. These three groups are described below.

(i) Rapid movement of a high energy heat source is found, for example, in laser surface treatment. The interface growth velocity in this process increases rapidly from zero at the bottom of the trace (melt pool) to a value close to the beam rate at the surface. The temperature gradient is highest at the bottom of the trace and decreases in the direction perpendicular to the trace surface (z). The absolute value of the cooling rate varies strongly in the z direction. The G/V ratio is infinite at the bottom of the trace and decreases exponentially with increasing z. The influence of these parameters leads to solidification by columnar (directional or constrained) growth.

(ii) High undercooling of the melt (before solidification) may be obtained using a large cooling rate. To obtain a large cooling rate, a small product size has to be produced, for example, in planar flow casting, splat quenching, and melt spinning. The interface growth velocity in this process decreases continuously from a maximum value at the ribbon chill surface to a lower value at the outer ribbon surface. The temperature

gradient is first negative at the chill surface, then becomes positive and reaches a maximum value at a small distance from the chill surface and finally decreases with distance away from the chill surface. The absolute cooling rate decreases strongly with distance away from the chill surface. The *G/V* ratio for this process increases from negative to a positive maximum value and finally decreases strongly as the distance away from the chill surface increases. Solidification under the influence of these parameters shows mixed behavior of directional and free growth. However, directional growth seems to be predominant.

(iii) High undercooling of the melt can be produced by the absence of nucleants, for example in levitation melting in ultra high vacuum while encapsulating the melt in glass. This process is also called *bulk undercooling*. The interface growth velocity decreases from a maximum value at the beginning of growth to a lower value as the growth proceeds. The temperature gradient is always negative and its absolute value ($|G|$) is inversely proportional to the velocity. The absolute value of the cooling rate increases slightly in the growth direction. The *G/V* ratio is always negative in this case. Solidification in this process proceeds with free (unconstrained) growth.

Atomisation, which is widely used for producing metal or alloy powders, can belong to category (ii) or (iii). Some powders produced from nucleant-free droplets are classified under bulk undercooling processes (group (iii)) while some other fine powders experience high cooling rates and may be classified in group (ii).

Rapid solidification starts after the nuclei have formed. Advance of the solid/liquid interface proceeds after nucleation and is controlled by the processing parameters mentioned above resulting in several possible morphologies. These morphologies include plane front, band, cell, dendrite, and eutectic. Under non-equilibrium conditions during rapid solidification, metastable crystalline, quasi-crystalline and amorphous phases can be formed in addition to those microstructural morphologies.

2.1 Undercooling

When a liquid alloy is broken up into a large number of fine droplets, as occurs in atomization, the most potent nucleation sites can become dispersed such that large liquid undercooling below the equilibrium liquidus may be achieved prior to nucleation [2.2, 2.3]. The concept of undercooling is illustrated schematically in Fig. 2.1. We may assume adiabatic conditions, i.e. the latent heat of solidification (ΔH) is absorbed fast enough within the system so that, effectively, any heat removal from the system during solidification is inconsequential. In this figure, three types of solidification can possibly occur [2.4].

In Case I (Fig. 2.1a) or *hypocooling*: $T_1 > T_2$ and $T_R > T_S$, the solidification starts in the massive mode, however local equilibrium and compositional partitioning can ensue when the interfacial temperature rises into the α + liquid field.

In Case II (Fig. 2.1b) or *critical undercooling*: $T_R = T_S$, the composition C_0 is undercooled into the single phase α field. Nucleation occurs at T_2 and the recalescence temperature (T_R) at the solid/liquid interface is raised to the solidus temperature (T_S). Solidification can take place massively or entirely within the single phase field and without compositional partitioning or local equilibrium at the interface.

In Case III (Fig. 2.1c) or *hypercooling*: $T_3 < T_2$, and $T_R < T_S$, the solidification starts and ends within the single phase α field. Both Case II and III result in segregation-free solidification, but because the nucleation rate is likely to be faster, and the growth rate slower, at the lower temperature, a smaller microcrystalline grain size can be expected if the solidification process can be depressed to the lower temperature.

A similar explanation using the concept of undercooling is also valid for extended (metastable) solid-solubility as shown schematically in Fig. 2.1d. When undercooling is achieved at high cooling rates, e.g. for the composition C_2 the dotted lines indicate extended compositions of the liquid and α phase coexisting below the eutectic temperature. If undercooling is high enough, $T \leq T_c'$, so that, with the increase of temperature caused by release of latent heat of solidification the material remains below the extension of the solidus line, massive solidification will result in a highly

supersaturated extended solution (α) with no compositional partitioning. Decomposition of such a solid solution ($\alpha \rightarrow \alpha + \beta$) as a result of solid state diffusion may result in a very fine quasi-eutectoid structure.

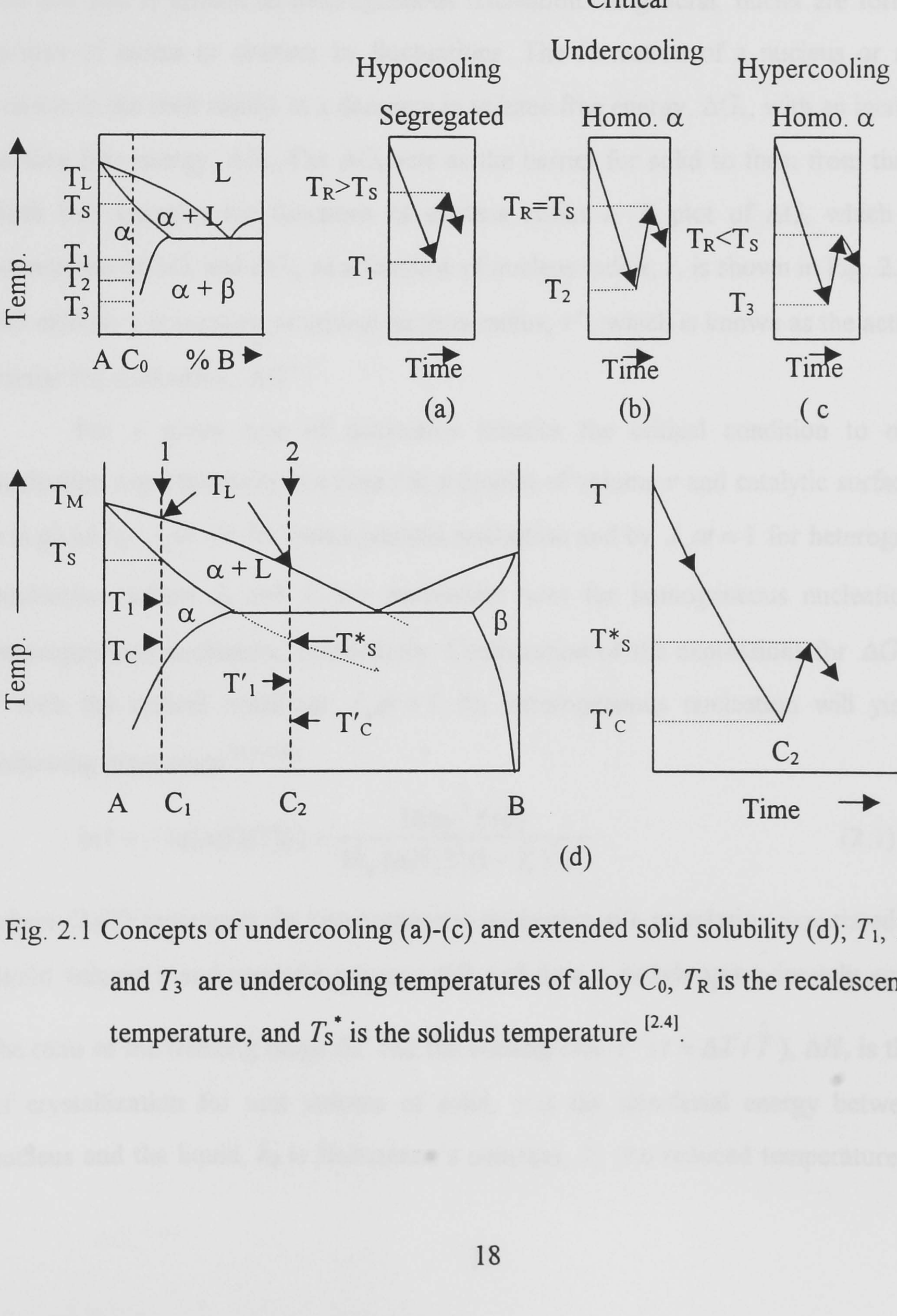


Fig. 2.1 Concepts of undercooling (a)-(c) and extended solid solubility (d); T_1, T_2, and T_3 are undercooling temperatures of alloy C_0, T_R is the recalescence temperature, and T_S^* is the solidus temperature [2.4].

2.2 Nucleation after Undercooling

Nucleation of a crystalline phase in an undercooled liquid phase may be classified according to two mechanistic types [2.5]. When nucleation occurs without an association with any catalytic sites, it can be classified as homogeneous nucleation. In the vast majority of experimental conditions, nucleation is initiated at some catalytic site and this is known as heterogeneous nucleation. In general, nuclei are formed as groups of atoms or clusters by fluctuations. The formation of a nucleus or a solid volume in the melt results in a decrease in volume free energy, ΔG_v, with an increase in surface free energy, ΔG_i. The ΔG_i acts as the barrier for solid to form from the melt. Both free energies are functions of nucleus radius r. A plot of ΔG, which is the summation of ΔG_i and ΔG_v, as a function of nucleus radius, r, is shown in Fig. 2.2. The ΔG exhibits a maximum, at critical nucleus radius, r^*, which is known as the activation barrier for nucleation, ΔG^*.

For a given type of nucleation kinetics the critical condition to observe nucleation experimentally in a time t in a droplet of volume v and catalytic surface area a is given by $J_v vt \approx 1$ for homogeneous nucleation and by $J_a at \approx 1$ for heterogeneous nucleation, where J_v and J_a are nucleation rates for homogeneous nucleation and heterogeneous nucleation, respectively. Combination of the expressions for ΔG^*, and J with the critical condition $J_a at \approx 1$ for heterogeneous nucleation will yield the following expression [2.6-2.9];

$$\ln t = -\ln\{a(\Omega(T))\} + \frac{16\pi\gamma^3 f(\theta)}{3k_B(\Delta H_v)^2(1-T_r)^2 T_r} \qquad (2.1)$$

where Ω (T) represents the heterogeneous nucleation site population associated with a liquid volume v and catalytic potency $f(\theta)$ and time t, which approximately equals to the ratio of the freezing range ΔT and the cooling rate $\dot{T}$ ($t \approx \Delta T / \dot{T}$), ΔH_v is the heat of crystallization for unit volume of solid, γ is the interfacial energy between the nucleus and the liquid, k_B is Boltzmann's constant, T_r, the reduced temperature, is the

ratio of temperature T and melting temperature T_M. A plot of temperature versus log t results in the c-shape curves as shown in Fig. 2.3, which indicate the temperature and time domains of crystallization upon continuous cooling. These c-shape curves are also known as time-temperature-nucleation (TTN) diagrams within which cooling curves can be plotted. The crossing of the cooling curve with the TTN curve indicates nucleation of the phase corresponding to that TTN curve. For a low cooling rate, $\dot{T}_3$, the cooling curve meets the TTN curve for the equilibrium product (labeled by 'het'), and this indicates that a stable product is preferentially nucleated. Similarly, for a larger cooling rate, $\dot{T}_2$, a metastable phase is expected to be formed. The fastest cooling rate, $\dot{T}_1$, corresponding to rapid quenching, leads to homogeneous nucleation. Note that as the cooling rate increases the temperature corresponding to the crossing point of the cooling curve and the TTN curve decreases. In other words, undercooling increases with increasing cooling rate. The relationship between the cooling rate and undercooling for nucleation has been stated elsewhere [2.10, 2.11].

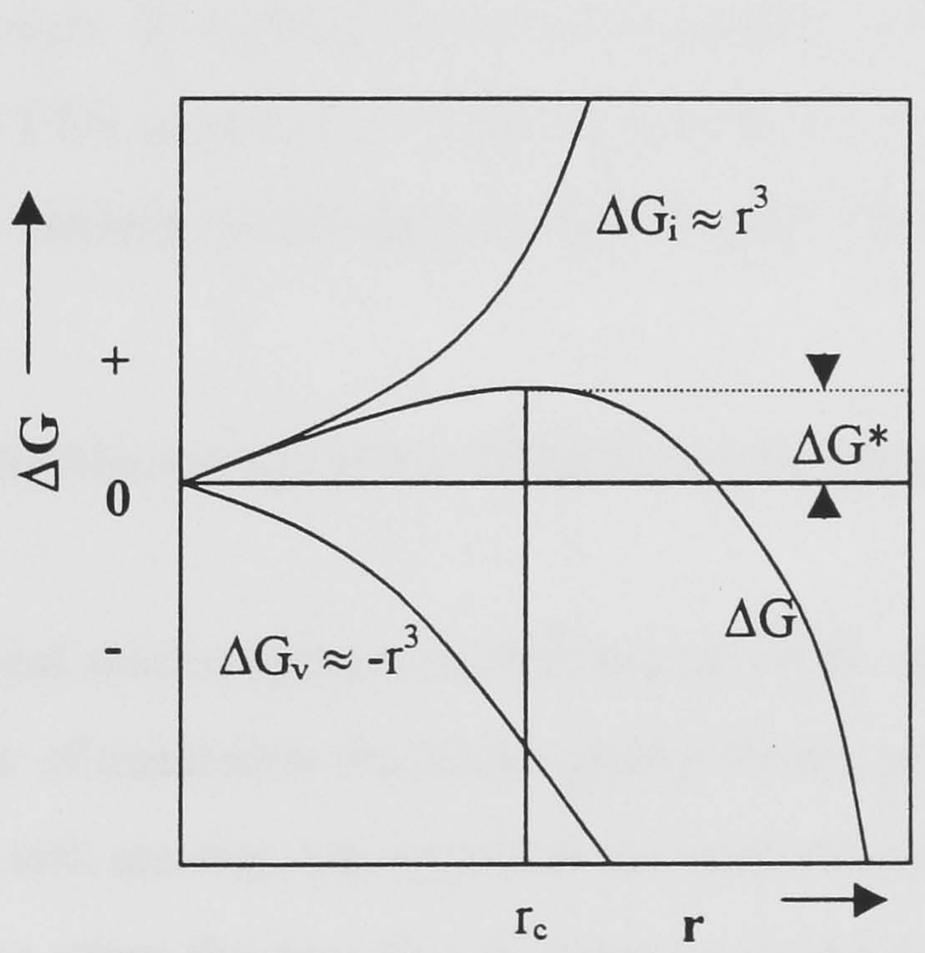


Fig. 2.2 Free energy of a solid particle formed in the melt by fluctuations. The activation barrier for nucleation, ΔG^*, is formed from (negative) volume contributions, ΔG_v, and (positive) interface contributions, ΔG_i [2.8].

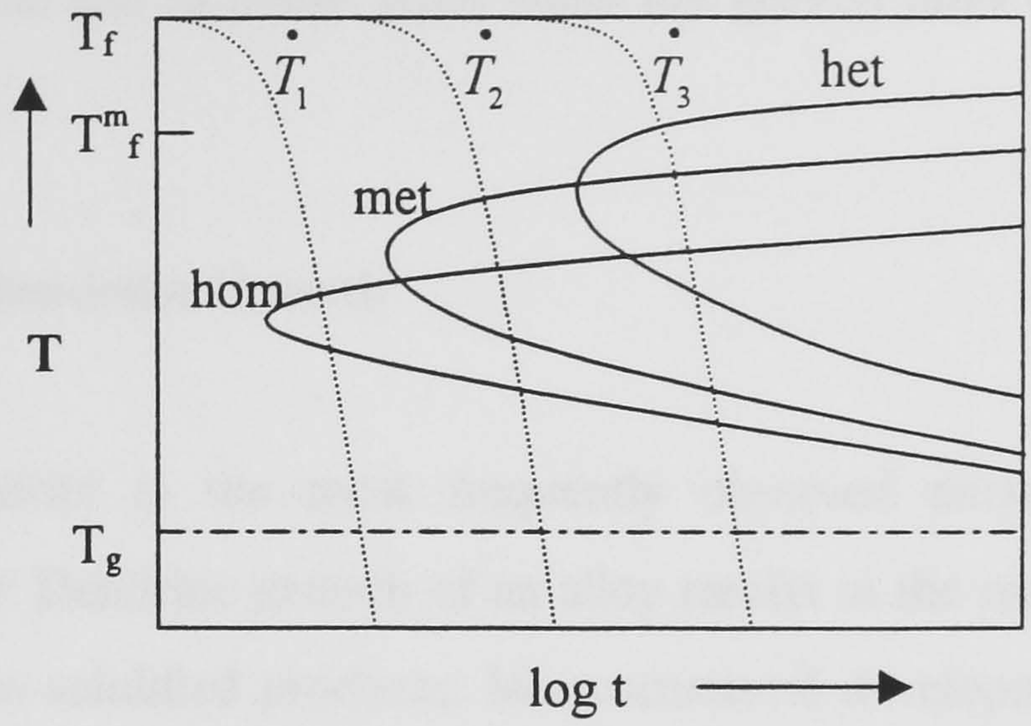


Fig. 2.3 Time-temperature-nucleation (TTN) curves (full lines). The curve labelled 'hom' is for homogeneous nucleation, that labelled 'met' for heterogeneous nucleation leading to a metastable product, and that labelled 'het' for heterogeneous nucleation leading to an equilibrium product. Nucleation occurs as the cooling curves (dotted lines) cross the TTN curves. T_f, T_f^m, and T_g indicate the equilibrium melting point, the metastable melting point and the glass temperature, respectively [2.8].

2.3 Growth by Movement of the Solid/liquid Interface

The final microstructure formed during rapid solidification is controlled in part by the number of nucleation events but mainly by the growth processes. There are two important growth mechanisms by which the solid can grow into the liquid. In the first, growth occurs when the heat flux is opposite to the solidification direction, i.e. from the superheated liquid into the solid. In this case the solid/liquid interface senses a positive temperature gradient in the liquid. Growth can also proceed into a negative temperature gradient in a liquid ahead of the solid/liquid interface. The former type of growth is known as constrained or directional growth, while the latter is unconstrained or free growth. The rate of advance of the solid/liquid interface or growth rate or

solidification velocity is a very important factor controlling the morphology of the final microstructures which may include dendrites, cells, planar front (and/or bands), and eutectics. In the range of rapid solidification, the morphologies change from dendrites to cells to bands and to planar front when the growth rates change from low to high values [2.1, 2.12].

2.3.1 Dendritic Growth

A dendrite is the most frequently observed microstructural feature in a solidified alloy. Dendritic growth of an alloy results in the most complicated structure in as-cast or as-solidified products. Microstructural development by dendritic growth can be classified into two solidification or growth modes owing to microstructural evolution under two distinctly different growth conditions, namely constrained or directional solidification, and unconstrained or free growth into an undercooled melt. The dendritic growth direction and the heat flow direction are parallel for free growth into an undercooled melt, whereas they are anti-parallel in directional solidification.

For the past two decades, theoretical models of dendritic growth have been studied and evaluated by several materials scientists [2.13-2.34]. Most models for dendrite formation at low growth rates and/or with small undercooling have been derived by assuming that the growth occurs under steady-state conditions. Local equilibrium at the advancing interface is assumed. In the case of rapid solidification, the non-equilibrium effects have been taken into account.

There are two main factors that govern dendritic growth, namely the dendrite tip selection criterion and total undercooling [2.23]. The selection criterion can be viewed as a balance between the destabilising effect of the solute and thermal gradients in the liquid for undercooled melt, and the stabilising effect of the interfacial energy. The total undercooling, ΔT, is the sum of different undercooling components. In the case of a phase diagram with linear liquidus and solidus lines, the individual undercooling components can be defined.

For free dendritic growth in an undercooled melt, the ΔT is the sum of thermal undercooling ΔT_T, solutal or constitutional undercooling ΔT_C, and curvature

undercooling ΔT_R [2.19-2.22]. In constrained dendritic growth in directional solidification, ΔT_T is omitted [2.23].

In rapid solidification, the non-equilibrium effects including (a) the effect of attachment kinetics at the interface [2.23], (b) the change in interface compositions due to thermodynamic constraint [2.2, 2.24], and (c) the variation in solute distribution coefficient as a function of velocity [2.25, 2.26], become important. These effects have to be included in the total undercooling for both free and constrained dendritic growths.

Recently, a steady-state free dendritic growth model accommodating non-local equilibrium tip conditions and curved liquidus and solidus has been developed [2.34]. This model can accommodate any expressions for the interfacial driving force, growth law, and interfacial solute trapping kinetics and thus is expandable for higher solute concentrations.

2.3.2 Cellular Growth

Cellular structures become stable at low and at high velocities. Directional solidification studies in the low velocity range showed that as the velocity was increased beyond the critical velocity, V_c, a planar interface became unstable and thus reorganize to form an array of cells [2.35]. With increased velocity, cells were unstable and cell-to-dendrite transition occurred. The dendrite-to-cell transition has been shown to occur at high velocities [2.36]. Cellular structures become stable at high velocity until the velocity reaches the limit of absolute stability, V_{ab} [2.37, 2.38].

Theoretical approaches for cellular growth have been taken for the case of low velocity [2.15] and high velocity [2.36] in directional solidification. Numerical models for cellular and dendritic growth [2.39-2.41] have recently been extended into the high velocity region [2.42]. The velocity dependent distribution coefficient, liquidus slope, and diffusion coefficient were employed in the extended model, which provided good agreement with experimental measurements.

2.3.3 Banded Structures

Banded structure is a new microstructural feature that has been observed in several alloys with medium to large equilibrium freezing range, ΔT_0 [2.18]. This structure, consisting of a regular succession of dark and light bands lying parallel to the solidification front, forms when the growth conditions approach absolute stability. The structure in the dark bands results from dendritic or eutectic growth depending on the alloy, whereas the light bands are due to planar growth. It has been proposed that during solidification of the banded structure, the cellular-planar growth process repeats itself [2.43]. Recently, it has been shown that a range of velocities exists where oscillatory instability of the solid/liquid interface occurs. The oscillations result in the formation of the banded structure [2.44, 2.45].

2.3.4 Planar Growth

When the growth velocity is equal to or greater than the absolute stability velocity, the planar front is stable and no segregation occurs. The absolute stability velocity for rapid planar growth in directional solidification, $(V_{abs})_D$ [2.43], is the extended form of the linear perturbation theory for the stability of a planar interface derived by Mullins and Sekerka [2.46]. It has been shown that the calculated values of $(V_{abs})_D$ were in good agreement with the experimental values of $(V_{abs})_D$ for rapidly solidified Ag-1Cu and Ag-5Cu alloys [2.43]. For rapid planar growth in undercooled melts, the planar front will be stable when the growth velocity satisfies the stability criterion. This criterion is determined by absolute stability velocity for rapid planar growth in undercooled melts, $(V_{abs})_U$, derived by Trivedi and Kurz [2.47].

2.3.5 Eutectic Growth

A eutectic structure is characterized by the simultaneous growth from a melt of two or more conjugated phases. Steady-state eutectic growth can be explained by the Jackson and Hunt (JH) model [2.48] in which the relationship between interface

undercooling, ΔT, lamellar spacing λ and velocity, V, has been derived under two assumptions. These assumptions are (i) λ is much smaller than the diffusion distance, D/V, where D is the diffusion coefficient of solute in liquid, (ii) ΔT is sufficiently small that the interface composition is approximately the same as the eutectic composition, C_E. However, under rapid solidification conditions, D/V can be small and ΔT can be large. Trivedi, Magnin, and Kurz (TMK) [2.49] have extended the JH model to rapid solidification conditions. The TMK model can also predict a limiting velocity for the formation of a regular, coupled eutectic structure. Recently, a more complete form of new model that includes non-equilibrium effects has been developed [2.50, 2.51]. Eutectic growth has been observed in rapid solidification of some alloys such as Al-Mn [2.52], Al-Cu [2.53-2.55], Al-Si [2.56] and Co-Sb [2.57].

2.4 Solid Solubility Extension

Solid solubility extension (SSE) is one of the major constitutional effects of rapid solidification of alloy melts. SSE can be explained using thermodynamics and kinetics. A classical explanation for SSE employing thermodynamics is the use of the common-tangent construction to define solid solubility limits [2.58]. Under rapid solidification conditions, such as high cooling rate and large undercooling, some equilibrium phases may be suppressed while some metastable phases, which have higher free energy than equilibrium phases, can be formed. The formation of the metastable β' phase (Fig. 2.4), by suppression of the equilibrium β phase, causes the Gibbs common tangent to touch the plot of free energy against composition of the major α phase at the concentration of C_α'. C_α' defines the solid solubility limit for the case in which the metastable β' phase is formed. Note that the C_α' is higher than the solid solubility limit (C_α) for the case in which the equilibrium β phase is formed.

The formation of an SSE-related segregation-free microstructure may be one explanation for SSE using kinetics. The formation of this microstructure is determined either by absolute stability [2.43. 2.46] or solute trapping [2.59]. Jones [2.58] has derived an expression for the critical concentration, C_0^{crit}, by combination for the expressions of the velocity for absolute stability and of the velocity-depending partition coefficient

under a specific condition. Below the C_0^{crit} value, the formation of the segregation-free solid is controlled by absolute stability, and beyond this value solute trapping will determine the onset of formation of the segregation-free solid.

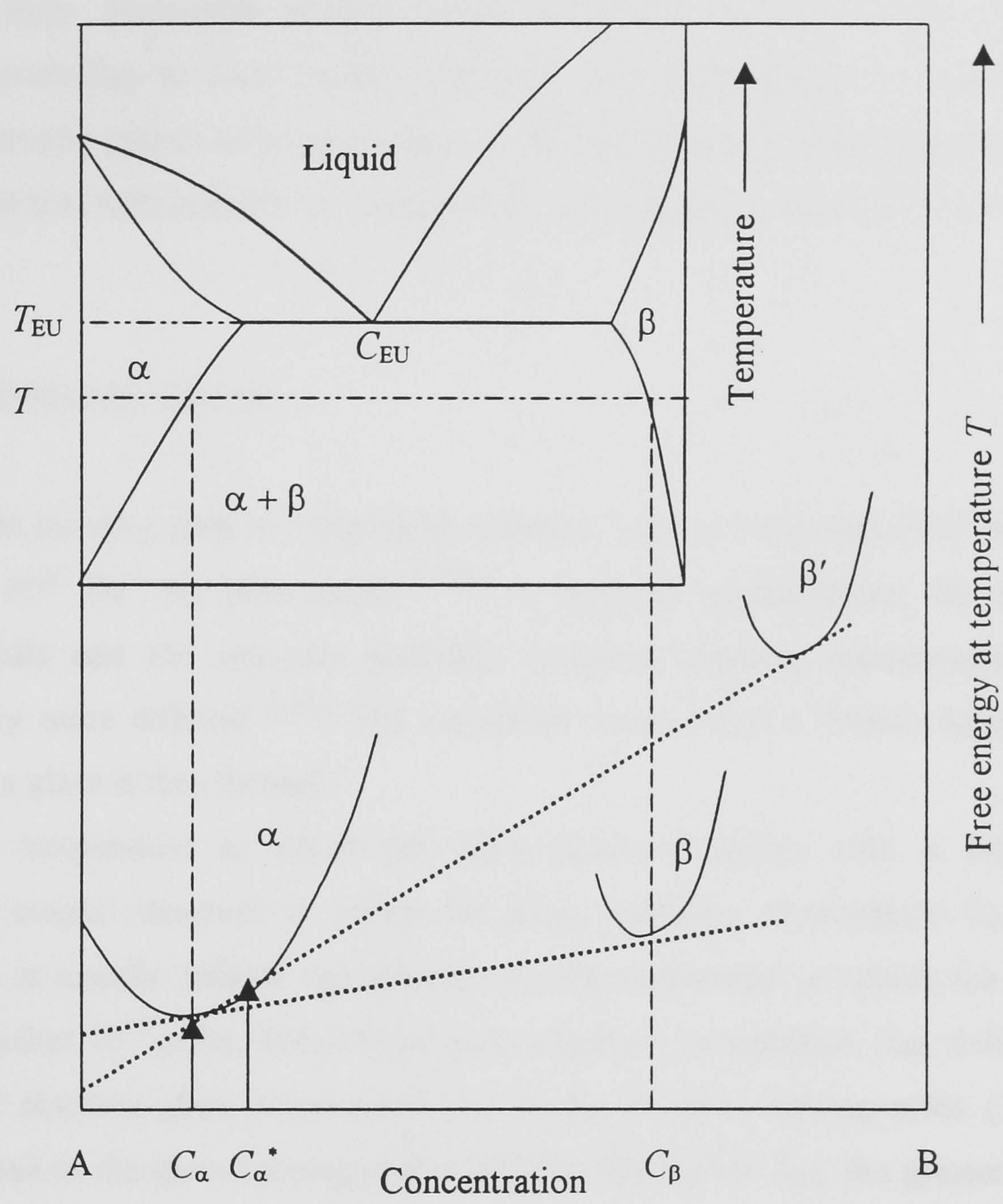


Fig. 2.4 Hypothetical diagram of free energy at temperature T against concentration for (major) phase α and (minor) phases β and β′ for a binary system A-B (adapted from Jones [2.58]). The figure illustrates the relationship between the hypothetical free energy diagram and the equilibrium phase diagram (inset) and the use of the common-tangent construction to define solid solubility limits.

2.5 Formation of Metastable Phases

In rapid solidification, an alloy is manoeuvered into a condition far from equilibrium, and its thermal energy is removed simultaneously to freeze it into a metastable state. Metastable phases, formed in rapidly solidified alloys, may be classified, according to their crystal structures, into three groups, (i) amorphous phases or metallic glasses with non-crystalline disordered atomic structures, (ii) quasi-crystalline phases with ordered but non-periodic atomic structures, and (iii) crystalline phases.

2.5.1 Metallic Glasses

When the alloy melt is cooled with extremely high cooling rates (>10^6 Ks^{-1} for alloys and 10^{10} Ks^{-1} for pure metals [2.60]) to suppress crystallisation, the density gradually falls and the viscosity gradually increases, making macroscopic flow progressively more difficult [2.61]. The amorphous structure of a "frozen liquid" or, commonly, a glass is then formed.

The temperature at which the alloy finally solidifies with a frozen-in amorphous atomic structure is called the glass transition temperature T_G. This temperature is usually defined operationally as the temperature at which the liquid viscosity reaches 10^{13} poise. The reduced glass transition temperature, T_{GR}, defined as the ratio of absolute glass temperature (T_G) to the absolute melting point (T_m), is closely related to the glass-forming ability (GFA). The higher T_{GR}, the greater is the glass-forming ability.

Metallic glasses can be formed in several materials [2.60-2.62]. Aluminium-based metallic glasses have attracted interest in development of new materials [2.63]. Metallic glasses with good ductility and promising tensile strengths as high as 1140 MPa have been reported in several Al-based alloys [2.64-2.72].

2.5.2 Quasi-crystalline Phases

The discovery of a quasi-crystalline phase was first reported in rapidly solidified Al-Mn, Al-Fe, and Al-Cr alloys [2.73]. The phase exhibited long-range orientation order and quasi-periodicity inconsistent with translation order. Since then several quasi-crystalline phases have been reported in rapidly solidified alloys, including icosahedral [2.73-2.8], decagonal [2.73-2.80], octagonal [2.81-2.86], and dodecagonal [2.87-2.90] phases. The icosahedral phase is quasi-periodic in three dimensions, whereas the decagonal, dodecagonal and octagonal phases are quasi-periodic in two dimensions and periodic in the third. A few quasi-crystalline phases exhibiting aperiodic translation along only one direction (one-dimensional quasi-crystal) have also been reported in some alloys [2.91-2.94]. Of these phases, icosahedral and decagonal phases have been most frequently observed.

Quasi-crystalline phases have been found in several alloys produced by different techniques such as rapid solidification, precipitation, solid state reaction, glass devitrification, and gas evaporation [2.74, 2.76]. Quasi-crystals can be divided into metastable and thermodynamically stable phases depending on the alloy type and composition [2.76, 2.78, 2.95, 2.96]. Stable quasi-crystals, produced by using rapid solidification or conventional casting, have structural perfection as high as the best crystals. In addition, these phases can be described by equilibrium phase diagrams and grown into large single grains [2.97].

Metastable quasi-crystalline phases are frequently prepared by rapid quenching of alloy melt. The concept of metastability of quasi-crystals is based on the fact that the internal energy lies in an intermediate state between crystal and amorphous solid [2.98, 2.99]. Metastable quasi-crystals transform to metastable or stable equilibrium crystalline phases on annealing at elevated temperatures. Crystalline phases having compositions and physical properties close to those of quasi-crystals, can be used to model the structure of quasi-crystals [2.100]. They are called "crystalline approximants".

2.5.3 Metastable Crystalline Phases

Metastable crystalline phases obtained from rapid solidification include highly supersaturated solid solution, nanocrystalline materials [2.101], and crystalline compounds. In rapidly solidified alloys, metastable crystalline phases are frequently observed in the inter-cellular/dendritic regions. In general, the cooling rate or undercooling required for formation of metastable crystalline phases is smaller than that for formation of amorphous, solid solution and quasi-crystalline phases (except stable quasi-crystalline phases). The metastable crystals may be obtained from transformation or decomposition of other non-equilibrium phases such as amorphous, solid solution, and quasi-crystalline phases during annealing. Examples of non-equilibrium crystalline phases, found in rapidly solidified Al-based alloys, have been reviewed in refs. [2.58] and [2.61].

2.6 Microstructures of Atomised Powders

2.6.1 Initially Undercooled Powders

When nucleation occurs in an undercooled melt droplet, the initial solidification rate is extremely rapid. This initial rate, however, depends strongly on the solid/liquid interface morphology. When the initial undercooling below the liquidus temperature, ΔT, is less than the ratio of L/C (where L is the latent heat per unit volume, and C the liquid heat capacity per unit volume), solidification can occur in three different morphologies, as shown in Fig. 2.5, for the case of nucleation on the powder surface [2.2, 2.102].

In Fig. 2.5 (a), a dendritic interface moves at near constant velocity across the entire particle to form a mixture of liquid and solid at the end of recalescence. The interdendritic regions solidify later by removal of latent heat from the particle surface at a much lower rate. In this case the microstructure is relatively uniform across the particle. This dendritic morphology is commonly observed in alloys having small freezing ranges such as nickel-base superalloys.

In Fig. 2.5 (b), a smooth (planar) interface moves partially across a particle to produce two zones, one solid and one liquid at the end of recalescence. Solidification is completed by removal of latent heat from the particle surface at a much slower rate to produce the coarse segregated structure shown on the right. In this case the microstructure varies across the particle. Two solidification mechanisms [2.103], namely recalescence and isothermal, have been suggested to be responsible for the formation of two microstructural zones. In the recalescence regime, the solid-liquid interface velocities are high, the undercooled droplet absorbs most of the released heat of fusion, and the external cooling plays a minor role. In the isothermal regime, solid-liquid interface velocities are lower, and strongly depend on the heat extraction at the melt droplet surface. The occurrence of two microstructural zones is frequently observed in rapidly solidified powders such as submicron powders of Al-Si and Al-Cu [2.104], and small size (-6 μm) powders of Al-Fe-Cr-Zr [2.105].

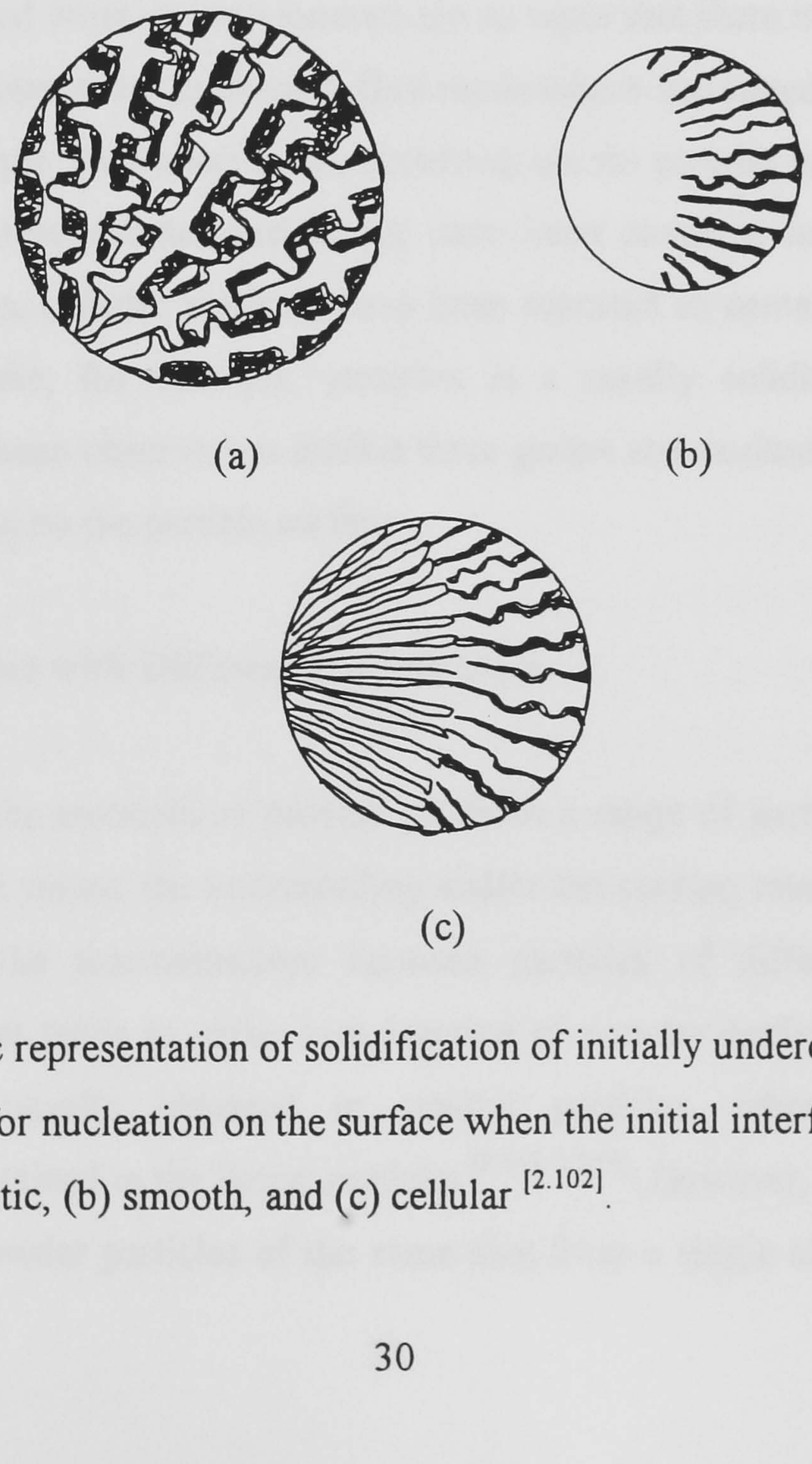


Fig. 2.5 Schematic representation of solidification of initially undercooled liquid droplets for nucleation on the surface when the initial interface is: (a) dendritic, (b) smooth, and (c) cellular [2.102].

In some aluminium alloy powders, the first zone may solidify with a finer cellular interface and the second zone then forms with a coarser structure after recalescence is complete as shown in Fig 2.5 (c). This microstructure is usually found in the rapidly solidified Al-Fe alloy powders [2.102, 2.106], splat-cooled Al-Fe alloys and melt-spun Al-Fe-Si alloys [2.107]. The first zone, designated as zone A, has a microcellular microstructure of limited etching response, and so cannot be resolved by optical microscopy. The second zone (zone B) has a coarser cellular microstructure which darkens on etching. Metastable second phases can be detected in the latter zone.

2.6.2 Powder Particles with Multiple Nucleation Sites

Alloy powder particles are frequently single grains implying that a single nucleation event is responsible for initiation of solidification. Single grain powder particles are achieved when growth kinetics are so rapid that there is insufficient time for a second nucleation event to occur before recalescence has raised the temperature. Particles with a single nucleation event occurring on the powder surface (indicating the existence of heterogeneous nucleation) have been observed in Al-8 Wt. % Fe [2.108]. In some cases, powder particles have been reported to contain more than one single nucleation site; for example, particles in a rapidly solidified Al-Fe-Cr-Zr powder [2.105] have been observed to exhibit three grains and nucleation of each grain appeared to originate on the particle surface.

2.6.3 Powders with Different Particle Sizes

In general, the atomisation process provides a range of particle sizes. As the powder particle size varies, the undercooling and/or the cooling rates change, leading to differences in the microstructure between particles of different sizes [2.109]. Structural refinement tends to occur as a function of powder particle size. The finer microstructure is usually obtained in smaller particles, whereas the coarser microstructure is obtained in the larger particles [2.105, 2.109]. However, this is not always the case because powder particles of the same size from a single atomising run may

solidify under different undercoolings resulting in different amounts of microstructural refinement.

2.6.4 Second Phase Precipitation during Solidification of Powders

The development of aluminium alloys with good elevated temperature strength may be achieved by introducing a stable dispersion of fine particles. This could be produced by precipitation from supersaturated solid solution or by the addition of hard particles to solid or liquid aluminium [2.110]. To achieve a suitable dispersion by a precipitation mechanism, it is required that some suitable alloying elements have to be added to the aluminium melt in order to form stable second phases during and/or after solidification. The transition elements appear to be the most promising additives because they have high solubility in the liquid state [2.60] (thus promoting good mixing) and the necessary low diffusivity in the solid state to prevent excessive phase coarsening. Since most transition elements have low equilibrium solid solubility limits in aluminium [2.111], phase separation and the formation of coarse primary intermetallic particles during conventional casting may retard the development of high temperature aluminium alloys. The techniques of rapid solidification offer the opportunity for extending solid solubilities and for refining microstructures thus preventing undesirable coarse intermetallics.

To obtain fine dispersoids evenly distributed in the final products, the ideal microstructure of as-atomised powders should consist of a partitionless dispersoid free solid solution or supersaturated solid solution. When the atomised powders are deformed under thermomechanical processing conditions the fine dispersoids can then be precipitated out of the solid solution to strengthen the final product. Theoretical cooling rates of between 10^{12} to 10^{15} Ks^{-1} [2.10] required for planar solidification in aluminium alloys are unlikely to obtain in gas atomisation processes which provide average cooling rates varying from 10^{2} Ks^{-1} in subsonic gas atomisation to 10^{5} Ks^{-1} in ultrasonic gas atomisation [2.112]. However, powders of small size range (from submicron up to about 20 μm) have been found to show partial or even complete partitionless microstructures [2.104, 2.105, 2.113, 2.114]. The partitionless microstructure in small particles has been attributed to fast cooling rate [2.60], high level of undercooling

[2.115, 2.116], and preferential nucleation of α-Al [2.117]. In contrast, the microstructure of larger particles normally consists of morphologies of micro-segregation (cells and dendrites) and intermetallic compounds. The existence of intermetallic compounds in coarser powder particles may be attributed to low cooling rate and insufficient undercooling. In powders solidified with micro-segregation, intermetallic compounds have usually been observed in inter-cellular/dendritic regions [2.102, 2.106, 2.110, 2.114, 2.118-2.122]. If the cooling rate is not fast enough to by-pass the nucleation of intermetallic compounds, the solute enriched particles will form first and in some cases the primarily crystallised particles may act as centres for α-phase matrix to grow on their surfaces [2.114, 2.119, 2.123, 2.124]. Some intermetallic particles may nucleate in the liquid alloy prior to atomisation. Examples of these particles, being trapped in partitionless regions, have been observed in Al-Mg-Mn alloy powders [2.113].

2.7 Phase Transformation in Rapidly Solidified Alloys

Rapidly solidified alloys are usually in the form of flakes, powders, or thin ribbons, which are unsuitable for some applications. To obtain a final product subsequent consolidation by thermomechanical processing is usually employed. Phase transformation of metastable materials is expected to occur when the as-solidified alloy is being consolidated. The requirements for processing of rapidly solidified alloys are therefore to avoid recrystallisation, decomposition or significant coarsening of microstructures. Solid state phase transformations include four types [2.125], namely precipitation, eutectoid reaction, polymorphous reaction, and peritectoid reaction. Precipitation or primary recrystallisation is the reaction by which particles of one crystalline or quasi-crystalline phase, with composition different from the matrix, are produced. During a eutectic transformation two crystalline phases grow cooperatively by a discontinuous reaction. There is no difference in the overall concentration across the reaction front; diffusion takes place parallel to the reaction front and the two components have to separate into two phases. A polymorphous transformation involves partitionless growth of one phase with different structure but the same composition as the matrix. In a peritectoid transformation a metastable phase reacts

with an embedding matrix and thus forms a new phase surrounding the metastable phase. Examples of phase transformations in rapidly solidified alloys are given below.

2.7.1 Transformation of Amorphous to Quasi-crystalline Phase

Transformation of amorphous or glassy alloys to quasi-crystalline phases have been reported in Al-Mn [2.126], Al-Mn-Si [2.127, 2.128], Al-Cu-V [2.128, 2.129], and Pd-U-Si [2.130-2.132] alloys. The devitrification from glassy to quasi-crystalline phase has been found to be analogous to the polymorphous transformation which proceeds via nucleation and growth processes. The nucleation is homogeneous, and a large number of nuclei are found in the early stage of transformation which can be explained by the existence of short-range icosahedral order in the corresponding glassy phase. The growth of icosahedral phases is due to atomic attachment at the particle interphase boundary.

2.7.2 Transformation of Quasi-crystalline to Crystalline Phase

The transformation of the quasi-crystalline phase has been observed to proceed either by a polymorphous or a eutectoid reaction or by precipitation [2.125]. In addition to those types of transformation, it has been reported [2.133, 2.134] that the transformation of icosahedral to Al_6Mn occurred via a peritectoid reaction. This transformation has been shown to proceed by nucleation and growth processes. Nucleation has been observed to occur heterogeneously at the icosahedral phase/Al-matrix interface. Growth seems to be controlled by long range diffusion, probably along the icosahedral phase/Al-matrix interface or through the growing Al_6Mn layer.

2.7.3 Transformation of Solid Solution to Intermetallic Phases

Precipitation of both metastable and stable phases from supersaturated solid solution has been studied in several rapidly solidified binary aluminium alloys such as Al-Cu, Al-Fe, Al-Hf, Al-Mn, Al-Mo, Al-Pd, Al-V, and Al-Zr. Brief descriptions of precipitation in these alloys are summarised in Table 2.1. In some investigations on

precipitation from solid solution in rapidly solidified Al-Fe, Guinier-Preston zones (GPZs) and θ″ were believed to exist in the precipitation series [2.136, 2.137]. However, it is probable that these stages are often suppressed in rapidly solidified Al-Fe powders [2.107, 2.138, 2.139], therefore they are omitted in the precipitation series. As in the case of rapidly solidified Al-Fe, there is no evidence of GPZ formation in rapidly solidified Al-Cu [2.135]. Stable or equilibrium phases may be precipitated directly from solid solution as in Al-Mo [2.142-2.144] and Al-V [2.146].

Table 2.1 Descriptions of precipitation from solid solution in rapidly solidified aluminium alloys

Alloy	Description of precipitation	Reference
Al-Cu	Solid solution → θ′ ($CuAl_2$) → θ ($CuAl_2$)	2.135
Al-Fe	(a) Solid solution → GPZ → θ″ → θ′ → Al_3Fe (b) Solid solution → θ′ → Al_3Fe	2.136, 2.137 2.107, 2.138, 2.139
Al-Hf	Solid solution → spherical Al_3Hf (LI_2) → laminated structure of Al_3Hf (LI_2) + Al_3Hf ($D0_{22}$)	2.140
Al-Mn	Solid solution → precipitates (at subgrain boundaries and within subgrians)	2.141
Al-Mo	Solid solution → $Al_{12}Mo$ (at grain boundaries) + dislocation networks separating Mo-denuded zone from Al-Mo solid solution (in Al-2.2 at. % Mo) Note: no dislocation netwroks in Al-0.7 at. % Mo	2.142-2.144
Al-Pd	Solid solution → Al_2Pd→Al_4Pd + Al_3Pd	2.145
Al-V	Solid solution → $Al_{10}V$ at grain boundaries	2.146

2.7.4 Transformation of Cellular/Dendritic Microstructure

Since the microstructure consists of a cellular/dendritic matrix enveloped with intercellular/dendritic networks of second phases, two different transformations may be expected to proceed simultaneously. Firstly, the networks of second phase break up

to form particles during annealing and with further annealing the particles spherodise. The shapes of second phase particles prior to spherodisation could be either needle-, rod-, or plate-like, depending on the type of second phase. This transformation has been observed at intercellular networks of rapidly solidified Al-Fe [2.147], Al-Cr-Fe [2.148], Al-Fe-Ni [2.106], Al-Fe-Ce-(Si) [2.149], Al-Fe-Mn [2.123], and Al-Mg-Fe [2.119]. Secondly, homogeneous nucleation within cellular/dendritic matrix leads to formation of second phase particles. The precipitation of particles within cells has been observed in rapidly solidified Al-Cr-Fe powders [2.148].

2.8 Coarsening of Second Phase Particles

The coarsening of second phase particles by solute diffusion through the matrix from dissolving particles to growing particles has been proposed by Lifshitz and Slyosov [2.150] and by Wagner [2.151], and is known as the LSW theory. The equation for coarsening of an array of spherical particles at temperature T is:

$$\bar{r}^{-3} - \bar{r}_0^{-3} = \frac{8\gamma D C_e V_m^2}{9RT} t = K't \qquad (2.2)$$

where $\bar{r}$ is the average radius of the growing particles at time t, $\bar{r}_0$ is the radius at the onset of coarsening process, γ is the interfacial free energy of the particle/matrix interface, D is the diffusion coefficient of the solute atoms in the matrix, C_e is the concentration of the solute atoms in equilibrium with a particle of infinite radius, R is the gas constant, T is the absolute temperature, and V_m is the molar volume of the precipitate. By modification of the LSW theory, an equation for disc-shaped particles can be obtained [2.152] as follows;

$$\bar{d}^3 - \bar{d}_0^3 = \frac{128\gamma^{(p)} K D C_e V_m^2}{9\pi RT} t = K^{\cdot} t \qquad (2.3)$$

where $\bar{d}$ is the mean diameter of the disc-shaped particle, $\gamma^{(p)}$ is the interfacial energy of the peripheral interface which is normal to the direction of measurement of d, K is the aspect ratio = d/h, where h is the thickness.

From both equations (2.2) and (2.3), parameters D and γ are important in controlling coarsening of second phase particles. Low diffusivity of solute atoms and low interfacial energy between the second phase particle and matrix inhibit the

coarsening process. Introduction of alloying elements with low solid solubility and low diffusivity, into aluminium alloys will therefore provide benefits in the form of stable second phase particles with low rates of coarsening at elevated temperature.

2.9 Microstructural Development in Powder Extrusion

Before extrusion, the powder is usually compacted from 85 % to 90 % theoretical density to produce a powder billet, which facilitates pre-extrusion handling and heating. The powder billet can be fully consolidated by extrusion. In extrusion, the load required to process a compacted powder billet to become 100 % dense can be determined experimentally, although the exact point at which this stage is reached is difficult to determine, and it is found to decrease with increasing extrusion temperature. The extrusion peak load can be observed in powder extrusion of some alloys such as Al-Mg [2.153], Al-Mn-Mg [2.154], particularly at low extrusion temperature. The peak has been attributed to the fact that a greater dislocation density is required to form the deformation zone than is required to maintain it during steady state extrusion [2.155].

To investigate powder consolidation by extrusion, a partially extruded and sectioned billet has been examined [2.156, 2.157]. The billet is extruded up to a point just beyond the peak load in order to ensure that the quasi-static deformation zone, a concept proposed by Sheppard and Castle [2.158, 2.159], is fully established. During extrusion, the powder billet is pressed to 100 % theoretical density. The voids, left by the cold compaction stage, are filled by re-packing of powder particles with the small powder particles occupying the interstices. All the 'trapped' air is expelled from between the powders before they start flowing into the deformation zone.

In direct extrusion, there exist two shear zones (Fig. 2.6) where deformation of a metal occurs [2.157]. The steady state flow patterns of the first shear zone are characterized by an elliptical region of intense shear which extends from the interface between billet and container towards the rear of the billet, right up to the die mouth. The second shear zone can be seen along the central axis of the billet where the maximum acceleration of material towards the die occurs. It is within this shear zone that a coherent and fully consolidated material is built from the original powder by the simultaneous shearing and welding.

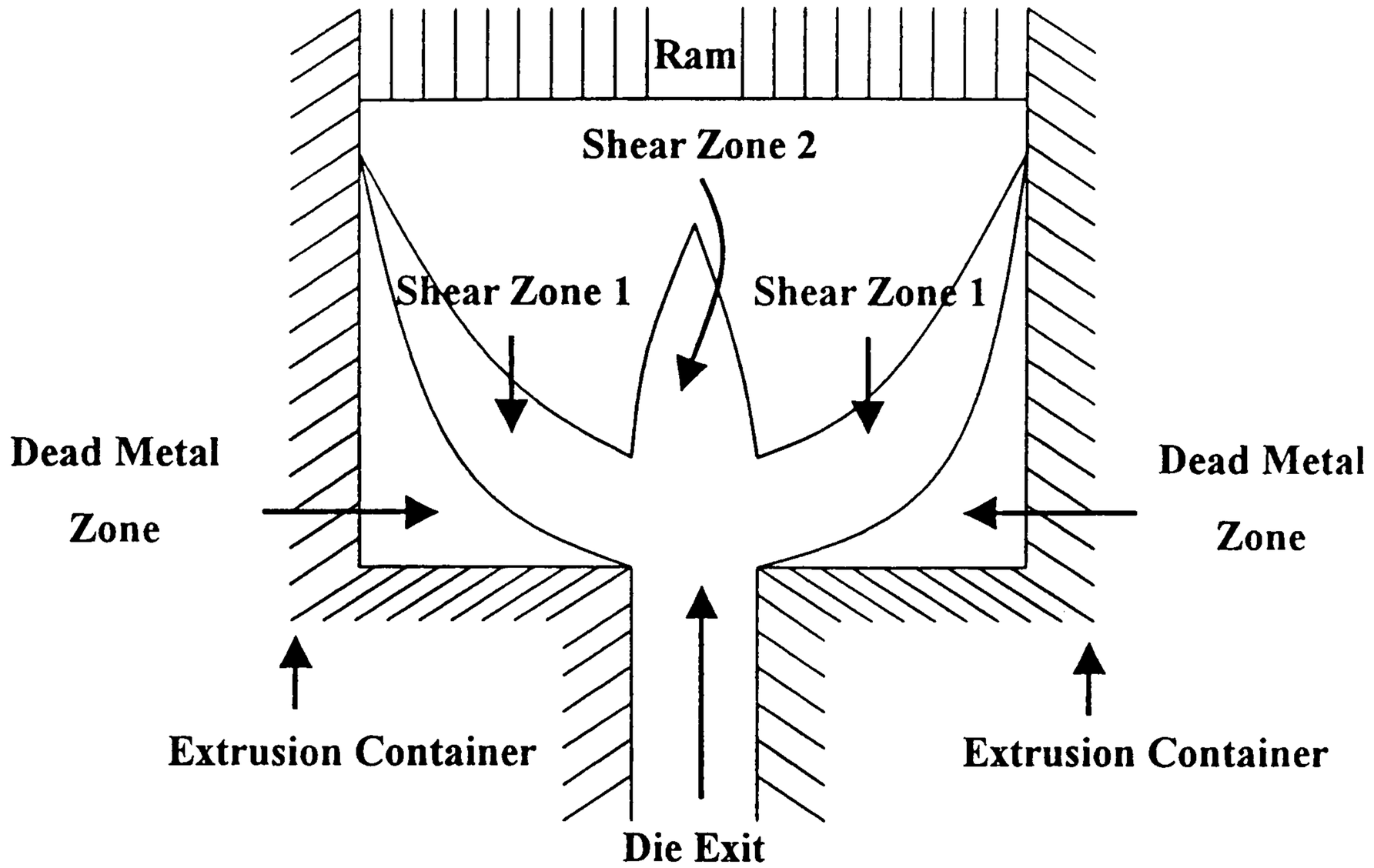


Fig. 2.6 A sketch showing shear zones in a metal billet during extrusion at a steady state flow pattern of a load/displacement curve. The figure is adapted from Fig. 3 (g) in ref. [2.198].

The work involved in building a coherent material from the shearing effect, namely 'redundant' work, has been proposed to perform the same function as sintering in the development of a coherent material from powders [2.160]. It is worth noting that not all the material within the deformation zone is fully consolidated [2.161, 2.162] (by fully consolidated we mean the original nature of the powder compact and the identities of the individual powder particles completely destroyed, and the final properties obtained). It may be concluded that the building of coherent material is a continuous welding and shearing process that continues until the shear strength of the inter-particle bonds assumes the properties of the final material.

2.10 Restoration Processes Operating during Extrusion of Metals

Extrusion is a deformation process in which plastic deformation occurs by dislocation motion and in which atomic bonds are individually broken and new bonds formed [2.163]. The plastic deformation during extrusion is effected by various mechanisms such as cross-slip, climb, and glide. More than one of these mechanisms may be operative to move dislocations at any one time. Where the operative mechanisms are dependent upon one another, the one that is slowest and requires the highest activation energy will govern the deformation and is rate controlling.

In operations producing high strains, such as extrusion, metals of high stacking fault energy (SFE) (i.e. aluminium and aluminium alloys, ∝-Fe and ferritic alloys, titanium and tungsten) undergo dynamic recovery followed by a small amount of static recovery and static recrystallisation. In the high SFE materials, climb aided by cross-slip has been established as the rate controlling mechanism [2.163]. In these materials vacancies exist in large numbers at high temperatures and they diffuse to dislocations, causing them to climb. Hence in these materials the activation energy will be more or less equal to that for self-diffusion depending upon the influence of cross-slip. The ease of dislocation climb and cross-slip promotes the dynamic recovery.

On the other hand, metals of low SFE (i.e. copper and copper alloys, γ-Fe and austenitic alloys, and nickel) may undergo both dynamic recovery and dynamic recrystallization during deformation followed by static recovery and recrystallisation during holding. However, dynamic recovery in low SFE materials may be less important because it may be impeded as the result of inherent difficulty in cross-slip and climb. The climb is difficult because the dislocations in low SFE materials are extended [2.163] or widely dissociated [2.164]. Before climb can occur over a length of dislocation line, the partial dislocations must re-associate. In these materials, glide is the predominant mechanism and the activation energy is thus specific to the deformation process [2.164].

In hot extrusion, dynamic softening processes usually occur as the material is being deformed. If the hot-extruded material is quenched immediately the microstructure resulting from dynamic softening processes may be preserved. However, if the hot-extruded material is slow cooled, the static softening processes may occur. A brief review of these processes is given below.

2.10.1 Dynamic Recovery

The process of dynamic recovery, occurring during the application of stress and strain at temperatures above 0.5 T_m [2.165] (where T_m is the melting point of the material in Kelvin), is dependent upon the dislocation climb and vacancy migration mentioned above. In high SFE materials, dynamic recovery is rapid and extensive at high temperature and is usually the only form of dynamic restoration that occurs [2.166].

The stress-strain curve of dynamic recovery is typically characterized by a rise to a plateau followed by a constant or steady state flow (Fig. 2.7). At the start of deformation the flow stress quickly rises to a maximum due to the generation and multiplication of dislocations [2.167]. Generally, dislocations generated in metals are mixtures of screw and edge. In the simple case, when only edge dislocations are considered, dislocations may be either positive or negative in sign. Unlike dislocations attract each other and, if they intersect, are mutually annihilated. On the other hand, like dislocations have stress fields which repel each other. As the dislocation density is increasing, dislocations initially form tangles but soon rearrange themselves into rough cells outlined by intersecting dislocations.

However, thermal activation will assist the dislocations to cross-slip and climb causing either annihilation by mutual interactions or rearrangement by repolygonization into well defined walls that are roughly equispaced. The increasing dislocation annihilation causes a reduction in the rate of work hardening until a steady state flow stress condition is reached, or in other words, the rate of work hardening by dislocation generation is in equilibrium with the annihilation rate. During deformation at strain rates greater than ~ 1 s^{-1} the heat generated by the work of deformation

cannot all be removed from the specimen and the temperature of the specimen rises during deformation [2.166]. This may then cause a reduction in the flow stress as straining proceeds.

During the steady state deformation (under constant temperature, strain rate, and flow stress), the stable equiaxed subgrains form and persist throughout this stage of the process without change in their size or wall density [2.165]. The subgrain misorientation also remains constant to preserve a constant dislocation density during high-temperature steady state deformation in hot working.

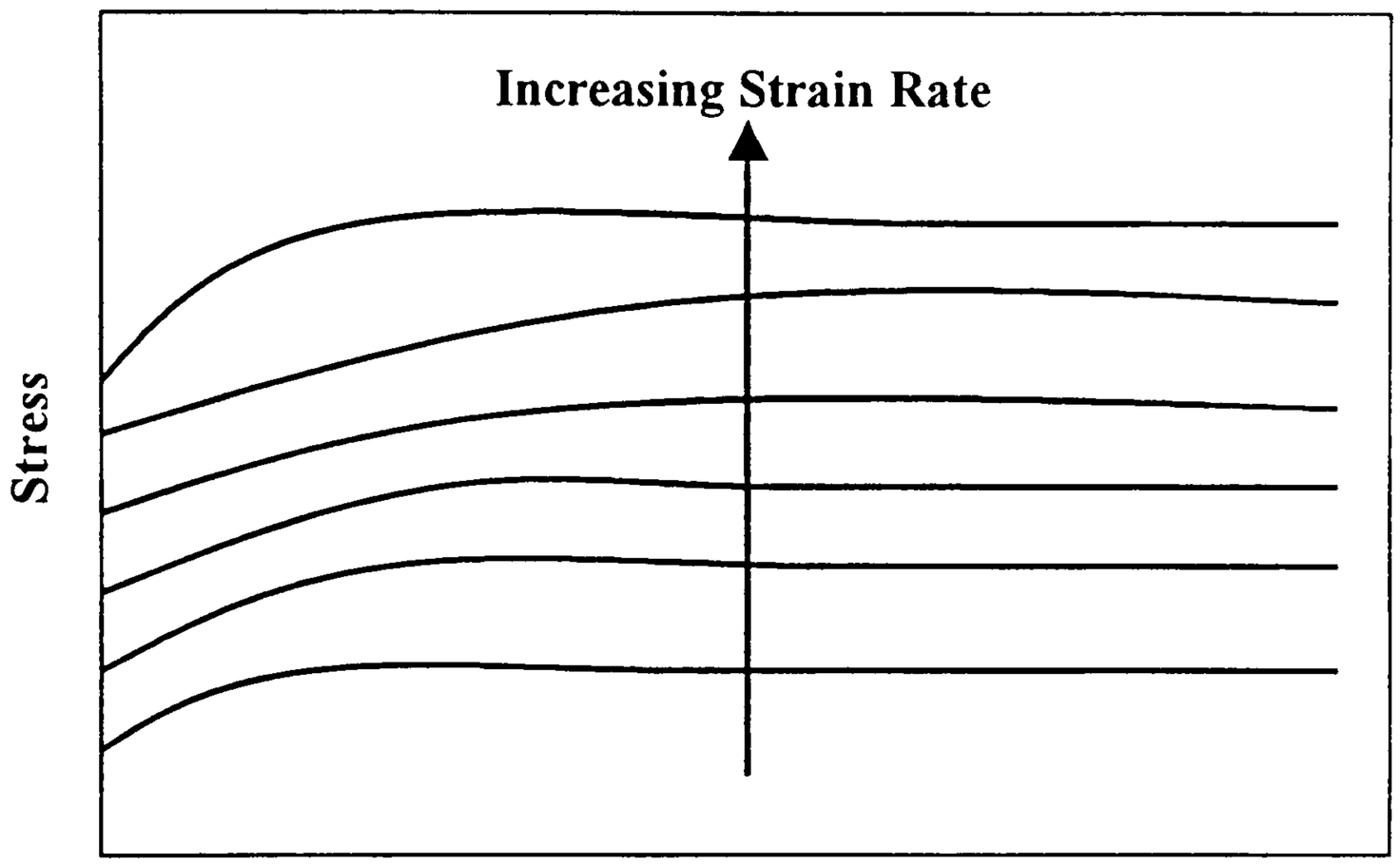


Fig. 2.7 Stress-strain curves for dynamic recovery (adapted from ref. [2.190]).

The subgrain size varies when the process variables are changed. Two important control variables that affect the subgrain size are temperature and strain rate [2.167, 2.168-2.171]. The subgrain size increases with an increase in temperature and with a decrease in strain rate. Deformation at high temperatures causes a higher rate of dislocation annihilation so the steady state is approached with a coarser substructure, and hence, also with a lower flow stress. Note that the rate of dislocation annihilation depends on the dislocation density, and on the ease of operation of recovery mechanisms, such as climb, cross-slip, and node unpinning. The stress required for deformation is inversely dependent on the subgrain diameter [2.169, 2.170].

2.10.2 Dynamic Recrystallization

In metals in which recovery processes are slow, such as those with a low or medium SFE, dynamic recrystallization may take place when a critical deformation condition is reached. Recrystallization is believed to occur by two different mechanisms [2.172]. The first mechanism known as *rotation* or *in situ* recrystallization is defined by a gradual increase in the misorientations of a stable dynamic recovery dislocation sub-cell structure. Eventually the misorientations are such that the sub-boundaries are indistinguishable from high angle grain boundaries. The second mechanism is characterized by a migration of pre-existing high angle grain boundaries through the deforming microstructure leaving a strain free region in their wake.

Dynamic recrystallization originates at high angle boundaries which can be either the original grain boundaries [2.166, 2.171, 2.173-2.176] or boundaries of dynamically recrystallized grains or boundaries created during straining (e.g. those associated with deformation bands) [2.166, 2.171, 2.176]. In addition, nucleation of recrystallization has been found to originate at interfaces between matrix and large second phase particles [2.177-2.185]. In some commercial aluminium-magnesium alloys, it has been suggested that the occurrence of dynamic recrystallization during hot working is due to its nucleation at second phase particles [2.186-2.188].

Development of microstructure during dynamic recrystallization starts preferentially at the original grain boundaries where new grains are subsequently nucleated and in this way a thickening band of recrystallized grains is formed. If there is a large difference in the original grain size and the recrystallized grain size then a necklace structure of grains may be formed. Finally, the material will become fully recrystallized if it is heavily deformed.

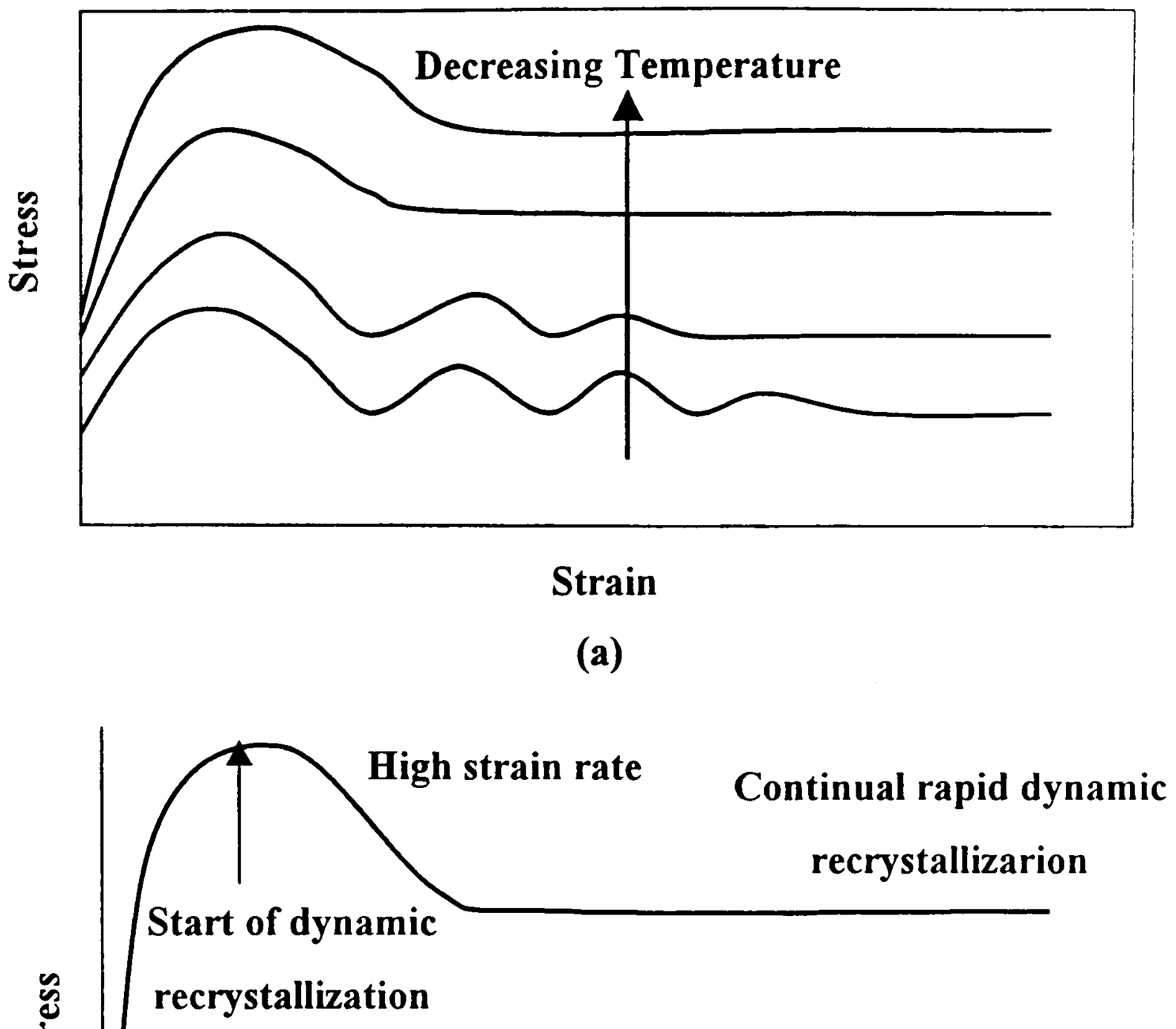


Fig. 2.8 Stress-strain curves for dynamic recrystallization:
(a) the effect of temperature [2.166], and (b) the effect of strain rate [2.167].

Dynamic recrystallization may be indicated by one or several peaks in the stress-strain curve at a comparatively low strain (Fig. 2.8). The peaks are followed a steady state plateau that may decline slightly due to deformational heating. The substructure generated in dynamic recrystallization varies with the process variables such as strain rate, and temperature [2.171, 2.189]. The size of dynamically recrystallized

grains increases with increasing temperature and decreasing strain rate. The size of dynamically recrystallized grains is inversely proportional to the steady-state flow stress [2.167, 2.171, 2.173, 2.175, 2.190].

2.10.3 Static Recovery

Static recovery is the process that occurs early in the annealing of cold- or hot-worked metals before the appearance of new strain-free grains. There is almost no motion of grain boundaries during recovery. By using light microscopy, there is little observable change in the microstructure of the elongated grains produced by working. Several mechanisms of recovery have been suggested [2.5, 2.191].

The temperature at which recovery is occurring may influence the mechanism which operates. For example, mechanisms involving vacancy motion, dislocation motion without climb, dislocation motion with climb, operate at low, intermediate, and high temperature ranges, respectively. Mechanisms that lead to changes in mechanical properties involve motion and rearrangement of dislocations.

In worked metals of high SFE, a cell structure (dislocation network) forms during deformation. When straining is interrupted, static recovery can gradually lead to considerable softening. The best-known mechanism for recovery is polygonization. By this mechanism, the dislocations within the cells are attracted into the cell walls and the redundant dislocations in the cell walls annihilate each other, leaving neat dislocation networks separating the polygonal crystallites.

The subgrains may grow larger as the shared subboundary between neighbouring subgrains is unraveled, and the individual dislocations move away, becoming incorporated in other boundaries or annihilated. By such a mechanism of growth, a cluster of subgrains may become a nucleus for subsequent recrystallization. In worked metals of low SFE, the dislocatons are present in planar arrays of high energy, which constitute a strong driving force for recrystalliztion.

2.10.4 Static Recrystallization

Static recrystallization occurs by the formation and growth of new grains that have much lower dislocation densities than the deformed grains they replace. Generally, static recrystallization occurs after recovery. Nucleation of static recrystallization may occur by several mechanisms. Recrystallization of hot-worked structures of Al-2Mg has been found to involve subgrain coalescence followed by boundary migration [2.192]. Subgrain coalescence by which the orientation mismatch between two neighboring grains has been eliminated, leads to the establishment of regions of low internal dislocation content surrounded by boundaries of high misorientation capable of migrating [2.167].

In metals of low SFE, the concentration of dislocations in the tangles is higher, and the cell walls appear to develop high misorientations, and therefore become capable of migrating. Once nuclei are formed, they grow into the deformed material by the migration of their boundaries. The driving force for migration is provided by the difference in dislocation density between the interior of a nucleus and the surrounding worked metal. The process of recrystallization is considered complete when all of the worked regions have been consumed, and the growing nuclei impinge upon each other.

2.11 Microstructures of Extruded Aluminium Alloys

2.11.1 Dynamic Recovery in Aluminium Alloys

Microstructural investigations of extruded rods from commercially pure aluminium billets [2.168, 2.193], as-cast aluminium alloy billets [2.159, 2.1163, 2.194] and aluminium alloy powder compacts [2.127, 2.138, 2.195], by light microscopy, have shown that a typical 'fibrous' structure appears across the sections of the rods. In aluminium

or aluminium alloys which undergo dynamic recovery, the fibrous structure consists of the original cast grains (or powder particles) elongated in the extrusion direction and having an aspect ratio roughly equal to the extrusion ratio. The fibrous effect is due to the high angles existing between the string-like grains.

When the fibrous structure is investigated by TEM, details of the microstructure are revealed. Microstructures of longitudinal sections of extruded product of Al-Mg-Si have been found to exhibit elongated subgrains formed by dynamic recovery, indicating their formation in the deformation zone before exit from the die [2.196]. The elongation of dynamically recovered subgrains has been shown [2.197] to increase with increasing strain and reduced deformation temperature.

Bands of subgrains bisecting the grains and elongated in the extrusion direction have been observed in extruded Al-5Mg alloy [2.198]. Misorientations are higher between these bands than between the subgrains within them. Subgrain banding occurs in the die entry region during upsetting and is a result of inhomogeneous deformation. This is probably aided by large grain sizes and heterogeneous grain size distribution.

During the steady-state deformation of aluminium, the dynamically recovered subgrains of transverse sections of extruded product are equiaxed with constant size and misorientation. The extruded subgrain size has clearly been established to be a function of the temperature-compensated strain rate.

2.11.2 Dynamic Recrystallization in Aluminium Alloys

Light micrographs of the cross section of extruded rods which undergo dynamic recrystallization, for example those of Al-5Mg-0.8Mn alloy [2.186, 2.199, 2.200], exhibited duplex structures in which the dominating feature is an annulus of recrystallized grains surrounding an inner 'fibrous' core consisting of original, dynamically recovered cast grains. The occurrence of recrystallization at the surface may be promoted by the conditions of more intense deformation due to the fact that the surface is generated by the intense bands of shear adjacent to the dead metal zone. It may also be promoted by the higher temperatures due to greater heat generation in

this area. The increased dislocation density and increased stored energy may provide a driving force for recrystallization. The depth of recrystallized surface layer depends on the process variables. The depth of recrystallization decreases linearly with the increasing natural logarithm of the temperature-compensated strain rate [2.200].

Nucleation of the recrystallized grains in aluminium alloys differs from that in low SFE materials in that it appears to occur mainly at second phase particles, dispersoids, or dislocation tangles at grain boundaries [2.201]. Evidence of dynamic recrystallization is provided by the presence of deformed substructures within equiaxed grains which supports the dynamic nature of the process (new grains nucleated are being deformed as they grow). Low angle boundaries are formed from the dislocation tangles within dynamically formed grains. With a concept of dynamic recrystallization, a range of grain misorientations can be expected, from low to high angles, since the grains are nucleated at different times during the deformation cycle.

The other evidence of dynamically recrystallized grains has been suggested to be the absence of fibrous elongated grains and the presence of equiaxed grains containing a substructure in the longitudinal section, for example in extrusion of Al-10Mg [2.202]. Dynamic recrystallization has also been observed in extrusion of Al-7Mg powder billets [2.201].

2.12 Transformation and Coarsening of Second Phase Particles in Extruded Aluminium Alloys

In addition to development of substructures by the restoration processes of recovery and recrystallization, microstructures of extruded aluminium alloys also include second-phase particles that originate from phase transformations occurring during either post-solidification, or preheating, or extrusion. Phase transformation during these processing stages can be explained as in § 2.7. However, the factors that control the transformation during annealing may be slightly different from those in extrusion. The precipitation temperature of equilibrium Al_8Fe_2Si phase during extrusion has been found to be lower than the precipitation temperature of the same

phase during a DSC study [2.203]. The lowering of precipitation temperature during extrusion results from the influence of strain.

The kinetics of coarsening show that second phase particle sizes increase with increasing preheating (exposure) time at a given temperature [2.204]. The diameter and volume fraction of second phase particles also increase with increasing extrusion temperature [2.205]. Since preheating takes a longer period of time than extrusion, reduction of preheating time by employing a faster heating rate, such as induction heating, may reduce coarsening of particles during consolidation.

2.13 Microstructural Inhomogeneity in Extruded Aluminium Alloys

Because of microstructural variation in an individual powder particle or in the range of powder particle size, the extruded products of powders may be expected to exhibit inhomogeneous microstructures. This phenomenon has been observed in the extruded product of Al-Fe-Ni-Co powders [2.196]. It was illustrated by the formation of a band of larger subgrains aligning in the extrusion direction and containing very few precipitates. The bands were bounded by oxide particles formed from the original powder particle surfaces. Above and below the band were finer subgrains with dense volume fractions of precipitates.

Ioannidis and Sheppard [2.148] have pointed out that the heterogeneity of the microstructure could be attributed to the variation in powder particle size, resulting in bands, aligned in the extrusion direction, with different-sized precipitates and subgrains. The size of the bands is restricted by oxide particles formed as surface layers during atomization and broken up during consolidation.

Microstructural inhomogeneity may also result from undeformed fine powder particles, typically with diameter < 10 μm [2.206, 2.207], which are found in most extruded powder compacts. The number of undeformed powder particles decreases with increasing extrusion temperature. This is due to the deformation of the powders being encouraged at high extrusion temperature.

CHAPTER 3

DEVELOPMENT OF RAPIDLY SOLIDIFIED Al-Fe-(V, Si) ALLOYS

Rapid solidification from the melt has opened up a new route to advanced alloy design by allowing greater constitutional and microstructural latitude than is possible using conventional metallurgical processes. Since the pioneer investigations on rapidly solidified materials by Duwez *et al.* [3.1-3.4], several high strength and elevated aluminium alloy systems have been developed employing RSP. The rapidly solidified aluminium alloys usually contain transition metals as alloying elements possessing high solubility in the liquid state but low diffusivity in the solid state.

There has been growing interest in the development of the Al-Fe based alloy system which is considered to be a potential candidate for light weight alloys with useful mechanical properties at elevated temperature. These properties are generally associated with a fine dispersion of thermally stable intermetallic phases with slow structural coarsening. Thermal stability of the microstructure is attributed to high activation energy for diffusion and low solubility in the solid state. The promising Al-Fe based alloy systems are Al-Fe-Ce [3.5-3.8], Al-Fe-Mo [3.9, 3.10], Al-Fe-Ni [3.11, 3.12], Al-Fe-Ti [3.13], Al-Fe-Zr [3.14, 3.15], and Al-Fe-V [3.16, 3.17]. Amongst these alloy systems, the Al-Fe-V alloys exhibit excellent strength, thermal stability, fracture toughness, and creep properties at both room and elevated temperatures. A review of the development of rapidly solidified binary Al-Fe and Al-V, ternary Al-Fe-V, and quaternary Al-Fe-V-Si alloys is given below.

3.1 Binary Al-Fe Alloys

The pioneer study of rapidly solidified Al-Fe alloys with iron content up to 39.2 wt. % using splat cooling revealed novel refined microstructures which were much different from those of conventional as-cast materials [3.18]. In the splat-cooled Al-Fe alloys containing 4 to 20 wt. % Fe there is a transition between two

optically distinct microstructures. The microstructure of the substrate side of the foil (zone A) is characterized by only a slight response to the etchant, revealing very fine primary dendrites (cells). The microstructure of the centre part of the foil (zone B) is characterized by strong response to the etchant, revealing much coarser and segregated dendrites. The microstructural transition from zone A to zone B has also been observed in the later investigations of rapidly solidified binary Al-Fe alloys, for example, the melt-spun Al-7.5 wt. % Fe [3.19], gas-atomised and melt-spun Al-8 wt. % Fe [3.20-3.23], and in melt-spun Al-2 to 8 wt. % Fe [3.24].

A significant improvement in mechanical properties, particularly properties at elevated temperatures, of rapidly solidified Al-Fe alloys over conventional heat resistant aluminium base alloys has been observed. This improvement was attributed to the fine scale and stability of the microstructures. The microhardness of zone A in Al-4 to 8 wt. % Fe was observed to be high and stable between 200 to 350 °C [3.18, 3.21, 3.23, 3.25]. However, due to the coarser scale and segregation in zone B, the microhardness of this zone was lower. Mechanical properties of extrusion consolidated rapidly solidified Al-Fe alloys have been shown to be improved and to be appropriate for both room and elevated temperature applications [3.25, 3.26].

The extension of solid solution, resulting from the large departure from equilibrium constitution because of solidification with high velocity, in binary Al-Fe alloys has been investigated by several authors [3.19, 3.27, 3.28]. Evidence of extended solubility of iron in the aluminium matrix has been given {4.4 at. % Fe (8.6 wt. %) in Al-Fe solid solution} for RSP.

The formation of metastable Al-Fe phases in rapidly solidified Al-Fe alloys has been the subject of many investigations over a number of years. It is well known that under different solidification conditions, competitive growth can result in the formation of several different intermetallic phases.

For the hypo-eutectic Al-Fe alloys, the formation of intermetallic phases designated as Al_3Fe, Al_6Fe, Al_xFe, Al_mFe, and Al_9Fe_2 during solidification has been suggested to be controlled primarily by melt composition and, particularly, by the local cooling rates (Fig. 3.1) [3.29]. Recently, it has been reported that the formation of intermetallics is controlled by growth rate [3.30]. The Al-Al_3Fe eutectic was found to predominate in the interdendritic regions of a hypo-eutectic Al-Fe alloy solidified with growth rates less than 15 mm/min. For growth rates between 15 and 30 mm/min, there was a mixture of Al_3Fe and Al_6Fe occurring in the interdendritic regions and the amount of Al_3Fe present in the mixed intermetallics

was found to decrease with increasing growth rate. For growth rates greater than 30 mm/min, the Al_6Fe phase was predominant.

For the Al-Fe alloys near the eutectic composition (≈ 1.8 wt. % Fe), the formation of Al-Al_3Fe eutectic could be replaced by the Al-Al_6Fe eutectic reaction when growth rates were higher than critical values (these values were composition dependent) [3.31]. The critical growth rate for Al-2.0 wt. % Fe was 3.6 mm/min. The Al_3Fe was completely absent when even higher growth rates were obtained. A similar result has been reported in that the equilibrium 'irregular-morphology' Al-Al_3Fe eutectic grows at growth rates less then 7 mm/min whereas the 'rod-like' Al-Al_6Fe eutectic predominates at growth rates greater than 7 mm/min [3.32].

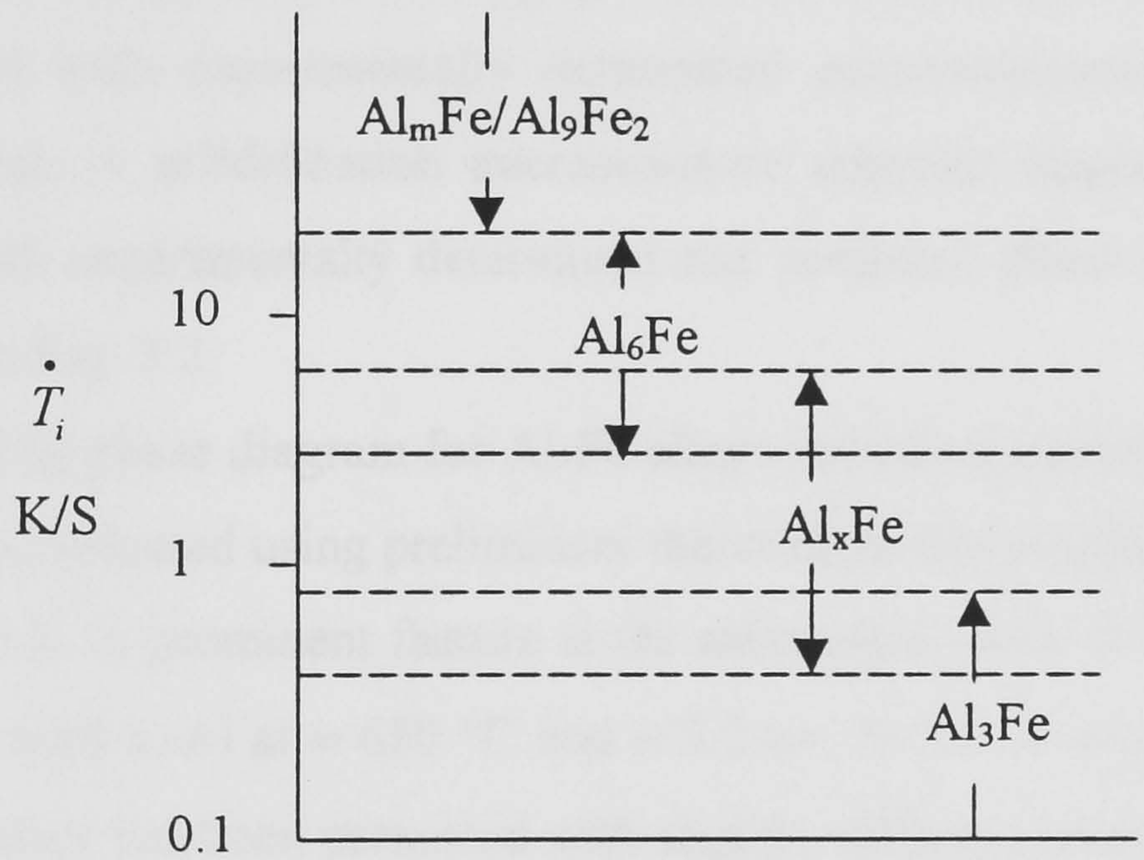


Fig. 3.1 Approximate cooling rate regimes for formation of the different intermetallic phases in hypoeutectic Al-Fe alloys [3.29].

Microstructures of the hyper-eutectic Al-Fe alloys, have been shown to be a function of both growth rate and alloy concentration. Investigations of Al-Fe alloys with 2.2 to 6.1 wt. % Fe, employing the Bridgman growth technique, have shown that Al-Al_3Fe eutectic either alone or together with α-Al or Al_3Fe was the predominant morphology at low growth rates (≤ 0.1 mm/s), whilst the Al-Al_6Fe eutectic alone or together with α-Al or Al_3Fe was observed at moderate growth rates (0.1 to 10 mm/s) [3.33]. The coexistence of primary Al_3Fe with Al-Al_6Fe was reported to persist to higher growth rates with increasing iron content.

Investigations have been extended to higher iron content binary Al-Fe alloys (up to 28.1 wt. % Fe) using Bridgman solidification with growth rates of 0.01-6.4 mm/s [3.34]. A morphology change in primary Al_3Fe from clustered and micro-faceted to plate-like, and finally needle-like, was found with increasing growth rates. The transition moved to a higher growth rate with increasing volume fraction of primary Al_3Fe. From experimental observations, it was proposed that the plate-like primary Al_3Fe developed from needle-like dendrite tips.

Recently, a laser surface treatment technique, which facilitates higher growth rates than those obtained by the Bridgman growth technique, has been used to study solidification behaviour of Al-Fe alloys with compositions up to 8 wt. %Fe [3.35]. Microstructures of laser surface treated Al-Fe alloys exhibited banded structures and plane fronts at high growth rates. In the same study, a comparison of predicted with experimentally determined microstructures showed satisfactory agreement. A solidification microstructure selection diagram (map) constructed from both experimentally determined and predicted phase boundaries [3.33, 3.35] is shown in Fig. 3.2.

The phase diagram for Al-Fe alloys including metastable phase boundaries has been evaluated using preliminary thermodynamic modelling [3.36], and is shown in Fig. 3.3. A prominent feature is the metastable phase Al_6Fe and its metastable eutectic with α-Al at ≈ 650 °C and ≈ 3.2 wt. % Fe. A similar phase diagram for Al-Fe alloys has been presented with slightly different eutectic composition of 3.5 wt. % Fe [3.31]. Recently, the eutectic growth temperature of the Al-Fe system has been measured as a function of growth rate [3.37]. The equilibrium eutectic temperature of α-Al-Al_6Fe was also determined and found to be 652.9 °C. This temperature was higher than the eutectic α-Al-Al_6Fe temperature of 650 °C obtained in ref. [3.36].

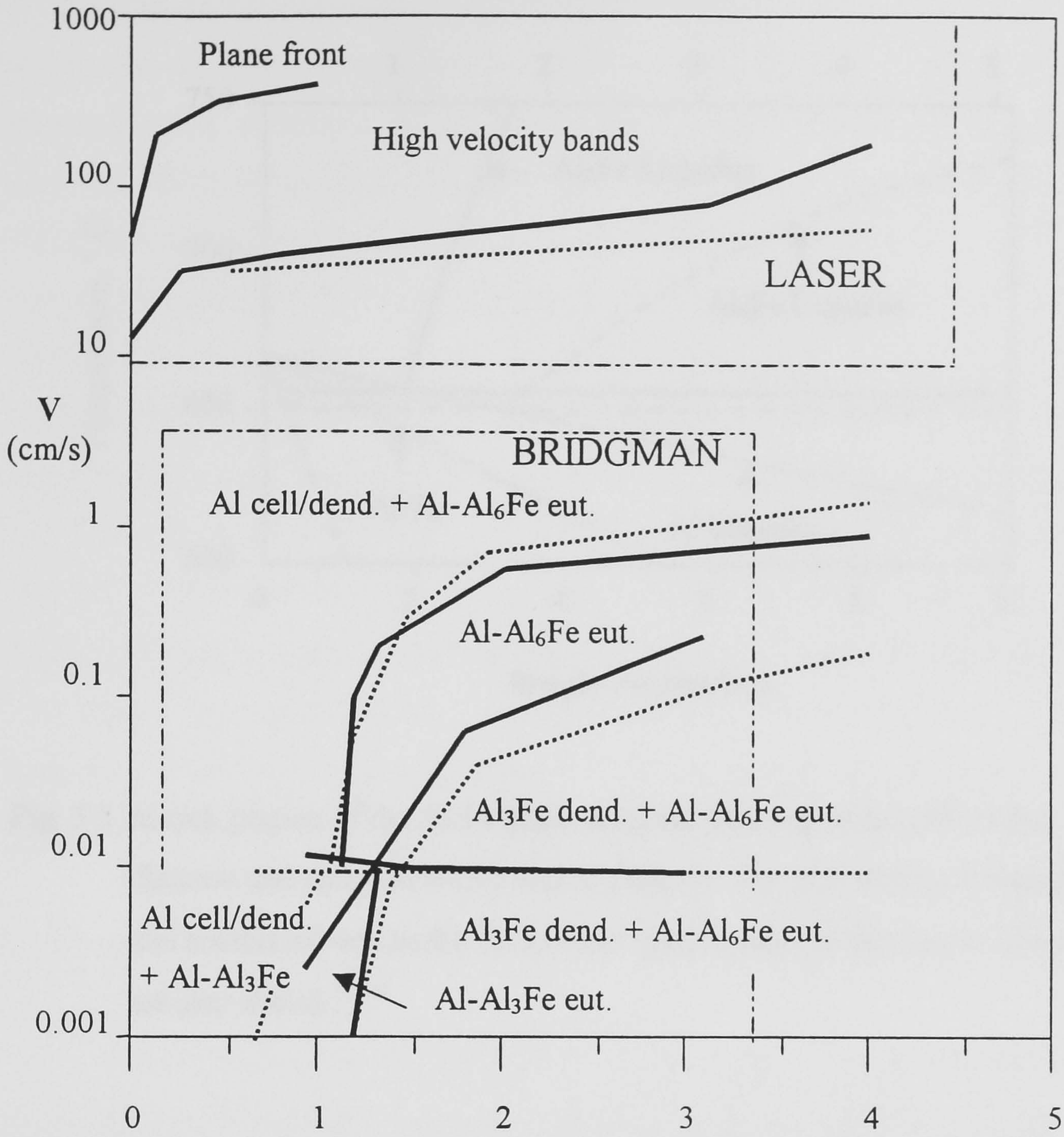


Fig. 3.2 Solidification microstructure selection diagram for Al-rich Al-Fe alloys. The full lines are experimentally observed boundaries. The lower part exhibits experimental results using the Bridgman growth technique ($V = 10^{-3}$ - 1 cm/s and $G \approx 10$ K/mm) [3.33]. The upper part exhibits experimental results from a laser surface treatment technique ($V = 1 - 3x10^{2}$ cm/s and $G \approx 2000$ K/mm) [3.35]. The dotted lines represent predictions for competitive growth modelling [3.35].

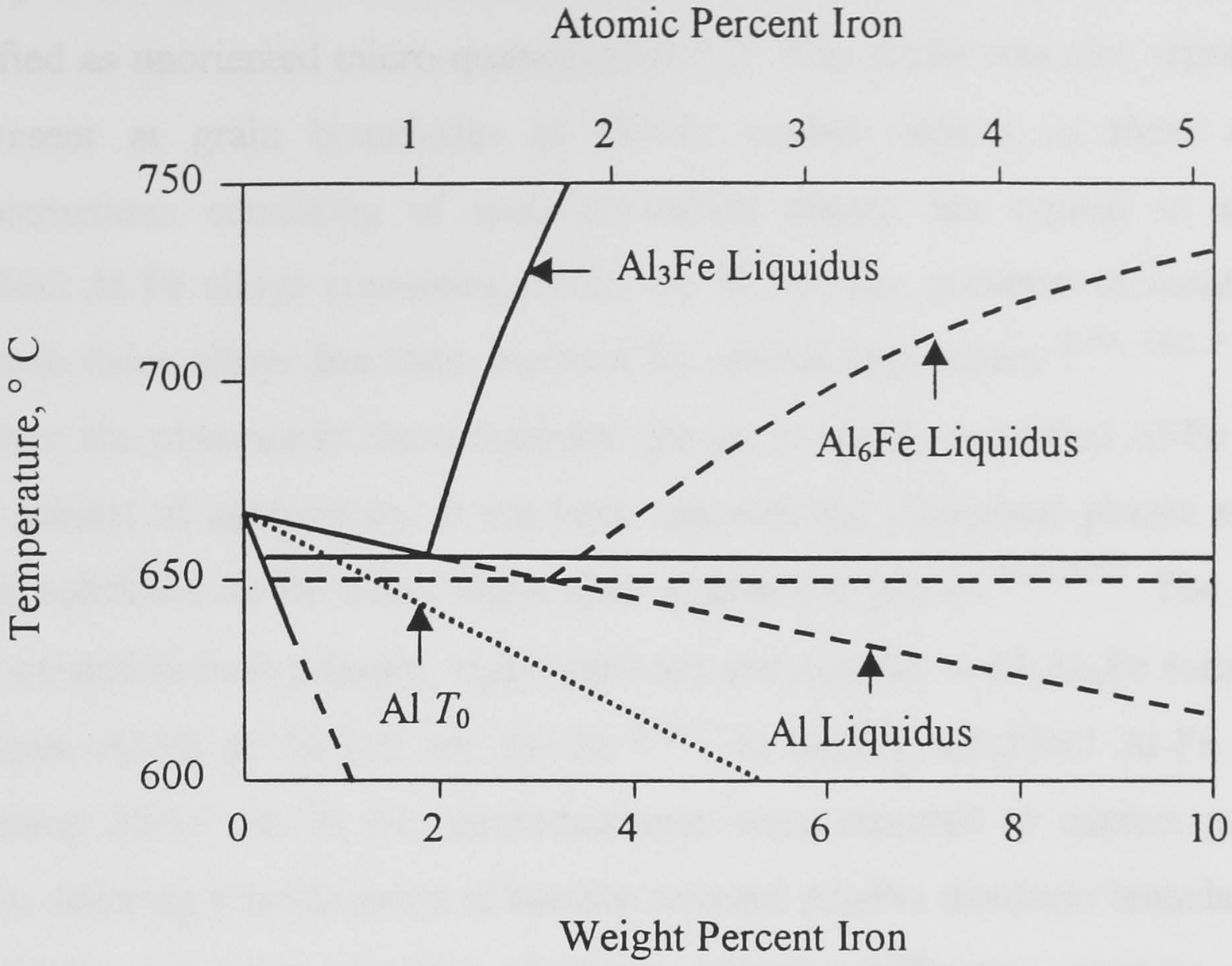


Fig. 3.3 Al-rich portion of the Al-Fe phase diagram showing stable (Al-Al_3Fe) diagram and metastable (Al-Al_6Fe) diagram. The extended α-Al liquidus and solidus as well as the T_0 curve for partitionless solidification of α-Al are also shown [3.36].

Microstructures of rapidly solidified hyper-eutectic Al-Fe alloys with up to 35 wt. % Fe have been reported to consist of different combinations of phases. The phases included primary α–Al, Al_3Fe, Al_6Fe, Al_mFe, quasi-crystalline phases (decagonal and icosahedral), and intercelluar/dendritic phases which could be Al_6Fe, Al_mFe or quasi-crystalline phases, depending on the cooling rate and the alloy composition. Before 1984, both the globular phases and the phases at the cell walls formed in rapidly solidified Al-Fe alloys were reported as being the same 'S' phase [3.38]. However, since the discovery of the icosahedral phase in rapidly solidified Al-Mn [3.39], the independently nucleating spherical primary particles, referred to as 'O' phase, possessing electron diffraction patterns with typical icosahedral symmetry, have been identified as icosahedral phase particles in the Al-Fe system [3.40]. The formation of an icosahedral phase was claimed to result from diffusionless solidification with growth rates of 1-2 ms^{-1}.

Melt-spun Al-Fe alloys containing up to 15 wt. % Fe were observed to solidify with microcellular structures, and the intercellular phases were later identified as unoriented micro-quasicrystals [3.41]. The Al_6Fe was also reported to be present at grain boundaries in slowly cooled regions in these alloys. Microstructures consisting of quasi-crystalline phases are typical in rapidly solidified Al-Fe alloys containing 15-22 wt. % Fe. The presence of icosahedral phases in these alloys has been reported by several researchers [3.39, 3.40, 3.42-3.46]. However, the presence of the icosahedral phases in rapidly solidified Al-Fe alloys is the subject of controversy. It has been reported that decagonal phases exist in rapidly solidified Al-Fe alloys rather than icosahedral phases [3.47-3.50]. The Al_mFe phase existed in both primary Al_mFe particles and eutectic α-Al-Al_mFe eutectic in melt-spun Al-10 at. % (19 wt. %) Fe [3.50]. In rapidly solidified Al-Fe alloys containing 25-35 wt. % Fe, microstructures were reported to contain primary $Al_{13}Fe_4$ showing a radial array of heavily twinned $Al_{13}Fe_4$ dendritic branches [3.40, 3.50]. There was close similarity between electron diffraction patterns of the decagonal, Al_mFe, and $Al_{13}Fe_4$ phases [3.49, 3.50], suggesting that the $Al_{13}Fe_4$, and Al_mFe phases may be approximants of the Al-Fe decagonal phase.

3.2 Binary Al-V Alloys

For the binary Al-V system (0-25 at. % V), the aluminium-rich side of the phase diagram is characterized by five peritectic reactions and four intermetallic compounds, Al_3V, Al_6V, Al_7V, and $Al_{10}V$ [3.51, 3.52] as shown in Fig. 3.4. These compounds are known to be formed at the successively lower temperatures, 1360, 736, 688, and 670 or 677 °C. The final peritectic reaction, occurring at about 661 °C, results in the formation of α-Al (about 0.2 at. % V).

Rapidly solidified binary Al-V alloys have been investigated by several researchers. Terminal solid solubility extension was found to vary from 1.1 at. % in plasma jet spray quenched [3.53] to 2 at. % V in splat quenched Al-V alloys [3.51]. Microstructures of splat-quenched binary Al-V alloys [3.51], with vanadium contents up to 24 at. %, were reported to be varied depending on nominal alloy compositions. In alloys with vanadium content up to 2 at. %, the microstructure consisted of major α-Al phase and small amount of unknown phases. The minor phases $Al_{10}V$ and Al_6V and traces of Al_3V and unknown phases existed in addition

to the major α-Al phase in alloys with 2 to 13 at. % V. In alloys with higher vanadium content, Al_3V became a dominant phase. The metastable icosahedral phase was observed in Al-13.9 at. % V as a minor phase.

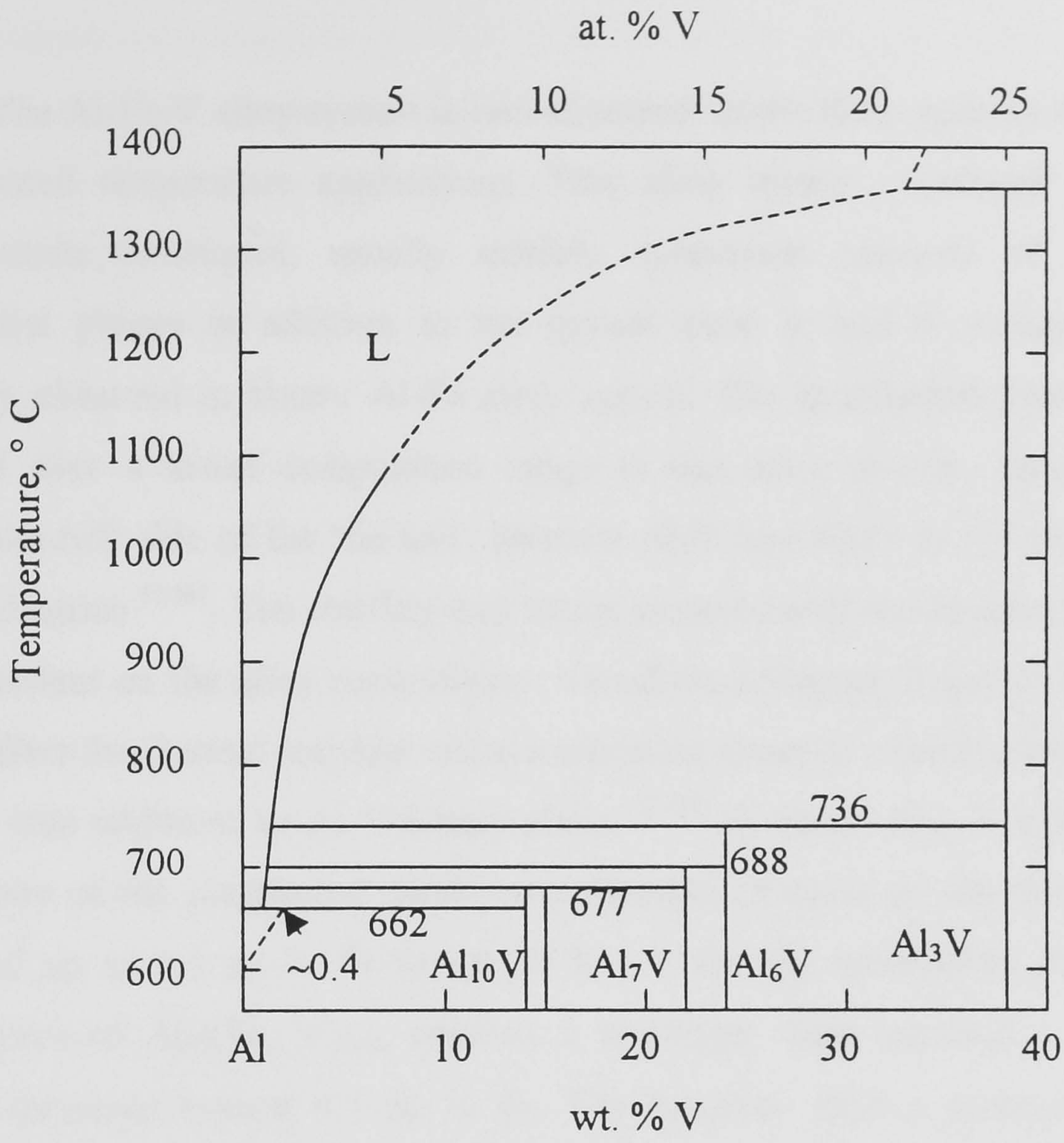


Fig. 3.4 Equilibrium phase diagram of Al-(0 - 40) at. % V [3.51].

The microstructures of the melt-spun Al-14.3 at. % V and Al-17.5 at. % V [3.54], were reported to consist of homogeneous fine equiaxed grains of icosahedral phase with aluminium solid solution existing in the intergranular regions. In these two alloys, the larger icosahedral grain size and smaller volume fraction of the intergranular aluminium phase were observed in the alloy with higher V content. The formation of a duplex structure consisting of dendritic Al_3V and aluminium was also reported in both alloys. Similar microstructures consisting of homogeneous large icosahedral grains with an average diameter of 2 μm were reported in melt-spun Al-16 at. % V alloy [3.55]. The composition of the icosahedral phase was found to be close to β-$Al_{23}V_4$. The intergranular phases were observed and assigned as I_1 and I_2. The I_1 phase consisted of a mixture of (Al, Si)-V with an

amorphous microstructure, while the I_2 was determined to be the same as α-$Al_{10}V$ (actual composition = $(Al_{0.93}\ Si_{0.07})_{11.35}\ V$).

3.3 Ternary Al-Fe-V Alloys

The Al-Fe-V alloy system is one of several Al-Fe alloy systems developed for elevated temperature applications. This alloy system, produced by rapid solidification techniques, usually exhibits substantial amounts of spherical icosahedral phases in addition to the typical zone A and B microstructures generally observed in binary Al-Fe alloy system. The icosahedral phase can be obtained over a broad composition range in this alloy system, spanning the aluminium-rich side of the 'tie-line' between Al_7V and Al_3Fe in the equilibrium ternary diagram [3.56]. The stability and lattice parameters of the icosahedral phase are dependent on the alloy composition. Vanadium additions to the Al-Fe binary alloys affect the thermal stability of the icosahedral phase to a much greater extent than do iron additions to Al-V binary alloys [3.57]. A linear drop in quasi-lattice parameters of the icosahedral phase was reported to occur as the iron content increased up to 6.5 at. % Fe (or at Fe:V = 1 for the icosahedral phase with composition of $Al_{87}(Fe,\ V)_{13}$), whereas a non-linear drop occurred as the iron content increased beyond 6.5 at. % Fe. The deviation from a linear trend was attributed to a clustering of vanadium (or iron) atoms in the icosahedral phase, leading to a contraction of the lattice [3.58].

In the early stage of development, investigations of the rapidly solidified Al-Fe-V alloy system (8 to 14 wt. % Fe, and 1 to 3.5 wt. % V) [3.59, 3.60] using melt-spinning technique have shown that microstructures of the as-cast products consist of zone A and Zone B, and the extent of both zones depends on the processing parameters, namely, surface velocity of casting or wheel speed. These alloys exhibited high microVickers hardness, but rather poor ductility at low temperatures. This would make the alloys difficult to form into desirable shapes and also inadequate for structural applications. Rapidly solidified Al-Fe-V with medium iron contents may exhibit sufficient mechanical properties for some elevated temperature applications. However, few investigations have been carried out on these materials.

Recently, rapidly solidified ternary Al-V-Fe alloy systems with high specific strength have attracted increasing interest. The melt-spun $Al_{94}V_4Fe_2$ (in at.

%) alloy system, for example, has been found to exhibit promising mechanical properties with high tensile strength (up to 1400 MPa) and good bending ductility. The high tensile strength was presumed to result from the formation of the nanoscale mixed structure in which the Al phase has enriched solute concentrations and contains a high density of interphase boundaries [3.61]. Moreover, the high tensile strength was also attributed to the homogeneous dispersion of nanoscale amorphous and icosahedral particles without periodic atomic configurations [3.62].

Two slightly different types of microstructures in the melt-spun Al-V-Fe with the same composition ($Al_{94}V_4Fe_2$) were observed by two research groups. The first type of microstructure consisted of a mixture of nanoscale amorphous + α-Al phases [3.61-3.64], whereas the second consisted of very fine-scale icosahedral phases in an α-Al matrix [3.65]. The difference was attributed to microstructural sensitivity to the alloy composition and the processing parameters. The formation of amorphous + α-Al phases was attributed to the suppression of the transition of supercooled liquid to icosahedral phase resulting from the retardation of the diffusivity of the solute elements [3.61. The deviation of alloy composition and the decrease in solidification velocity caused the formation of the fine scale icosahedral and α-Al phases.

3.4 Quaternary Al-Fe-V-Si Alloys

The dispersion strengthened Al-Fe-V-Si alloys have been developed using rapid solidification techniques to compete with titanium alloys in moderately elevated temperature service environments. This alloy system was first developed by Allied-Signal Corporation using the processes of melt spinning, comminution, compaction or vacuum hot pressing, and consolidation by extrusion or forging [3.66]. The alloy exhibits good combinations of strength, ductility, and fracture toughness [3.66-3.68]. The fatigue crack growth resistance, creep rupture properties and corrosion resistance in the Al-8.5Fe-1.7V-1.3Si or 8009 or FVS 0812 alloy (the number in alloy composition is stated in wt. %), have been found to exceed those in conventional aluminium alloys such as the 2000 and 7000 series [3.69, 3.70]. The excellent mechanical and chemical properties of Al-Fe-V-Si alloys are

attributed to fine scale (~30-80 nm size), high volume fraction, homogeneous distribution, and thermal stability of the nearly spherical α- or bcc-silicide phase.

It has been reported that a more specific composition of the silicide phase may be represented by the following: $Al_{12.0\text{-}14.0}(Fe, V)_3Si_{0.9\text{-}1.29}$ where the Fe:V ratio can also be altered to values between 5:1 and 11.5:1 [3.71]. However, a more recent investigation has reported that the composition of the α_{13}-Al-Fe-V-Si phase {bcc (Im3) [α-AlFeSi type; designated α_{13}]} found in the melt-spun Al-8.3Fe-0.8V-1.75Si is $Al_{13.37}(Fe, V)_3Si_{1.11}$and that of the α_{12}-Al-Fe-V-Si phase {primitive cubic (Pm3) [α-AlMnSi type; designated α_{12}]} found in the melt-spun Al-5.9Fe-1.92V-2.42Si is $Al_{12.86}(Fe, V)_3Si_{2.1}$ [3.72]. Variations in composition of the silicide phase have so far not proven to be significant when taken together with the other effects that alter mechanical properties in this alloy system (i.e. volume fraction, grain size, particle size distribution, etc.) [3.71]. The lattice parameter of the silicide phase was observed to be altered by the change in Fe:V and Al:Si ratios and varied between 1.2607 to 1.2620 [3.71]. By using the convergent beam electron diffraction (CBED) technique, a slightly smaller lattice parameter of 1.256 nm has been found for the silicide phase in the melt-spun Al-8.1Fe-1.8V-0.7Si alloy [3.73].

The addition of V to Al-Fe-Si alloys has been proven to stabilise the cubic silicide phase [3.74]. Transformation of this phase was not observed after annealing at 425 °C for 6 months [3.75]. This was attributed to excellent thermal stability resulting from low coarsening rates of the phase (2.9×10^{-26} to 8.4×10^{-27} m^3/h at 425 °C [3.69, 3.74]). Because the silicide phase particles coarsened slowly, the rapidly solidified Al-Fe-V-Si alloy could retain its room temperature strength up to 500 °C for moderate annealing times (<100 hrs.) [3.76].

The as-cast microstructures of melt-spun Al-Fe-V-Si alloys [3.77, 3.78] have been reported to vary depending on casting conditions and also through the thickness of the ribbon. Two types of alloy ribbons have been found in the melt-spun Al-8.5Fe-1.3V-1.7Si alloy [3.77]. The first type was completely zone A ribbon in which microquasi-crystalline phase precipitated in intercellular regions. The second type was mixed zone A and zone B ribbon in which silicide phase, transformed from microquasi-crystalline phase due to recalescence, was observed in intercellular regions. In both cases, globular particles of clustered microquasi-crystalline phase were present near the air side of the ribbons. The globular particles of clustered microquasi-crystalline phase and the intercellular

microquasi-crystalline phase were claimed to nucleate prior to the formation of aluminium cells [3.77]. The size of globular icosahedral particles was observed to depend on processing parameters, namely, the ejecting temperature and the holding time before ejection [3.78]. Lower ejecting temperature and shorter holding time favoured formation of larger globular phases. Microstructural evolution in the melt-spun alloy with a composition of $Al_{80}Fe_{10}V_{10}Si_6$ [3.79] was reported to be slightly different, particularly in the regions where quasi-crystalline phases formed. A crystalline ring of small cubic-structure silicide particles has been observed to surround a quasi-crystalline phase. Decomposition of the quasi-crystalline phase resulted in formation of polycrystalline aggregates of cubic crystals with irrational twinning leading to icosahedral symmetry in reciprocal space.

Recently, melt-spun $Al_{93.3}Fe_{4.3}V_{0.7}Si_{1.7}Mm_x$ (x = 0.5, 1, 3), Mm = 55Ce, 29La, 11Nd, and 5Pr (wt. %) [3.80], has been found to exhibit different microstructures from the well known melt-spun Al-Fe-V-Si alloys. For x = 0.5, the microstructure consisted of mixed phases of α-$Al_{13}(Fe, V)_3Si_1$, and Al_8Fe_4Mm. Only Al_8Fe_4Mm phase was observed in the microstructure for x = 1, whereas quasi-crystalline $Al_{20}Fe_5Mm$ phase was identified for x = 3.

Annealing (at 400 °C for 2 hours) and *in situ* hot-stage TEM studies of rapidly solidified Al-Fe-V-Si ribbons [3.77] revealed that in the completely zone A ribbon, intercellular microquasi-crystalline particles were unstable and decomposed at a very fast rate, resulting in a coarse distribution of silicide particles. The decomposition of the intercellular microquasi-crystalline particles assisted the decomposition of globular particles, resulting in a very coarse distribution of silicide particles after annealing. In the mixed zone A and zone B ribbon, decomposition of globular particles resulted in the precipitation of silicide particles along cell boundaries. Microstructures of as-annealed rapidly solidified Al-Fe-V-Si ribbons [3.81] at temperatures up to 510 °C for 100 hours revealed no evidence of growth or coarsening of silicide particles. However, polygonal h.c.p. $Al_2(Fe, V, Si)$ dispersoids appeared when the temperature rose to 650 °C. After annealing at 650 °C for longer time (25 hours), the microstructure was observed to consist of spherical bcc α-$Al_{13}(Fe, V)_3Si$, polygonal hcp $Al_2(Fe, V, Si)$, and band-shaped $(Al, Si)_{13}Fe_4$ particles.

The microstructure of the as-consolidated rapidly solidified Al-Fe-V-Si alloys consists of near spherical silicide particles decorating both grain and subgrain boundaries as well as within grain interiors [3.82]. The size of the silicide particles varies with the processing/consolidation time and temperature but typically ranges in the 20- to 100-nm-diameter size. There is a large volume fraction of silicide particles uniformly distributed in the matrix, but there is a tendency to form agglomerates of silicide at the former cell boundaries. The silicide particles are randomly oriented and do not exhibit any consistent crystallographic orientation relationship to the matrix. The grain size of these materials is in the range of 0.5 to 2 μm.

Since the production route of Allied Signal consists of many processing steps, alternative production routes for rapidly solidified Al-Fe-V-Si are desirable for reducing processing and manufacturing costs. The atomized melt deposition technique (AMD) [3.84, 3.85] and spray forming [3.86] to produce near net shape products have been studied. The microstructural refinement and uniformity in distribution of dispersoids in the matrix was observed to be related to the processing parameters such as melt superheat, nozzle-to-substrate distance, and metal gas flow rate. Microstructural evolution in the as-deposited materials was similar to that of materials obtained from melt-spinning process. Mechanical properties of the as-deposited materials were poor, but could be improved by the subsequent consolidation processes such as hot-isostatic pressing and extrusion. Recently, the strength achieved in the extrusion consolidated products [3.86] of the spray formed Al-Fe-V-Si alloy (FVS611) has been reported to be only 61 % of that achieved in the consolidated products of planar flow-cast materials. This might be attributed to the fact that the alloy produced by spray forming experienced lower cooling rates than the alloy produced by planar flow-casting.

CHAPTER 4

EXPERIMENTAL PROCEDURE

The processing route used for the elevated temperature Al-Fe-(V, Si) alloys in this investigation consisted of several processing steps, namely, gas atomization, powder classification, cold compaction and extrusion. The first two steps were carried out by ALPOCO (the powder supplier), whereas the last two steps were carried out at Department of Materials, Imperial College. In this thesis, characterisation (phase identification and microstructural observation) of the materials after each processing step was carried out in order to provide understanding of the microstructural evolution during processing. Investigations of phase transformation reactions, taking place during thermal analysis study of the as-atomised powders and heat-treatment of the consolidated products, are the important sections of this thesis. To understand the process-microstructure-property relationship of both alloys, mechanical tests were performed on the consolidated alloys. Details of experimental procedure are given below.

4.1 Characterisation of the As-atomised Powders

4.1.1 Powder Particle Size Distribution

Powder particle size distribution of each powder particle size fraction was determined using a Malvern Laser Particle Sizer. An example of information obtained from this method and some definitions of powder particle diameters are given in Appendix A1. Note that this method is limited for particles with diameters less than 10 μm because fine particles tend to form agglomeration, which causes an error during measuring particle size distribution.

4.1.2 Phase Identification and Powder Microstructure Investigation

Phase identification of the as-atomised powders was carried out using X-ray diffraction (XRD) and a transmission electron microscopy (TEM) equipped

with energy dispersive X-ray spectroscopy (EDS). Microstructures of the as-atomised powders were investigated using TEM, and scanning electron microscopy (SEM). Details of sample preparation for XRD, TEM and SEM are given below.

(1) XRD

In order to facilitate powder handling and the XRD scan, each powder size fraction was cold compacted to a pellet of diameter 1.5 cm. One surface of each powder pellet was ground until smooth and flat. For phase identification, the powder pellet was spun and continuously scanned from $2\theta = 15$ to 50° employing a Phillips PW 1700 series automated powder diffractometer and CuK_α radiation (40 kV and 40 mA) filtered with a secondary graphite crystal monochromater.

(2) TEM

Foils of the as-atomised powders embedded in a nickel matrix were prepared using electrolytic deposition of nickel. A full description of the preparation of powders embedded in nickel is given in ref. [4.1]. The foil was ground to a thickness of 100-200 μm. Discs of 3 mm diameter were subsequently punched from the foil. The disc was thinned electrolytically using a Struers Tenupol jet polishing machine, with a solution (by volume) of 10% percholic acid, 10% 2-butoxyethanol, and 80% ethanol, operating at –35 °C and 65 V. Microstructural observation and phase identification were carried out using either a JEOL-JEM-100CX, operating at 100 kV or a JEOL-FX2000EM equipped with a LINK X-ray Analytical Systems, operating at 200kV.

(3) SEM

A powder embedded resin was ground with a fine SiC grinding paper (no. 1200) and polished with diamond paste (3 μm followed by 1 μm). The powders were etched with Keller's reagent. The polished surface of the resin was then coated with gold. Microstructural observation was carried out using a JEOL JSM T220.

4.1.3 Lattice Parameter Determination

Each sample for lattice parameter determination was prepared using the same method as for phase identification by XRD. The powder pellet of each size fraction was spun and continuously scanned over a range of 2θ in order to get XRD peaks corresponding to the Al [400], [331], [420], and [422] reflections. The apparent lattice parameter was calculated from each d-spacing corresponding to each XRD peak and plotted against the respective Nelson Riley function. The actual lattice parameter was taken as the intercept value obtained by extrapolating the trend line to intercept the lattice parameter axis.

4.1.4 Thermal Analysis

Thermal analysis of the as-atomised powders was carried out by differential scanning calorimetry (DSC) using a Stanton Redcroft DSC 1500 machine. Experiments were carried out at a heating rate of 10 °C/min over the temperature range 200-600 °C and under argon to prevent oxidation of the samples. Sample sizes of ~ 45 mg were used, with Al_2O_3 as a reference.

4.2 Powder Consolidation

4.2.1 Cold Compaction

To make the powder billets, 500 grams of each powder size fraction was filled into a 60 mm die, previously coated with a slurry of zinc stearate in acetone. The ram was then pressed into the die using a Tangye compression press with a pressure of 500 MPa.

4.2.2 Hot Extrusion

Before extrusion, each powder billet was heated up to 500 °C using an air-circulating furnace. The preheated billet was then filled immediately into the liner (in the extrusion container) previously heated to 450 °C. Extrusion of each powder billet was carried out using an ENEFCO 5MN hydraulic vertical press acting in the direct mode. The extrusion conditions were the same for all powder billets. The conditions used were an extrusion ratio of 18:1 and a ram speed of 3 mm/sec. All the powder billets were extruded into rod-shaped products. The die face was lubricated with a graphite-based lubricant. The emerging extruded rod was water-quenched.

4.3 Mechanical Testing

4.3.1 Compression Test

Cylinder-shaped compression test specimens, with diameter of 8 mm and height of 10 mm, were machined from each extruded rod. The specimens were tested using a MAYES machine equipped with a Severn furnace (SFL model RHS 1259). The data of compression stress and strain were recorded using a computer. The test was performed with 30% total strain, at a constant strain rate of 0.001 s^{-1}, and at temperatures of 25 °C and 250 °C.

4.3.2 Short Rod Fracture Toughness Test

Two Terratek short rod fracture toughness (TSRFT) specimens were machined form each extruded rod. The test was performed using a cross head speed of 0.5 mm/ min. A full description of this test is given in ref. [4.2].

4.4 Heat-treatment

The extruded RS-Al-Fe-V rod produced from a powder size fraction with volume median diameter (D[v,0.5]) = 50 μm and the extruded RS-Al-Fe-V-Si rod produced from a powder size fraction with D[v,0.5] = 31 μm were selected for heat-treatment study. Note that the definition of D[v,0.5] is given in Appendix A1. The aim for heat-treatment is to study phase transformation reactions taking place during exposure to elevated temperatures. The specimens taken from the extruded rod were wrapped with aluminium foil and heated at different temperatures and times. Heat-treatments were performed at 500, 550, and 600 °C for times up to 72 hours.

4.5 Phase Identification and Microstructural Investigation of Bulk Materials (Consolidated Alloys, Mechanically Tested Specimens and Heat-treated Specimens)

(1) XRD

An XRD specimen was cut from each bulk material in order that the XRD specimen surface was parallel to the extrusion direction. The specimen was polished using grinding papers and diamond paste. The XRD scan was carried out using the method given in (§ 4.1.2).

(2) TEM

Discs with 3 mm diameter, made from each bulk material, were thinned electrolytically using a Struers Tenupol jet polishing machine with a solution (by volume) of 30 % nitric acid in methanol, operating at 20 V and –30 °C.

CHAPTER 5

RESULTS AND DISCUSSION

5.1 Characterisation of the As-atomised Powders

5.1.1 Powder Size Distribution

In this investigation, rapidly solidified Al-Fe based alloys with nominal composition Al-6.5Fe-1.5V and Al-6.5Fe-1.5V-1.7Si were investigated. Henceforth, the terms, RS-Al-Fe-V and RS-Al-Fe-V-Si will be used to represent the rapidly solidified Al-6.5Fe-1.5V and rapidly solidified Al-6.5Fe-1.5V-1.7Si alloys, respectively. The as-atomised powders produced by inert gas atomisation processing were classified into size fractions. These powder size fractions facilitated the study of microstructural evolution during processing of these alloy powders. In general, powder particle size together with other factors, such as cooling rate, undercooling, and solidification velocity, control solidification behaviour of alloy liquid droplets dictated the final powder microstructures. Microstructures and mechanical properties of the as-consolidated products of alloy powders also have close relationships with original powder microstructures.

The size distribution of each powder size fraction was determined using a Malvern Laser Particle Sizer. Three types of powder particle sizes or diameters (their definitions are given in Appendix A.1) including the equivalent volume mean diameter or De Broucker mean (D[4,3]), the equivalent surface area mean diameter or Sauter Mean Diameter (D[3,2]), and the volume median diameter (D[v,0.5] or D_{50} or $D_{0.5}$) of RS-Al-Fe-V and RS-Al-Fe-V-Si powders are given in Table 5.1.1. The De Broucker mean, the average size based on unit weight of particle, shows where the mass of the system lies. The Sauter Mean Diameter is the average size based on specific surface per unit volume. The D[v,0.5] is the value for which 50 percent of the particles (population) measured are less than the stated size. For simplicity and

because of the normal size distribution given for all powder size fractions, the volume median diameter, D[v,0.5], was chosen to represent each powder size fraction.

Table 5.1.1 Particle diameters of RS Al-Fe-V and RS Al-Fe-V-Si powders.

Alloy	Particle diameter, μm		
	D[4,3]	D[3,2]	D[v,0.5]
RS-Al-Fe-V (0-7 μm)	9	7	8
RS-Al-Fe-V (7-11 μm)	11	10	11
RS-Al-Fe-V (11-18 μm)	15	14	14
RS-Al-Fe-V (18-32 μm)	25	18	24
RS-Al-Fe-V (32-45 μm)	40	36	37
RS-Al-Fe-V (45-63 μm)	52	49	50
RS-Al-Fe-V (18-45 μm)	28	24	25
RS-Al-Fe-V-Si (0-7 μm)	8	6	7
RS-Al-Fe-V-Si (7-18 μm)	18	8	11
RS-Al-Fe-V-Si (11-32 μm)	29	14	17
RS-Al-Fe-V-Si (18-45 μm)	34	24	31

5.1.2 Powder Microstructures

5.1.2.1 Fine Powders (< 5 μm)

The observation of powder microstructures by TEM revealed that there was similarity in microstructural morphologies of both RS-Al-Fe-V and RS-Al-Fe-V-Si alloys. Most fine powder particles with diameters of up to 5 μm exhibited very fine microstructures (Fig.5.1.2.1 (a) and (b)). Observations by TEM, using higher magnification, revealed that the microstructure consisted of fine, discrete rounded particles with diameters less than 50 nm distributed homogeneously throughout the matrix (Fig. 5.1.2.1 (c)). This microstructure was obviously different from the

microcellular structure shown in Fig. 5.1.2.1 (d). Selected area electron diffraction patterns (SADP) of the area consisting of fine, discrete rounded particles in both alloy powders exhibited diffuse rings and some diffracted spots from aluminium (insets in Fig. 5.1.2.1 (c) and (d)).

In previous investigations on splat-quenched Al-Fe [5.2], atomised Al-Fe [5.3], and Al-Fe-Ce [5.4] alloys, the microstructures that consisted of microcells have been designated as 'zone A' whereas the microstructures that consisted of coarse and segregated dendrites have been designated as 'zone B'. However, in order to distinguish the microstructures consisting of fine, discrete rounded particles distributed homogeneously in the matrix from the microstructures consisting of microcells with intercellular particles (Fig. 5.1.2.1 (d)), the 'zone A' is designated for the former microstructures and the 'zone B' is designated for the latter one.

Microstructures consisting of fine particles randomly oriented in the matrix (zone A) have also been reported in sub-micron Al-Si alloy powders [5.5], and melt-spun Al-Fe [5.6], Al-Fe-Ni [5.7], and Al-Fe-Mo-V [5.8] alloys. Formation of zone A is not well understood. Explanations for formation of zone A have been given by several authors [5.6, 5.7]. Chu and Granger [5.6] suggested that the formation of fine particles in zone A microstructures of melt-spun binary Al-Fe alloys was attributed to the segregation during solidification rather than solid-state decomposition after solidification because of their random orientation with respect to the α-Al matrix.

Boettinger *et. al.* [5.7] found that the morphological transition of the intercellular phases occurred according to solidification velocity in rapidly solidified Al-Fe-Ni alloy. They reported that the intercellular phase morphology changed from continuous forms at low velocities to discrete rounded particles at high velocities. A mechanism for the occurrence of round particles at high velocities involves the formation and subsequent solidification of the isolated droplets of solute-rich liquid within α-Al matrix. The droplets are formed by a pinching-off of liquid in the grooves in a cellular liquid/solid interface.

The formation of zone A may be explained by considering the interaction between the solidification fronts and freely dispersed particles [5.9-5.13]. Before discussing the formation of zone A, it is worth identifying the freely dispersed particles present in the melt before the solidification front of the α-Al starts growing.

The freely dispersed particles forming in the undercooled melt droplets may be one of three phases, namely, the amorphous phase [5.14, 5.15], the Frank-Kasper phase [5.16], or the quasi-crystalline phase [5.17]. These phases are likely to be present in the solid state to preserve the icosahedral nearest-neighbour coordination i.e. a short-range order exhibited by metallic melts [5.17]. SADPs with a diffuse ring as shown in Fig. 5.1.2.1 (c) and (d) may lead to the conclusion that the precipitates in zone A should be amorphous phases (normal metallic glasses). However, it has been speculated that an SADP with diffuse rings may result from a 'special amorphous phase, which is not a normal metallic glass (dense random packing model) but an orientationally disordered microquasi-crystalline phase [5.18-5.21]. In a melt-spun Al-Fe-Mo-V ribbon [5.8], a microstructure consisting of very fine and uniformly distributed particles in an α-Al matrix (similar to the morphology of zone A in the alloys investigated in this study) also exhibited an SADP with diffuse rings. When a convergent beam electron diffraction (CBED) technique was performed on a single fine particle, an SDAP with fivefold symmetry, which is a common feature of the icosahedral phase, was obtained.

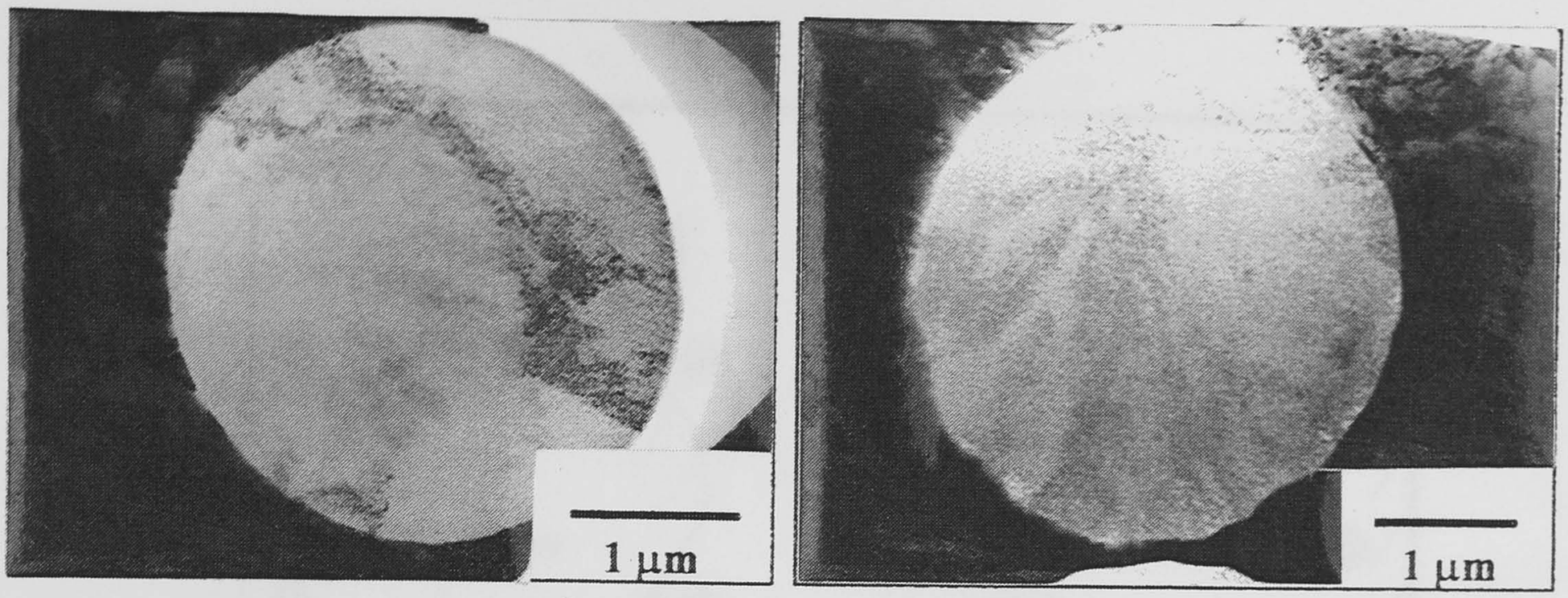
Owing to the reasons given above, it is speculated that the fine particles in zone A of both RS-Al-Fe-V and RS-Al-Fe-V-Si alloy powders could be microquasi-crystalline phases. The presence of microquasi-crystalline icosahedral (MI) phases in zone B of RS-Al-Fe-V powder particles (§ 5.1.3.2) may also lead to the speculation that the fine particles in zone A could be MI phase particles.

The formation of zone A may occur by the following mechanism. After a melt droplet has been highly undercooled, nucleation events of the MI phase particles occur throughout an alloy melt droplet whereas the nucleation events for stable Al_6Fe and equilibrium $Al_{13}Fe_4$ are suppressed. After nucleation, the MI phase particles grow further and disperse in the liquid alloy. As the MI phase particles are growing, the nucleation of the α-Al occurs at the surface of an alloy melt droplet. The α-Al front advances with a planar front into liquid. In rapid solidification, the planar front velocities are extremely high [5.22-5.26], and this is so for the solidification velocities of the α-Al front in small powder particles (although the velocities cannot be experimentally determined during solidification of metal powders). Because of high solidification front velocities, the fine dispersed MI phase particles are engulfed. This

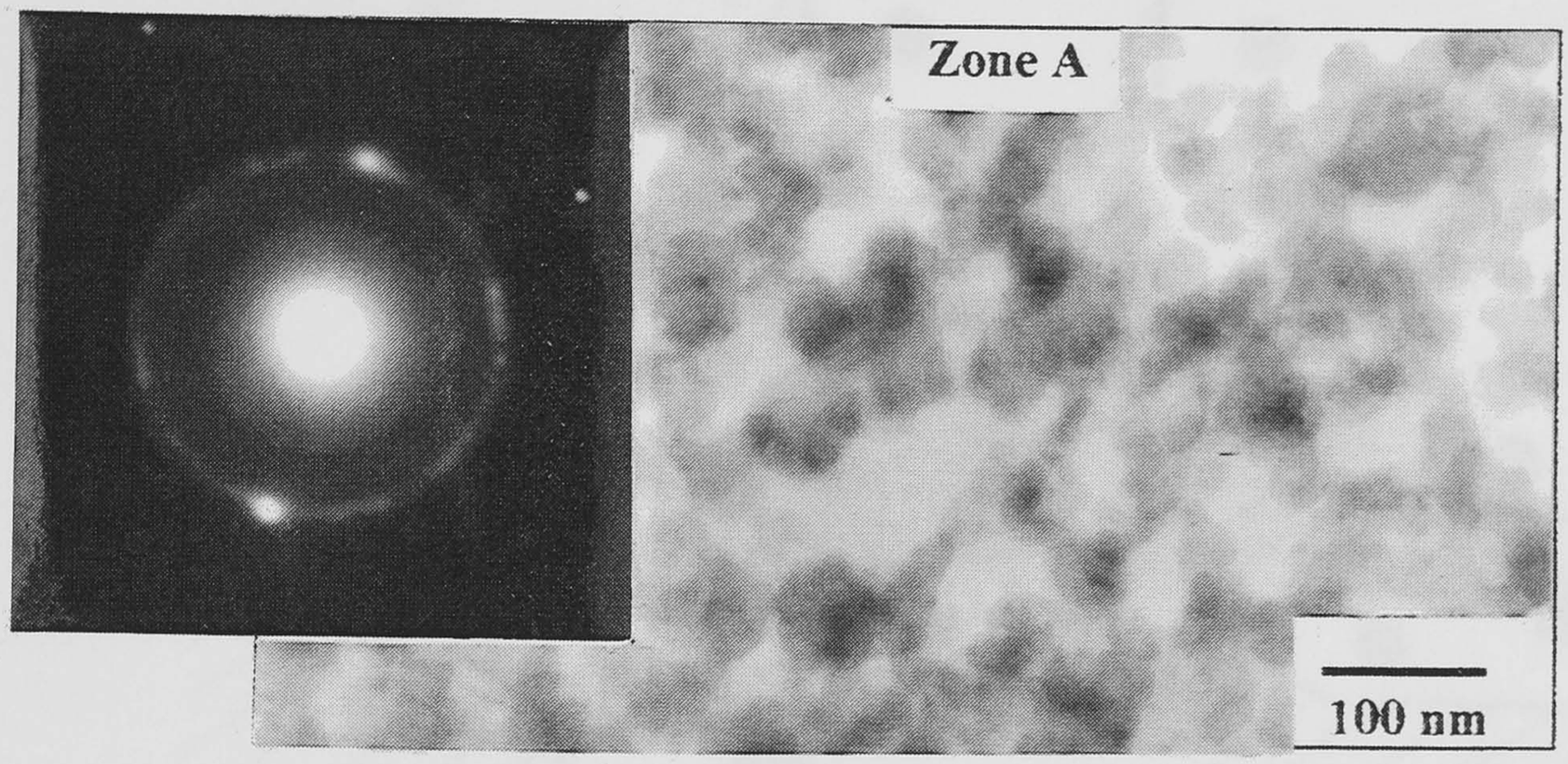
particle engulfment by a planar or a smooth solidification front is illustrated schematically in Fig.5.1.2.2 (a).

The segregation-free solid could not be observed in either RS-Al-Fe-V and RS-Al-Fe-V-Si powders. The reason for the absence of segregation-free microstructures in these two alloys may be attributed to the formation of the MI phase particles as explained above. The formation of segregation-free solid from the melt in the Al-Fe alloy system is determined by solute trapping at all concentrations [5.27, 5.28]. A very high velocity is required to initiate solute trapping in the Al-Fe alloy system. Recently, the solid-liquid interface velocity required for Al-Fe alloys to solidify with a planar front during rapid solidification was experimentally measured using a laser surface treatment [5.26]. With increasing growth velocity, the microstructures of low Fe containing Al-Fe alloys (with < 0.5 wt. % Fe) were observed to transform from dendritic to banded and finally to precipitation-free. The growth rates, required for transition from banded to precipitation-free microstructure, were found to increase with increasing alloy content. In higher Fe content Al-Fe alloys (with 2.0 to 8.0 wt. % Fe), precipitation-free structures were hardly observed even at for a growth velocity greater than 2.0 m/s. This may confirm that Al-Fe alloys have high resistance to the formation of segregation-free microstructure.

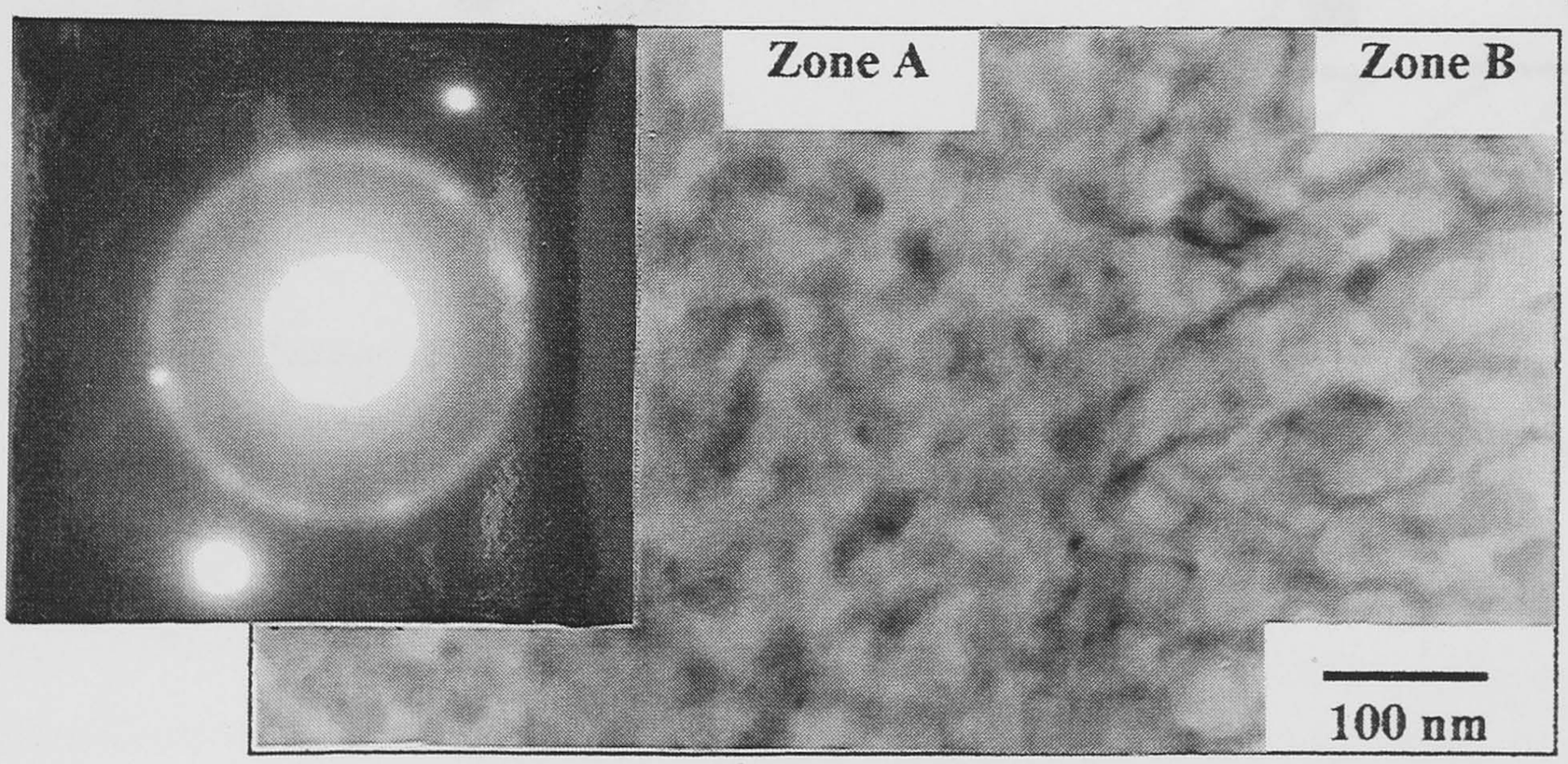
In the Al-Cu and Al-Mn alloy systems, the observed and predicted velocities of less than 2.3 m/s [5.28] were required for segregation-free solidification in Al-Cu and Al-Mn alloys with the same solute contents (< 9 wt. % solute). Microstructural investigations of some alloy powders, such as Al-Cu and Al-Cr-Fe-Zr [5.29], Al-Mg-Mn and Al-Li-Cr-Fe and Al-Cr-Fe [5.30-5.32], Al-Cr-Zr [5.32], and Al-Mn-Cr [5.33], have shown that segregation-free microstructures could be formed in these alloys. It should be noted that Fe is not the main alloying element in the iron containing alloys listed above. The influence of Fe on the segregation behaviour in those alloys may be insignificant compared that of Cu, Mn, and Cr. The formation of segregation-free solid observed in those alloys may be strongly influenced by Cu, Mn, and Cr elements, which have larger partition coefficient values (k) and smaller values of freezing range ΔT compared to those of Fe.



(a) RS-Al-Fe-V (b) RS-Al-Fe-V-Si



(c) RS-Al-Fe-V



(d) RS-Al-Fe-V-Si

Fig. 5.1.2.1 Examples of microstructures and SADPs of zone A exhibited by fine RS-Al-Fe-V and RS-Al-Fe-V-Si powder particles.

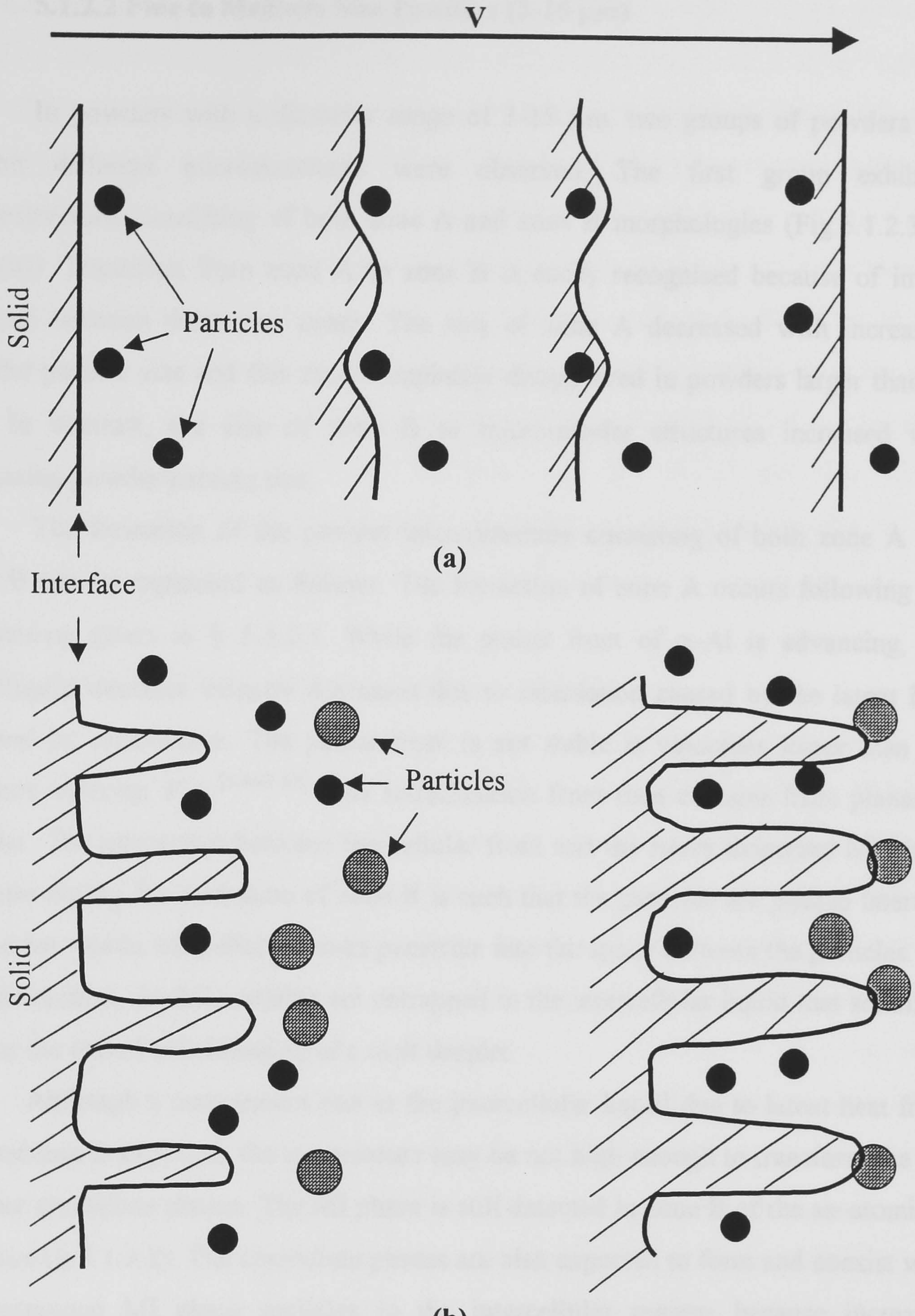


Fig. 5.1.2.2 Schematic diagram showing interaction between second phase particles and planar (a) and cellular (b) solidification fronts (adapted from Asthama *et. al.* [5.9]).

5.1.2.2 Fine to Medium Size Powders (3-15 μm)

In powders with a diameter range of 3-15 μm, two groups of powders that exhibit different microstructures were observed. The first group exhibited microstructures consisting of both zone A and zone B morphologies (Fig.5.1.2.3 (a) and (b)). Transition from zone A to zone B is easily recognised because of image contrast between these two zones. The size of zone A decreased with increasing powder particle size and this zone completely disappeared in powders larger than 10 μm. In contrast, the size of zone B or microcellular structures increased with increasing powder particle size.

The formation of the powder microstructure consisting of both zone A and zone B can be explained as follows. The formation of zone A occurs following the mechanism given in § 5.1.2.1. While the planar front of α-Al is advancing, the solid/liquid interface velocity decreases due to retardation caused by the latent heat released by recalesence. The planar front is not stable at velocities lower than the absolute velocity, V_{abs} [5.34-5.36]. The solidification front then changes from planar to cellular. The interaction between the cellular front and the freely dispersed MI phase particles during the formation of zone B is such that the particles are pushed laterally or in other words, the cellular trunks penetrate into the space between the particles. By this interaction, the MI particles are entrapped in the intercellular liquid that solidifies later at the end of solidification of a melt droplet.

Although a temperature rise in the intercellular liquid due to latent heat from recalescence is expected, the temperature may be not high enough to transform the MI to other crystalline phases. The MI phase is still detected in zone B of the as–atomised powders (§ 5.1.3.2). The crystalline phases are also expected to form and coexist with the entrapped MI phase particles in the intercellular regions because increased temperature in the intercellular liquid may promote the formation of crystalline phases.

The second group of powders exhibited almost entirely zone B morphology. Nucleation sites were also observed to be on the surface of the melt droplet (Fig.5.1.2.3 (c) and (d)). After nucleation, growth proceeded by a cellular mode and as

the growth proceeded the cells became coarser. The cell spacings were observed to increase with increasing distance away from the nucleation site. In some powders, globular phases were observed in the region consisting of coarse cellular microstructures. The globular phase particles were later identified (§ 5.1.3.2) as a globular cluster of randomly oriented MI (GCMI) phase. The microstructure consisted of coarse cells or dendrites with GCMI particles and is designated here as 'zone C'.

Note that the GCMI particle is not a single quasi-crystal as the latter exhibits SADPs with arrays of sharp Bragg spots whereas the former exhibit SADPs with ring patterns. It has been reported that single quasi-crystals form independently in the melt by homogeneous nucleation and diffusionless growth with rates of 1-2 m/s in melt-spun Al-Fe alloys [5.37]. Although nucleation of the GCMI particles occurs homogeneously, the growth mechanism or clustering of these particles is not understood yet.

5.1.2.3 Medium to Coarse Powders (> 15 μm)

The microstructures observed in medium to coarse powders with diameters greater than 15 μm consisted of zone B and zone C. The GCMI particles (also the zone C) were always observed at some distance away from the nucleation site for solidification of α-Al. The size and volume fraction of GCMI particles in zone C increased with increasing distance away from the nucleation site and also with increasing powder particle size. Nucleation sites for solidification of α-Al, were observed to be on the surface of the melt droplet. This suggests that nucleation of α-Al in coarse powder particles may occur heterogeneously. The growth of α-Al in coarse powders started via a cellular mode and then changed to a dendritic mode. The morphological transition from cellular to dendritic can be clearly seen in SEM images (Fig. 5.1.2.4 (a) and (b) for powder particles sectioned along the growth direction, and (c) and (d) for powder particles sectioned normal to the growth direction).

The formation of zone C can also be explained by the interaction of the solidification fronts with the dispersed particles in the melt [5.9-5.13]. The dispersed particles in zone C are GCMI particles. Long before the interaction occurs, the MI particles grow further (clustering) to form GCMI particles. The coarse cellular or

dendritic fronts advancing with low velocities (indicated by large cell or dendrite spacings) would push the large, freely dispersed GCMI particles some distance before the particles are entrapped by the solidified materials. The evidence of particle pushing during solidification is the presence of GCMI particles far away from the nucleation site for solidification of cellular or dendritic α-Al phase (Figs. 5.1.2.3 (d) and 5.1.2.5 (c)). It is interesting to note that the GCMI particle sizes are as large as the cellular or primary dendritic spacings. It is impossible for these particles to be entrapped in the smaller size intercellular/interdendritic regions. The GCMI phase particles are surrounded by cellular/dendritic microstructures.

As in the intercellular liquid in zone B, increased temperature and increased solute content in the intercellular/interdendritic liquid in zone C are expected. The crystalline phases are likely to form in conjunction with the MI phase in the intercellular/interdendritic liquid. The continuous forms of metastable Al_6Fe phase were observed in the intercellular/interdendritic regions of coarse RS-Al-Fe-V powders (§ 5.1.3.2).

5.1.2.4 Nucleation in Powders

Powder microstructures usually exhibit a single nucleation site indicating that a powder particle is a single grain. A single grain powder particle occurs when growth kinetics are so rapid that there is insufficient time for a second nucleation event to occur before recalescence has raised the temperature. The nucleation site is usually observed at the surface of the powder. This indicates that nucleation in a melt droplet occurs heterogeneously. The presence of multiple grains in a single powder particle, as shown in Fig. 5.1.2.5, resulting from multiple nucleation events in a melt droplet, was observed. It may be implied that atomisation cannot totally split catalytic sites for nucleation down to one site per melt droplet. Multiple grains in a single powder particle have also been observed in rapidly solidified Al-Fe-Cr-Zr powders [5.29].

Grains formed from nucleation events occurring at nearly the same time were observed in some powders (Fig. 5.1.2.5 (a) and (c)). In those cases, the grain sizes were usually equal and the grains oriented symmetrically. Nuclei may have formed at

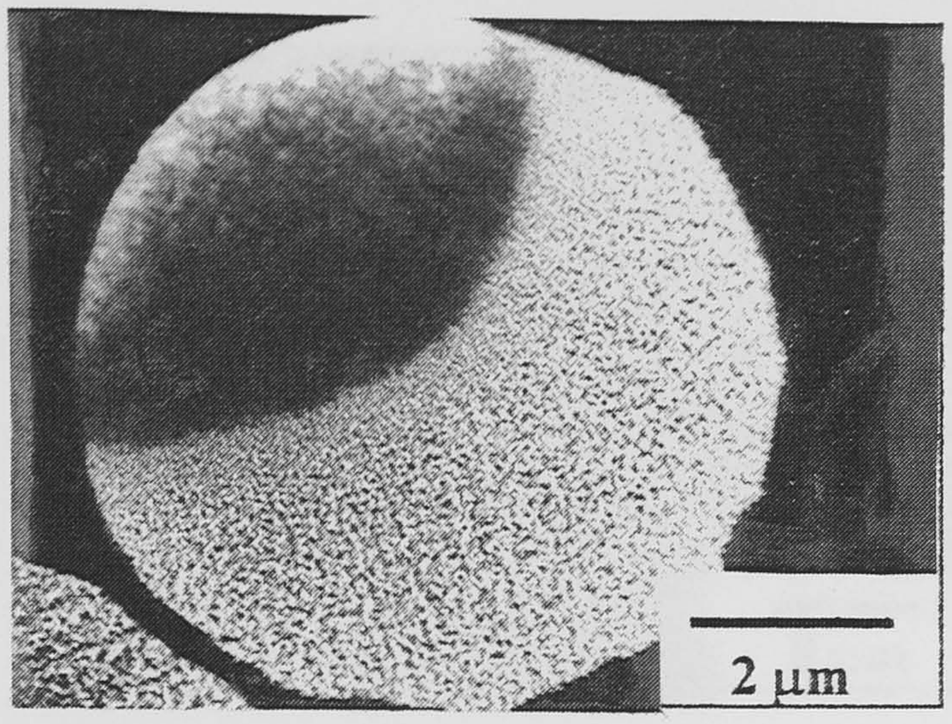
different times resulting in the formation of grains with different sizes as clearly shown in the coarse irregular-shaped powder particle (Fig. 5.1.2.5 (d)).

Nucleation in large melt droplets may be triggered by a small satellite particle. Collision or impingement of smaller solidified powder particles on the larger molten or semimolten droplets occurs during atomisation processing. The smaller powder particle, when impinging on a larger melt droplet, acts as a catalytic site for nucleation. Microcells of a larger powder particle grow and propagate from the surface of a smaller powder particle as can be clearly seen in Fig.5.1.2.6.

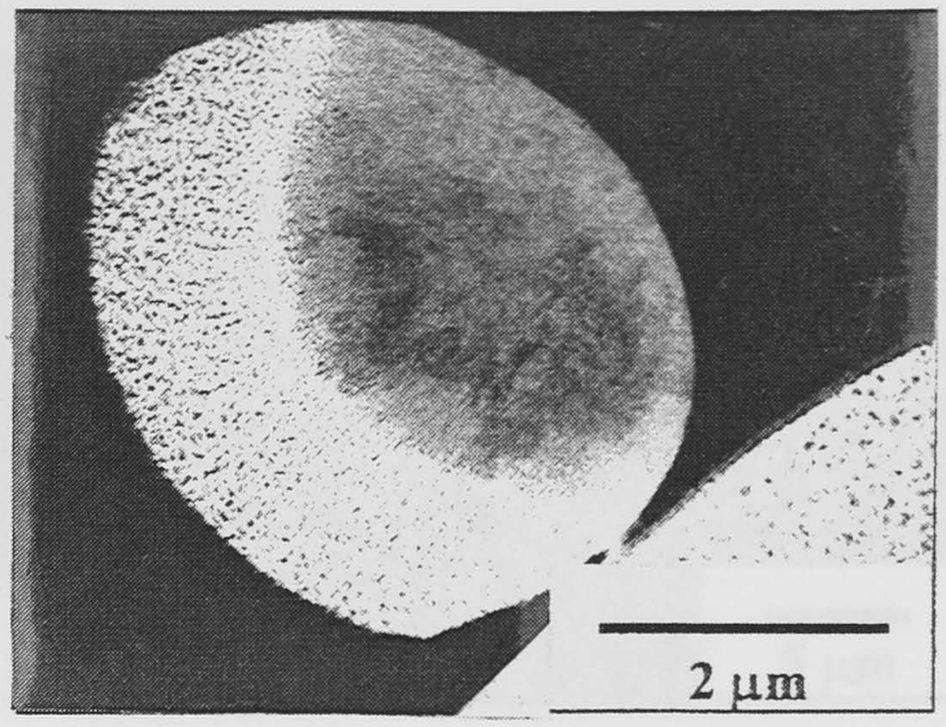
Satellites, in the form of one powder particle attached to another powder particle, were not observed in fine powders with comparable sizes because solidification in a fine powder particle occurs rapidly before impingement by other fine powder particles. Collisions involving solidified powder particles cannot generate satellites.

5.1.2.5 Irregular-shaped Powder Particles

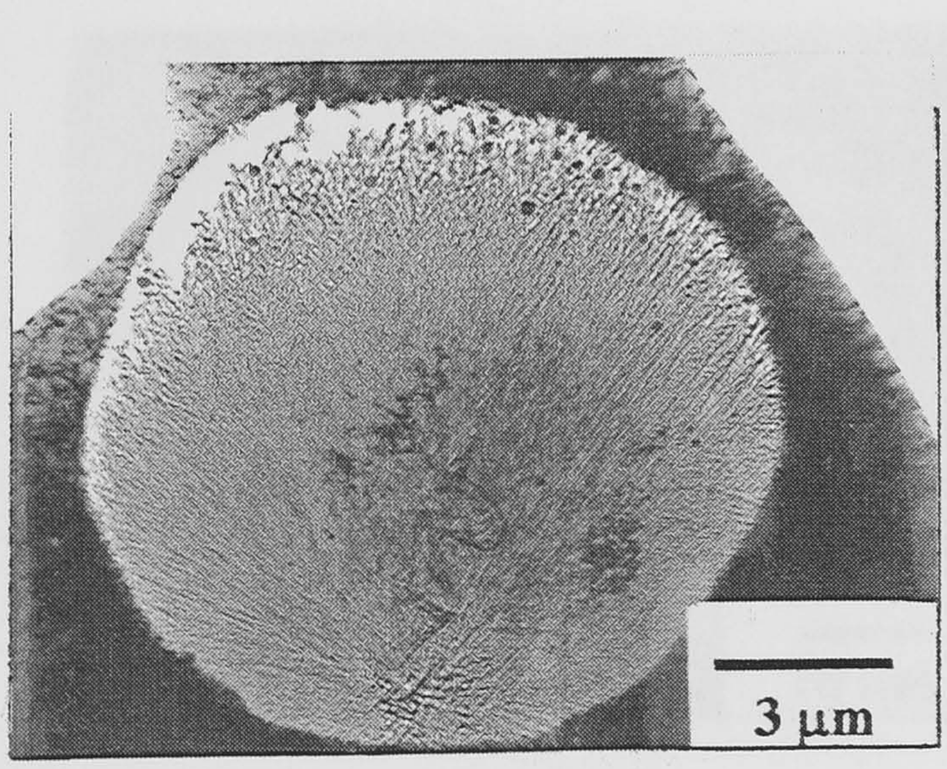
In general, spherical or nearly spherical shaped powder particles of aluminium or aluminium alloys are produced by inert gas atomisation. However, powders with irregular shape were observed in both RS-Al-Fe-V and RS-Al-Fe-V-Si alloys (Fig.5.1.2.7). During atomisation processing, two different processes namely spherodisation and solidification occurred. The irregularity of powder shape indicated that solidification of the melt droplets occurred very fast so that the melt had insufficient time to complete spherodization. Irregularly shaped powders were found in a wide range of powder sizes (Fig. 5.1.2.5 (d), 5.1.2.6, and 5.1.2.7).



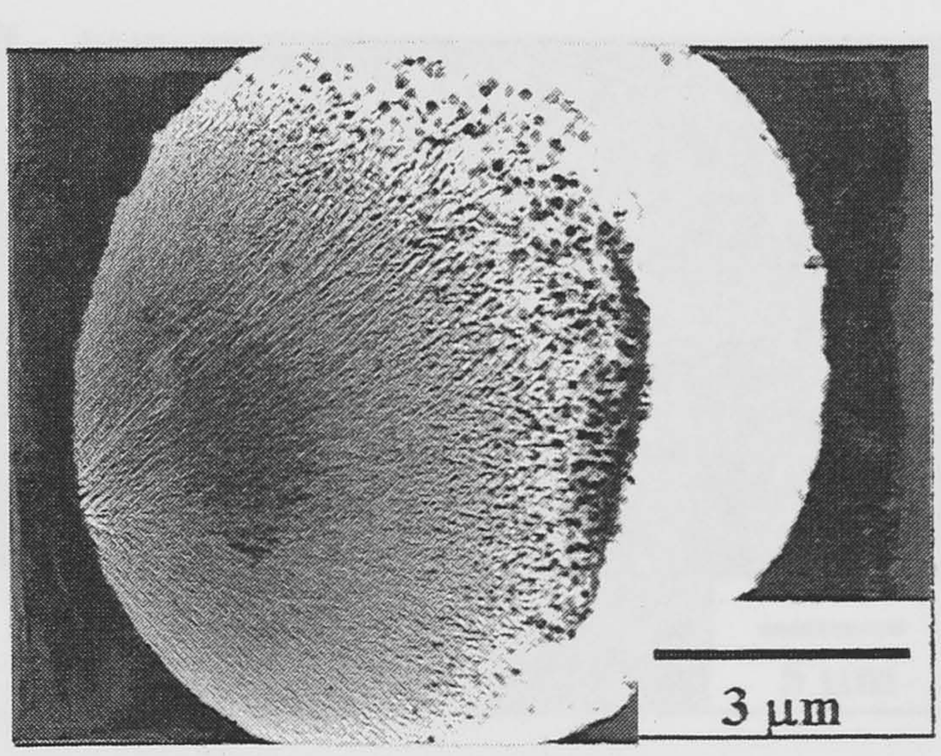
(a) Zone A and zone B in a RS-Al-Fe-V powder particle



(b) Zone A and zone B in a RS-Al-Fe-V-Si powder particle

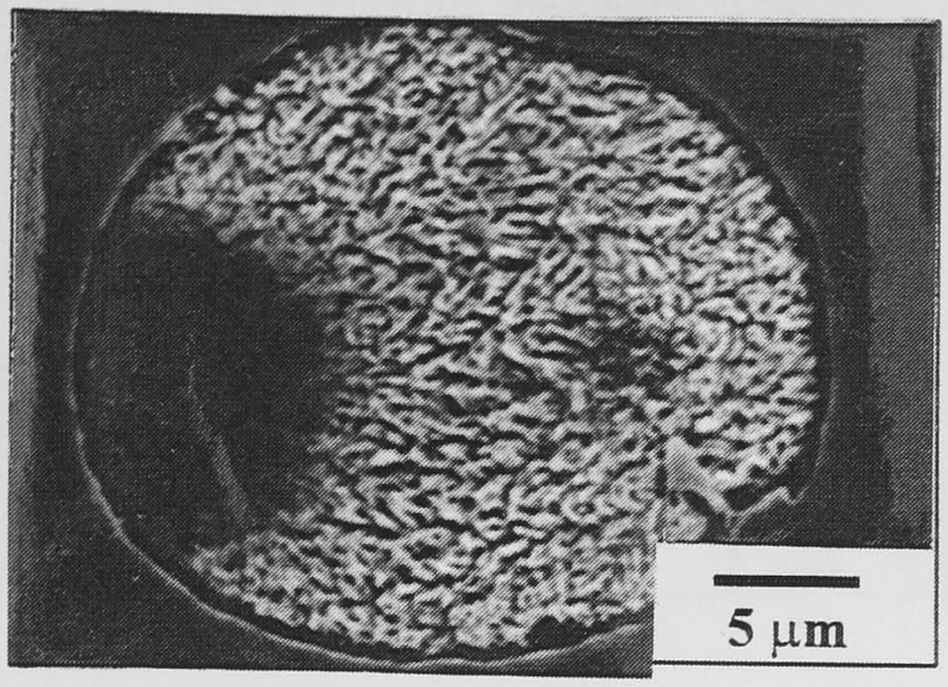


(c) Zone B in a RS-Al-Fe-V powder particle

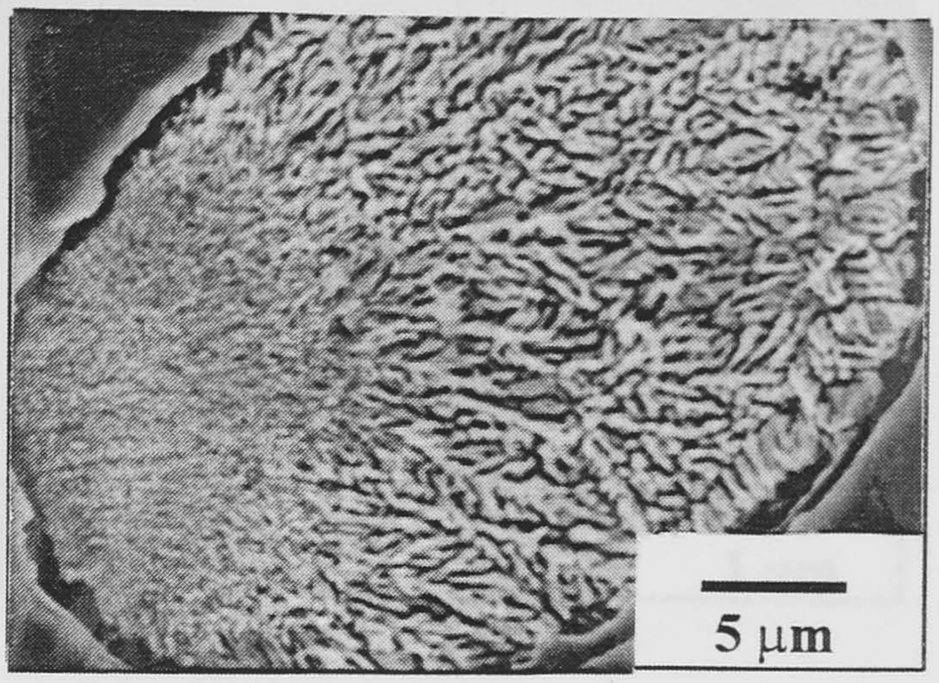


(d) Zone B and zone C in a RS-Al-Fe-V powder particle

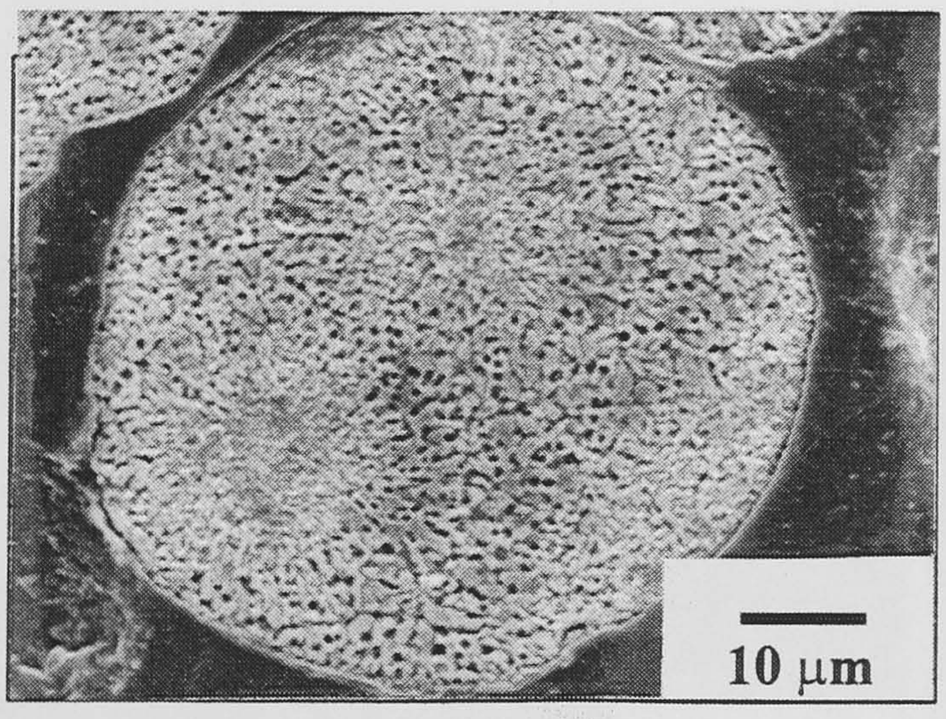
Fig. 5.1.2.3 Examples of microstructures exhibited by fine to medium RS-Al-Fe-V and RS-Al-Fe-V-Si powders.



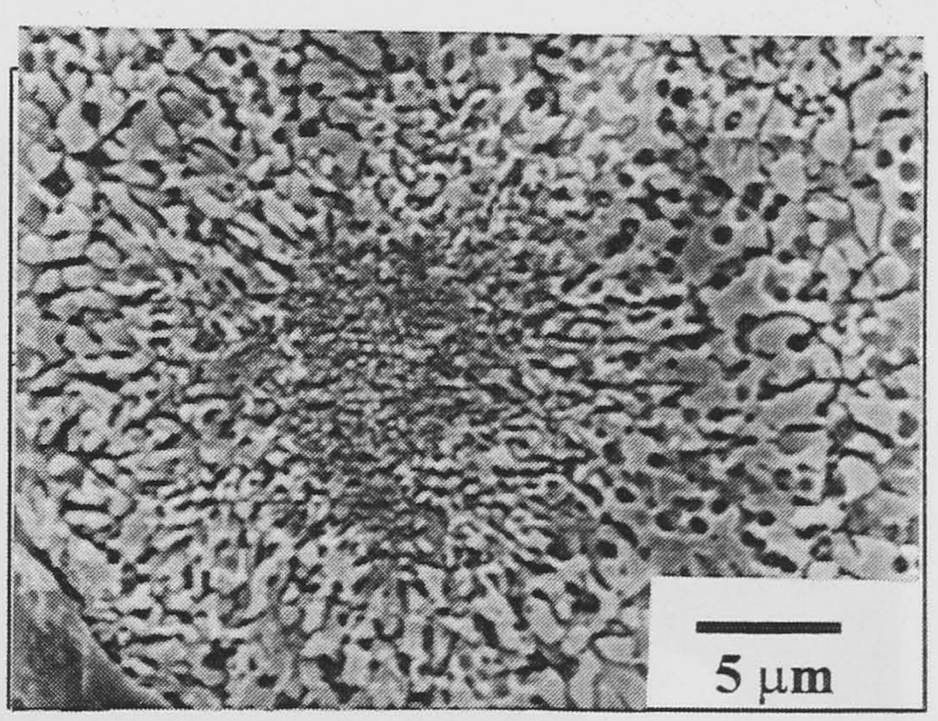
(a)



(b)

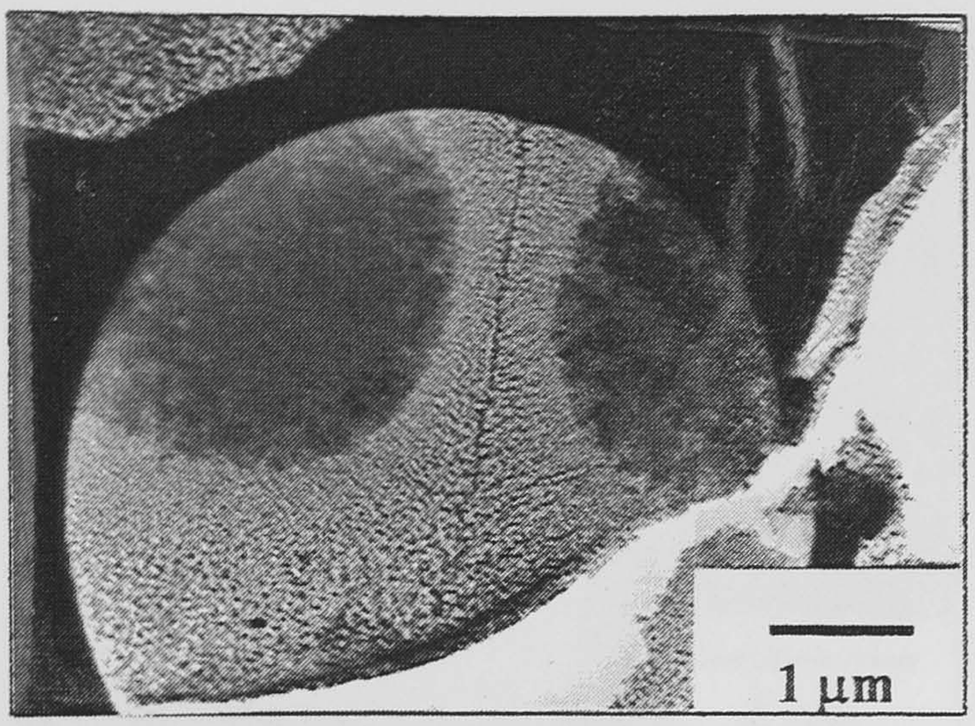


(c)

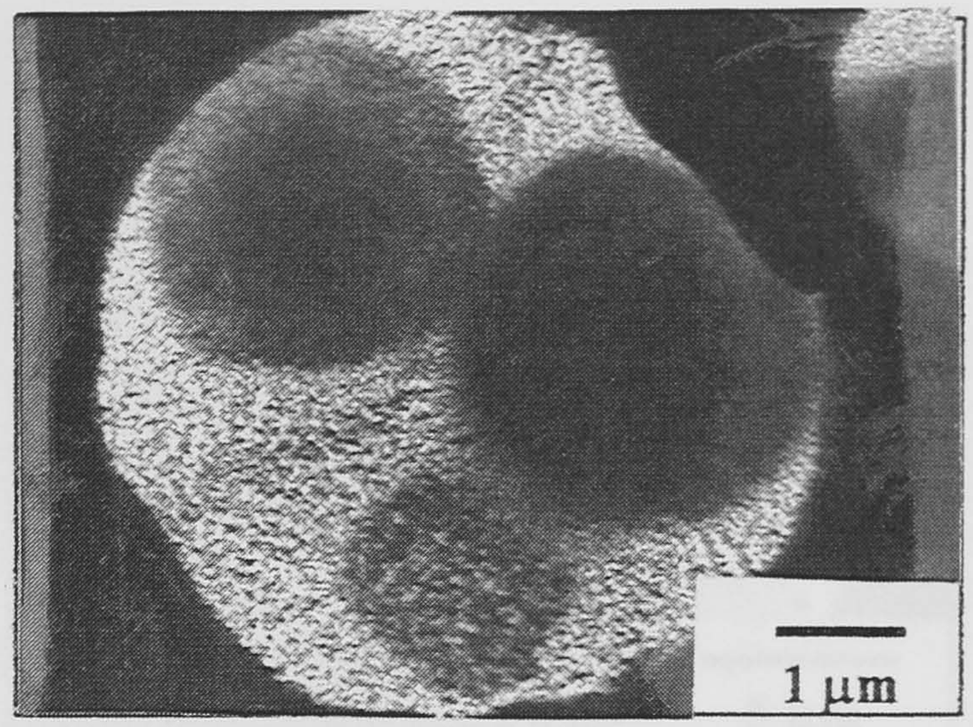


(d)

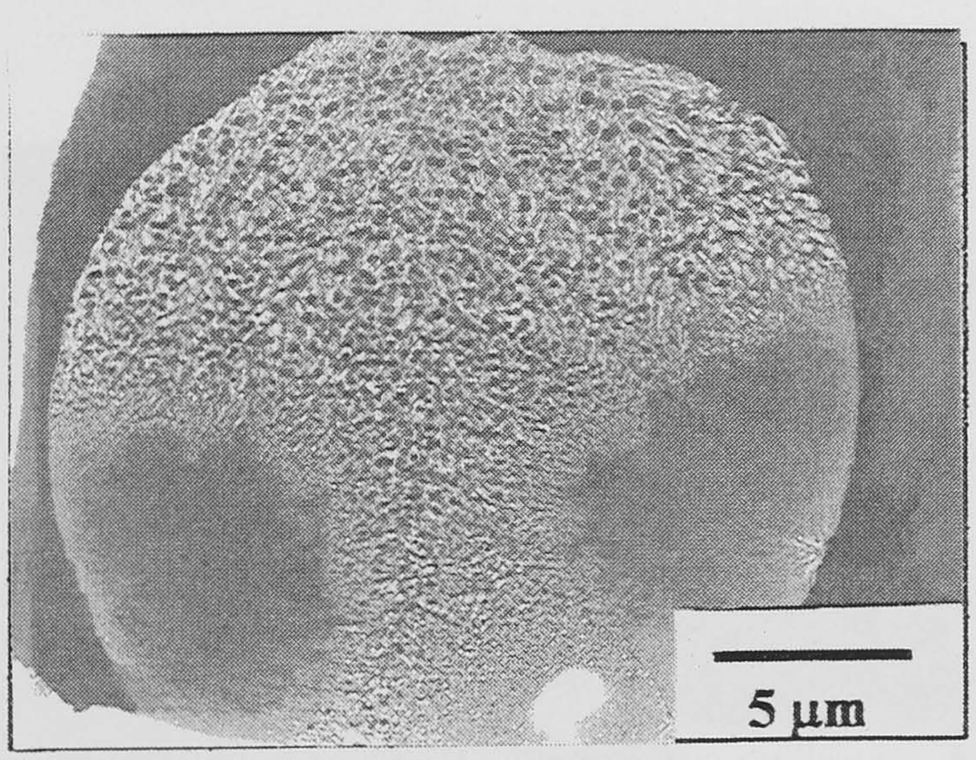
Fig. 5.1.2.4 SEM micrographs of coarse RS-Al-Fe-V powders; morphological transition from cells to dendrites in powder particles sectioned along ((a) and (b)), and normal to ((c) and (d)) the growth direction.



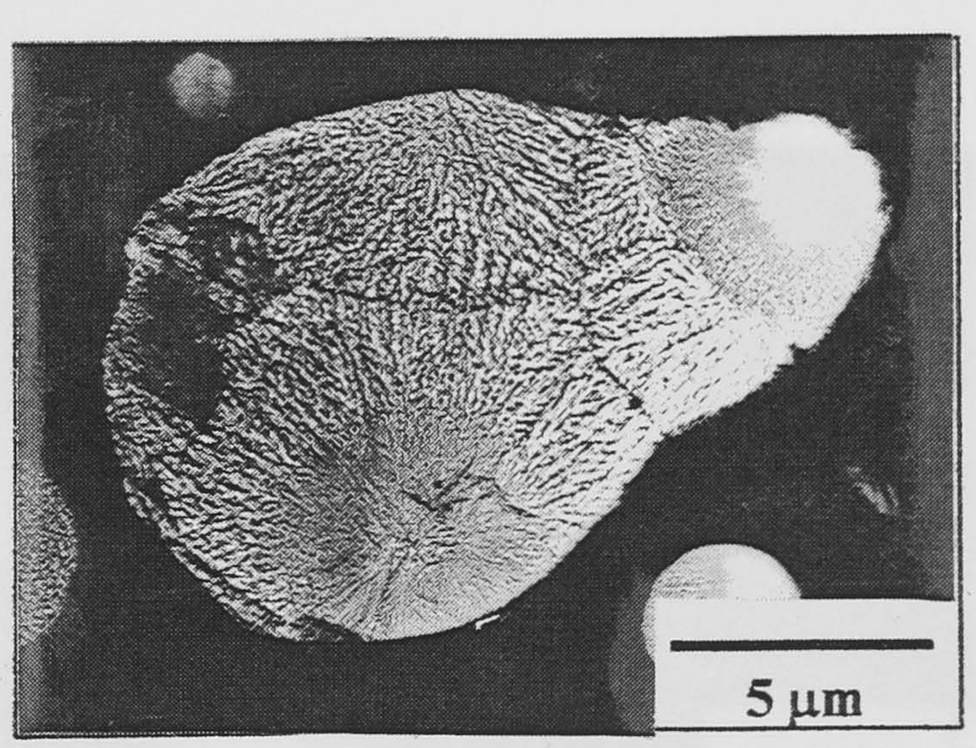
(a) A RS-Al-Fe-V-Si powder particle



(b) A RS-Al-Fe-V powder particle

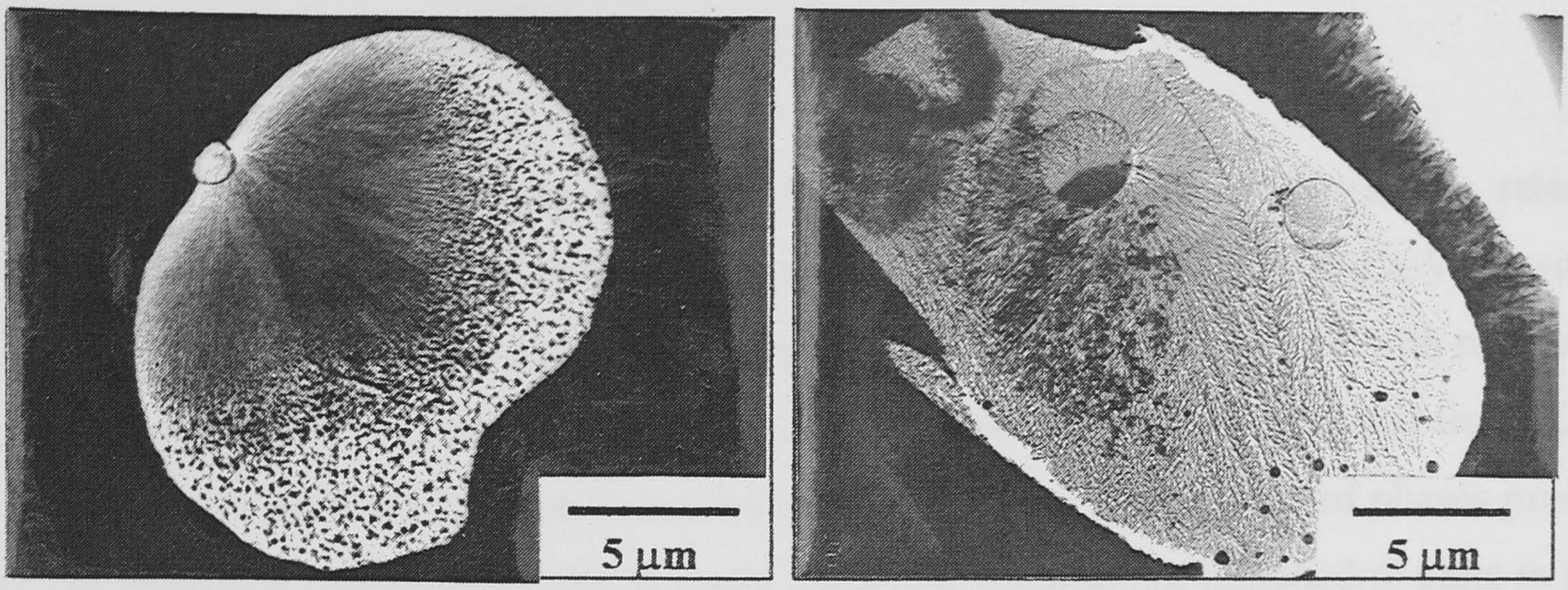


(c) A RS-Al-Fe-V powder particle



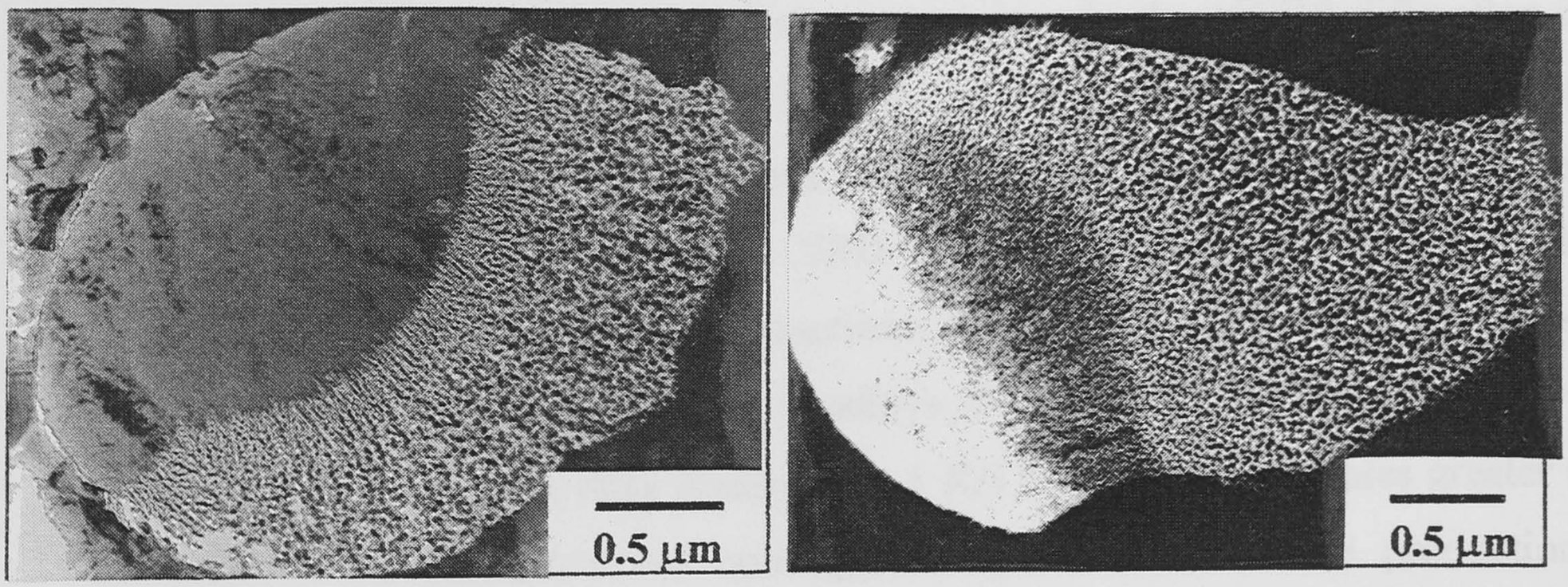
(d) A RS-Al-Fe-V powder particle

Fig. 5.1.2.5 Examples of the RS-Al-Fe-V and RS-Al-Fe-V-Si powders showing more than one nucleation site.



(a) RS-Al-Fe-V powder particles (b) RS-Al-Fe-V powder particles

Fig. 5.1.2.6 Showing a fine satellite particle acting as the nucleation site for solidification of a coarse powder particle.



(a) A RS-Al-Fe-V powder particle (b) A RS-Al-Fe-V-Si powder particle

Fig. 5.1.2.7 Irregular-shaped powder particles of (a) RS-Al-Fe-V and (b) RS-Al-Fe-V-Si alloys.

5.1.3 Phase Identification in the As-atomised RS-Al-Fe-V Powders

5.1.3.1 Phase Identification by XRD

Table 5.1.3.1 contains a summary of the observed *d*-values, the relative intensities (I/I_0) and the possible phases in the as-atomised RS-Al-Fe-V powders (excluding aluminium peaks). The values of I/I_0 in the table are quoted with respect to that of the Al (111) peak. It was recognised that the information obtained from XRD could only be used for identifying the type, but not the morphology of phases present in materials. For example, XRD could detect the presence of icosahedral units in RS-Al-Fe-V powders but could not identify their morphological details. Phase identification by TEM revealed that the phases constructed of icosahedral units in RS-Al-Fe-V powders were in the form of either MI or GCMI particles (§ 5.1.3.2). Henceforth, the term 'I' will be used to represent a single-phase icosahedral particle, which exhibits SADPs with arrays of sharp diffraction spots similar to those obtained from normal crystals, and the term 'PCI' to represent the phases constructed with icosahedral units. By this definition, I, MI, and GCMI phases are included in PCI.

Phase identification was carried out by comparing the measured *d*-values and relative intensities with those of known phases given in the JCPDS diffraction data cards, i.e. numbers 41-1285, 44-1195 for Al_6Fe, and PCI phases, respectively (see Table A3.1 in Appendix). Two phases, namely Al_6Fe and PCI, were likely to be present in RS-Al-Fe-V powders. The XRD peaks corresponding to the Al_6Fe phase could be detected in all powder size fractions. The Al_6Fe is the common phase found in several rapidly solidified Al-Fe based alloys. Formation of this phase in binary Al-Fe alloys requires cooling rates greater than 5 K/s [5.38] and growth rates greater than 0.1 mm/s [5.39]. The calculated cooling rates associated with the production of aluminium and aluminium alloy powders with diameters of up to 100 μm by gas atomisation were reported to be in the range of 10^2-10^5 K/s [5.40-5.43]. This range of cooling rates is sufficient for the formation of Al_6Fe phase in RS-Al-Fe-V powders.

The XRD peaks from the PCI phase may be indexed using sets of six digit numbers [5.44, 5.45]. However, simple indexing (in Table 5.1.3.1) could be done by

following the prescription given in refs. [5.46], and [5.47]. The icosahedral edge length, *a*, calculated from the XRD data by using the method given in ref. [5.41] was 0.510 ± 0.004 nm. The value *a* in rapidly solidified binary Al-Fe and Al-V alloys is independent of composition over a wide composition range; *a* is about 0.508 nm and 0.526 nm in Al-Fe and Al-V, respectively [5.48]. However, the value *a* in ternary Al-Fe-V alloys is dependent on the Fe:V atomic ratio [5.48, 5.49]. For example in the alloys with composition $Al_{87}(V, Fe)_{13}$, the value of *a* decreases (from the value *a* of Al-V to the value *a* of Al-Fe) with increasing Fe content or Fe:V atomic ratio. Because the Fe:V atomic ratio of RS-Al-Fe-V powders (with nominal composition of Al-6.5Fe-1.5V) is 4:1, the value of *a* in this alloy is expected to be close to that of binary Al-Fe alloys. The calculated *a* value of 0.510 ± 0.004 nm in RS-Al-Fe-V powders is close to the *a* value of 0.508 nm in rapidly solidified binary Al-Fe alloys. This result supports that expectation.

Table 5.1.3.1 XRD data and possible phases in RS-Al-Fe-V powders.

Measured *d*-spacing (nm)	Powder volume median diameter, (*D*[v,0.5], μm)						Possible phase (see Table A3.1 in Appendix)
	8	11	14	24	37	50	
0.384	0.3	0.5	0.3	0.6	0.4	0.4	PCI (110 001)
0.243	2.1	1.8	1.5	1.4	1.9	1.6	unknown
0.217	0.8	1.8	2.0	3.0	3.1	3.8	PCI (100 000) + Al_6Fe
0.211	0.2	2.9	2.2	2.0	1.8	0.6	Al_6Fe
0.206	3.0	3.2	4.5	5.2	5.9	6.4	PCI (110 000) + Al_6Fe
0.150	0.2	0.3	0.4	0.6	0.4	0.3	PCI (111 000) + Al_6Fe
0.127	0.3	0.4	0.4	0.7	0.9	0.9	PCI (101 000)
	Relative intensity (I/I_0)						

5.1.3.2 Phase Identification by TEM and EDS

The bright field TEM image and the SADP of globular particles in RS-Al-Fe-V powders are shown in Fig. 5.1.3.1. The SADP exhibited several electron diffraction rings. The rings exhibiting strong intensities (rings R1 and R2) are clearly seen. The measured *d*-values and relative intensities of electron diffraction rings were compared to those of the I-Al_4Mn phase [5.47] (Table 5.1.3.2) and it was found that they matched very well.

In general, I phase particles exhibit SADPs displaying arrays of sharp spots with fivefold, threefold, and twofold rotationally symmetric axes. An example of such SADPs of I phase particles in the as-extruded RS-Al-Fe-V alloy is shown in Fig. 5.3.3.2.3. However, all the globular particles investigated in the as-atomised RS-Al-Fe-V powders exhibited SADPs with diffraction rings. This may indicate that globular particles could be globular clusters of randomly oriented microquasi-crytalline icosahedral (GCMI) phases. The EDS analyses performed on several globular particles revealed that the composition of these particles was Al_x(Fe, V) where x was in the range of 5 to 6. For simplicity, the globular particles are designated here as 'GCMI-Al_x(Fe, V)'.

The SADP of zone B in RS-Al-Fe-V powders (Fig. 5.1.3.2) is similar to that of the GCMI particles mentioned above. The measured *d*-values and relative intensities of rings R1 and R2 of zone B were very close to those of the GCMI-Al_x(Fe, V) particles. In addition to the rings R1 and R2, the SADP also exhibited weak and diffuse rings (R4 and R5). The similarity in SADPs of GCMI-Al_x(Fe, V) particles and of zone B may indicate that the intercellular phases (in zone B) could be very fine, randomly oriented microquasi-crystalline icosahedral (MI) phase.

The MI phases have also been observed in the microcellular structures (similar to zone B of RS-Al-Fe-V powders) of laser surface treated Al-Fe [5.26, 5.50] and melt-spun Al-Fe-Si alloys [5.21]. The other form of quasi-crystalline phases, designated as T′ phase, has also been found in microcellular structures of melt-spun Al-Fe-Mo and Al-Fe-Ce alloys [5.8, 5.51]. The T′ phases were in fact a decagonal (D) phase [5.52].

In this study, no attempt had been made to identify the D phase in the intercellular regions. However, it is speculated that the D phase may solidify in conjunction with the MI phase in intercellular liquid of zone B. The formation of the D phase is favoured at slower solidification velocities or slower quenching rates than those required for the I phase formation [5.53-5.56]. The solute rich intercellular liquid in zone B, resulting from solute rejection during solidification of cellular α-Al front, contains freely dispersed MI particles. During solidification of α-Al phase, the temperature of the intercellular liquid is expected to increase due to latent heat released by recalescence. The increased temperature is not high enough to dissolve the MI particles, but is able to reduce the level of undercooling. Thus solidification velocities of the intercellular liquid are slow. Both high solute content and increased temperature can probably promote the formation of D phase on the surface of MI phase. The D phase has been observed to solidify on the surface of I phase in rapidly solidified Al-Mn alloys when the solidification velocities decreased [5.53, 5.54].

The measured *d*-values and relative intensities of a GCMI-Al_x(Fe, V) particle in zone C and of the intercellular phases in zone B, along with the reported values of the I-Al_4Mn (JCPD card no. 44-1195) are summarised in Table 5.1.3.2.

The EDS analyses performed on coarse cellular structures with cell spacings of 180-360 nm in zone C revealed the segregation of the iron and vanadium elements (see Appendix A2). It was observed that although there was supersaturation of Fe within the cells, Fe tended to segregate to cell walls or intercellular regions where the formation of Al_6Fe phase occurred. Little vanadium could be detected both within cells and at cell walls. Depletion of vanadium in coarser cellular structures of zone C may be attributed to the segregation of V to the GCMI-Al_x(Fe, V) particles during their growth.

The Al_6Fe phase has been observed to exist in the forms of lamellar or rod Al-Al_6Fe eutectics in Al-Fe alloys solidified with low solidification velocities [5.57-5.61]. In some cases [5.57, 5.59, 5.62], the Al-Al_6Fe eutectics were observed in the intercellular/interdendritic regions. However, in this investigation, the Al-Al_6Fe eutectics were not observed in the intercellular/interdendritic regions of the as-atomised RS-Al-Fe-V powders. The Al_6Fe phase was found to be in the forms of continuous intercellular/interdendritic networks. The absence of the Al-Al_6Fe

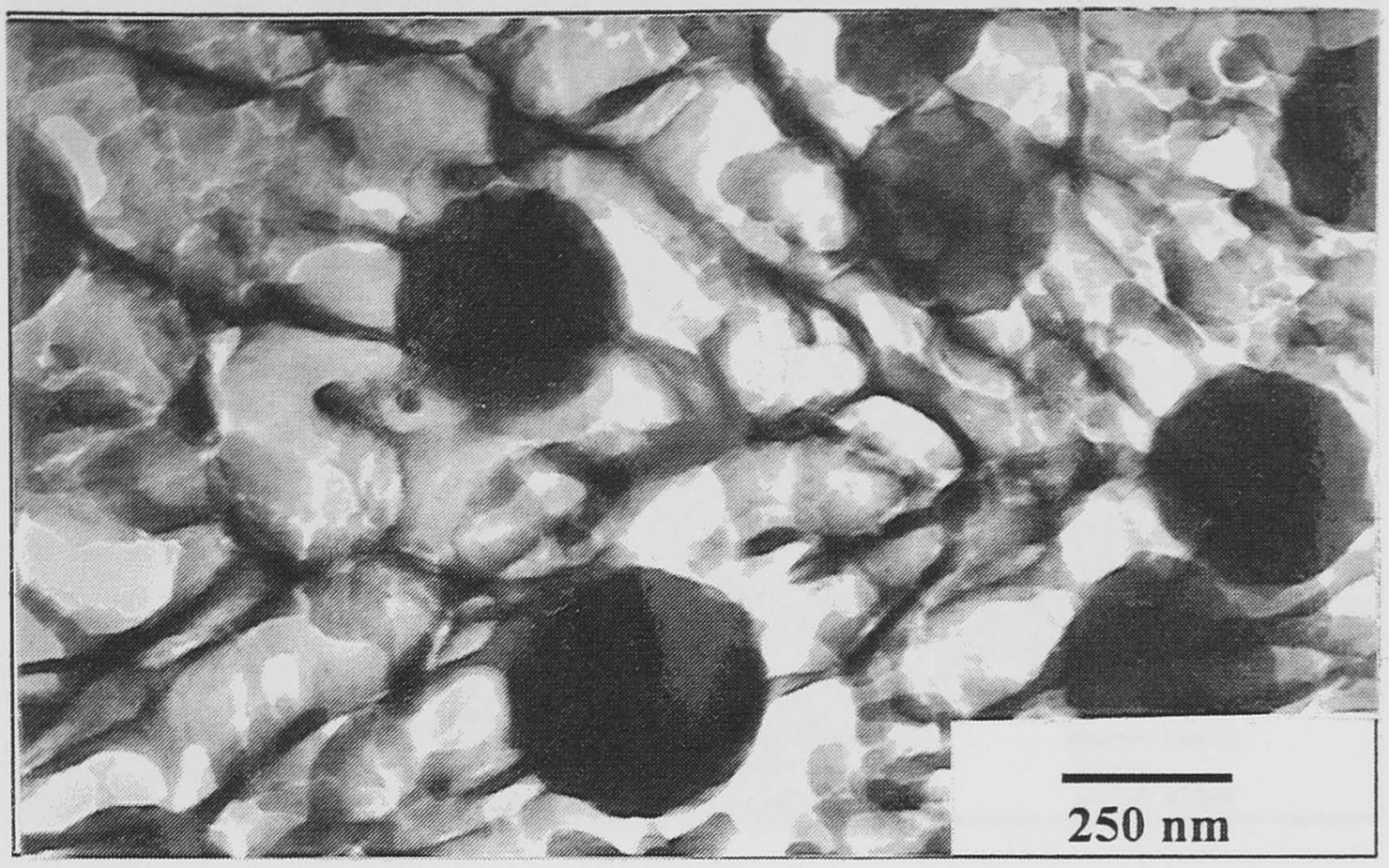
eutectics in the as-atomised RS-Al-Fe-V powders may be attributed to the fact that powder particles result from solidification of melts with high solidification velocities.

Recently, in laser surface treated Al-4 at. % Fe the transition from Al-Al_6Fe eutectic to primary Al-dendrites was observed to occur at high solidification velocities ($\geq$ 0.9 cm/s) [5.42]. A similar morphological transition with change in solidification velocity has also been observed in electron beam surface melted Al-Fe-Ni alloy [5.7]. With low solidification velocities (indicated by electron beam scan velocities of between 0.25 cm/s – 2.5 cm/s), a eutectic α-Al-$Al_9(Fe, Ni)_2$ microstructure was produced. A cellular microstructure with continuous $Al_9(Fe, Ni)_2$ in the intercellular regions was produced with medium velocities (indicated by electron beam scan velocities of between 2.5 cm/s – 100 cm/s). The $Al_9(Fe, Ni)_2$ in the intercellular regions became as rounded particles or dispersoids for high velocities (indicated by electron beam scan velocities of > 100 cm/s).

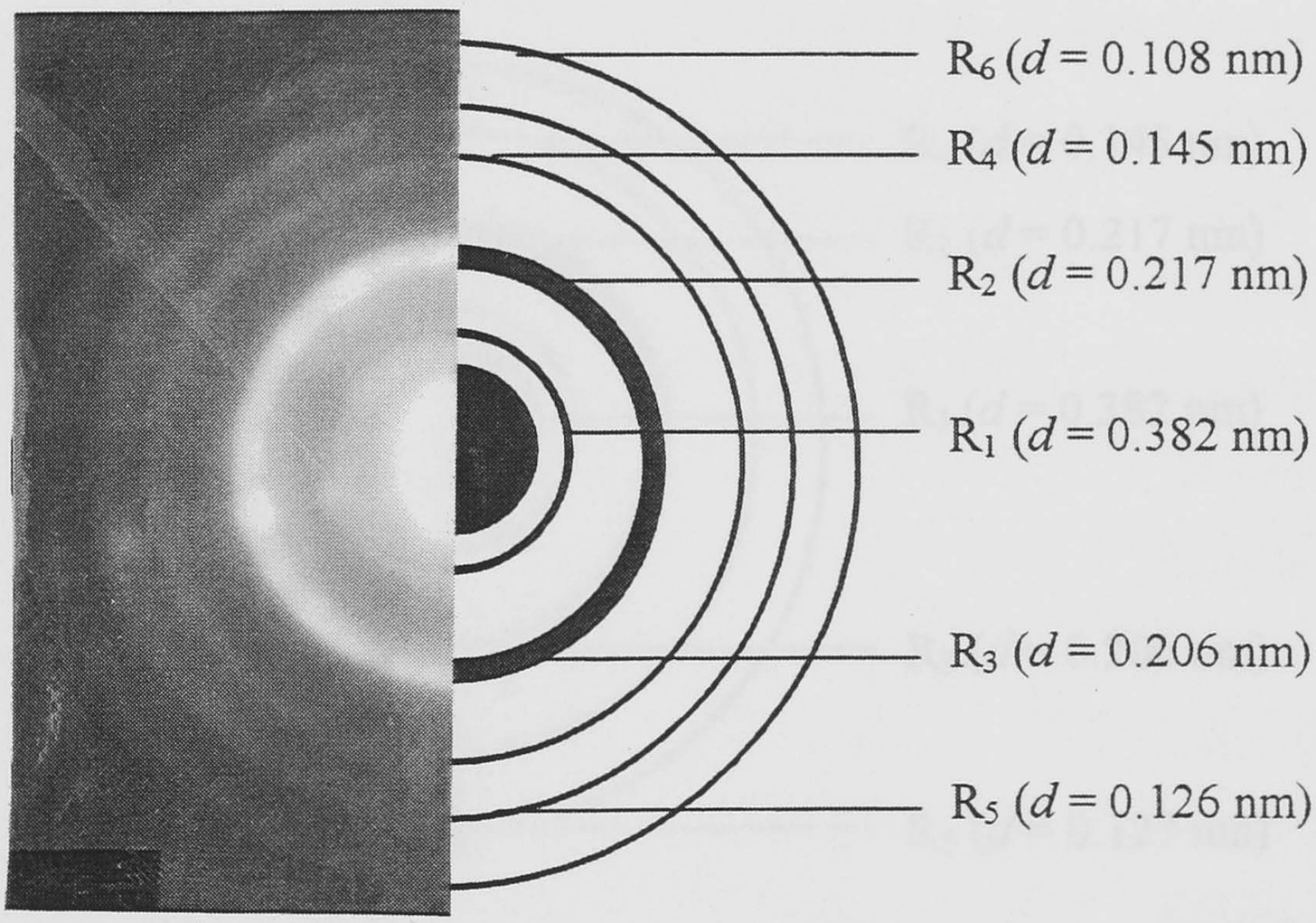
Table 5.1.3.2 Showing the measured *d*-values and relative intensities of a GCMI-$Al_x(Fe, V)$ phase particle (Fig. 5.1.3.1 (b)) and intercellular phases (Fig. 5.1.3.2 (b)) in the as-atomised RS-Al-Fe-V powders, compared to those values of the I-Al_4Mn phase [5.47].

Ring number	GCMI-$Al_x(Fe, V)$ particle		Intercellular phase		I-Al_4Mn		
	d-value, (nm)	I/I_0	*d*-value, (nm)	I/I_0	*d*-value, (nm)	I/I_0	Idexing
R1	0.382	M + D	0.382	M + D	0.3850	22	110001
R2	0.217	S + D	0.217	S + D	0.2170	100	100000
R3	0.206	S + D	0.206	S + D	0.2065	78	110000
R4	0.145	W	0.145-0.127	W + D	0.1459	11	111100
R5	0.126	W			0.1275	20	101000
R6	0.108	W	0.108	VW	0.1085	7	200000

Note: VW = very weak, W = weak, M = medium, S = strong, and D = diffused.

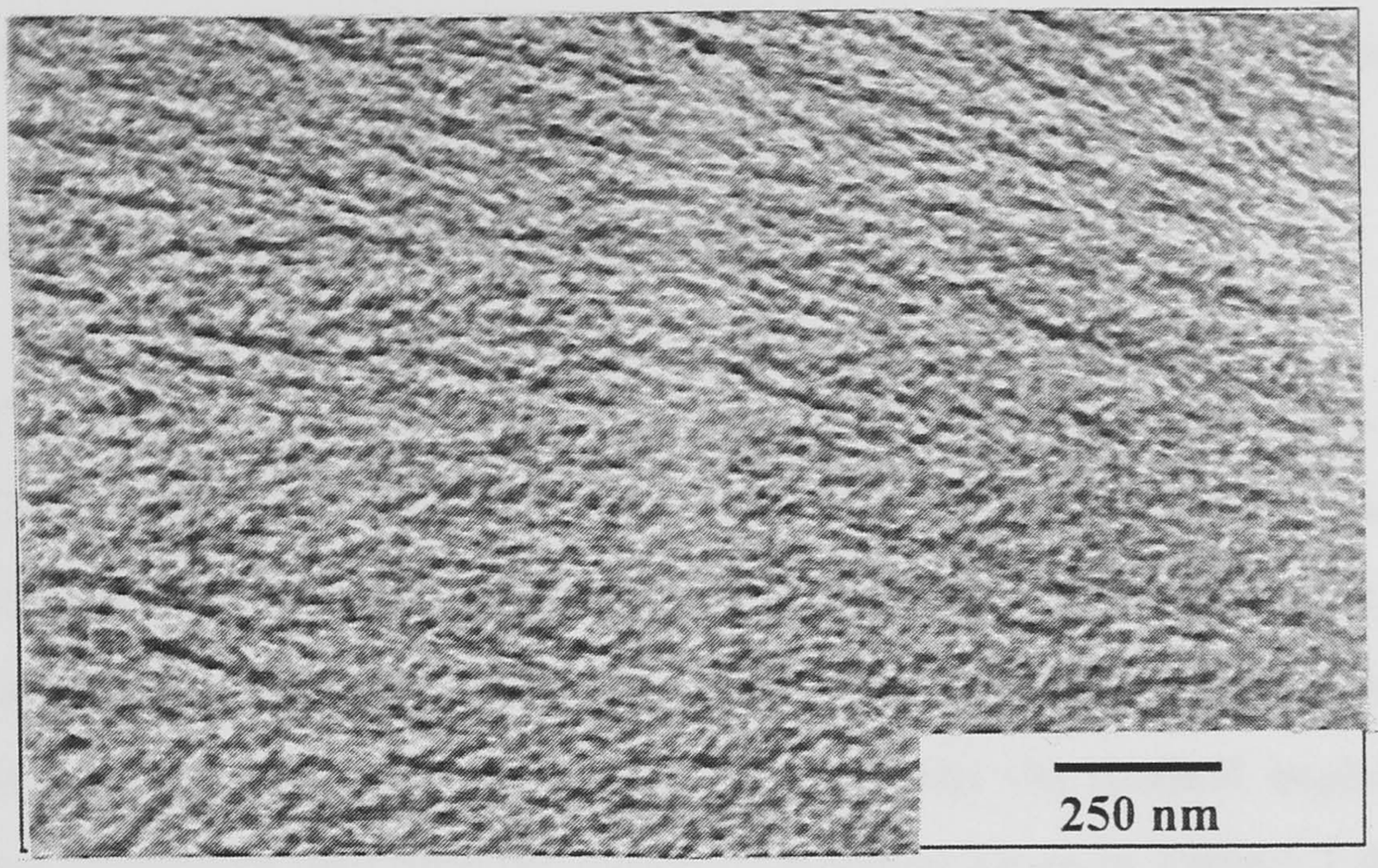


(a)

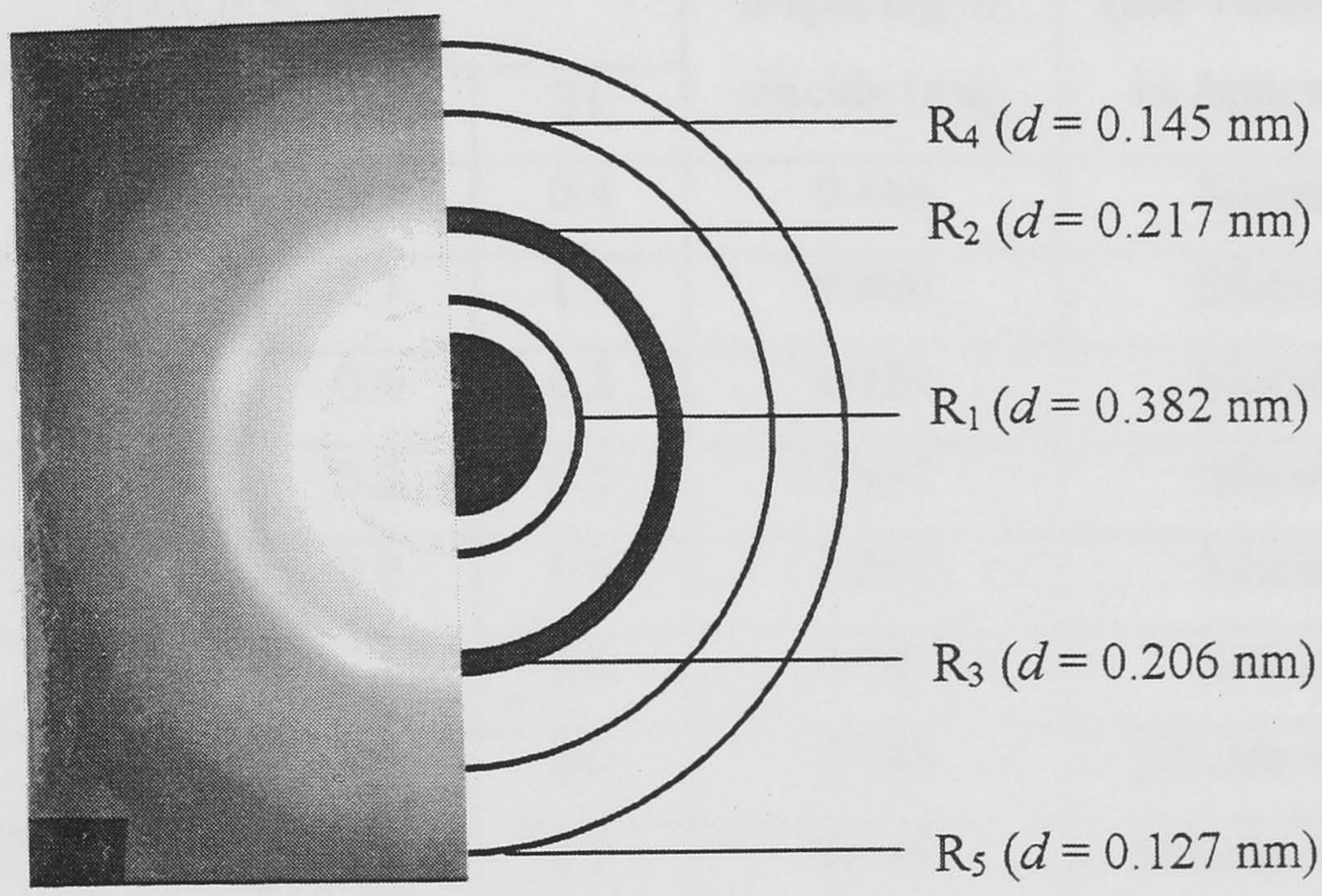


(b)

Fig. 5.1.3.1 Bright field TEM image of GCMI phase particles in coarse cellular microstructures (zone C) of coarse RS-Al-Fe-V powders (a) and SADP (b).



(a)



(b)

Fig. 5.1.3.2 Bright field TEM image (a) and SADP (b) of microcellular structures (zone B) of fine RS-Al-Fe-V powders.

5.1.4 Phase Identification in the As-atomised RS-Al-Fe-V-Si Powders

5.1.4.1 Phase Identification by XRD

The XRD data of RS-Al-Fe-V-Si powders is shown in Table 5.1.4.1. By using the JCPDS cards numbers 6-669 and 44-1195, the XRD peaks could be identified as the reflections from silicide and PCI phases (see Table A3.2 in Appendix). Note that the calculated *d*-spacings of the bcc-Al_{13} (Fe, V)$_3$Si phase (calculation was done by using the lattice parameter = 1.261 nm (§ 5.3.4) and the method explained in ref. [5.63]) matched quite well with the measured *d*-values given in Table 5.1.4.1.

Table 5.1.4.1 XRD data and possible phases in RS-Al-Fe-V-Si powders.

Measured *d*-spacing (nm)	Powder volume median diameter, (*D*[v,0.5], μm)				Calculated *d*-spacing of silicide (nm)	Possible phase (see Table A3.2 in Appendix)
	7	11	17	31		
0.445	0.2	0.2	0.3	0.4	0.446	Silicide
0.400	0.5	0.7	1.7	1.3	0.400	Silicide
0.343	02	0.2	0.4	0.2	0.364	Silicide
0.337	0.2	0.2	0.2	0.3	0.337	Silicide
0.258	0.2	0.4	0.2	0.2	0.257	Silicide
0.247	0.4	0.3	1.1	0.6	0.247	Silicide
0.217	1.7	2.3	4.0	2.9	0.216	Silicide + PCI
0.210	0.5	0.7	0.7	1.7	0.210	Silicide + PCI
0.149	0.2	0.3	0.3	0.2	0.149	Silicide
0.127	1.2	1.4	1.8	1.1	0.127	Silicide + PCI
	Relative intensity (I/I_0)					

The icosahedral edge length, *a*, determined from XRD data of RS-Al-Fe-V-Si powders was 0.510 ± 0.001 nm. The values of *a* obtained from the RS-Al-Fe-V and RS-Al-Fe-V-Si powders are nearly identical. This indicates that addition of silicon

(1.7 wt. %) to the ternary Al-6.5Fe-1.5V alloy has a minimal effect on the icosahedral edge length or quasi-lattice parameter of the PCI. A minimal effect of silicon addition on the icosahedral edge length has also been reported in rapidly solidified Al-(Fe, V, Si) alloys [5.48].

5.1.4.2 Phase Identifications by TEM and EDS

There were two types of globular particles observed in RS-Al-Fe-V-Si powders. The first type exhibited sharp spots similar to those obtained from a single crystal (Fig. 5.1.4.1). The arrays of diffraction spots in SADPs did not possess a long-range periodic translational order, but showed a crystallographically forbidden rotational fivefold symmetry. The SADPs (Fig. 5.1.4.1) indicate that the first type is I phase. The second type exhibited SADPs with diffraction rings (the SADPs are not shown). This may indicate that the second type could be GCMI phase. It was found that the composition of globular particles (both types), determined by EDS, was $(Al, Si)_x(Fe, V)$ where x was in the range of 5 to 6. The first type of globular particle is designated as 'I-$(Al, Si)_x(Fe, V)$' and the second type as 'GCMI-$(Al, Si)_x(Fe, V)$' here.

The SADP of intercellular phases in RS-Al-Fe-V-Si powders (Fig. 5.1.4.2 (a)) exhibited continuous diffraction rings (Fig. 5.1.4.2 (b)). The *d*-values and relative intensities of electron diffraction rings given in Table 5.1.4.2 matched those of I Al_4Mn phase [5.47]. This indicates that the intercellular phases were fine, randomly oriented MI particles. In coarse cellular microstructures as shown in Fig. 5.1.4.3, very fine intermetallic dispersoids with particle sizes less than 50 nm homogeneously distributed within cell interiors were observed. The presence of dispersoids in coarse microstructures of coarse RS-Al-Fe-V-Si powder particles may indicate that there is no extension of solid solubility in coarse powder particles of this alloy. Very little solute content in solid solution in coarse RS-Al-Fe-V-Si powder particles was observed (§ 5.1.5).

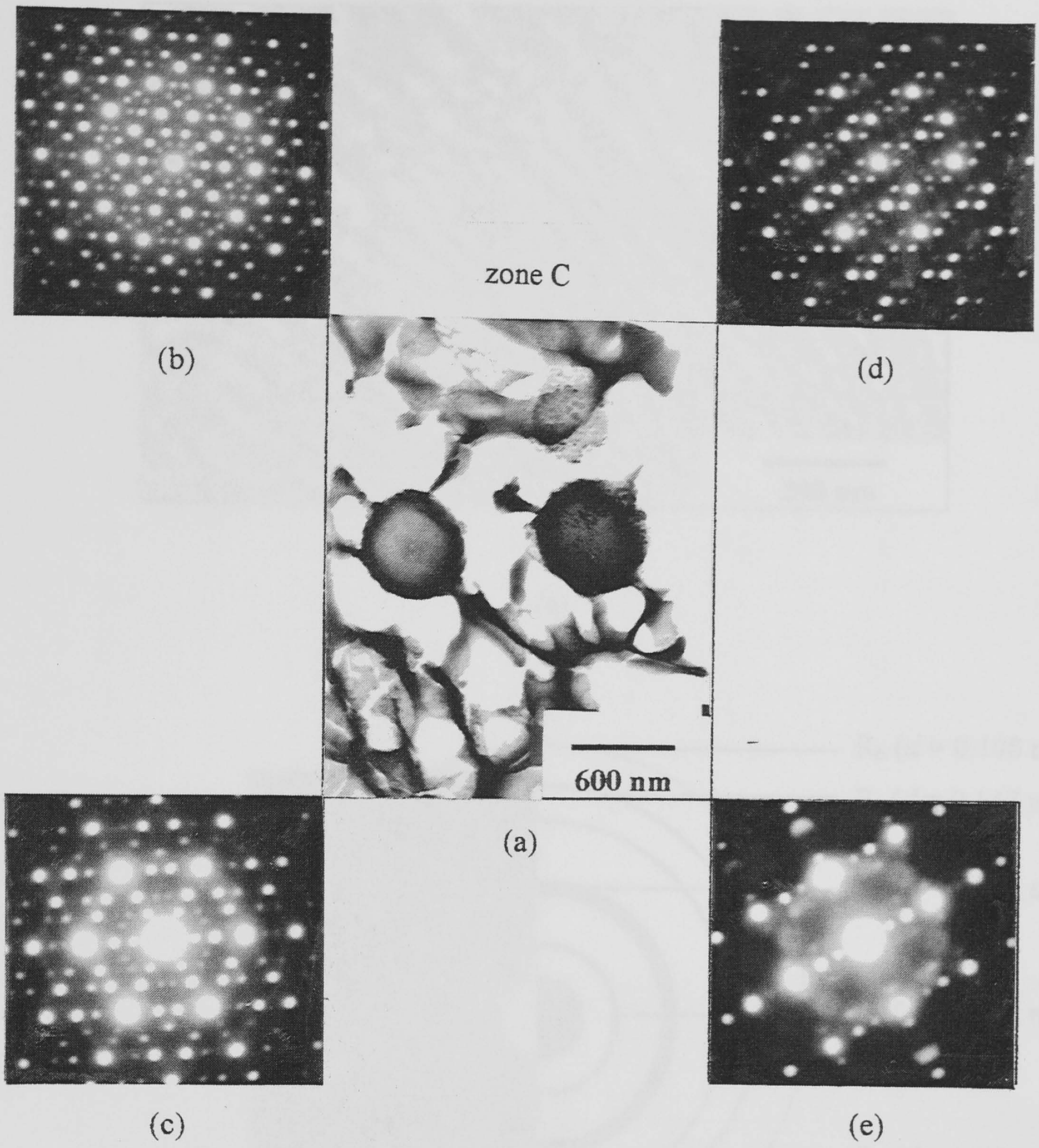
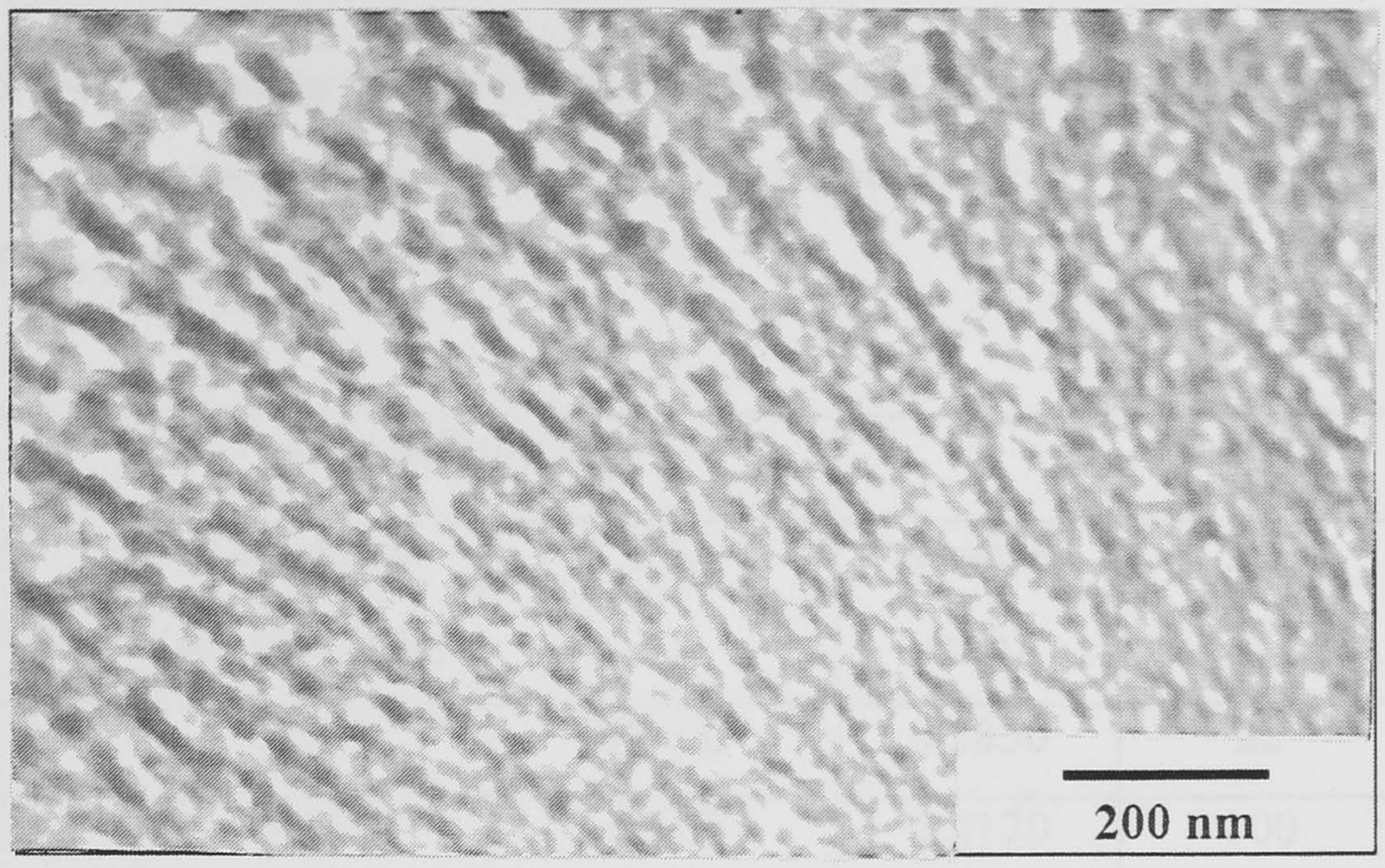
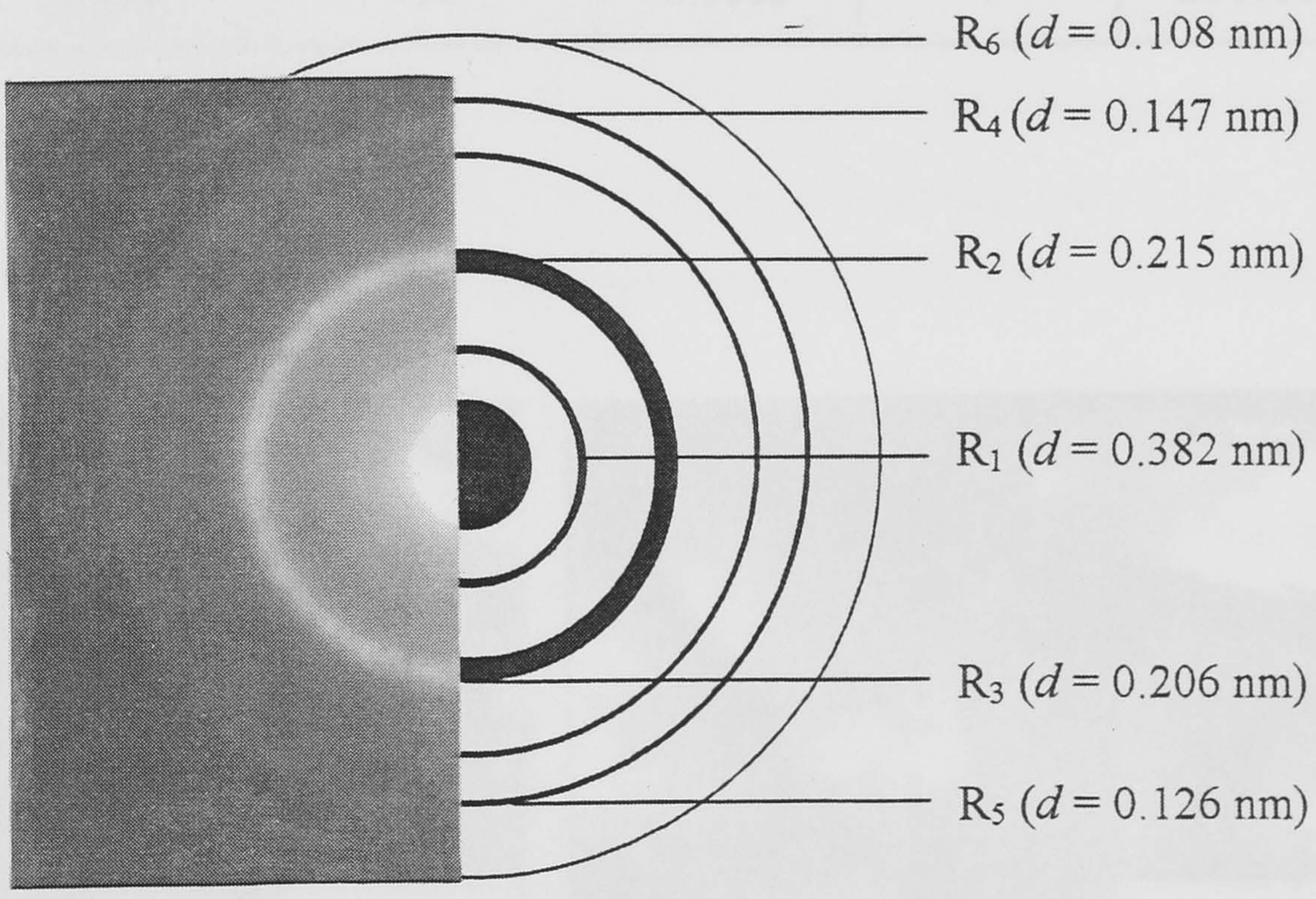


Fig. 5.1.4.1 Bright field TEM image of I-(Al, Si)$_x$(Fe, V) particles in coarse cellular microstructures of coarse RS-Al-Fe-V-Si powders (a) and SADPs showing fivefold (b), threefold (c), twofold (d), and pseudo twofold (e) symmetries, respectively.



(a)



(b)

Fig. 5.1.4.2 Bright field TEM image (a) and SADP (b) of microcellular structures (zone B) of RS-Al-Fe-V-Si powders.

Table 5.1.4.2 Showing the measured *d*-values and relative intensities of intercellular phases in the as-atomised RS-Al-Fe-V-Si powders (Fig. 5.1.4.2 (b)), compared to those of the I-Al_4Mn phase [5.47].

Ring number	Intercellular phase		I-Al_4Mn		
	Measured *d*-value (nm)	I/I_0	*d*-value (nm)	I/I_0	Indexing
R1	0.382	M + D	0.3850	22	110001
R2	0.215	S + D	0.2170	100	100000
R3	0.206	S + D	0.2065	78	110000
R4	0.147	W	0.1459	11	111100
R5	0.126	M	0.1275	20	101000
R6	0.108	W	0.1085	7	200000

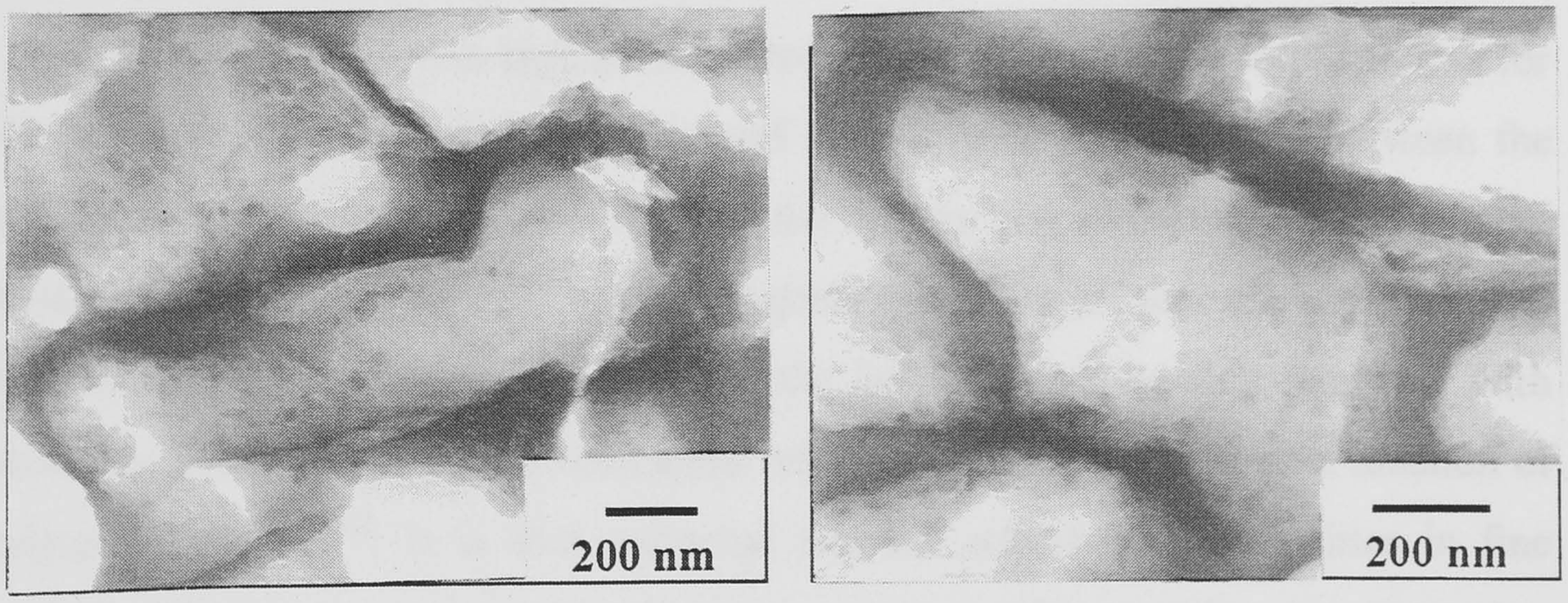


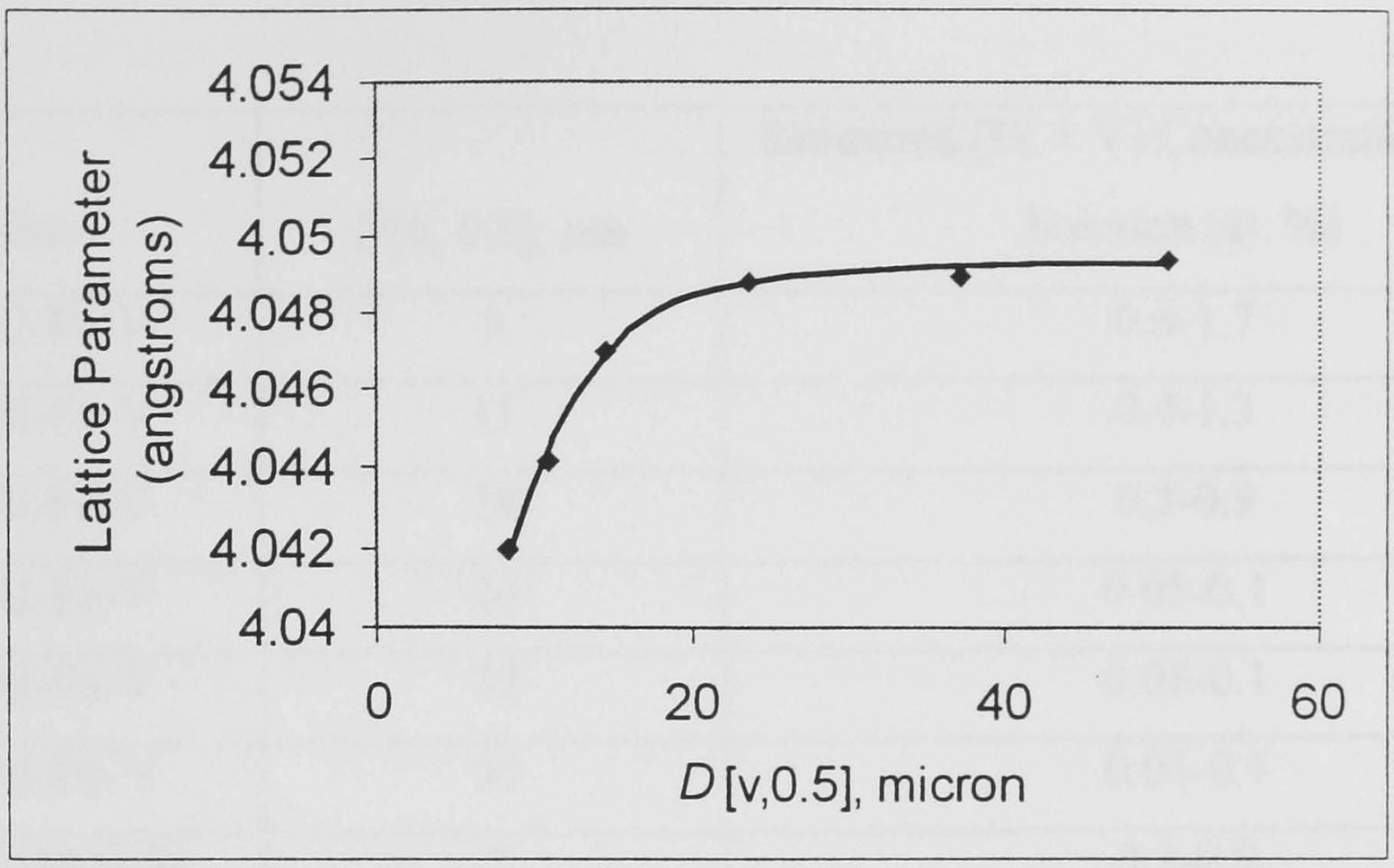
Fig. 5.1.4.3 Coarse cellular microstructures (zone C) of coarse RS-Al-Fe-V-Si powder particles consisting of fine dispersoids.

5.1.5 Lattice Parameters of the As-atomised Powders

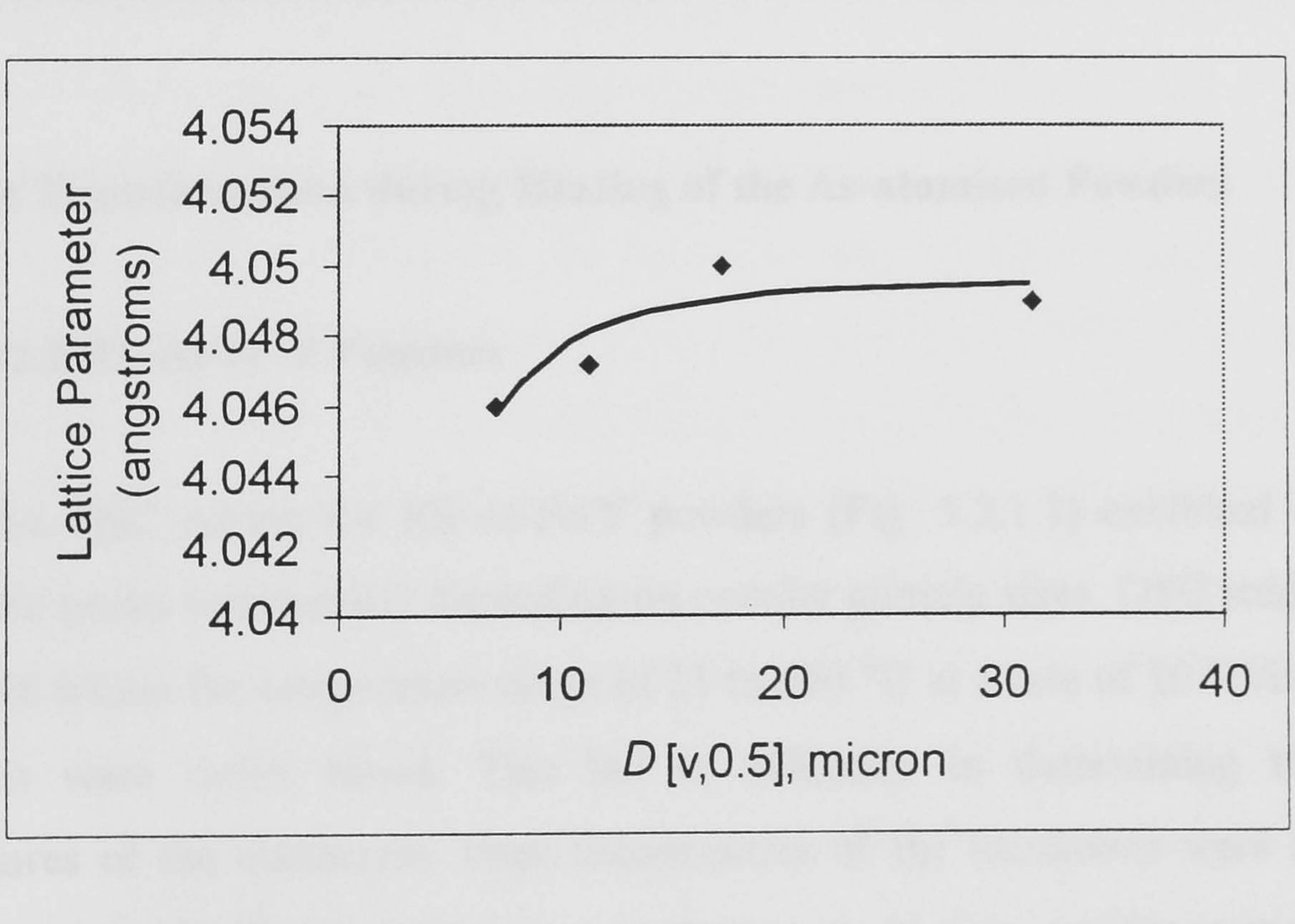
The lattice parameter is usually used to monitor extension of solid solubility due to rapid quenching from the melt [5.64]. It has been reported that the solute iron in binary Al-Fe solid solution alters the lattice parameter resulting in decreased lattice parameters with increased iron concentration [5.64, 5.65]. The value of lattice parameter for each powder fraction was calculated from Al XRD peaks with high 2θ angle by using the Nelson-Riley function. The plots of the calculated lattice parameters versus the powder sizes (D[v,0.5]) of Al-Fe-V and Al-Fe-V-Si alloys are presented in Fig. 5.1.5.

For simplicity, the RS-Al-Fe-V alloy was assumed to be a pseudo binary Al-(Fe, V) system. By comparing the calculated lattice parameter for each RS-Al-Fe-V powder fraction with the lattice parameter-iron concentration curves of rapidly solidified binary Al-Fe alloys [5.64, 5.65], the concentration of (Fe + V) in solid solution in α-Al matrix can be estimated (Table 5.1.5). A similar assumption was made for the case of RS-Al-Fe-V-Si powders, i.e. that this alloy was a pseudo (Al, Si)-(Fe, V) binary system. The estimated (Fe + V) concentration in solid solution for each RS-Al-Fe-V-Si powder fraction is given in Table 5.1.5.

It was observed that high solute content could be retained in solid solution for fine powder particles. It has been reported that there is a relationship between the cooling rate and powder particle size, i.e. the cooling rate increased with decreasing powder particle size [5.24, 5.66]. The relationship between the cooling rate and undercooling [5.67] seems to indicate that the level of undercooling increases with increasing cooling rate. The solidification velocity has been found to be a function of undercooling [5.68-5.70]. It is thus expected that the solidification velocities in fine powder particles are greater than those in coarse powder particles. An increasing solute content in solid solution as a function of solidification rate has been also reported [5.71]. It can be concluded here that the solute content in solid solution increases with decreasing powder particle size, which is perhaps one of the important factors determining the extension of solid solubility. The data, given in Table 5.1.5, supports this conclusion.



(a)



(b)

Fig. 5.1.5 Plot of lattice parameters against powder particle sizes of (a) RS-Al-Fe-V alloy and (b) RS-Al-Fe-V-Si alloy.

Table 5.1.5 Estimated (Fe + V) content in solid solution for each powder size fraction of RS-Al-Fe-V and RS-Al-Fe-V-Si alloys.

Alloy	*D*[v, 0.5], μm	Estimated (Fe + V) Concentration in Solid Solution (at. %)
RS-Al-Fe-V	8	0.6-1.7
RS-Al-Fe-V	11	0.4-1.3
RS-Al-Fe-V	14	0.3-0.9
RS-Al-Fe-V	24	0.05-0.1
RS-Al-Fe-V	37	0.05-0.1
RS-Al-Fe-V	50	0.05-0.1
RS-Al-Fe-V-Si	7	0.3-0.9
RS-Al-Fe-V-Si	11	0.2-0.6
RS-Al-Fe-V-Si	17	0.0
RS-Al-Fe-V-Si	31	0.05-0.1

5.2 Phase Transformation during Heating of the As-atomised Powders

5.2.1 RS-Al-Fe-V Powders

The DSC curves for RS-Al-Fe-V powders (Fig. 5.2.1.1) exhibited different exothermic peaks (exotherms) depending on powder particle sizes. DSC studies were carried out within the temperature range of 25 to 600 °C at a rate of 10 °C/min. DSC exotherms were rather broad. This led to difficulty in determining the onset temperatures of the exotherms. Peak temperatures of the exotherms were therefore chosen to represent the transformation temperatures. In fine powder particles (≤ 5 μm), two exotherms designated as exotherm A and exotherm B, corresponding to peak temperatures of 360 and 500 °C, respectively, were observed. The exotherm A disappeared in coarser powder particles. For powder size fractions with *D*[v, 0.5]

equal to or greater than 15 μm, there appeared an exotherm with peak temperature of 450 °C and this was designated as exotherm C.

The exotherm A was closely related to zone A. The magnitude of exotherm A and the size of zone A both decreased with increasing powder particle size. Therefore the exotherm A results from transformation reactions occurring in zone A. As mentioned earlier (§ 5.1.2), zone A consists of MI phase particles randomly distributed in supersaturated solid solution. The exotherm A can be related to either transformation reactions of solid solution or MI phase particles. However, the exotherm A was not observed in medium and coarse powder particles, which also contain the MI phases in the intercellular regions. Therefore, the exotherm A corresponds to precipitation of phases from solid solution rather than transformation of MI phase particles. The possible phase resulting from precipitation from solid solution could be Al_6Fe. Precipitation of Al_6Fe particles during annealing treatment of splat-cooled Al-Fe alloy has been reported to occur in the temperature range of 300 to 470 °C [5.72]. The peak temperature of the exotherm A is in this temperature range.

The exotherm C was observed only in coarse powder particles (≥ 15 μm) which contain GCMI particles. The magnitude of the exotherm C increased with increasing powder particle size. This trend was consistent with the increase of size and volume fraction of GCMI phase particles with increasing powder particle size. The exotherm C is therefore attributed to the thermally assisted transformation from the GCMI phase to other phases. Microstructures of the as-extruded alloy produced from coarse powder particles exhibited globular I phase particles. This may indicate that the exotherm C corresponds to the transformation reaction from GCMI phase to I phase. Because size, shape, and composition of both GCMI and I phases are the same, the transformation from GCMI to I phase is a polymorphous reaction. SADPs of I phase (§ 5.3.3.2) exhibited sharp diffraction spots whereas those of GCMI phase exhibited ring patterns. This indicates that the transformation is related to structural ordering during heating of GCMI phase.

The measured exotherm C peak temperature obtained in this investigation falls in the transformation temperature range determined for the icosahedral phases in rapidly solidified Al-Mn [5.73], and Al-Fe-V alloys [5.74, 5.75]. The transformation temperatures of icosahedral phases were reported be in the range of 420 to 500 °C for

splat-quenched Al-Mn, and in the range of 400 to 585 °C for melt-spun Al-Fe-V alloys. In both cases, the peak temperatures for transformation of icosahedral phases varied with alloy composition.

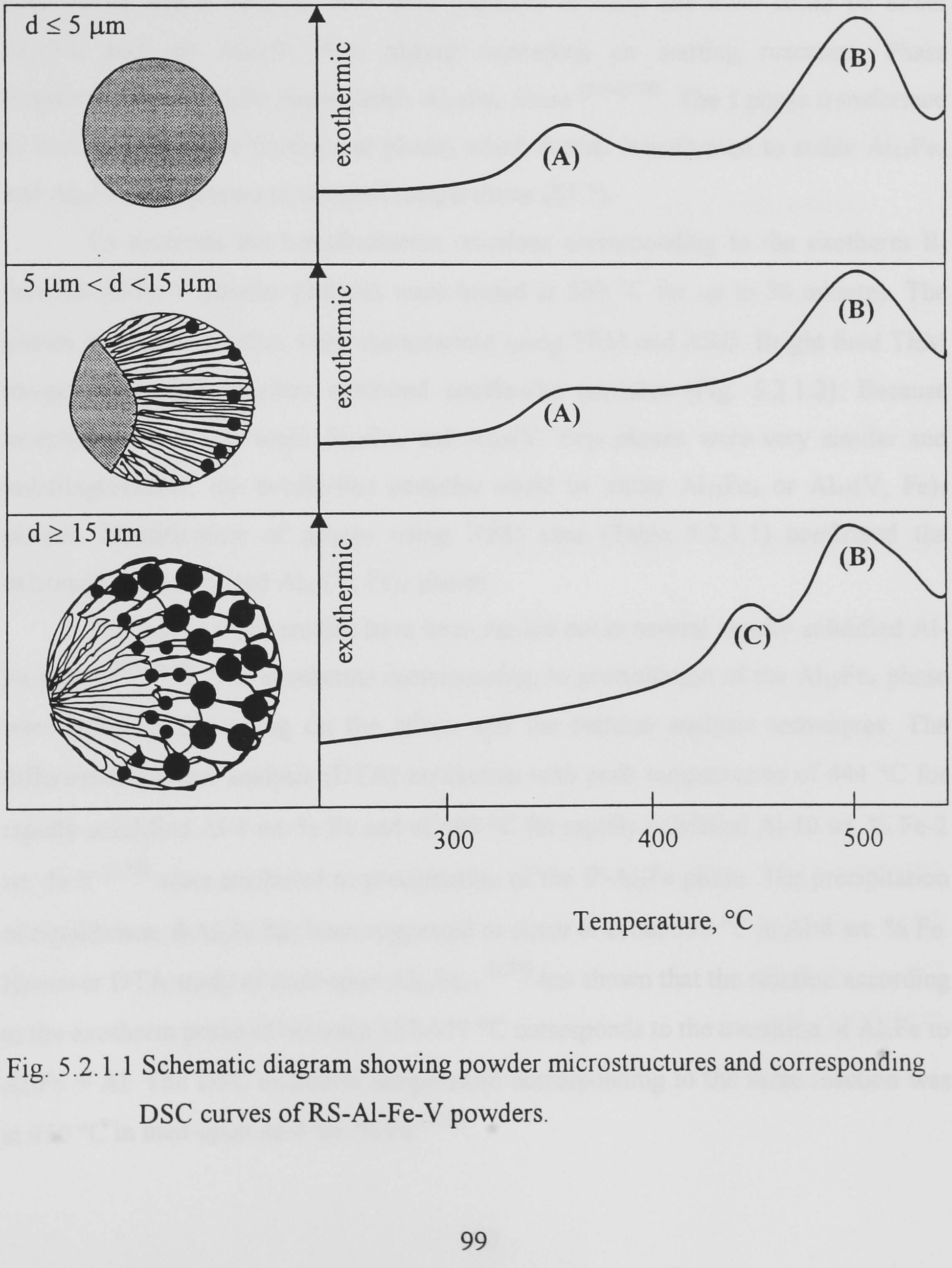
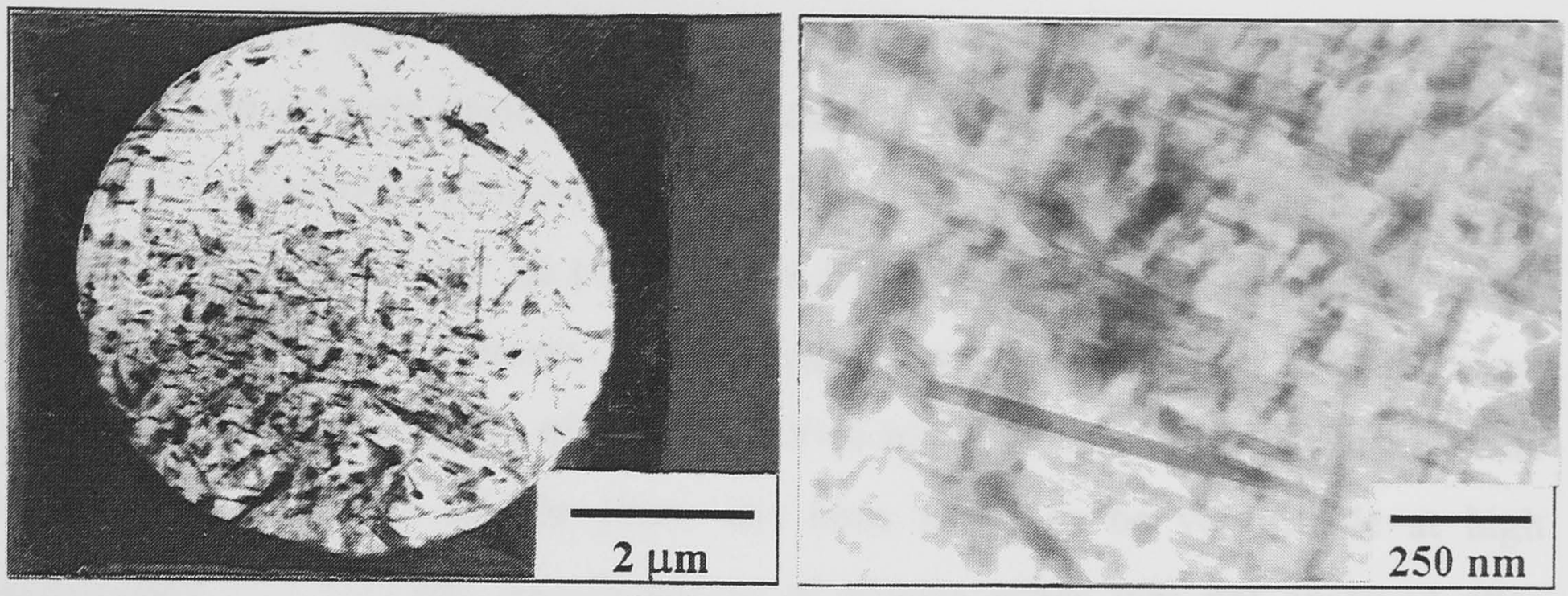


Fig. 5.2.1.1 Schematic diagram showing powder microstructures and corresponding DSC curves of RS-Al-Fe-V powders.

The exotherm B was common in all powder sizes. The reactions corresponding to the exotherm B are likely to be several transformations occurring at nearly the same temperature range. The starting reactants for these reactions are metastable phases including Al_6Fe, I, and MI phases. As mentioned above, the Al_6Fe phase might result from the precipitation from solid solution in zone A, while the I phase probably resulted from the polymorphous transformation of GCMI phase in zone C. The MI phase in the intercellular regions of zone B and zone C did not transform at temperature below 450 °C. The final products of these reactions could be either $Al_{13}Fe_4$ and/ or $Al_{45}(V, Fe)_7$ phases depending on starting reactants. Phase transformation of Al_6Fe phase yields $Al_{13}Fe_4$ phase [5.76-5.78]. The I phase transformed to intermediate phase (hexagonal phase) which further transformed to stable $Al_{13}Fe_4$ and $Al_{45}(V, Fe)_7$ phases at elevated temperatures (§5.7).

To ascertain the transformation reactions corresponding to the exotherm B, fine RS-Al-Fe-V powder particles were heated at 500 °C for up to 30 minutes. The phases in heated powders were characterised using TEM and XRD. Bright field TEM images of heated powders exhibited needle-like particles (Fig. 5.2.1.2). Because morphologies of fine scale $Al_{13}Fe_4$ and $Al_{45}(V, Fe)_7$ phases were very similar and indistinguishable, the needle-like particles could be either $Al_{13}Fe_4$ or $Al_{45}(V, Fe)_7$ phases. Identification of phases using XRD data (Table 5.2.1.1) confirmed the existence of $Al_{13}Fe_4$ and $Al_{45}(V, Fe)_7$ phases.

Thermal analysis studies have been carried out in several rapidly solidified Al-Fe alloys [5.76-5.78]. The exotherms corresponding to precipitation of the $Al_{13}Fe_4$ phase were different depending on the alloys and the thermal analysis techniques. The differential thermal analysis (DTA) exotherms with peak temperatures of 444 °C for rapidly solidified Al-8 wt. % Fe and of 495 °C for rapidly solidified Al-10 wt. % Fe-2 wt. % V [5.76] were attributed to precipitation of the θ'-Al_3Fe phase. The precipitation of equilibrium θ-Al_3Fe has been suggested to occur at about 595 °C in Al-8 wt. % Fe. However DTA study of melt-spun $Al_{86}Fe_{14}$ [5.77] has shown that the reaction according to the exotherm peaks of between 527-577 °C corresponds to the transition of Al_6Fe to Al_3Fe + Al. The DSC exotherm temperature corresponding to the same reaction was at 450 °C in melt-spun Al-8 wt. % Fe [5.78].



(a) A heated RS-Al-Fe-V powder (b) Magnification of (a)

Fig. 5.2.1.2 Bright field TEM images of a RS-Al-Fe-V powder particle heated at 500 °C for 10 minutes.

Table 5.2.1.1 XRD data and possible phases of heated RS-Al-Fe-V powders (excluding Al peaks).

Measured *d*-value (nm)	Relative intensity	Possible phase (see Table A3.3 in Appendix)
0.394	1.2	$Al_{13}Fe_4$
0.350	0.7	$Al_{13}Fe_4$
0.333	0.6	$Al_{13}Fe_4$
0.215	1.8	$Al_{13}Fe_4 + Al_{45}(V, Fe)_7$
0.209	4.0	$Al_{13}Fe_4 + Al_{45}(V, Fe)_7$
0.206	4.3	$Al_{13}Fe_4 + Al_{45}(V, Fe)_7$

5.2.2 RS-Al-Fe-V-Si Powders

The DSC scan of fine RS-Al-Fe-V-Si powder particles showed that the transformation reaction associated with exotherm A was absent. The DSC scans of RS-Al-Fe-V-Si powder particles (Fig. 5.2.2) exhibited a single exotherm with peak temperature at 400 °C for all powder size fractions. The single exotherm may be attributed to the fact that several transformation reactions occur near or at the same temperature. Microstructures of RS-Al-Fe-V-Si powders consist of PCI and silicide phases (§ 5.1.4). The silicide phase has been found to be very stable at high temperature [5.79, 5.80]. The transformation of silicide phase was not observed after heating at 425 °C for 6 months [5.81]. This may suggest that the transformation of the silicide phase does not correspond to the exotherm with a peak temperature of 400 °C.

The possible reactions associated with the exotherm may be the transformation reactions from PCI to other metastable and/or stable phases. It has been found that addition of silicon to RS-Al-Fe-V has a minimal effect on quasi-lattice parameters, but a pronounced effect in reduction of stability of I phase [5.48]. The *in situ* hot-stage TEM studies of melt spun Al-Fe-V-Si alloy [5.82] have revealed the decomposition of unstable MI phase particles at 400 °C. This decomposition also assisted the decomposition of GCMI and I phase particles resulting in doughnut-shaped aggregates of silicide particles. In this study, the PCI phases were not observed in microstructures of the as-extruded products produced from RS-Al-Fe-V-Si powders (§ 5.3.2). This suggests that PCI phases transform to silicide during extrusion and this transformation also corresponds to the DSC exotherm.

A single DSC exotherm has also been observed in RS-Al-Fe-V-Si alloys produced by inert gas atomisation (IGA) and atomised melt deposition (AMD) [5.83]. The exotherm peak temperature of RS-Al-Fe-V-Si alloys produced by IGA technique was 430 °C, whereas that of RS-Al-Fe-V-Si alloys produced by AMD technique was 370 °C. DTA study of melt-spun Al-13.4Fe-0.85V-2.23Si alloy [5.84] showed that there was a single exotherm at 650 °C. This exotherm was attributed to a phase transition from the cubic α-phase (silicide) to hexagonal θ-Al_2(Fe, V, Si) phase. The exotherm

was not reported although there were some transformation reactions occurring at temperatures below 600 °C.

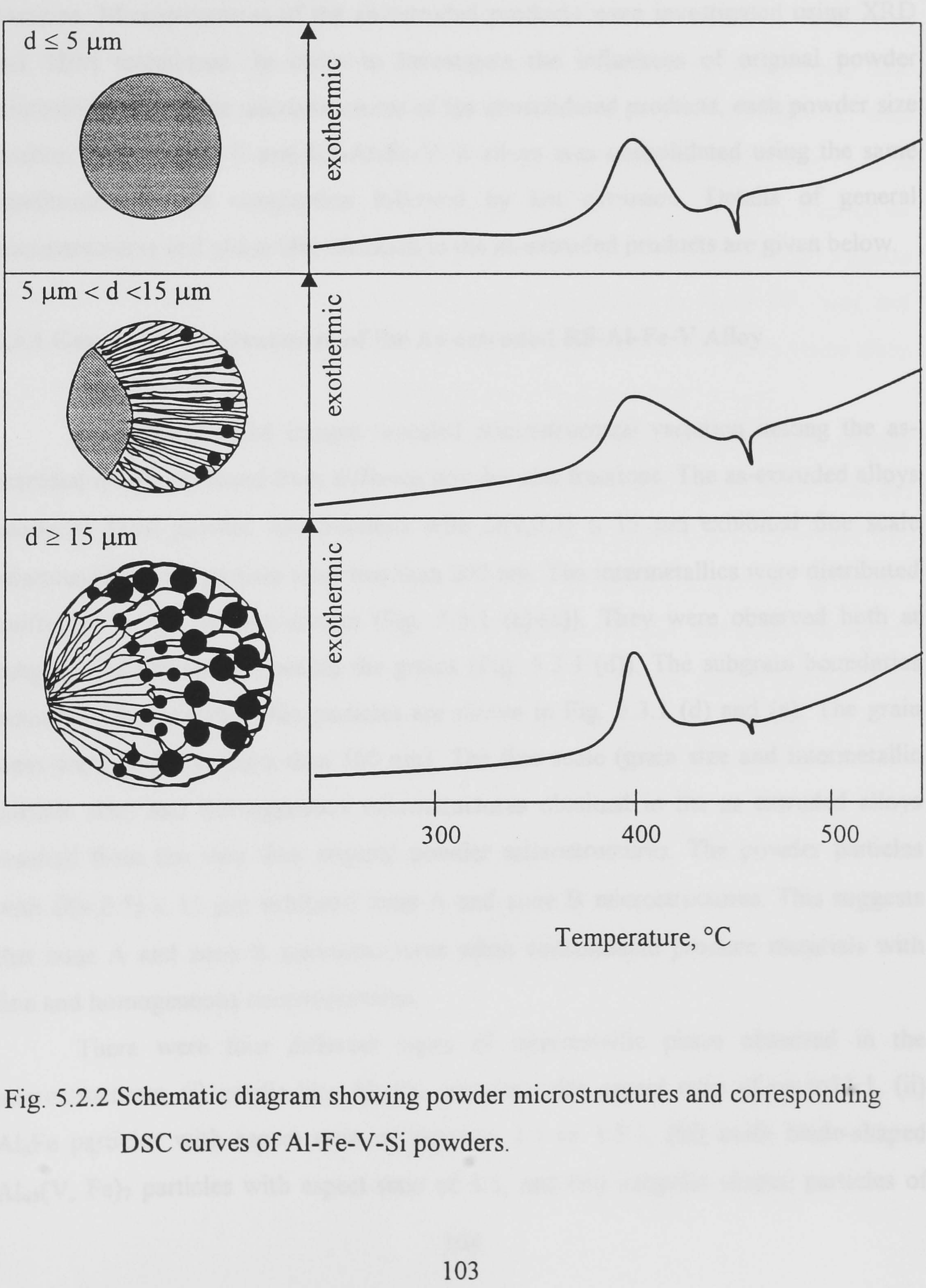


Fig. 5.2.2 Schematic diagram showing powder microstructures and corresponding DSC curves of Al-Fe-V-Si powders.

5.3 Microstructures of the As-extruded Alloys

The powder particles exhibit microstructural variation over the range of particle sizes as mentioned in § 5.1. This variation may cause a difference in microstructures of the as-extruded alloys produced from different powder size fractions. Microstructures of the as-extruded products were investigated using XRD and TEM techniques. In order to investigate the influences of original powder microstructures on the microstructures of the consolidated products, each powder size fraction of RS-Al-Fe-V and RS-Al-Fe-V-Si alloys was consolidated using the same conditions by cold compaction followed by hot extrusion. Details of general microstructures and phase identification in the as-extruded products are given below.

5.3.1 General Microstructures of the As-extruded RS-Al-Fe-V Alloy

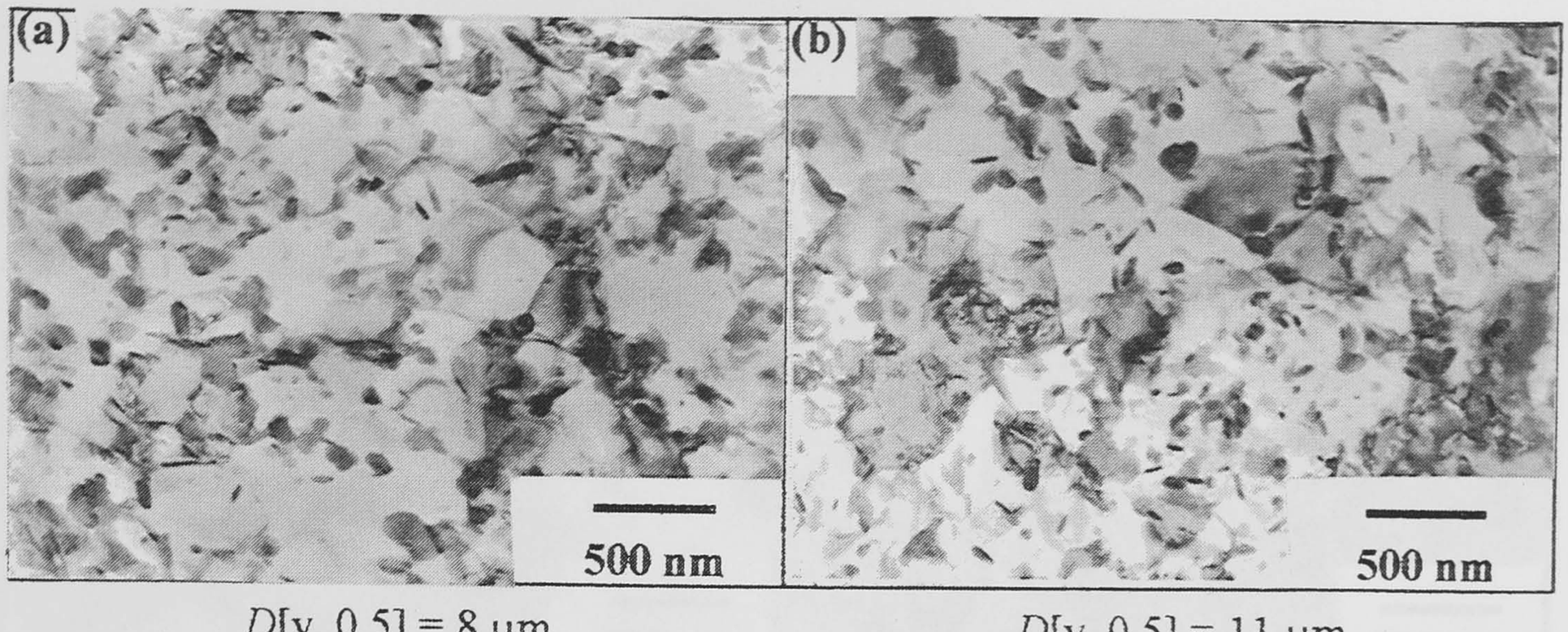
Bright field TEM images revealed microstructural variation among the as-extruded alloys produced from different powder size fractions. The as-extruded alloys produced from powder size fractions with $D[v,0.5] \leq 15$ μm exhibited fine scale intermetallics with particle sizes less than 200 nm. The intermetallics were distributed uniformly in the microstructures (Fig. 5.3.1 (a)-(c)). They were observed both at subgrain boundaries and within the grains (Fig. 5.3.1 (d)). The subgrain boundaries pinned by fine intermetallic particles are shown in Fig. 5.3.1 (d) and (e). The grain sizes were very fine (less than 500 nm). The fine scale (grain size and intermetallic particle size) and homogeneous microstructures obtained in the as extruded alloys resulted from the very fine original powder microstructures. The powder particles with $D[v,0.5] \leq 15$ μm exhibited zone A and zone B microstructures. This suggests that zone A and zone B microstructures when consolidated produce materials with fine and homogeneous microstructures.

There were four different types of intermetallic phase observed in the microstructures; (i) needle-like $Al_{13}Fe_4$ particles with aspect ratio of up to13:1, (ii) Al_6Fe particles with aspect ratio of between 1:1 to 1.5:1, (iii) knife blade-shaped $Al_{45}(V, Fe)_7$ particles with aspect ratio of 5:1, and (iv) irregular shaped particles of

unknown Al-Fe-V phase with aspect ratio of 10:1. Details of these intermetallics are given in § 5.3.3.

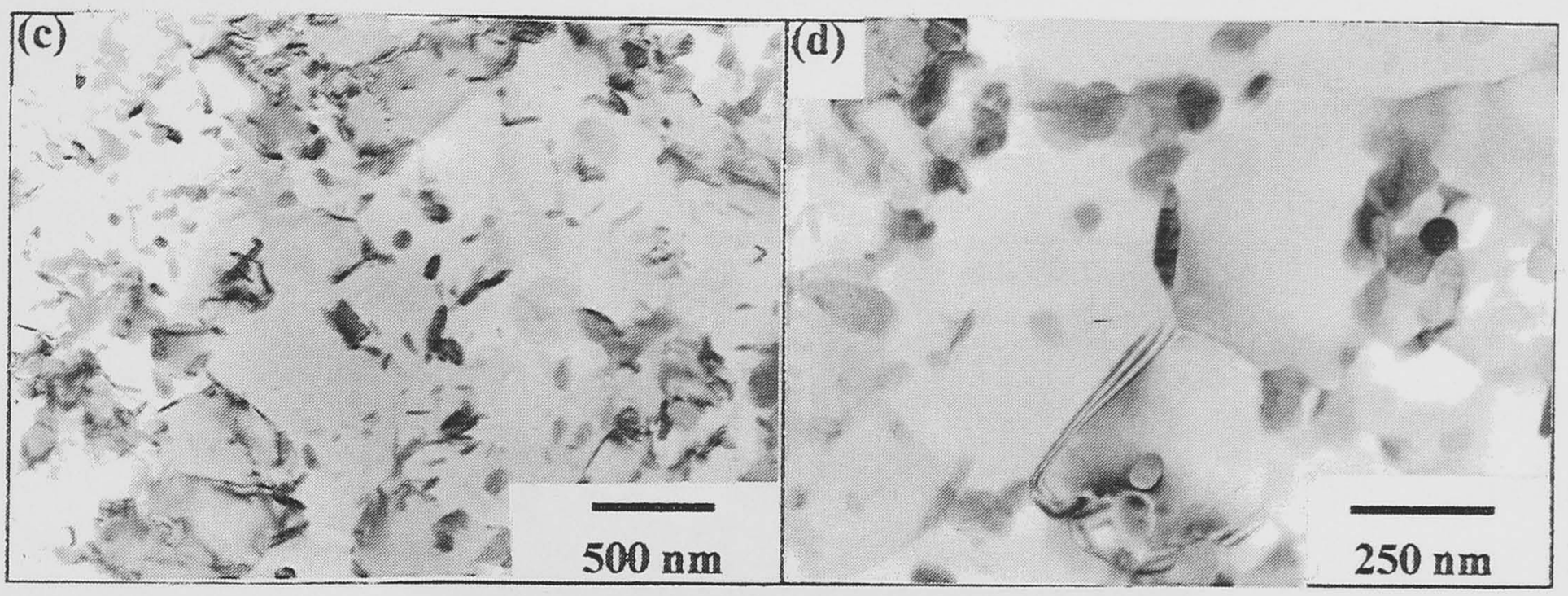
Microstructures of the as-extruded alloys produced from powder size fractions with $D[v,0.5] > 15$ μm were inhomogeneous. They exhibited banded structures (Fig. 5.3.1 (h)). The banded microstructures consisted of two different bands; (i) the band, designated as band I, containing only fine scale intermetallic particles distributed uniformly throughout the matrix, and (ii) the band, designated as band II, containing both fine scale intermetallic particles and coarse globular particles. Note that microstructures of the as-extruded alloys produced from powder size fractions with $D[v,0.5] \leq 15$ μm consisted of only band I. The sizes of globular particles in band II varied from 200 to 500 nm (Fig. 5.3.1 (f) and (g)). The size and volume fraction of globular particles increased with increasing $D[v,0.5]$ value of powder size fraction extruded. The intermetallic particle-free band, designated as band III, was not observed in the as-extruded RS-Al-Fe-V alloy. The grain size of the as-extruded alloy produced from coarse RS-Al-Fe-V powder particles was less than 500 nm.

The banded structures are replicas of the inhomogeneity of the original powder microstructures. Since band I microstructures are similar to the microstructures of the as-extruded alloys produced from powder size fractions with $D[v,0.5] \leq 15$ μm, the band I may be formed from zone A and zone B of powder microstructures. However, there is no zone A present in powder particles larger than 15 μm. The band I in the as-extruded alloy produced from powder particles larger than 15 μm results from zone B. The globular particles are present in only zone C of powder microstructures. Thus the band II results from zone C.



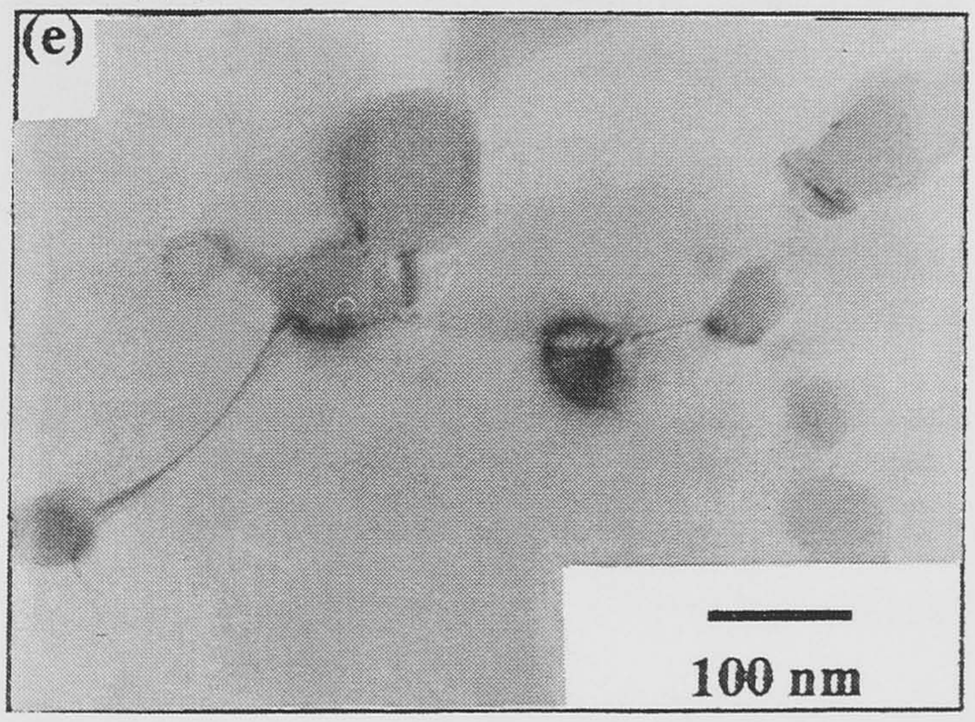
D[v, 0.5] = 8 μm

D[v, 0.5] = 11 μm



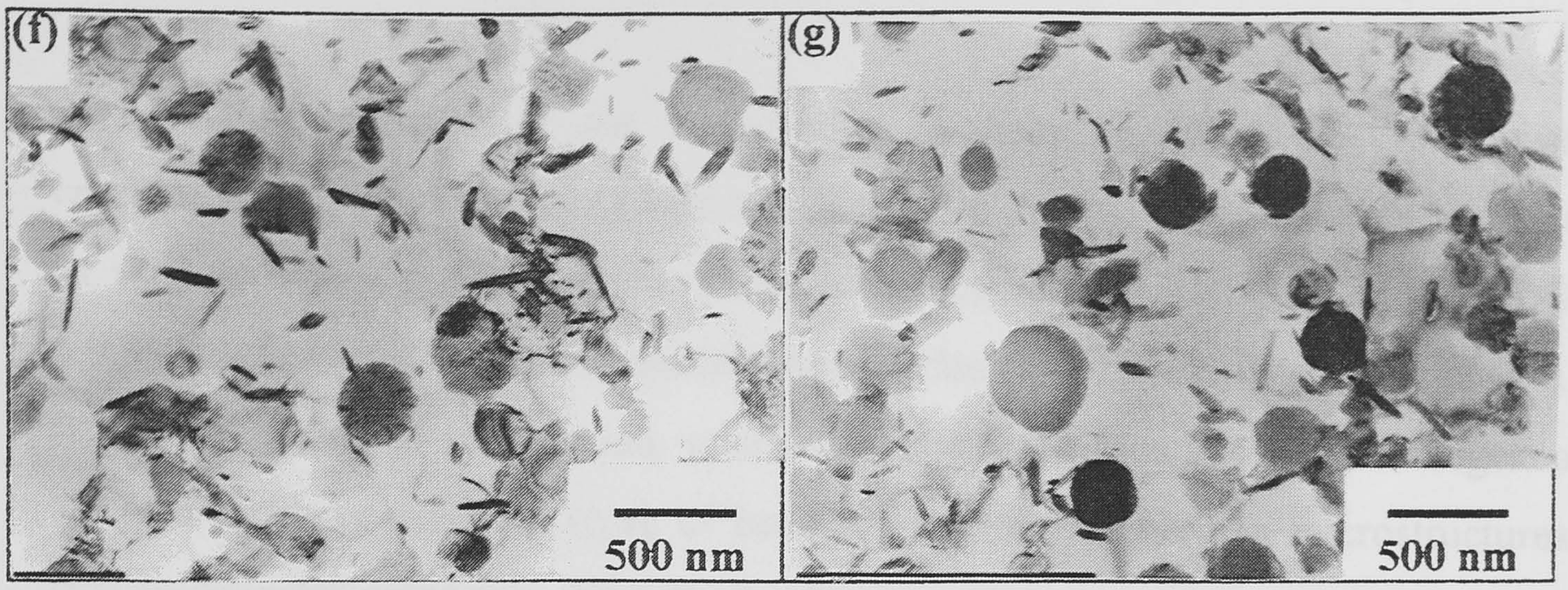
D[v, 0.5] = 14 μm

D[v, 0.5] = 11 μm



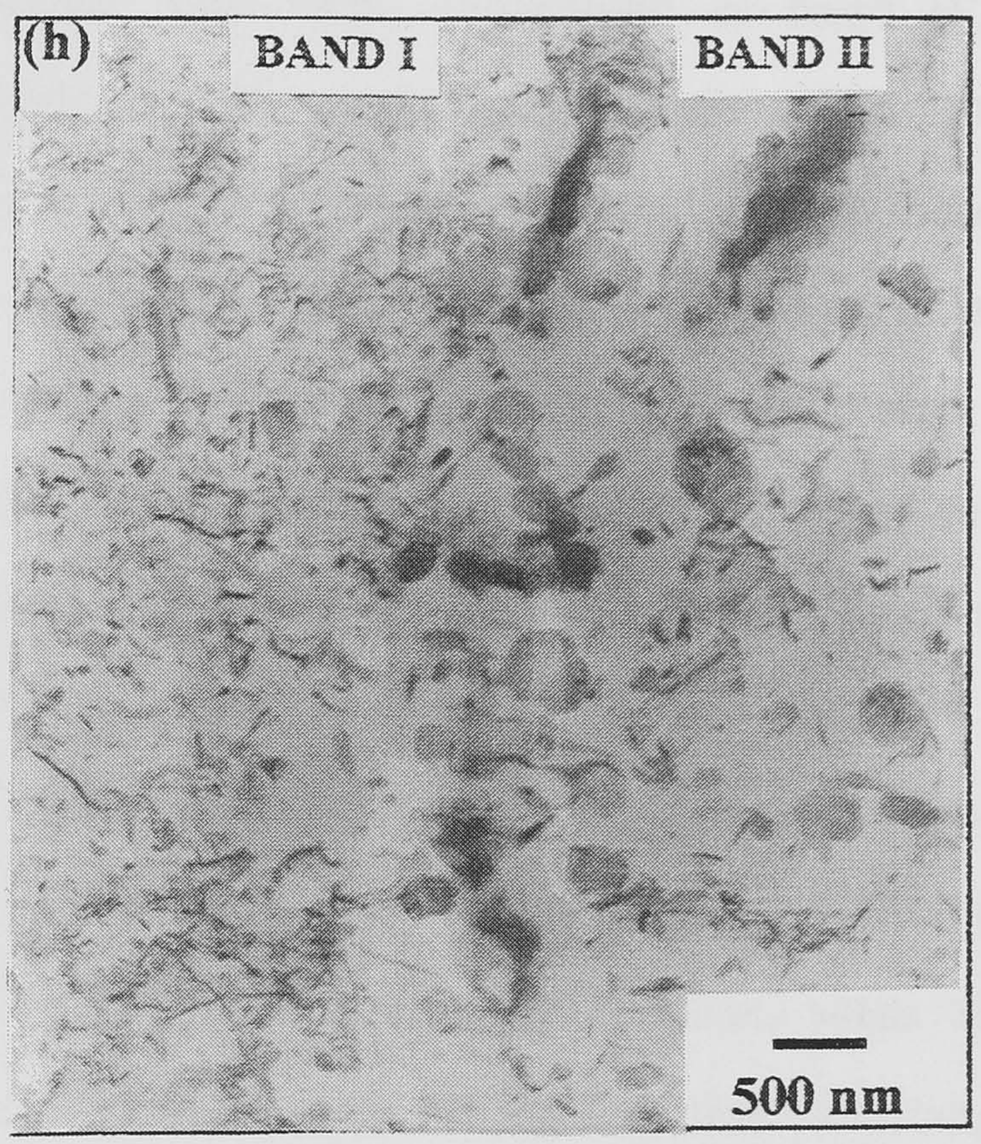
D[v, 0.5] = 11 μm

Fig. 5.3.1 Bright field TEM images of the as-extruded products of RS-Al-Fe-V powders.



D[v,0.5] = 25 μm

D[v,0.5] = 50 μm



D[v,0.5] = 50 μm

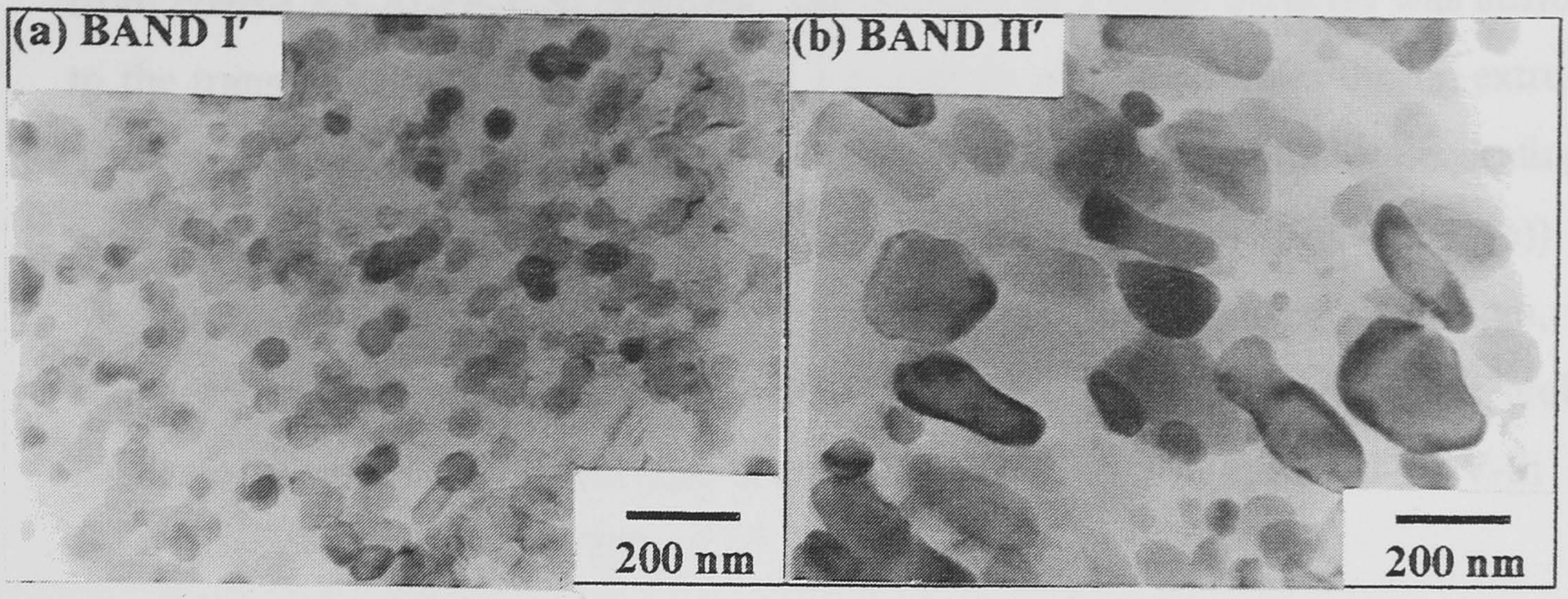
Fig. 5.3.1 Bright field TEM images of the as-extruded products of RS-Al-Fe-V powders (continued).

5.3.2 General Microstructures of the As-extruded RS-Al-Fe-V-Si Alloy

Microstructures of the as-extruded products of RS-Al-Fe-V-Si powders consisted of silicon containing intermetallic particles decorating subgrain boundaries as well as within grain interiors. Phase identifications by XRD, TEM and EDS (§ 5.3.4) indicated that the silicon containing particles were bcc-$Al_{13}(Fe, V)_3Si$ phases.

With careful observation, microstructures were found to be inhomogeneous. There were three different types of banded structure observed in microstructures of the as-extruded products. The band, designated as band I′, consisted of nearly spherical, fine silicide phases with particle size less than 80 nm uniformly distributed in the matrix (Fig. 5.3.2 (a)). Because of the fine scale size and uniform distribution of the silicide particles, the band I′ may result from the original zone A and zone B of powder microstructures. The band, designated as band II′, consisted of coarse elongated silicide phases with particle sizes larger than 80 nm (Fig. 5.3.2 (b)). Elongation of the silicide particles may have resulted from incomplete spheroidization of the decomposed coarse cell walls. The intermetallic particle-free band, designated as band III′, represented the area consisting of only matrix (Fig. 5.3.2 (c)). The formation of band III′ is not understood. A band of larger subgrains aligned in the extrusion direction and containing very few precipitates has been observed in the as-extruded products of Al-Fe-Ni-Co powders [5.85].

Some coarse plate-like particles (Fig. 5.3.2 (d)) were also observed to be adjacent to band III′ in microstructures of the as-extruded alloy produced from powder size fraction with D[v,0.5] = 31 μm. These particles were identified as hexagonal phase particles (§ 5.3.4.2). It is worth noting here that the hexagonal phase may form directly from the melt during solidification of coarse RS-Al-Fe-V-Si powder particles in which little undercooling is obtained rather than by transformation of GCMI and/or I phase particles during extrusion. This is due to two reasons. First, the MI, GCMI and I phase particles in melt-spun Al-Fe-V-Si alloy transformed directly to silicide phase particles [5.82], so no intermediate phases were observed. Second, the hexagonal phase was observed to form directly from the melt on the air-side of the Al-Fe-V-Si alloy strips where little undercooling was achieved [5.86].



D[v, 0.5] = 7 μm

D[v, 0.5] = 7 μm

D[v, 0.5] = 31 μm

D[v, 0.5] = 31 μm

Fig. 5.3.2 Bright field TEM images of the as-extruded products of RS-Al-Fe-V-Si powders. The figure shows; (a) band I′, (b) band II′, (c) band III′, (d) plate-like hexagonal phase particles adjacent to band III′, and (e) doughnut-shaped precipitates of the silicide phase.

The I phase particles were not observed in the as-extruded alloys produced from coarse RS-Al-Fe-V-Si powders. The absence of I phase particles was attributed to the transformations from GCMI and I phases to silicide particles during extrusion. The products of the transformation reactions were the silicide particles decorating the grain boundaries in the form of doughnut-shaped aggregates (Fig. 5.3.2 (e)). The doughnut-shaped precipitates of silicide phase, with the core being aluminium, were found to be the intermediate products during the decomposition of the globular particles of clustered microquasi-crystalline phase in melt-spun Al-Fe-V-Si alloy studied by *in situ* hot-stage TEM [5.82].

The grain size measurement was difficult for the as-extruded RS-Al-Fe-V-Si alloys. The presence of an abundance of very fine silicide phase particles along grain boundaries and within the grains causes the difficulty in grain size measurement. However, the grain size of the alloys was found to be less than 500 nm. Since the majority of microstructures (second phase particles and grain sizes) of the as-extruded RS-Al-Fe-V-Si alloy are very fine and fairly homogeneous it would suggest that excellent mechanical properties could be achieved from this alloy.

5.3.3 Phase Identification in the As-extruded RS-Al-Fe-V Alloy

5.3.3.1 XRD

Four different phases, namely $Al_{13}Fe_4$, $Al_{45}(V, Fe)_7$, Al_6Fe and I phases could be identified from XRD data (Table 5.3.1). The Al_6Fe particles present in the microstructure of the as-extruded alloy resulted from the decomposition of solid solution and of the intercellular phases during preheating and extrusion. Some Al_6Fe particles further transformed to equilibrium $Al_{13}Fe_4$ particles, whereas some did not transform. The reason for the remaining of some Al_6Fe particles in the microstructure of the as-extruded alloy may be attributed to the fact that the processing steps of preheating and extrusion are carried out over a short period of time. The emerging extruded rod is also water-quenched. These would inhibit or limit the transformation reaction of some Al_6Fe particles.

Table 5.3.1 XRD data and possible phases in the as-extruded RS-Al-6.5Fe-1.5V alloys produced from different powder size fractions.

Measured *d*-spacing (nm)	Powder volume median diameter, (*D*[v,0.5], μm)						Possible phase (see Table A3.4 in Appendix)
	8	11	14	24	37	50	
0.439	0.3	0.6	0.8	0.9	1.4	2.4	Al_6Fe
0.396	2.6	3.4	5.2	2.5	2.0	2.9	$Al_{13}Fe_4$
0.369	1.5	2.4	3.7	3.1	2.0	1.3	$Al_{13}Fe_4$ + Al_6Fe
0.350	1.6	2.3	1.8	0.6	1.7	1.9	$Al_{13}Fe_4$
0.326	0.3	0.6	1.3	0.4	0.3	0.5	Al_6Fe
0.244	1.6	2.4	2.7	2.6	2.8	0.8	$Al_{45}(V, Fe)_7$ + unknown
0.224	2.2	1.2	3.0	0.8	1.0	1.8	Al_6Fe + $Al_{45}(V, Fe)_7$
0.217	3.0	5.1	7.5	4.6	6.7	8.5	I + Al_6Fe + $Al_{45}(V, Fe)_7$
0.215	4.4	6.1	7.8	3.8	4.0	4.6	Al_6Fe + $Al_{45}(V, Fe)_7$
0.209	9.2	13.9	17.2	6.7	6.0	6.5	$Al_{13}Fe_4$ + $Al_{45}(V, Fe)_7$
0.206	11.1	16.0	23.6	14.1	11.6	16.9	I + Al_6Fe + $Al_{13}Fe_4$ + $Al_{45}(V, Fe)_7$
	Relative intensity (I/I_0)						

Some XRD reflections of the I phase overlap with the strong reflections of other phases. Identification of the phases present in the as-extruded RS-Al-Fe-V alloy without the aid of TEM may lead to errors. However, the microstructural investigations by TEM (§ 5.3.3.2) confirm the existence of Al_6Fe, $Al_{45}(V, Fe)_7$, $Al_{13}Fe_4$ and I phase particles in this material. The I phase particles are products of the polymorphous transformation reaction of the GCMI particles during extrusion. This

reaction was already observed in the DSC study of the as-atomised powders (§ 5.2.1). By using the method explained in ref. [5.47], the average quasi-lattice parameter of the I phase was found to be 0.513 ± 0.007 nm. This value is in the range of 0.508 to 0.526 nm previously found for some melt-spun Al-Fe-V alloys [5.48, 5.74].

5.3.3.2 TEM and EDS

The XRD peak intensities of minor (less abundant) intermetallic phases are very weak. The XRD peaks of one phase may overlap with those of other phases. These make XRD incapable of identifying minor phases in a complicated alloy system. The TEM equipped with EDS provides opportunity for identification of an individual intermetallic particle. The useful information obtained from TEM and EDS includes SADPs and compositions. The intermetallics found in the as-extruded RS-Al-Fe-V alloys are given below.

(1) $Al_{13}Fe_4$

The $Al_{13}Fe_4$ phase is the most common phase frequently observed in the Al-Fe based alloys, particularly in the alloys prepared by conventional casting. The needle-like $Al_{13}Fe_4$ particles were the major phase found in the as-extruded products of RS-Al-Fe-V powders. They were observed to be very fine with particle sizes of 50-500 nm long x 5-50 nm wide. Details of this phase such as crystal structure, electron diffraction patterns and composition is given in § 5.7.1.

(2) $Al_{45}(V, Fe)_7$

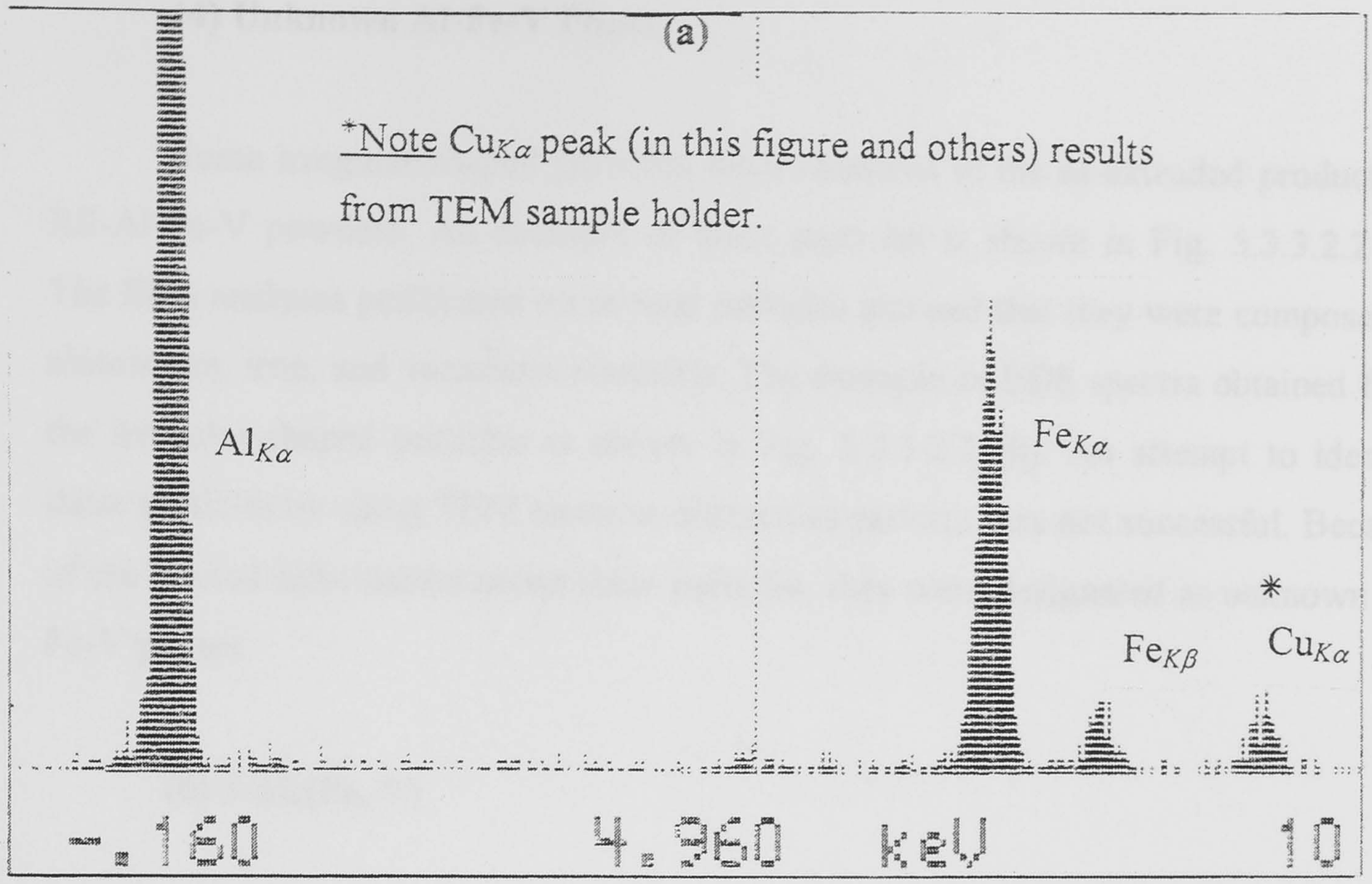
In microstructures of the as-extruded RS-Al-Fe-V alloy, the $Al_{45}(V, Fe)_7$ phases were observed in the forms of very fine knife blade-shaped particles with aspect ratio of 5:1. The size and shape of the $Al_{45}(V, Fe)_7$ phase was similar to those of the $Al_{13}Fe_4$ phase. Few $Al_{45}(V, Fe)_7$ particles were observed compared to $Al_{13}Fe_4$ particles. Because of similarity in morphology and the fine size of $Al_{45}(V, Fe)_7$ and $Al_{13}Fe_4$ phases, it may be difficult to distinguish the former phase from the latter

phase. Identification of very fine intermetallic particles by using information obtained from SADPs or CBED is possible but very difficult. The easy and quick way to distinguish the $Al_{45}(V, Fe)_7$ phase from the $Al_{13}Fe_4$ phase is using EDS analysis. Because there is a very small amount of vanadium in the $Al_{13}Fe_4$ phase, the particles which exhibit strong EDS peak of vanadium are therefore identified as the $Al_{45}(V, Fe)_7$ phase rather than the $Al_{13}Fe_4$ phase. More details of the $Al_{45}(V, Fe)_7$ phase are given in § 5.7.

(3) Al_6Fe

The Al_6Fe particles were frequently observed in all the as-extruded products of RS-Al-Fe-V powders. The size of the Al_6Fe particles varied between 100 and 400 nm. Identification of the Al_6Fe particles is shown in Fig. 5.3.3.2.1. A bright field image and SADPs are displayed in Fig. 5.3.3.2.1 (b). The composition of this phase obtained from EDS was 24.53 ± 1.97 wt. % (13.85 ± 1.25 at. %) Fe with the balance aluminium (Note that vanadium was hardly detected in this phase). The EDS spectrum is shown in Fig. 5.3.3.2.1 (a). The Al_6Fe particles observed in the microstructures of the as-extruded products of RS-Al-Fe-V powders may form either by the decomposition of the coarse intercellular phases or by precipitation from solid solution. During heating of rapidly solidified Al-Fe alloys the precipitation of the Al_6Fe phase was observed to occur at 300 °C and this phase transformed completely to the $Al_{13}Fe_4$ phase at 500 °C [5.87]. The decomposition at cell boundaries resulting in formation of the $Al_6(Fe, Mn)$ particles has been observed in rapidly solidified Al-Fe-Mn alloy [5.88]. The Al_6Fe phase is frequently observed in the Al-Fe alloys produced by techniques in which a molten alloy solidifies with high cooling rates (> 1 K/s) [5.38, 5.89] or with high solidification velocities (> 0.1 mm/s) [5.89-5.61, 5.90].

The structure of the Al_6Fe phase is isostructural with the Al_6Mn [5.91-5.93] and α-(Al-Cu-Fe) [5.93, 5.94] phases. The crystal structure of the Al_6Fe phase is orthorhombic with space group of Ccmm or $Ccm2_1$ [5.91, 5.93, 5.94] and lattice parameters of a = 0.6492, b = 0.7437, and c = 0.8788 nm [5.92, 5.93]. These values are nearly the same as those given by Black *et al.* [5.94] for the unit cell of α-FeCuAl, their values being a = 0.64343, b = 0.74604, c = 0.87768 nm (all ± 0.00010 nm).



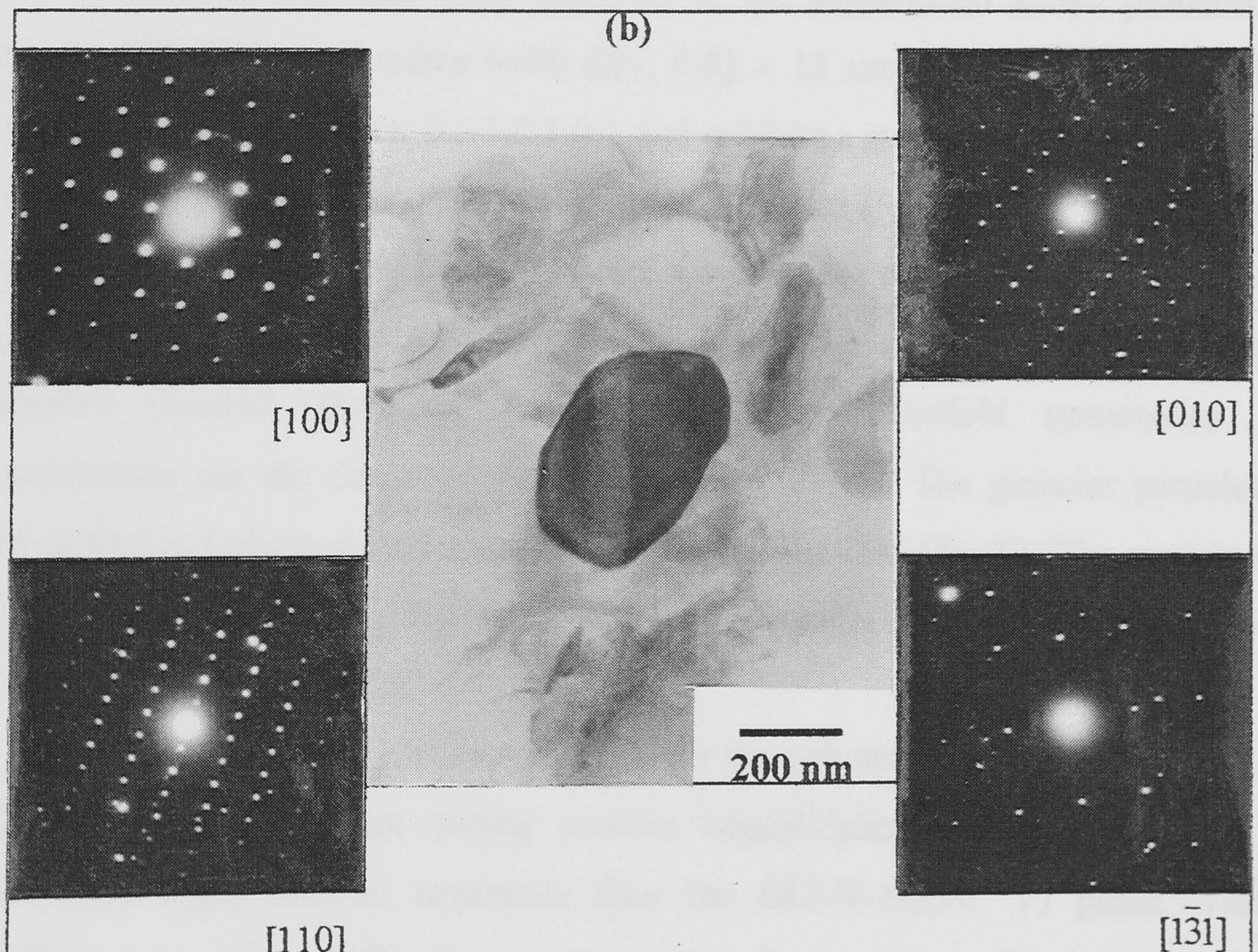


Fig. 5.3.3.2.1 Identification of the Al_6Fe phase: (a) EDS spectrum, (b) a bright field TEM image and SADPs.

(4) Unknown Al-Fe-V Phase

Some irregular-shaped particles were observed in the as-extruded products of RS-Al-Fe-V powders. An example of these particles is shown in Fig. 5.3.3.2.2 (a). The EDS analyses performed on several particles showed that they were composed of aluminium, iron, and vanadium elements. The example of EDS spectra obtained from the irregular-shaped particles is shown in Fig. 5.3.3.2.2 (b). An attempt to identify these particles by using TEM electron diffraction patterns was not successful. Because of the limited information about these particles, they were designated as unknown Al-Fe-V phases.

(6) I-Al_x(Fe, V)

Globular particles were observed in the as-extruded alloys produced from coarse RS-Al-Fe-V powders (with D[v, 0.5] > 15 μm). An example of a globular particles, is shown in Fig. 5.3.3.2.3 (a), and exhibits a striation contrast of radial lines. EDS analyses performed on several globular particles (Fig. 5.3.3.2.3 (b)) revealed that their composition was Al_x(Fe, V), where x was in the range of 5 to 6. SADPs of the globular particle (Fig. 5.3.3.2.3 (a)) exhibited arrays of sharp diffraction spots that display fivefold, threefold, twofold, and pseudo-twofold symmetries. These symmetries are the characteristics of I phase [5.95-5.100]. The globular particles were identified as I phase particles and designated here as I-Al_x(Fe, V). The particle size of I-Al_x(Fe, V) phase was relatively coarse (with diameters of up to 1000 nm) compared to that of $Al_{13}Fe_4$ and Al_6Fe.

The I-Al_x(Fe, V) phase resulted from the polymorphous transformation of the GCMI-Al_x(Fe, V) phase during powder consolidation. The I-Al_x(Fe, V) phase exhibited more ordered structures than the GCMI-Al_x(Fe, V) phase. This was indicated by sharp diffraction spots of the former phase. During consolidation, structural ordering of the GCMI-Al_x(Fe, V) phase to form the I-Al_x(Fe, V) phase may be influenced by both thermal and mechanical effects. DSC studies of RS-Al-Fe-V powders suggested that the structural ordering occurred at 450 °C.

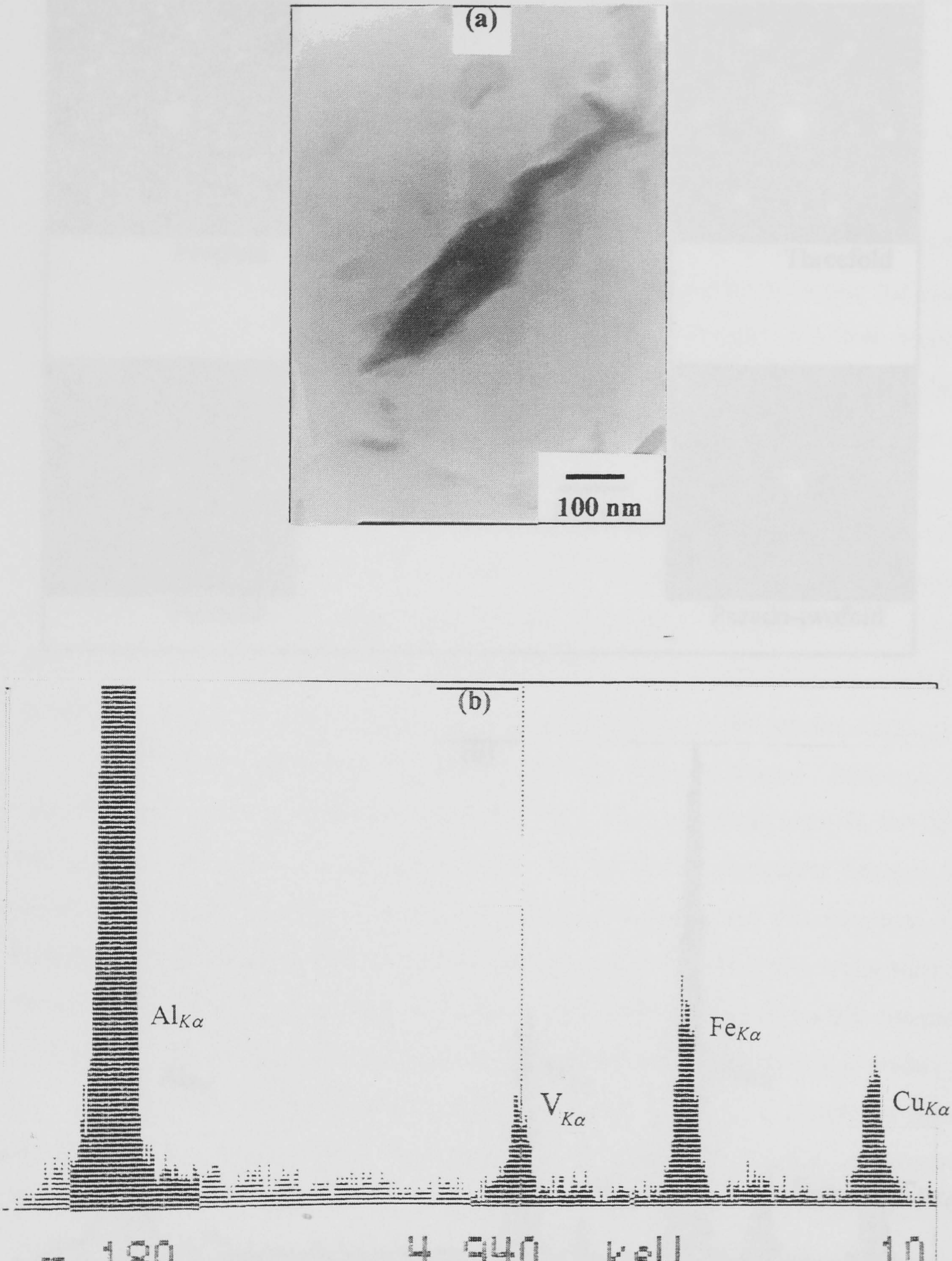


Fig. 5.3.3.2.2 Showing a bright field TEM image (a) and EDS spectrum of the unknown Al-Fe-V phase.

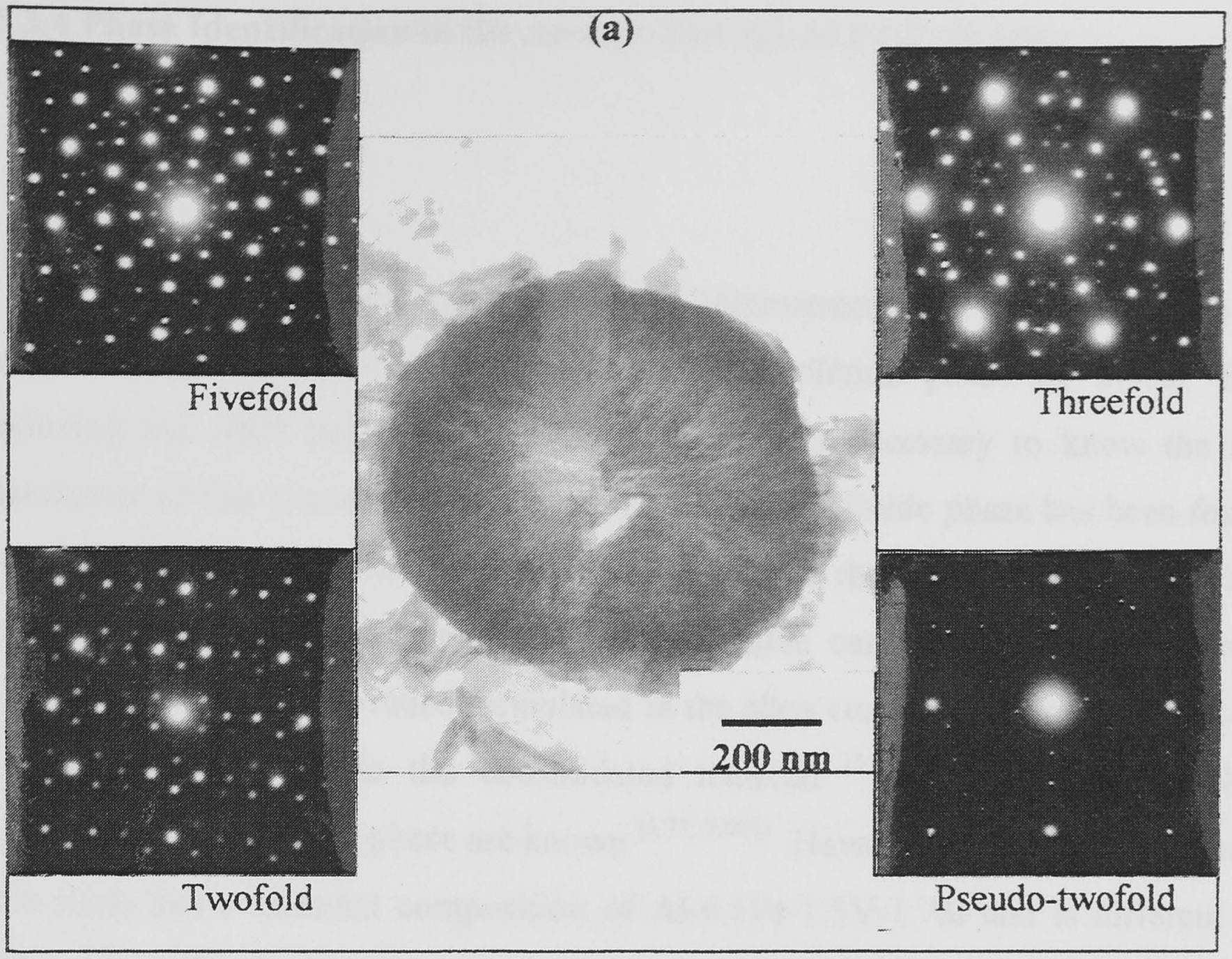


Fig. 5.3.3.2.3 Identification of the I phase: (a) a bright field TEM image of the I phase particle with SADPs, (b) EDS spectrum.

5.3.4 Phase Identification in the As-extruded RS-Al-Fe-V-Si Alloy

5.3.4.1 XRD

The most predominant phase in the microstructure of the as-extruded alloy produced from RS-Al-Fe-V-Si powders is the silicide phase (§ 5.3.2). Before indexing the XRD peaks of the silicide phase it is necessary to know the lattice parameter of this phase. The lattice parameter of the silicide phase has been found to vary significantly with the Fe:V and Al:Si ratios in the composition of the silicide phase [5.75]. The composition of the silicide phase can be controlled because the nominal Fe:V and Al:Si ratios formulated in the alloy composition are carried through to the silicide phase in the consolidated material [5.75]. Some values of lattice parameter of the silicide phase are known [5.75, 5.101]. However, the alloy investigated in this study has a nominal composition of Al-6.5Fe-1.5V-1.7Si and is different from those of the RS-Al-Fe-V-Si alloys reported in refs. [5.75] and [5.101]. It is therefore worth determining the lattice parameter of the silicide phase in the present alloy.

The lattice parameter was determined by XRD technique. Although the specimens of the as-extruded RS-Al-Fe-V-Si alloy were not single crystals, the XRD technique should give a satisfactory value for the lattice parameter because the microstructure of this alloy contained high volume fraction of the silicide phase. The intensities of XRD peaks from this phase (excluding those of Al) were strong whereas those from other minor intermetallic phases were very weak and hardly detected. Therefore, there was no interference resulting from the peaks of other minor phases.

To determine the lattice parameter of the silicide phase, the apparent lattice parameters were plotted against the Nelson-Riley function (N-R function) as shown in Fig. 5.3.4.1. The apparent lattice parameters were calculated by using the standard method given in ref. [5.63]. The value a_0, representing the lattice parameter value corresponding to N-R function = 0, was obtained from the interception of the plot's trend line with the lattice parameter axis. The actual lattice parameter, designated as $\overline{a_0}$, was the averaged value of a_0 values obtained from several measurements. The $\overline{a_0}$ was found to be 1.261 ± 0.001 nm. This $\overline{a_0}$ is different from the value a = 1.256 nm

obtained by using CBED technique in a rapidly solidified Al-8.1Fe-1.8V-0.7Si alloy [5.101]. As the Fe:V ratios are very close, the difference in lattice parameter values may be attributed to the differences in Al:Si ratio.

Having obtained the lattice parameter of 1.261 nm, the XRD peaks from the silicide phase were successfully indexed (in Table 5.2.2). It was observed that the XRD peaks, excluding those of Al, corresponded to the silicide phase. Although the coarse plate-like H-$(Al, Si)_5(Fe, V)$ phase (§ 5.3.4.2) was also observed by TEM in some extruded products of this alloy, the XRD reflections from this phase could not be detected. This was attributed to the small amount (volume fraction) of this phase in this alloy.

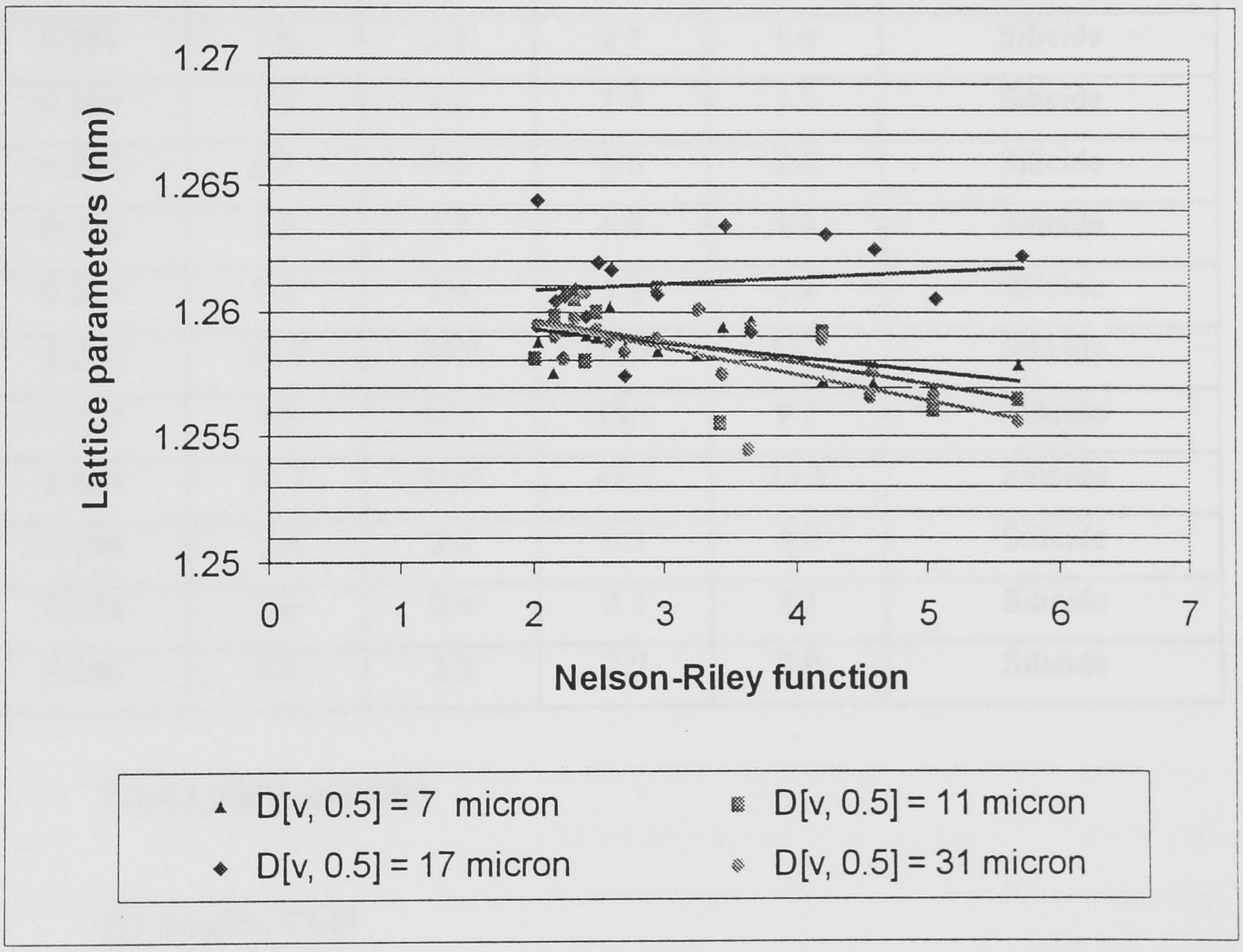


Fig. 5.3.4.1 Plot of apparent lattice parameters against the N-R function for the as-extruded products produced from different RS-Al-Fe-V-Si powder size fractions.

Table 5.3.4 XRD data and possible phase in the as-extruded Al-6.5Fe-1.5V-1.7Si alloys produced from different powder size fractions.

Measured *d*-spacing (nm)	Powder volume median diameter, (D[v, 0.5], μm)				Possible phase (see Table A3.5 in Appendix)
	7	11	17	31	
0.444	2.6	2.0	2.9	2.4	Silicide
0.397	11.1	10.3	15.5	9.7	Silicide
0.363	3.1	2.8	3.7	3.2	Silicide
0.336	3.9	3.6	4.8	2.8	Silicide
0.296	1.3	1.6	1.8	1.3	Silicide
0.281	1.6	1.5	2.4	1.4	Silicide
0.268	1.0	1.1	1.4	1.2	Silicide
0.247	4.2	3.3	5.6	3.9	Silicide
0.230	6.0	5.3	6.8	5.9	Silicide
0.223	2.2	2.4	3.2	2.8	Silicide
0.216	24.7	24.2	30.7	22.7	Silicide
0.210	9.9	10.1	13.1	9.7	Silicide
0.204	31.1	33.0	44.3	33.6	Silicide
0.199	5.4	3.4	6.3	4.9	Silicide
0.194	1.9	2.4	3.3	2.1	Silicide
0.186	2.0	2.3	2.7	2.0	Silicide

5.3.4.2 TEM and EDS

(1) $Al_{13}(Fe, V)_3Si$

Microstructural investigation by TEM as mentioned in 5.3.2 showed that there were two types of intermetallic phase, i.e. fine spherical silicide and coarse plate-like particles, found in the as-extruded RS-Al-Fe-V-Si alloy. The silicide phase was identified by XRD as a body centred cubic (bcc) phase. SADPs of a spherical silicide

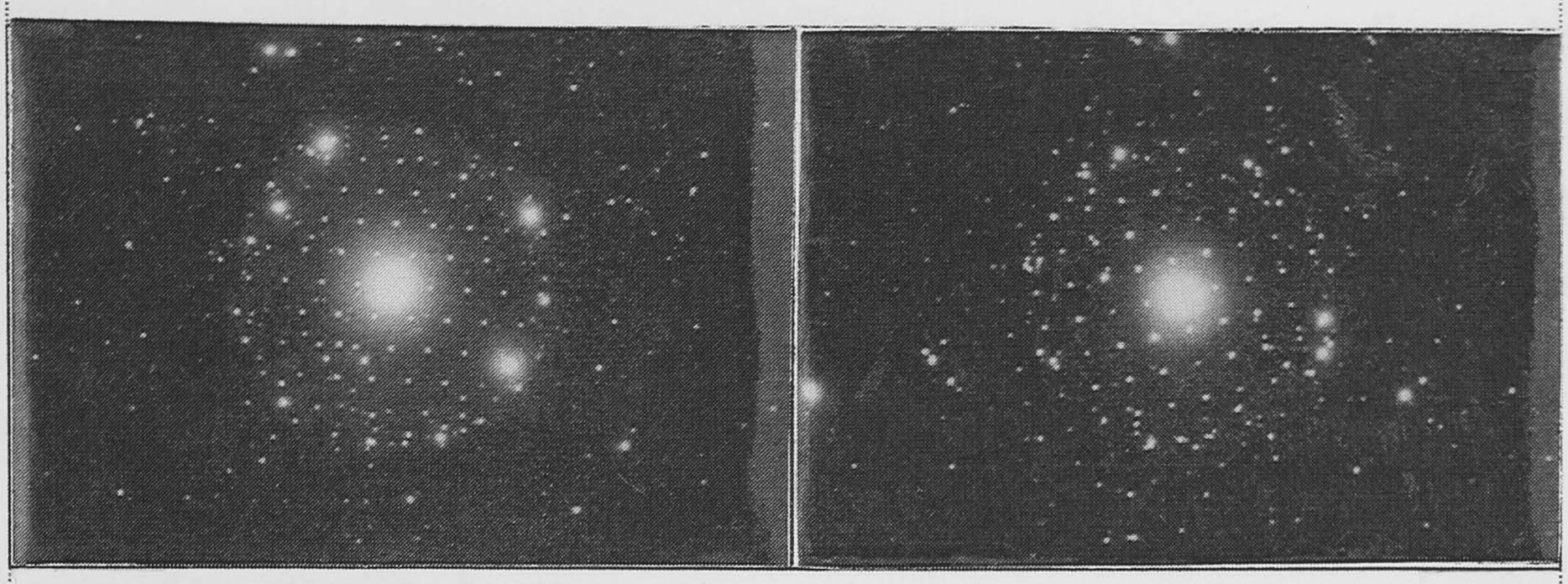
particle as shown in Fig. 5.3.4.2 (a) confirm that the crystal structure of this phase is bcc. Because of the fine size of bcc-silicide particles, chemical analyses on these particles using EDS analyses led to an error in determining the composition. However, the composition of this phase could be obtained with more accuracy when coarse bcc-silicide particles were determined (§ 5.7.2). The composition of this phase was found to be $Al_{13}(Fe, V)_3Si$.

(2) H-$(Al, Si)_5(Fe, V)$

SADPS of coarse plate-like particles as shown in Fig. 5.3.4.2 (b) are identical to the zone $[11\bar{2}0]$ and zone $[12\bar{3}0]$ patterns of the H-$Al_x(Fe, V)$ phase (§ 5.7.1) and of a metastable hexagonal phase found in strip-cast and spray-cast Al-Fe-V-Si alloys [5.86]. The composition of coarse plate-like particles determined using EDS analyses was found to be $(Al, Si)_5(Fe, V)$. This may conclude that the plate-like particle is hexagonal phase. This phase is designated as H-$(Al, Si)_5(Fe, V)$.

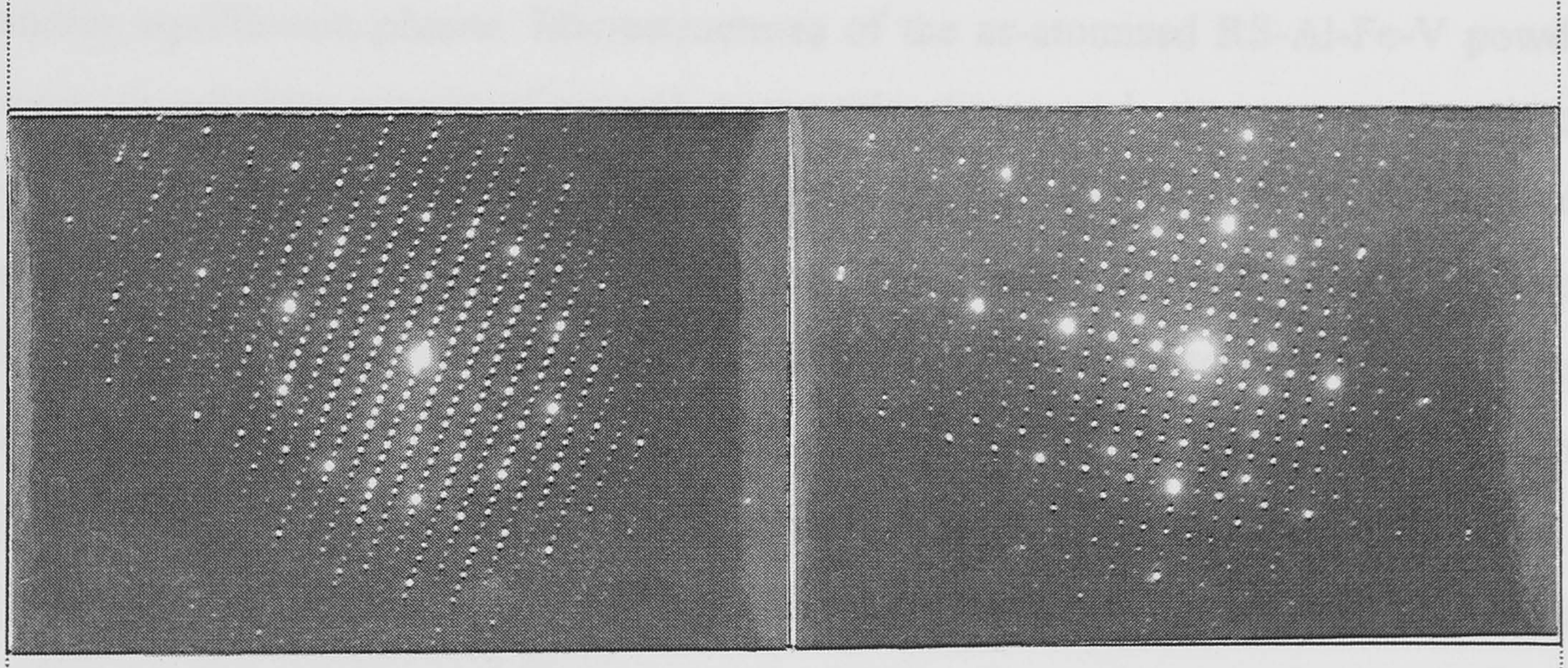
The lattice parameter of H-$(Al, Si)_5(Fe, V)$ phase measured from SADPs was found to be $a = 2.52 \pm 0.04$ nm and $c = 1.24 \pm 0.01$ nm with c/a ratio = 0.5. This lattice parameter is slightly different from that of H-$Al_x(Fe, V)$ phase (§ 5.7.1) and of the hexagonal phase reported in ref. [5.86]. Note that the lattice parameter of H-$Al_x(Fe, V)$ phase is $a = 2.59$ nm and $c = 1.30$ with c / a ratio = 0.5, while that of the hexagonal phase reported in ref. [5.86] is $a = 2.514$ nm and $c = 1.257$ nm with c/a ratio = 0.5. The slight difference in the measured values of the lattice parameter obtained in this investigation from the value given in ref. [5.86] may be attributed technical error occurring during operating TEM. Normally, the lattice parameter determined from TEM is less accurate than that determined from XRD. However, since the volume fraction of the hexagonal phase in both as-extruded RS-Al-Fe-V and as-extruded RS-Al-Fe-V-Si alloys was very small, the XRD reflections from the hexagonal phase were very weak. Lattice parameter measurement of the hexagonal phase by XRD techniques is therefore impossible.

(a) $Al_{13}(Fe, V)_3Si$ phase



[111] [100]

(b) H-$(Al, Si)_5(Fe, V)$ phase



[$1\,1\bar{2}0$] [$12\bar{3}0$]

Fig. 5.3.4.2 Electron diffraction patterns of intermetallic phases in the as-extruded RS-Al-Fe-V-Si alloy.

5.4 Phase Transformation during Extrusion of Powders

During consolidation processing of powders by cold compaction and hot extrusion, transformation reactions involving the original phases in the powders are expected to occur. However, it is impossible to observe these reactions directly during processing of the powders. The DSC studies of powders provide indirect information about the transformations of phases during exposure to high temperatures. Transformation reactions of the phases during processing of powders may be deduced from those obtained from DSC studies. Details of the transformations are given below.

5.4.1 RS-Al-Fe-V Alloy

During consolidation of powders, the interaction of both thermal and mechanical effects led to the transformation of metastable phases to other metastable and/or equilibrium phases. Microstructures of the as-atomised RS-Al-Fe-V powders were observed to consist of several metastable phases such as, super-saturated solid solution (in zone A microstructures), MI (in zone A and zone B microstructures), Al_6Fe (in continuous forms of coarse intercellular networks), and GCMI (in zone C microstructures) phases. The transformation reactions of these intermetallic phases during extrusion of RS-Al-Fe-V powder, deduced from DSC studies of RS-Al-Fe-V powders (§ 5.2), can be represented by the schematic diagram shown in Fig. 5.4.1.

The solid solution in zone A microstructures decomposes to form Al_6Fe phase at 360 °C. Two phase transformations occur at the same temperature of 500 °C. These are the reactions of $Al_6Fe \rightarrow Al_{13}Fe_4$ and MI $\rightarrow Al_{45}(V, Fe)_7 + Al_{13}Fe_4$. The GCMI phase particles transform to the globular I phase particles at 450 °C.

The unknown Al-Fe-V phase particles were also observed in the as extruded products of RS-Al-Fe-V powders. The formation of this phase is not yet well understood. Transformation reaction resulting in the formation of this phase cannot be given here.

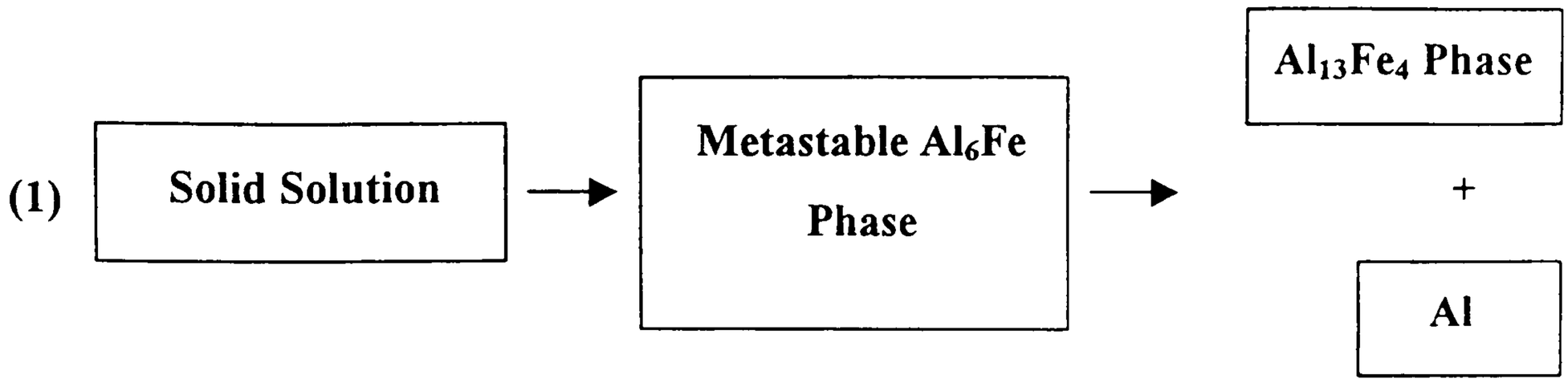


Fig. 5.4.1 Schematic diagram showing phase transformation reactions during extrusion of RS-Al-Fe-V powders.

5.4.2 RS-Al-Fe-V-Si Alloy

There were several phase transformations observed in the DSC studies of RS-Al-Fe-V-Si powders (§ 5.2). These reactions included the decompositions of MI, GCMI-$(Al, Si)_x(Fe, V)$ and I-$(Al, Si)_x(Fe, V)$ phases. The decompositions of these phases yielded the same product (bcc-$Al_{13}(Fe, V)_3Si$ phase) as indicated by a single DSC exothermic peak at 400 °C. The H-$(Al, Si)_5(Fe, V)$ phase, which probably formed directly from the melt (during solidification of coarse melt droplets), did not transform during extrusion. Phase transformations during extrusion of the RS-Al-Fe-V-Si powders deduced from DSC studies are summarised schematically in Fig. 5.4.2.

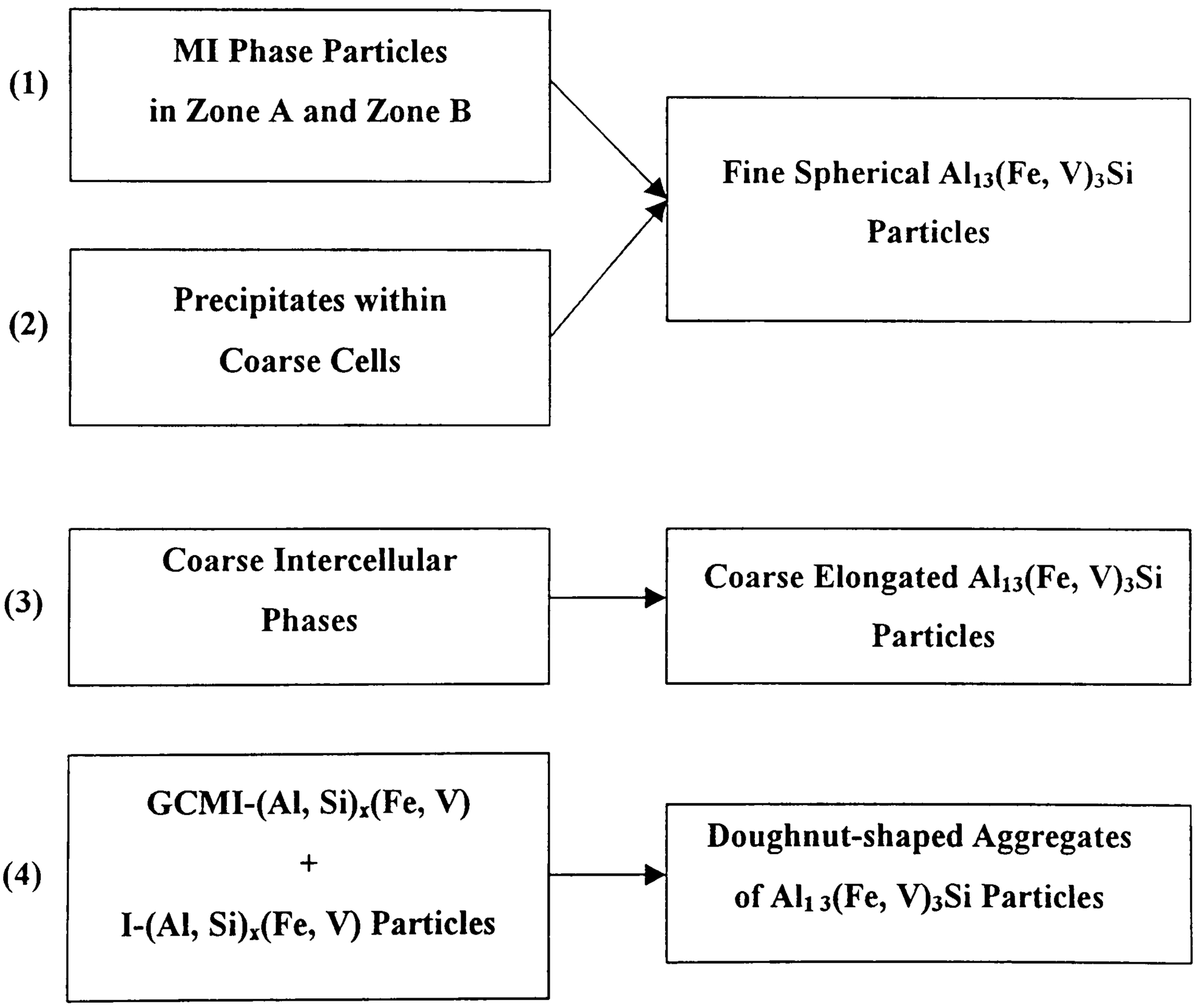


Fig. 5.4.2 Schematic diagram representing phase transformations during extrusion of RS-Al-Fe-V-Si powders.

5.5 Mechanical Properties of the As-extruded Alloys

As already mentioned there were differences in microstructures of the as-extruded alloys produced from different powder size fractions. Thus an influence of powder size fractions, which control microstructures of the as-extruded alloys, on mechanical properties would be expected. In order to study this effect, compression tests have been carried out on specimens of the as-extruded alloys produced from different powder size fractions. The tests were performed at room temperature and 250 °C with a constant strain rate of 0.001 s^{-1}. The 0.2 % compression strengths (0.2 % CS) at both test temperatures were measured and plotted against the powder sizes. In addition to the 0.2 % CS, the fracture toughness values of the as-extruded alloys were also determined.

5.5.1 Compression Strength of RS-Al-Fe-V Alloy

The plot of compression strengths of the as-extruded RS-Al-Fe-V alloy against powder size is shown in Fig. 5.5.1.1. The strength (0.2 % CS) was observed to decrease with increasing powder particle size. The decrease in strength may be attributed to coarse and inhomogeneous microstructures as observed in the as-extruded alloys produced from coarse powders. The banded structures in such alloys may have a detrimental effect on strength.

The trend of the plot of 0.2 % CS against powder particle size (Fig.5.5.1.1) was found to be similar to that of the plot between the maximum extrusion pressure and powder particle size (Fig. 5.5.1.2). The pressure required for extrusion of a powder billet decreased with increasing powder particle size. The results given in both Figs. 5.5.1.1 and 5.5.1.2 suggest that powder particle size and powder microstructure have significant influence on the processing of powders and mechanical properties of the final products. There should also be an interrelationship between powder hardness, extrusion pressure and mechanical properties of the as-extruded products. This would relate the original powder microstructures and the final microstructure of the as-extruded products. The interrelationship can be qualitatively explained, for example,

in the case of a fine powder size fraction, as follows. Fine powder particles exhibit finer microstructures and high hardness. The pressures required for extrusion of these powders is thus high. Because the original microstructures of these powders are fine, the final microstructures of the as-extruded products are also fine. The finer the microstructure the better the mechanical properties.

Fig. 5.5.1.3 shows comparatively the strengths of the I phase containing alloy (the as-extruded alloy produced from the powder size fraction with D[v, 0.5] = 50 μm or 'IPC alloy') and the non I phase containing alloy (the as-extruded alloy produced from the powder size fraction with D[v, 0.5] = 8 μm or 'NIPC alloy') at different test temperatures. The IPC alloy exhibits inferior strength to the NIPC alloy at all test temperatures. This indicates that the presence of large I phase particles, with diameters as large as the grain sizes (500-1000 nm diameter), does not improve the strength. The large size of I phase particles limits their ability to pin the grain boundaries and inhibit the displacement of dislocations so they do not effectively strengthen the alloy.

However, it was observed that the rate of decrease in strength with increasing temperature (indicated by the slopes of the curves in Fig 5.5.1.3) of the IPC alloy was lower than that of the NIPC alloy. This may be attributed to the fact that the coarsening rate of the globular I phase particles during exposure to high temperatures is slower than that of other intermetallic particles. Because of the low coarsening rate of globular I phase particles, a homogeneous distribution of these particles in the microstructure is expected to improve creep rupture properties of IPC alloy. However, the proof of this expectation is beyond the scope of this study.

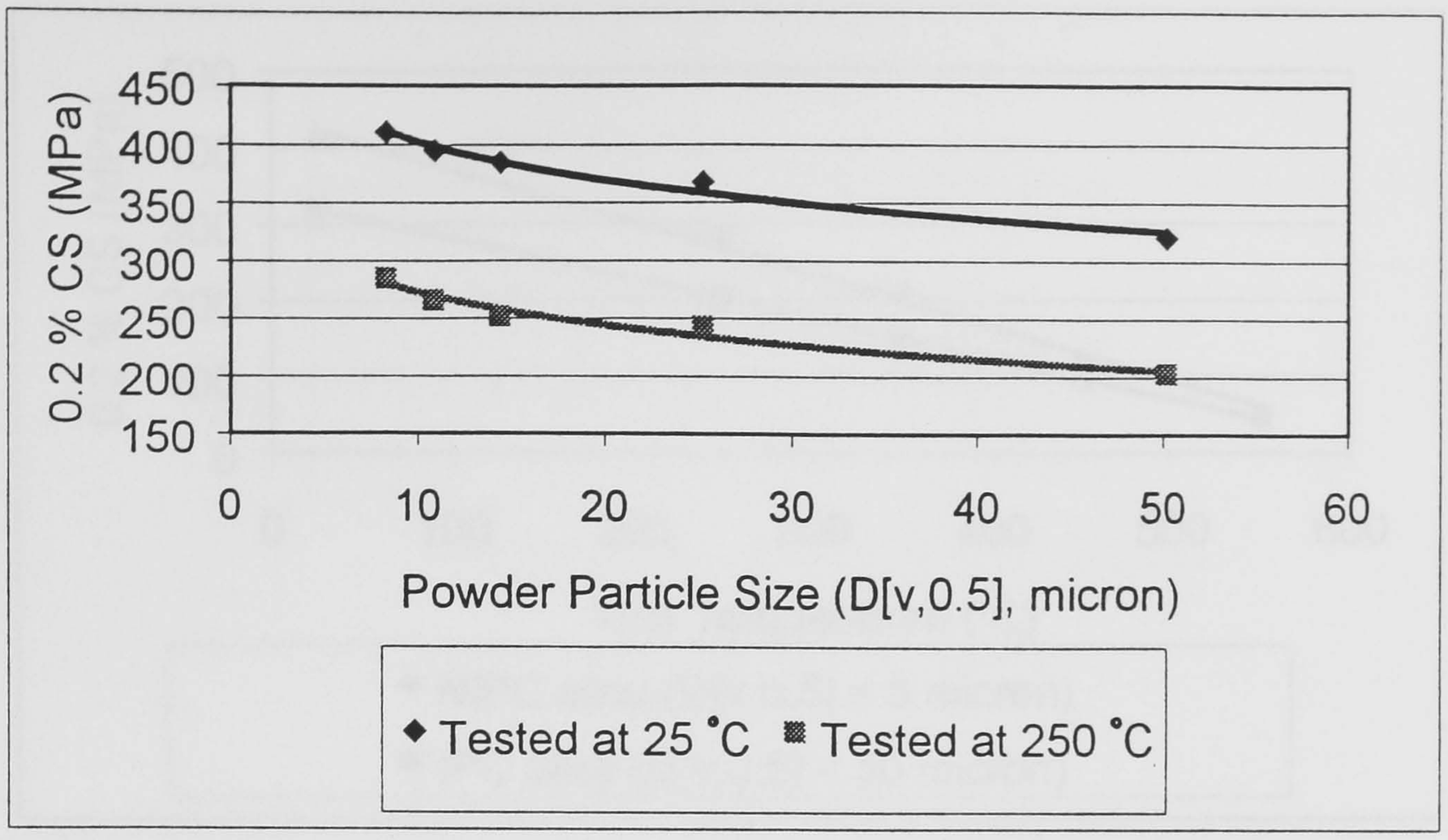


Fig. 5.5.1.1 Plot of 0.2 % CS as a function of powder particle size and test temperature of the as-extruded RS-Al-Fe-V alloys.

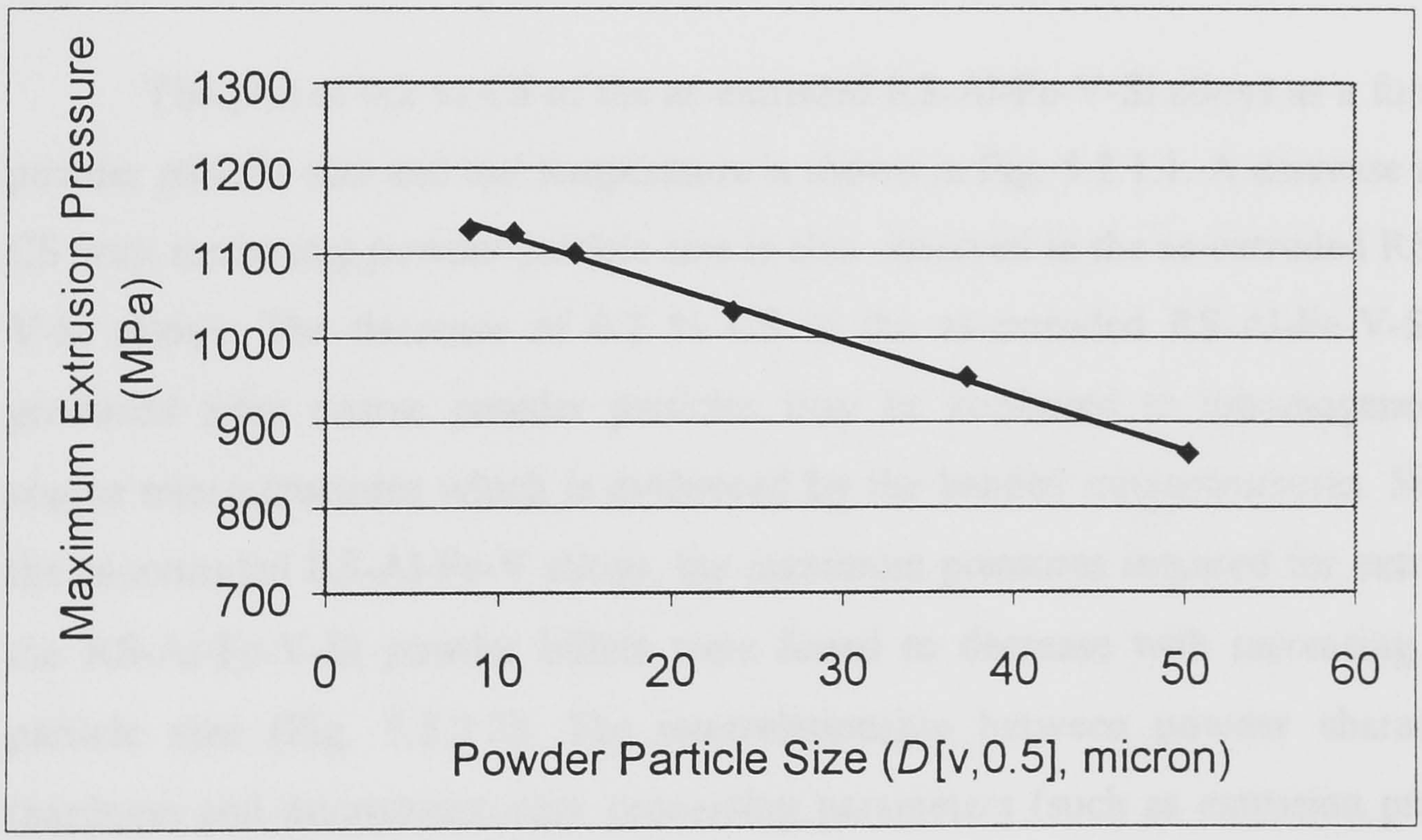


Fig. 5.5.1.2 Plot of maximum extrusion pressure as a function of powder particle size of RS-Al-Fe-V powders.

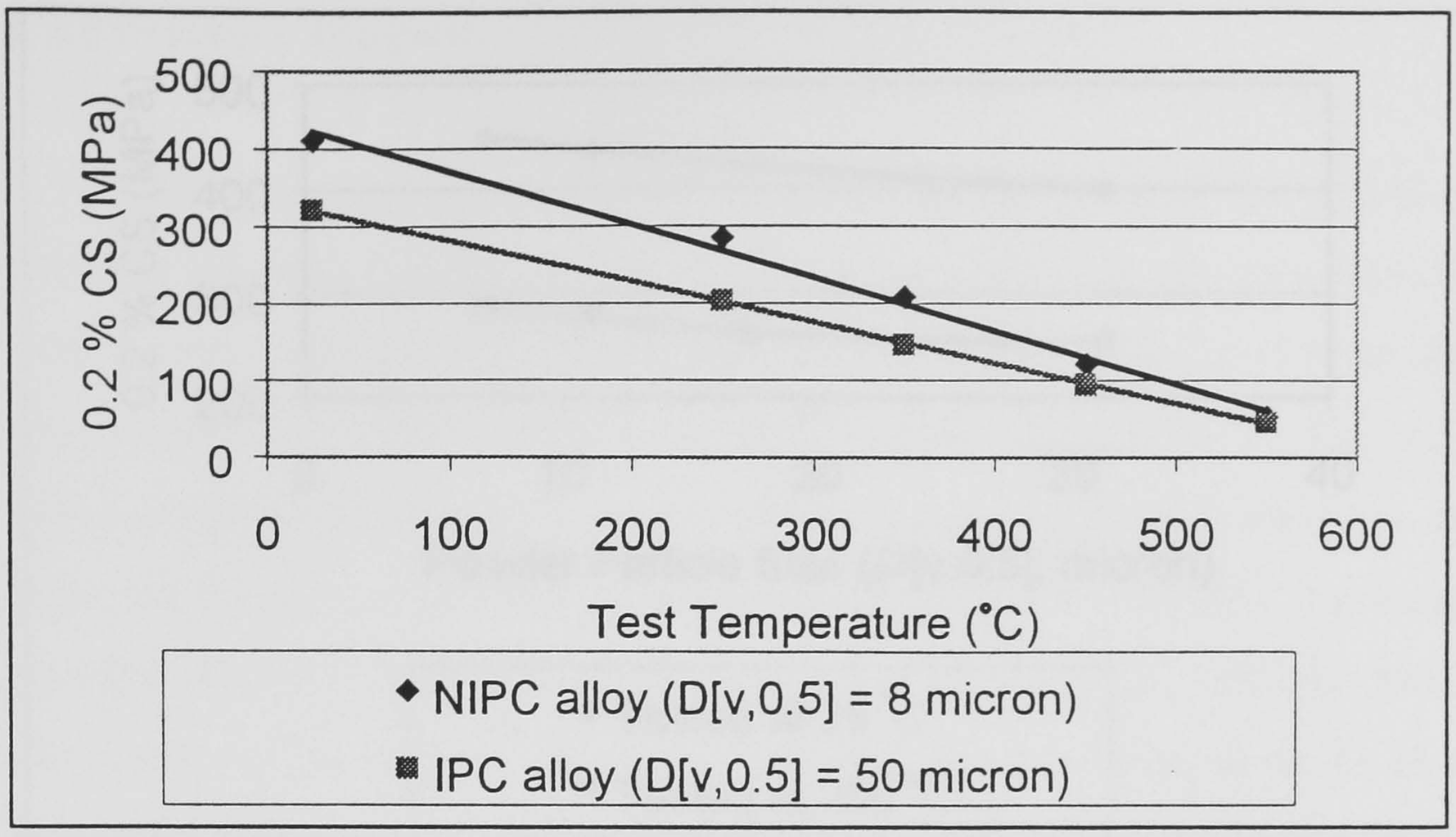


Fig. 5.5.1.3 Plot of 0.2 % CS of the IPC and NIPC alloys as a function of test temperature.

5.5.2 Compression strength of RS-Al-Fe-V-Si Alloy

The plot of 0.2 % CS of the as-extruded RS-Al-Fe-V-Si alloys as a function of powder particle size and test temperature is shown in Fig. 5.2.1.1. A decrease in 0.2 % CS with increasing powder particle size is also observed in the as-extruded RS-Al-Fe-V-Si alloys. The decrease of 0.2 % CS in the as-extruded RS-Al-Fe-V-Si alloys produced from coarse powder particles may be attributed to inhomogeneous and coarse microstructures which is evidenced by the banded microstructures. Similar to the as-extruded RS-Al-Fe-V alloys, the maximum pressures required for extrusion of the RS-Al-Fe-V-Si powder billets were found to decrease with increasing powder particle size (Fig. 5.5.2.2). The interrelationship between powder characteristics (hardness and microstructures), processing parameters (such as extrusion pressures), and microstructures and mechanical properties of the as-extruded products of RS-Al-Fe-V-Si alloy may be similar to that of RS-Al-Fe-V alloy.

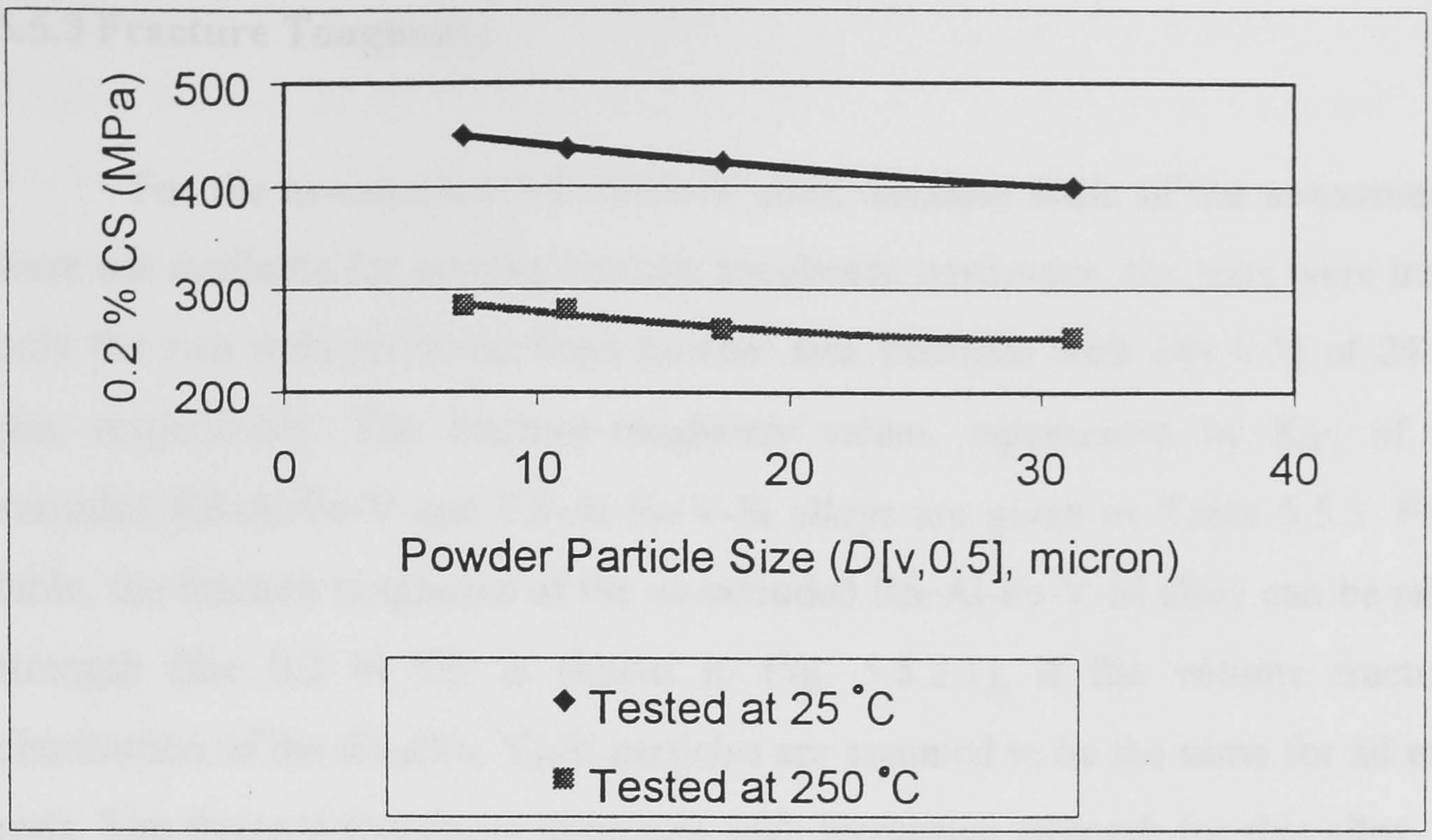


Fig. 5.5.2.1 Plot of 0.2 % CS as a function of powder particle size and test temperature of the as-extruded RS-Al-Fe-V-Si alloys.

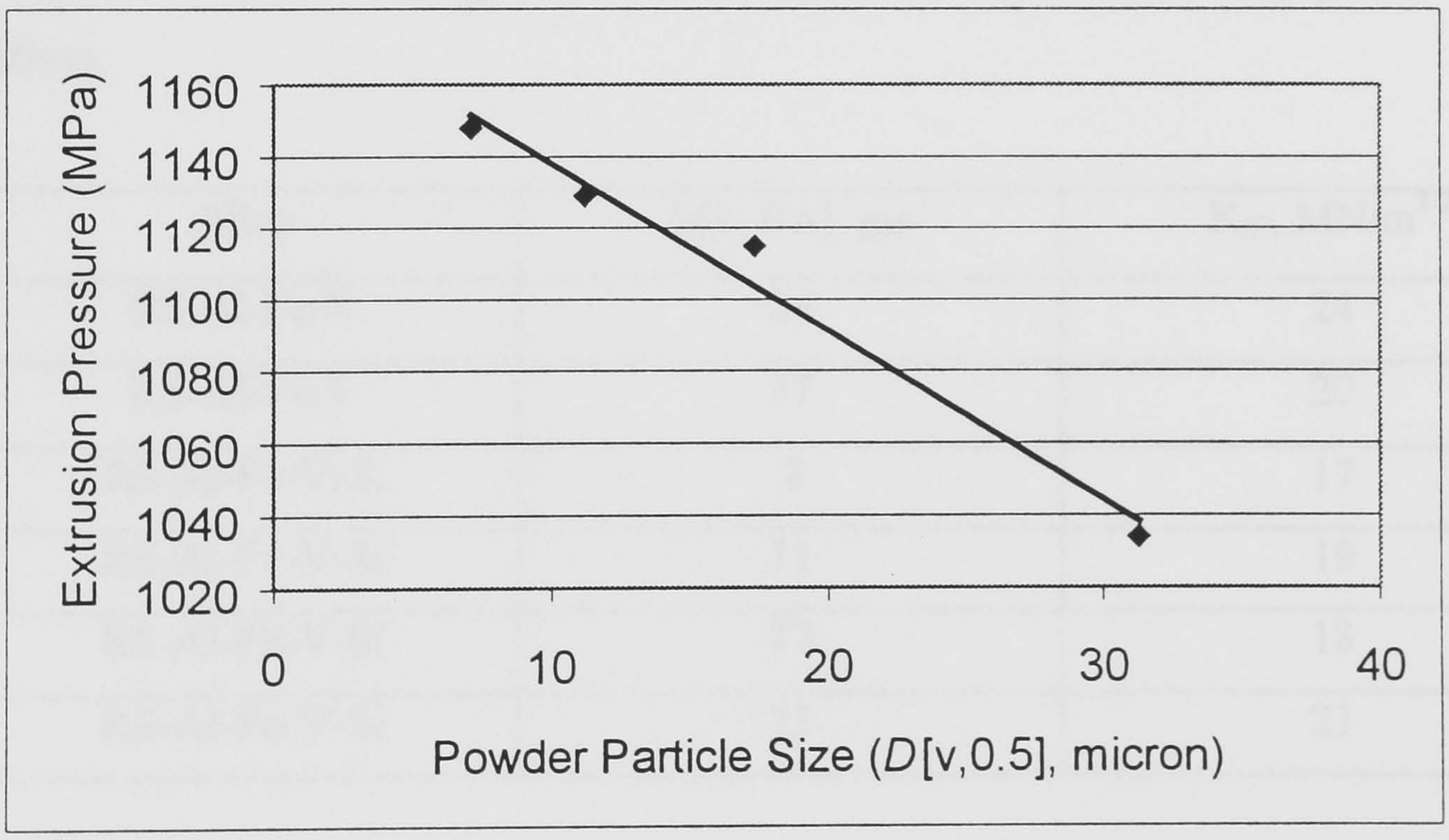


Fig. 5.5.2.2 Plot of maximum extrusion pressure as a function of powder particle size of RS-Al-Fe-V-Si powders.

5.5.3 Fracture Toughness

For the as-extruded RS-Al-Fe-V alloy, because some of the as-extruded rods were not available for making fracture toughness specimens, the tests were limited to only the two rods produced from powder size fractions with D[v,0.5] of 24 and 37 μm, respectively. The fracture toughness values, represented by K_{IC}, of the as-extruded RS-Al-Fe-V and RS-Al-Fe-V-Si alloys are given in Table 5.5.3. From the table, the fracture toughness of the as-extruded RS-Al-Fe-V-Si alloy can be related to strength (the 0.2 % CS is shown in Fig. 5.5.2.1), if the volume fraction and distribution of the $Al_{13}(Fe, V)_3Si$ particles are assumed to be the same for all extruded rods. The fracture toughness decreases with increasing strength for this alloy. This is attributed to a reduction in the work needed to link the voids in the higher strength alloys. The loss of fracture toughness with increasing strength has been also reported in other aluminium alloys [5.102, 5.103].

Table 5.5.3 Fracture toughness of the as-extruded RS-Al-Fe-V and RS-Al-Fe-V-Si alloys.

Alloy	D[v, 0.5], μm	K_{IC}, $MN/m^{3/2}$
RS-Al-Fe-V	24	24
RS-Al-Fe-V	37	20
RS-Al-Fe-V-Si	7	17
RS-Al-Fe-V-Si	11	19
RS-Al-Fe-V-Si	17	18
RS-Al-Fe-V-Si	31	21

However, when the K_{IC}-values of the as-extruded RS-Al-Fe-V rods produced from powders with D[v,0.5] of 24 and 37 μm are compared, it is seen the toughness decreases with decreasing strength (the 0.2 % CS is shown in Fig. 5.5.1.1). The loss of fracture toughness with decreasing strength for this case may be attributed to the

influence of volume fraction of the globular I phase particles. It was already mentioned in § 5.1.2.3 that for medium to coarse RS-Al-Fe-V powders, the size and volume fraction of the GCMI phase increases with increasing powder particle size. The as-extruded alloy produced from the powder size fraction with the larger D[v,0.5] value should contain coarser and a greater volume fraction of I phase particles. The greater volume fraction of particles causes a reduction in fracture toughness. An approximate analysis predicts that K_{IC} varies as $f_c^{-1/6}$, where f_c is the volume fraction of the particles [5.102].

5.6 Microstructures of Tested Specimens

5.6.1 Compressed Specimens

Microstructural changes, in terms of coarsening of intermetallic particles, change of grain shape and size, and phase transformations, during deformation by compression tests have been observed by using TEM. Slices from compressed specimens were sectioned parallel to the compression direction (Fig. 5.6.1.1) and ground to a thickness of 200 μm. The thin foils for TEM were prepared by using the same method as that for preparation of the as-extruded alloy specimens.

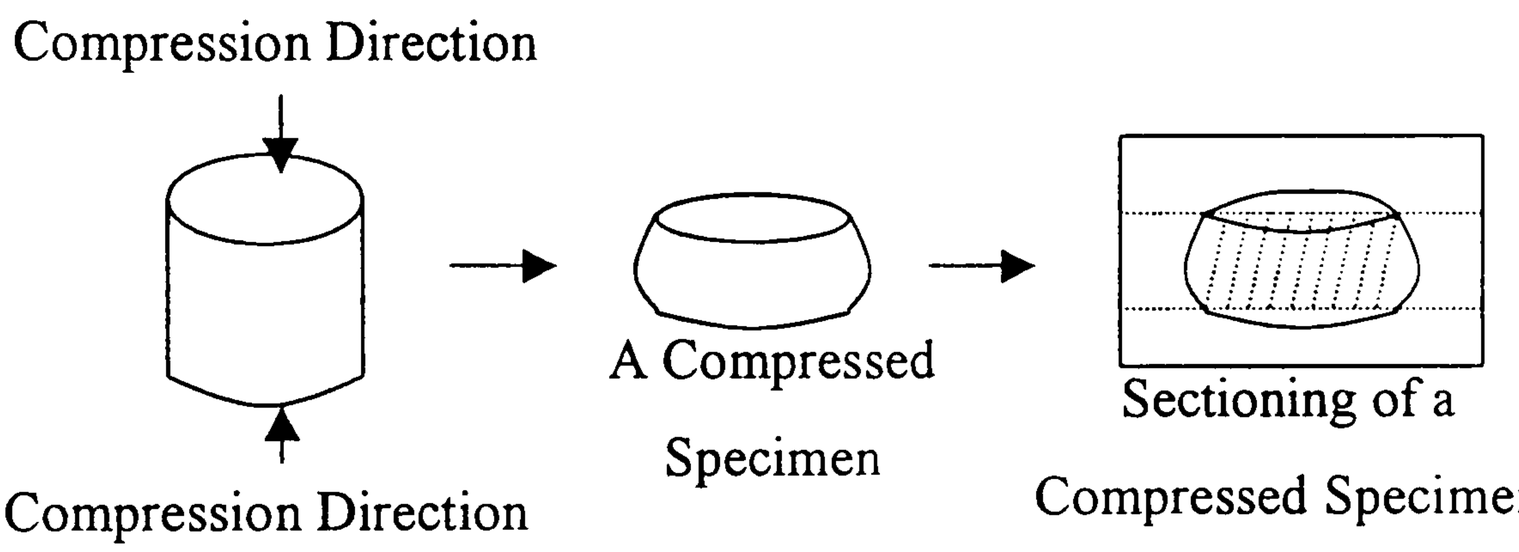


Fig. 5.6.1.1 Schematic diagram showing compression of an alloy specimen, a compressed specimen and sectioning of a compressed specimen.

5.6.1.1 Al-Fe-V Alloy

The band I microstructures of an alloy compressed at room temperature (Fig. 5.6.1.2 (a)) exhibited collapsed grains and intermetallic particle aggregation. The intermetallic particles (spherical Al_6Fe and needle-like $Al_{13}Fe_4$ and knife blade-shaped $Al_{45}(V, Fe)_7$ particles) were compressed to aggregates along the grain boundaries of the flattened grains.

In the band I microstructures of an alloy compressed at 250 °C, coarsening of intermetallic particles, particularly $Al_{13}Fe_4$ particles, was observed (Fig. 5.6.1.2 (d)). The $Al_{13}Fe_4$ particle coarsening was indicated by a morphological change i.e. from needle-like to rod-like and plate-like. Particle aggregation along grain boundaries was also observed. In some areas of microstructure, the longitudinal

axes of some rod-like $Al_{13}Fe_4$ particles were oriented in a common direction (Fig. 5.6.1.2 (c) and (d)). The inter-particle distances in the direction normal to the longitudinal axes of the $Al_{13}Fe_4$ particles were small. This indicates that the compressive direction is normal to the longitudinal axes of the $Al_{13}Fe_4$ particles.

The band II microstructures of a specimen compressed at room temperature exhibited a few elongated grains with longitudinal axes normal to the compression direction (Fig. 5.6.1.2 (b)). No sign of phase transformation of the globular I phase particles was observed. However, when the compression temperature was increased to 250 °C, coarsening of $Al_{13}Fe_4$ phase particles and phase transformation of the globular I phase particles were observed. Figure 5.6.1.2 (c) and (e)) shows an I-Al_x(Fe, V) particle (marked I) and some globular crystalline particles. The crystalline particles were identified as hexagonal crystals with compositions close to that of the I-Al_x(Fe, V) phase. The hexagonal phases (marked H) were designated as H-Al_x(Fe, V).

It was found that transformation from the I-Al_x(Fe, V) phase to the H-Al_x(Fe, V) phase occurred via a thermally activated polymorphous transformation reaction which involves partitionless growth of the (H-Al_x(Fe, V) phase with different structure but the same composition as the I-Al_x(Fe, V) phase (§ 5.7). It was observed that this transformation reaction occurred during heat-treatment of the as-extruded RS-Al-Fe-V alloy, produced from coarse RS-Al-Fe-V powders, at 550 °C for 30 minutes. However, during compression testing at 250 °C some I-Al_x(Fe, V) particles transformed to H-Al_x(Fe, V) particles. The reason for the transformation of I-Al_x(Fe, V) particles taking place during compression testing at 250 °C is not understood.

Most H-Al_x(Fe, V) particles were not stable and exhibited peritectoid reaction with α-Al matrix at their peripheries, i.e. $Al_x(Fe, V) + yAl \rightarrow Al_{x+y}(Fe, V)$ which is indicated by a light region surrounding a dark core or a particle centre. The EDS analyses performed on several hexagonal particles revealed that there were solute gradients across the particles, i.e. Fe and V contents in the light region were less than in the dark core. The peritectoid transformation reaction may be the beginning of transformation from H-Al_x(Fe, V) particles to other equilibrium phase particles. This reaction has been observed in the transformation from I phase to Al_6Mn phase during annealing of melt-spun Al-Mn alloys [5.104-5.105]. This may suggest that the mechanisms for transformation reactions from I phase to

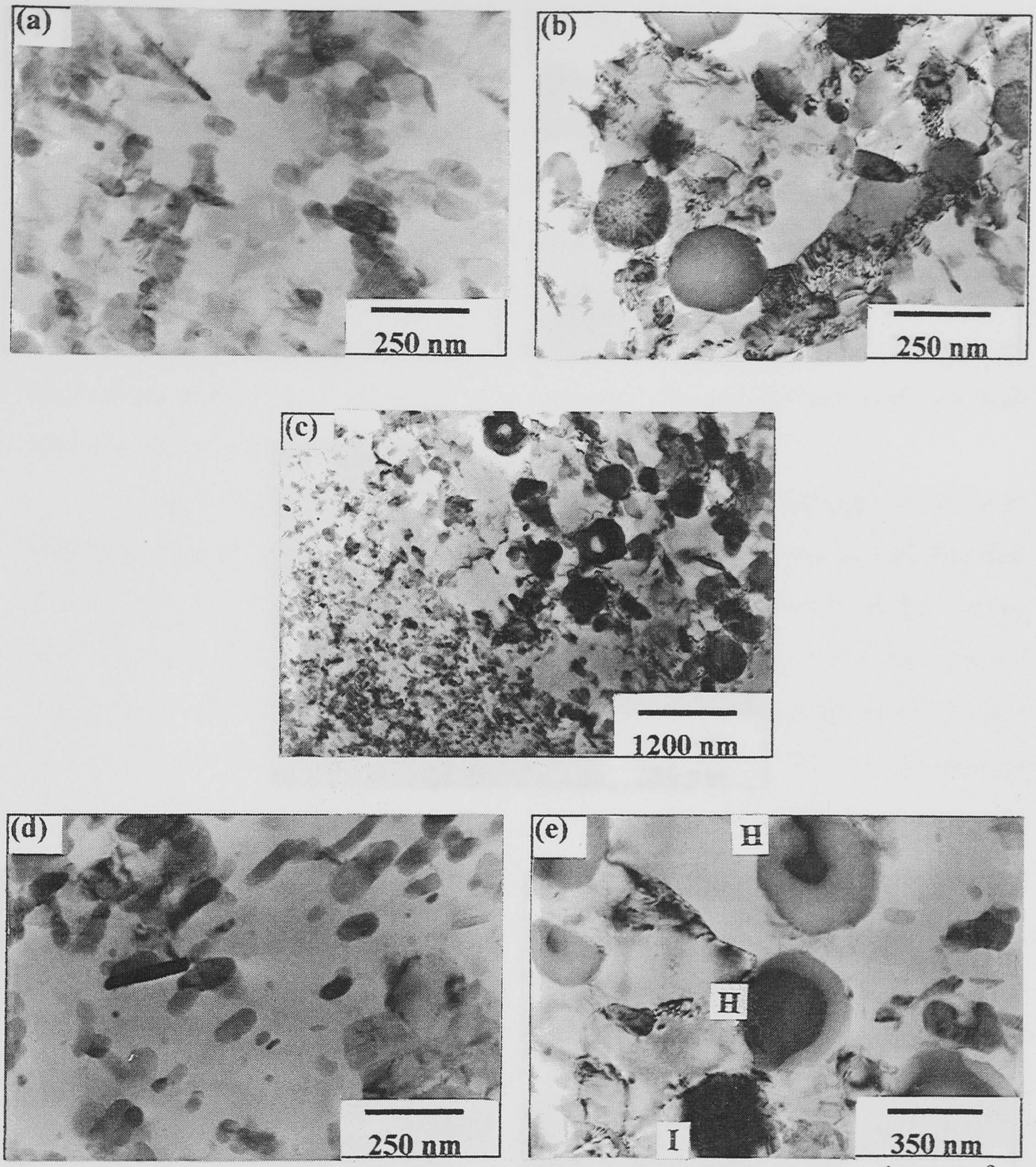
metastable phase(s) and to equilibrium phase(s) are different in rapidly solidified Al-Fe-V and Al-Mn alloys.

5.6.1.2 Al-Fe-V-Si Alloy

Microstructures of the RS-Al-Fe-V-Si alloy compressed at room temperature exhibited slight changes in terms of particle size and distribution of $Al_{13}(Fe, V)_3Si$ particles. The size and distribution of fine $Al_{13}(Fe, V)_3Si$ particles in the band I′ microstructures (Fig. 5.6.1.3 (a)) and of coarse $Al_{13}(Fe, V)_3Si$ particles in the band II′ microstructures (Fig. 5.6.1.3 (b)) were similar to the microstructures of the as-extruded alloy. The grain size and shape also exhibited slight changes.

When the alloy was compressed at 250 °C, the band I′ exhibited aggregation of fine $Al_{13}(Fe, V)_3Si$ particles (Fig 5.6.1.3 (c) and (d)). Although the $Al_{13}(Fe, V)_3Si$ particles have been reported to be thermally stable due to very slow coarsening rates of between 2.9×10^{-6} and 8.4×10^{-27} m^3/h at 425 °C [5.106-5.108], some evidence of particle coarsening was also observed (marked by an arrow in Fig. 5.6.1.3 (d). The coarsening of the $Al_{13}(Fe, V)_3Si$ particles may be assisted by both pressure, which mechanically compressed the particles together, and heat which, thermally accelerated the diffusion of constituent elements of the $Al_{13}(Fe, V)_3Si$ phase.

The band II′ microstructures of the alloy compressed at 250 °C exhibited elongated grains (Fig. 5.6.1.3 (e)). The coarse $Al_{13}(Fe, V)_3Si$ particles decorated the grain boundaries. The particle aggregation in the band II′ microstructures was not as obvious as in the band I′ microstructures. This is attributed to the fact that the original inter-particle distance between the coarser particles within band II′ microstructures is greater than that in the band I′ microstructures.



All specimens were compressed with 30 % total strain at a constant strain rate of

$0.001\ s^{-1}$.

Fig. 5.6.1.2 Bright field TEM images of compressed RS-Al-Fe-V alloy specimens;

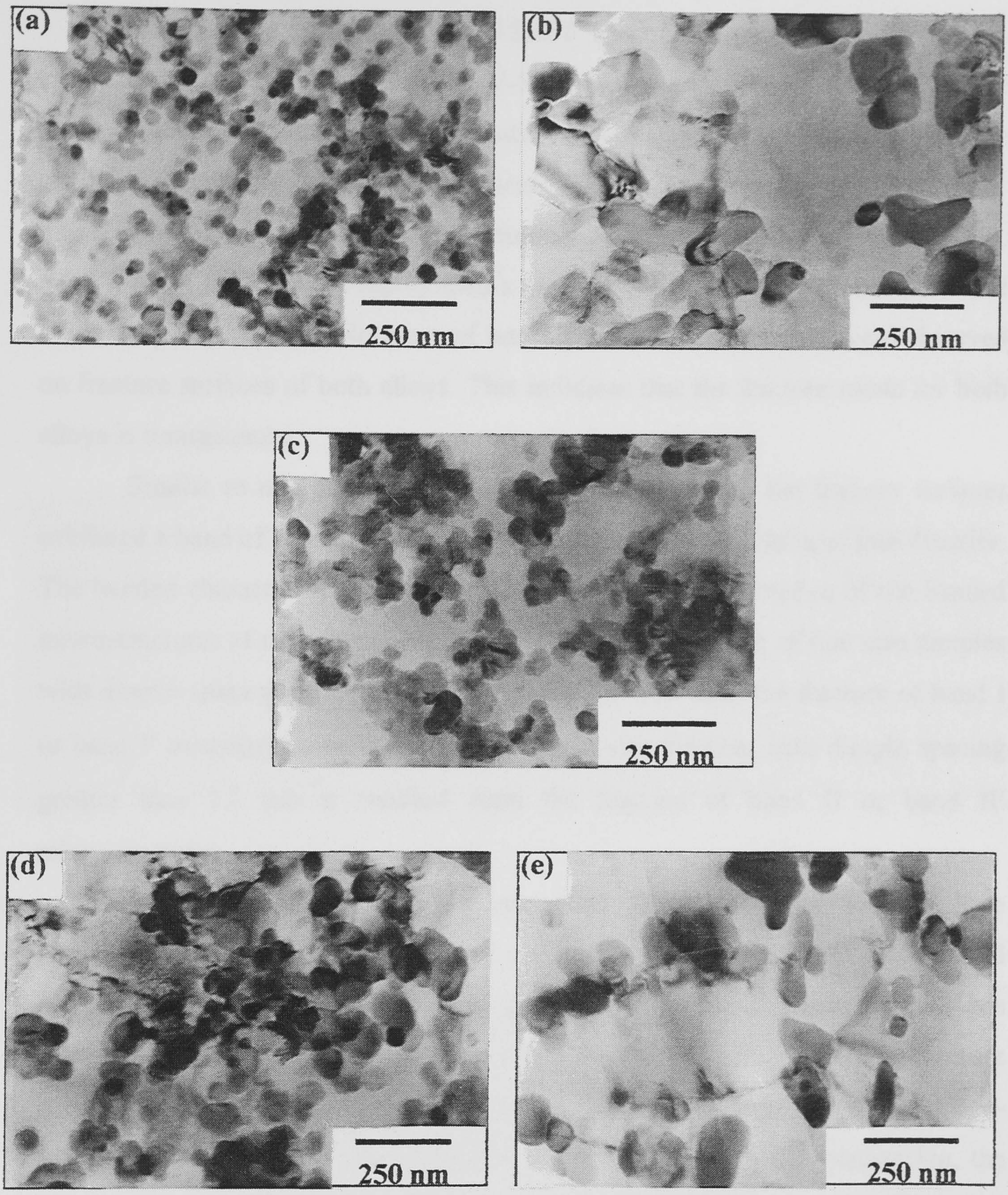
(a) band I of the specimen compressed at room temperature,

(b) band II of the specimen compressed at room temperature,

(c) band I and band II of the specimen compressed at 250 °C,

(d) band I of the specimen compressed at 250 °C (higher magnification),

(e) band II of the specimen compressed at 250 °C (higher magnification).



All specimens were compressed with 30 % total strain at a constant strain rate of $0.001\ s^{-1}$.

Fig. 5.6.1.3 Bright field TEM images of compressed RS-Al-Fe-V-Si alloy specimens;

(a) band I′ of the specimen compressed at room temperature,

(b) band II′ of the specimen compressed at room temperature,

(c) and (d) band I′ of the specimen compressed at 250 °C,

(e) band II′ of the specimen compressed at 250 °C.

5.6.2 Short Rod Fracture Toughness Specimens

The fracture surfaces of the TSRFT specimens, produced from the as-extruded RS-Al-Fe-V and RS-Al-Fe-V-Si alloys, tested at room temperature are shown in Fig. 5.6.2. At a low magnification of x200, the fracture surfaces near the crack tips exhibited fibrous structures (Fig.5.6.2 (a) and (b)). At higher magnifications of x2000 and x5000, numerous dimples could be observed (Fig. 5.6.2 (c)-(f)). Each dimple represented a void caused by cracking or decohesion of a second phase particle. No areas of intercrystalline facet fracture were observed on fracture surfaces of both alloys. This indicates that the fracture mode for both alloys is transgranular.

Similar to microstructures of the as-extruded alloys, the fracture surfaces exhibited a band of coarse dimples sandwiched by areas consisting of fine dimples. The banded character of the fracture surfaces is probably a replica of the banded microstructures of the as extruded alloys. The areas consisting of fine size dimples with dimple spacing of up to 1 μm may have resulted from the fracture of band I or band I′ microstructures. The band of coarse size dimples with dimple spacing greater than 1.5 μm is resulted from the fracture of band II or band II′ microstructures.

The dimple spacing was greater than the diameter of second phase particles. This may be attributed to the fracture mechanism. After the void nucleation at the interface between matrix and a second phase particle has occurred, the voids grow further under tension until they coalesce and the fracture is completed. It has been reported that the dimple spacing relates to the centre-to-centre spacing of second phase particles [5.102]. According to this relationship, the formation of banded fracture surfaces can be explained as follows. The fracture of band I (I′) microstructures, consisting of fine second phase particles with small centre-to-centre spacing, would result in formation of areas consisting of fine dimples. Similarly, the fracture of bands II (II′) microstructures, consisting of coarse second phase particles with large centre-to-centre spacing, would result in formation of coarse dimples.

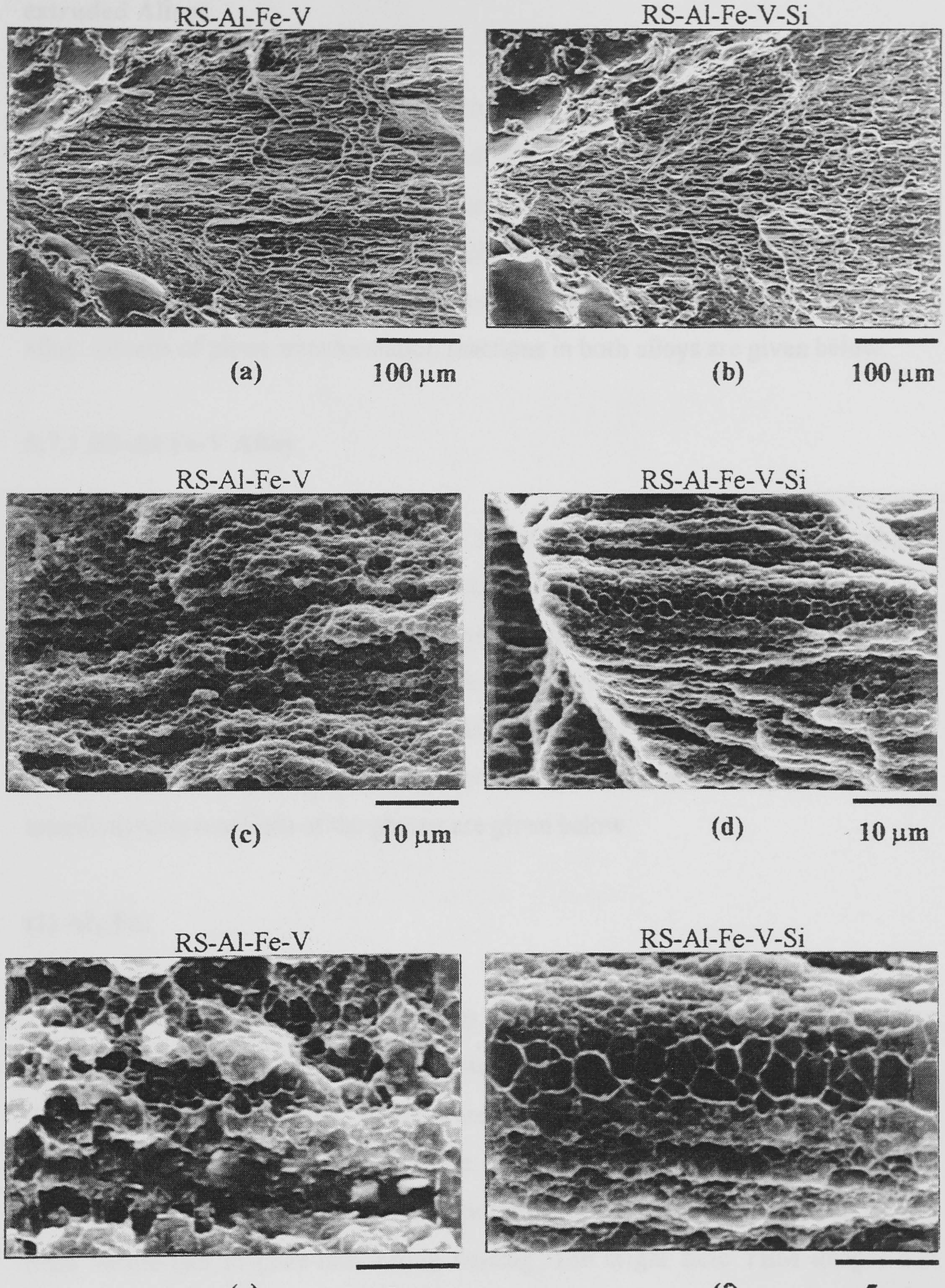


Fig. 5.6.2 Fracture surfaces of the as-extruded RS-Al-Fe-V and RS-Al-Fe-V-Si alloys.

5.7 Coarsening and Phase Transformation during Heat-treatment of the As-extruded Alloys

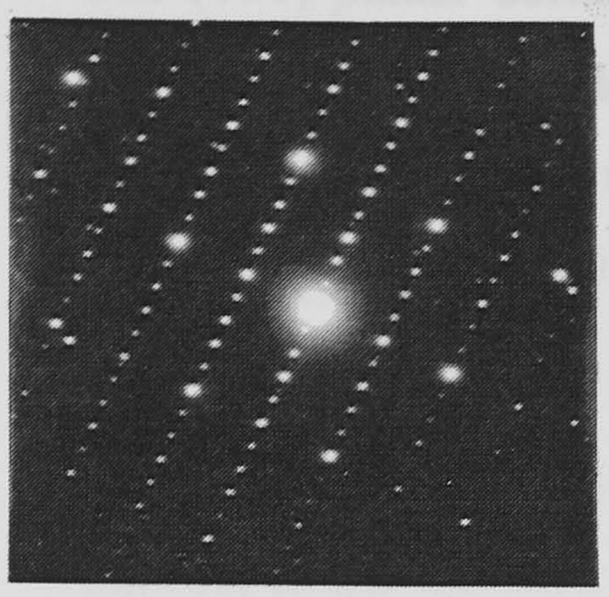
The thermal stability of microstructures was studied by heat-treatment of the as-extruded alloys at 500, 550 and 600 °C for different times and water quenching immediately after heating. Phase identification in the heat-treated alloys was carried out using TEM and EDS. It was observed that the phase transformations in RS-Al-Fe-V alloy were different from those in RS-Al-Fe-V-Si alloy. Details of phase transformation reactions in both alloys are given below.

5.7.1 RS-Al-Fe-V Alloy

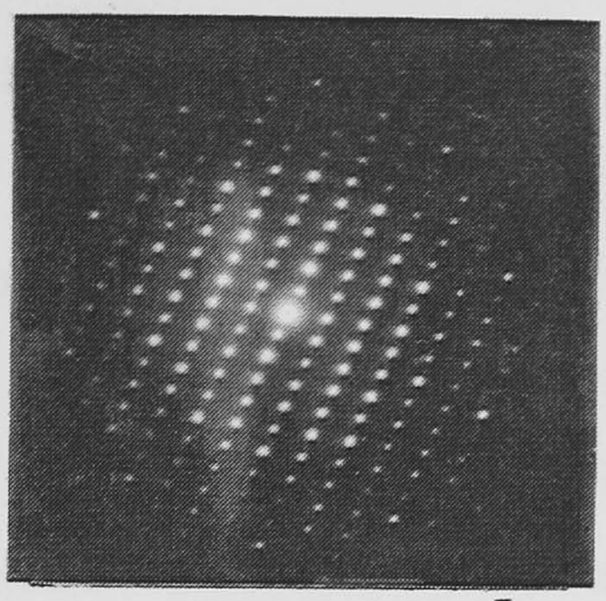
Phase identifications in (§ 5.3.3) revealed that the intermetallic phases found in the as-extruded RS-Al-Fe-V alloy included $Al_{13}Fe_4$, Al_6Fe, I-Al_x(Fe, V), Al_{45}(V, Fe)$_7$ and unknown Al-Fe-V phases. The stable needle-like $Al_{13}Fe_4$ phase particles were observed to coarsen during heating, whereas other metastable phases (Al_6Fe, I-Al_x(Fe, V), and unknown Al-Fe-V phases) decomposed or transformed to metastable and/or stable phases. Details of coarsening and transformation reactions of the phases are given below.

(1) $Al_{13}Fe_4$

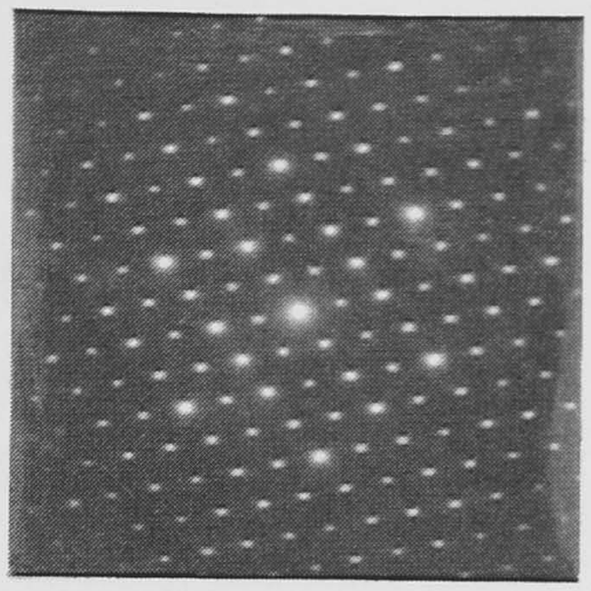
The needle-like $Al_{13}Fe_4$ particles coarsened dramatically during annealing at high temperatures. It was observed that in an alloy heated at 550 °C for 48 hours the particle sizes of $Al_{13}Fe_4$ phase were large (900 nm wide x 1400 nm long) whereas the original sizes of this phase in an as-extruded alloy were small (5-50 nm wide x 50-500 nm long). The morphology of the $Al_{13}Fe_4$ particles transformed from needle-like to plate-like during heating. The bright field TEM images and SADPs of the $Al_{13}Fe_4$ particles observed in the RS-Al-Fe-V alloy heated at 550 °C for 48 hours are shown in Fig. 5.7.1.1. The equilibrium $Al_{13}Fe_4$ phase has C2/m monoclinic lattice with lattice parameters of a = 1.5489, b = 0.8083, and c = 1.2476 nm and β = 107.70 [5.109-5.110]. There are 100 atoms in one unit cell: 24 Fe atoms and 76 Al atoms for the ideal structure [5.109].



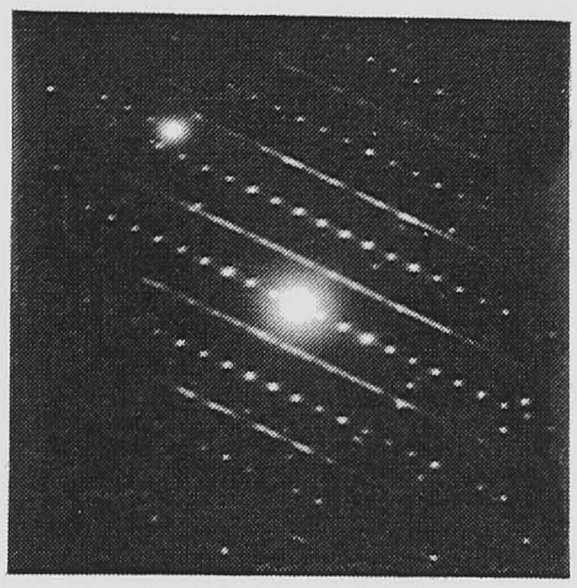
(a) [100]



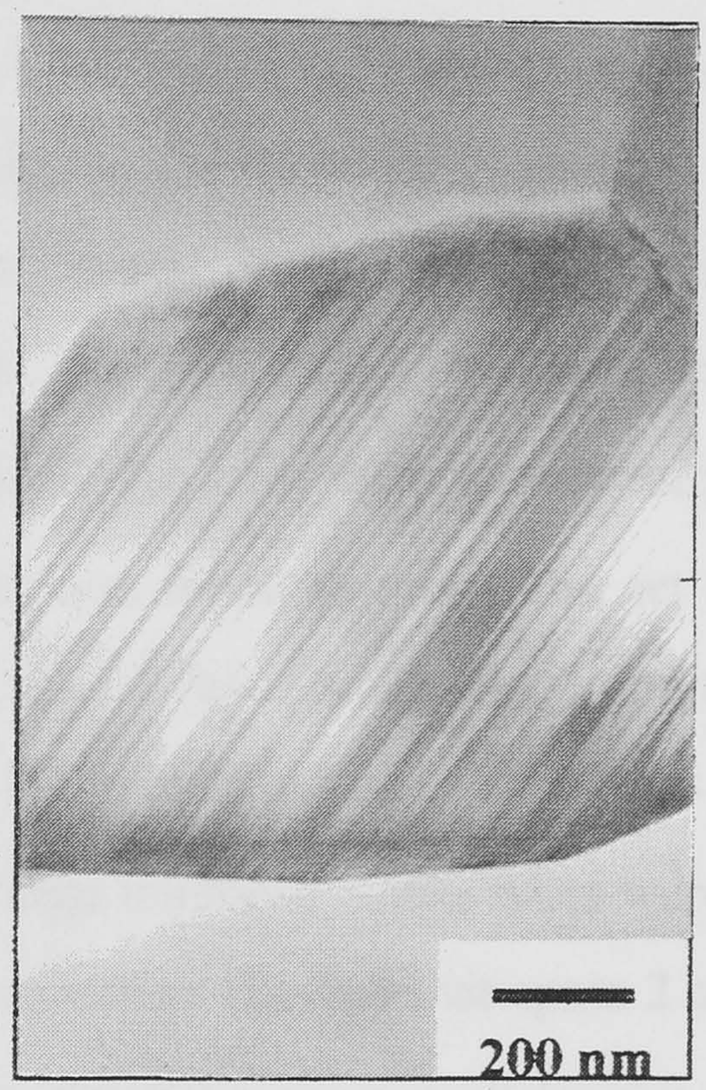
(b) [0$\bar{1}$0]



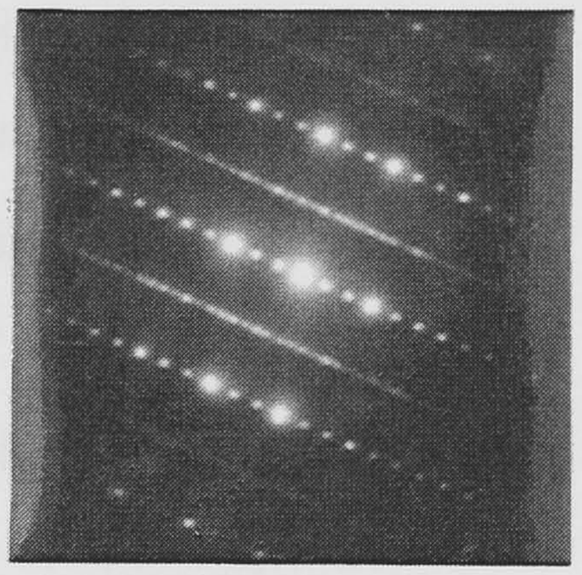
(c) [001]



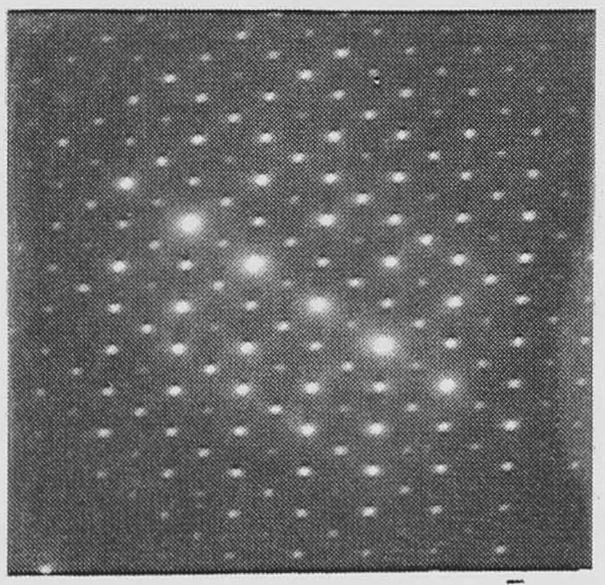
(d) [1$\bar{1}$0]



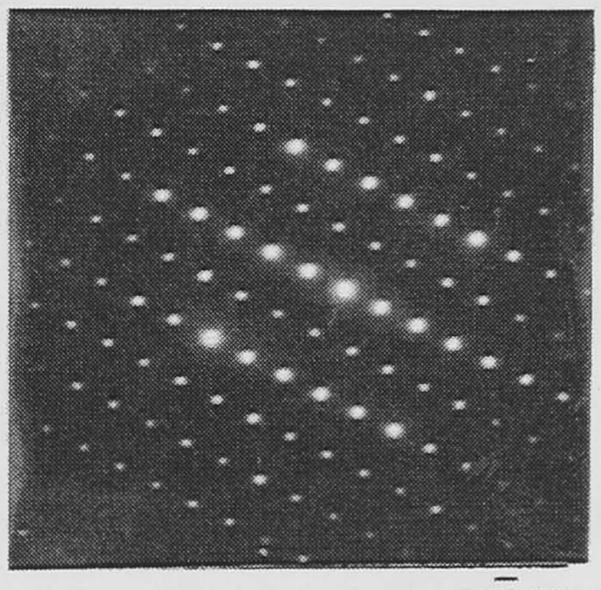
(e)



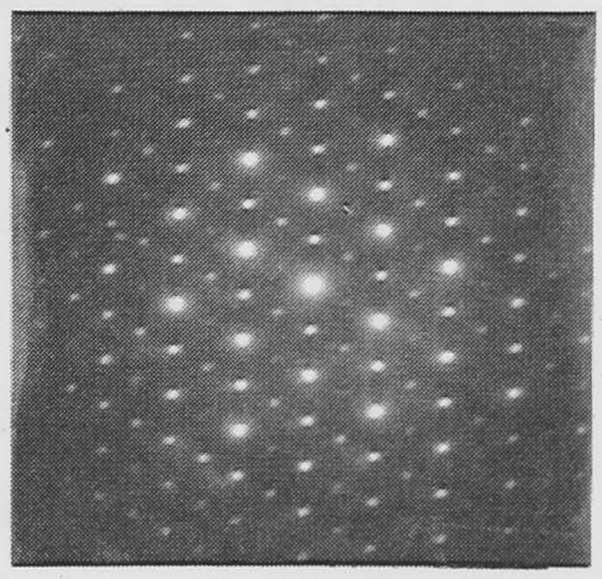
(f) [130]



(g) [1$\bar{1}$4]



(h) [1$\bar{3}$2]



(i) [134]

Fig. 5.7.1.1 TEM bright field image and electron diffraction patterns of the equilibrium $Al_{13}Fe_4$ phase.

A large particle of $Al_{13}Fe_4$ phase shown in Fig. 5.7.1.1 is highly faulted. The (001) planar defects are seen as fine parallel contrast bands lying parallel to one another. The stacking faults which give rise to the (001) planar defects or microtwins have also been observed in β-Al_5FeSi phase particles [5.111], $Al_{13}Fe_4$ phase particles [5.112, 5.113], and low-temperature Mg_2NiH_4 phase particles [5.114, 5.115].

In SADPs of an $Al_{13}Fe_4$ phase particle, a pronounced faulting was indicated by, for example in the [110] orientation, the rows of reciprocal points, parallel to the 001-row, smeared into continuous intensity lines. These lines result from stacking faults on the (001)-plane. In this investigation, the presence of stacking faults on (001)-plane was confirmed by SADPs with zone $[1\bar{1}0]$ and zone [130] axes (Fig. 5.7.1.1 (d) and (f), respectively) which showed continuous intensity lines lying parallel to the {001} directions.

Some SADPs, for example in Fig. 5.7.1.1 (g) and (i), exhibited complicated arrays of diffracted spots. The spots linked by solid lines in a schematic solution of a SADP as shown in Fig. 5.7.1.2 (a) were successfully indexed as a zone $[1\bar{1}4]$ pattern. This set of spots was found to match the set of spots in the zone $[1\bar{1}4]$ pattern as shown in Fig. 5.7.1.2 (b) of some $Al_{13}Fe_4$ particles. However, there were some extra spots in Fig. 5.7.1.2 (a), indicated by arrows 1, 2, 3, and 4, which could not be indexed by using digit numbers. These spots were not part of the zone $[1\bar{1}4]$ pattern either. Close examination showed that spots 2 and 3 were part of the zone $[\bar{1}\bar{1}4]$ pattern, while spots 1 and 4 were part of the zone [001] pattern (Fig. 5.7.1.2 (c)).

Similar to the pattern in Fig. 5.7.1.1 (g) discussed above, the pattern in Fig. 5.7.1.1 (i) was composed of zone [134], zone $[\bar{1}3\bar{4}]$ and zone $[10\bar{1}]$ patterns. This indicates that each electron diffraction pattern in Fig. 5.7.1.1 (g) and (i) results from superposition of three patterns. These complicated diffraction patterns also indicate that the $Al_{13}Fe_4$ crystal is twinned. Twinning is commonly observed in the $Al_{13}Fe_4$ crystal. A successful attempt to produce a non-twinned $Al_{13}Fe_4$ crystal has been reported only for a very small crystal [5.116]. Twinned crystals were found in $Al_{13}Os_4$ [5.117], $Al_{13}Ru_4$ [5.118], $Al_{13}Co_4$ [5.119], and $Ni_3Zn_6Ga_4$ [5.120]. It is interesting to note here that these crystals are isostructural with the $Al_{13}Fe_4$ crystal.

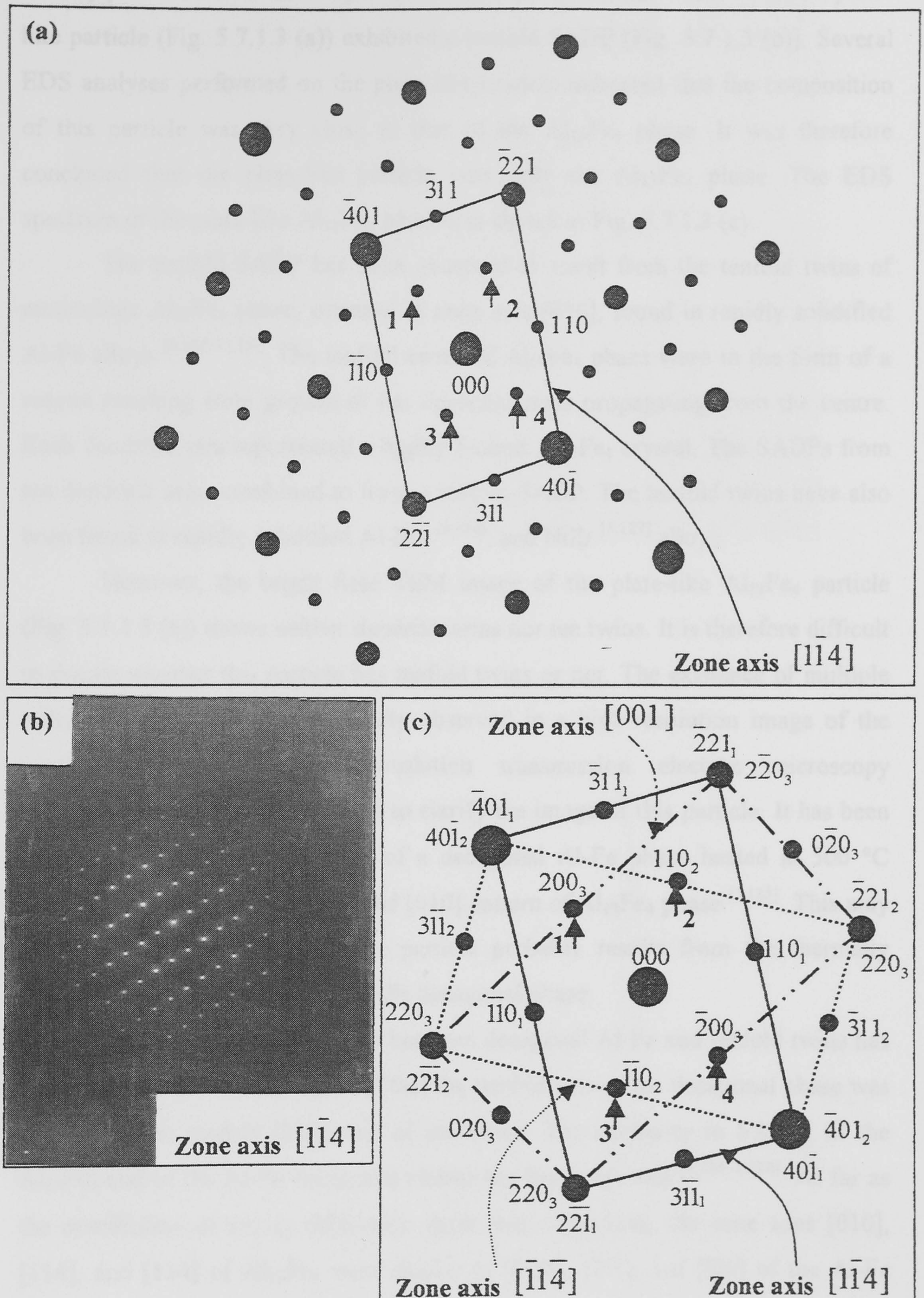


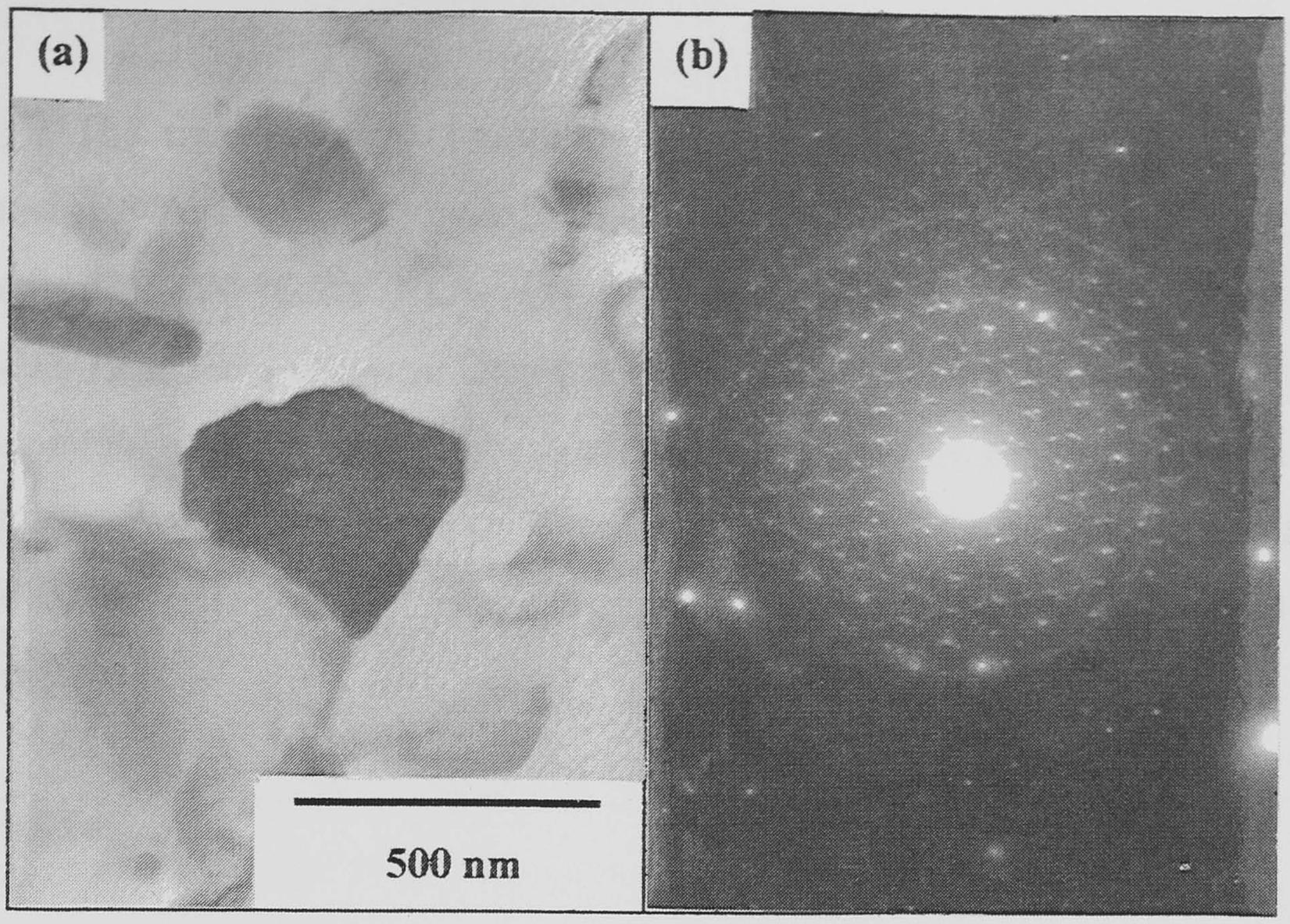
Fig. 5.7.1.2 Schematic solutions ((a) and (c)) and electron diffraction pattern (b) with a $<1\bar{1}4>$ beam direction for the $Al_{13}Fe_4$ phase.

In a heat-treated specimen (heated at 500 °C for 120 minutes) of RS-Al-Fe-V alloy produced from coarse powders with diameters greater than 45 μm, a plate-like particle (Fig. 5.7.1.3 (a)) exhibited a tenfold SADP (Fig. 5.7.1.3 (b)). Several EDS analyses performed on the plate-like particle indicated that the composition of this particle was very close to that of the $Al_{13}Fe_4$ phase. It was therefore concluded that the plate-like particle was truly the $Al_{13}Fe_4$ phase. The EDS spectrum of the plate-like $Al_{13}Fe_4$ particle is shown in Fig. 5.7.1.3 (c).

The tenfold SADP has been observed to result from the tenfold twins of monoclinic $Al_{13}Fe_4$ phase, oriented in zone axis [010], found in rapidly solidified Al-Fe alloys [5.121-5.125]. The tenfold twins of $Al_{13}Fe_4$ phase were in the form of a rosette resulting from growth of ten dendritic arms propagating from the centre. Each dendritic arm represented a highly faulted $Al_{13}Fe_4$ crystal. The SADPs from ten dendritic arms combined to form a tenfold SADP. The tenfold twins have also been found in rapidly solidified Al-Mn [5.126], and NiZr [5.127] alloys.

However, the bright field TEM image of the plate-like $Al_{13}Fe_4$ particle (Fig. 5.7.1.3 (a)) shows neither dendritic arms nor ten twins. It is therefore difficult to decide whether this particle has tenfold twins or not. The existence of multiple twins in the particle can be clearly observed in a high-resolution image of the particle. Unfortunately, high-resolution transmission electron microscopy (HRTEM) has not been employed to clarify the image of this particle. It has been observed that the tenfold SADP of a decagonal Al-Fe phase heated at 500 °C transformed to a blurred and faulted [010] pattern of $Al_{13}Fe_4$ phase [5.123]. This may imply that the plate-like $Al_{13}Fe_4$ particle probably results from the thermally activated transformation of the Al-Fe decagonal phase.

An orientation relationship between decagonal Al-Fe and tenfold twins has been studied [5.123]. It was reported that the tenfold axis of the decagonal phase was parallel to the tenfold [010] axis of the twins. The similarity in SADPs of the $Al_{13}Fe_4$ and of the Al-Fe decagonal phases has been reported [5.124, 5.128]. As far as the distribution of strong diffraction spots was concerned, the zone axes [010], [114], and [134] of $Al_{13}Fe_4$ were similar to [D10], [D3], and [D5] of the Al-Fe decagonal phase. This suggests that the $Al_{13}Fe_4$ phase may be the structural approximant of the Al-Fe decagonal phase.



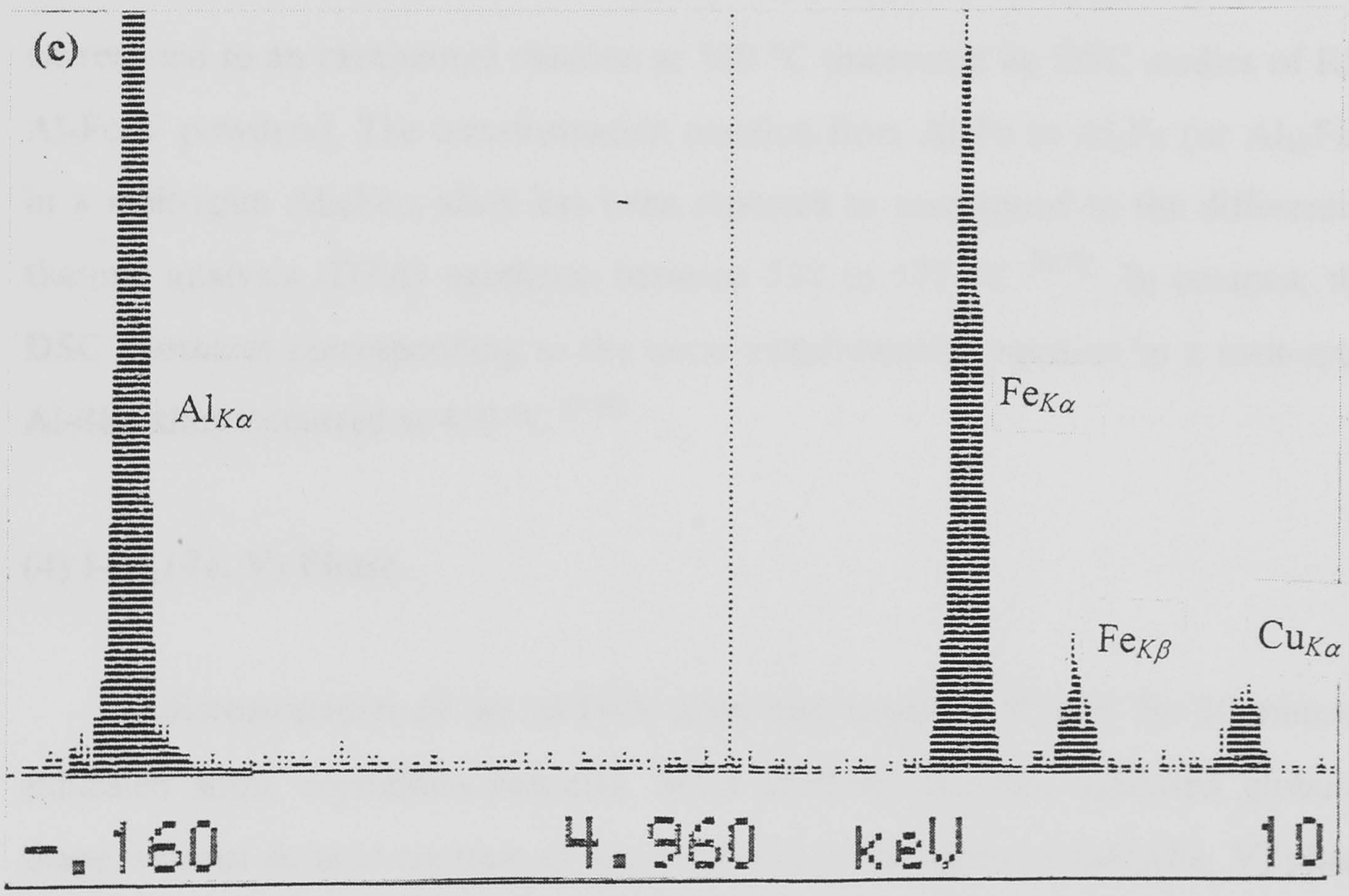


Fig. 5.7.1.3 Identification of a plate-like $Al_{13}Fe_4$ particle exhibiting a tenfold SADP: (a) bright field TEM image, (b) tenfold SADP, and (c) EDS spectrum.

(2) Unknown Al-Fe-V Phase

The transformation reaction of the unknown Al-Fe-V phase in a heat-treated RS-Al-Fe-V alloy was not clearly understood. However, after heat-treatment at 500 °C for 2 hrs, only two equilibrium phases, namely $Al_{13}Fe_4$ and $Al_{45}(V, Fe)_7$, were observed. Intermediate phases between the unknown Al-Fe-V phase and the equilibrium $Al_{13}Fe_4$ and $Al_{45}(V, Fe)_7$ phases were not observed. This may suggest that the unknown Al-Fe-V phase is metastable and decomposes to equilibrium $Al_{13}Fe_4$ and $Al_{45}(V, Fe)_7$ phases during heating at elevated temperatures.

(3) Al_6Fe

The metastable Al_6Fe phase particles completely disappeared from microstructures of the heat-treated RS-Al-Fe-V alloy after heat-treatment at 500 °C for 2 hours. Transformation reaction from Al_6Fe to $Al_{13}Fe_4$ was found to correspond to an exothermal reaction at 500 °C (measured by DSC studies of RS-Al-Fe-V powders). The transformation reaction from Al_6Fe to Al_3Fe (or $Al_{13}Fe_4$) in a melt-spun $Al_{86}Fe_{14}$ alloy has been reported to correspond to the differential thermal analysis (DTA) exotherm between 527 to 577 °C [5.77]. In contrast, the DSC exotherm corresponding to the same transformation reaction in a melt-spun Al-8Fe alloy occurred at 450 °C [5.78].

(4) I-Al_x(Fe, V) Phase

Microstructures of the Al-Fe-V alloy heat-treated at 550 °C for 30 minutes exhibited some crystalline particles. Most of these particles exhibited globular shape without striated contrast as was observed in the globular I-Al_x(Fe, V) phase particles. The composition of the crystalline phase, determined by using EDS, was found to be Al_x(Fe, V) where x is in the range of 5-6. The similarity in both morphology (particle shape) and composition would suggest that the I-Al_x(Fe, V) phase transforms polymorphously to the crystalline phase during heating at high temperatures. A bright field TEM image and EDS spectrum of a crystalline phase

particle are shown in Fig. 5.7.1.4. The particle exhibited hexagonal shape when the electron beam was parallel to the [0001] zone axis.

The SADPs and the CBED whole patterns of the globular crystalline particle are shown in Fig. 5.7.1.5. For simplicity, the CBED whole pattern according to the SADP with [0001] zone axis is designated as '[0001] CBED whole pattern'. The symmetry of the [0001] CBED whole pattern shown in Fig. 5.7.1.5 (h) is 6mm. From Table 2 in the article of Buxton *et al.* [5.129], the possible diffraction groups are 6mm and $6mm1_R$. For the $[10\bar{1}0]$ CBED whole pattern (Fig. 5.7.1.5 (f)), the symmetry is 2mm which places the diffraction groups as 2mm and $2mm1_R$. For the $[21\bar{3}0]$ CBED whole pattern (Fig. 5.7.1.5 (b)), the symmetry is 2mm which places the diffraction groups as 2mm and $2mm1_R$. The possible crystal point groups determined by using Table 3 in ref. [5.129] are summarised in Table 5.7.1. The only crystal point group consistent with all the symmetries mentioned above is 6/mmm. This indicates that this phase has hexagonal crystal structure. This phase is designated as H-Al_x(Fe, V).

Table 5.7.1 All possible crystal point groups corresponding to the CBED whole patterns shown in Fig. 5.7.1.5.

Zone axis	Deduced diffraction group	Possible crystal point groups							
		mm2	mmm	4/mmm	6mm	$\bar{6}$m2	6/mmm	m3	m3m
[0001]	6mm				*				
	$6mm1_R$						*		
$[10\bar{1}0]$	2mm	*				*			
	$2mm1_R$		*	*			*	*	*
$[21\bar{3}0]$	2mm	*				*			
	$2mm1_R$		*	*			*	*	*

The lattice parameter of the H-Al_x(Fe, V) phase determined from several electron diffraction patterns is $a = 2.59 \pm 0.03$ nm, $c = 1.30 \pm 0.01$ nm of which c/a ratio is 0.5. These values are slightly different from those of H-$(Al, Si)_5$(Fe, V) phase (§ 5.3.4.2) and of the hexagonal phase observed in strip-cast and spray-cast

Al-Fe-V-Si alloys [5.86]. The difference may be caused by an error occurring during operation of the TEM (technical error).

Phase transformation reactions from icosahedral phases to crystalline hexagonal phases have been observed during heating of some rapidly solidified Al-Mn alloys [5.53, 5.73, 5.130-5.135]. It was found that the hexagonal λ-Al_4Mn phase could be formed by solid state transformation of the icosahedral phase at temperatures above 750 °C [5.134, 5.135]. Another form of hexagonal Al-Mn phase, μ-Al_4Mn, was found to form by solid-state transformation at 800 °C for 4 hours from the initial phases (probably icosahedral and decagonal phases) of rapidly solidified Al-35 wt. % Mn [5.130]. The phase transformation reactions of λ- and μ- phases may correspond to the reaction series of icosahdral phase → Al_6Mn phase → decagonal phase → hexagonal λ phase → hexagonal μ phase obtained by successive heating of the splat-quenched Al_4Mn alloy [5.73]. In the silicon containing Al-Mn alloys, it has been reported that the icosahedral AlMnSi phase transformed to hexagonal β-AlMnSi phase on heating at 700 °C [5.131-5.133].

The morphology (or particle shape) and composition of both I-Al_x(Fe, V) and H-Al_x(Fe, V) phases were similar. The intermediate phases between I-Al_x(Fe, V) and H-Al_x(Fe, V) phases were not observed. It may be concluded here that the transformation reaction from I-Al_x(Fe, V) phase to H-Al_x(Fe, V) phase occurs via polymorphous phase transformation. This reaction is different from the phase transformation sequence in rapidly solidified Al-Mn alloys mentioned above.

The orientation relationship between icosahedral phase and hexagonal phase has been reported, for example $\langle i2\rangle_{icosa}$ // $[11\bar{2}0]_{hexa}$, and $(110000)_{icosa}$ // $(1\bar{1}00)_{hexa}$ in strip-cast and spray-cast Al-Fe-V-Si alloys [5.86]. However, it was observed that there was no orientation relationship between I-Al_x(Fe, V) and H-Al_x(Fe, V) phases in a heat-treated RS-Al-Fe-V alloy. The juxtaposition of the I-Al_x(Fe, V) phase and the H-Al_x(Fe, V) phase is shown in Fig. 5.7.1.6 (a). The SADP, resulting from diffraction from both phases and taken with the electron beam parallel to the fivefold axis of the I-Al_x(Fe, V) phase ($\langle i5\rangle_{icosa}$) is shown in Fig 5.7.1.6 (b). The zone [0001] pattern of the H-Al_x(Fe, V) phase is a few degrees out of zone. That is indicated by the curved arrays of diffraction spots. This result contradicts the relationship of $\langle i3\rangle_{icosa}$ // $[0001]_{hexa}$ found in ref. [5.86] because if this relationship is correct, the [0001] zone axis of the H-Al_x(Fe, V) phase must be

32° away from the <i5> of the I-Al_x(Fe, V) phase. Note that the $<i3>_{icosa}$ is 32° away from the $<i5>_{icosa}$.

Some hexagonal crystalline phases have been reported to be approximants having crystal structure related to that of quasi-crystalline phases. The approximants have been found in several aluminium alloy systems such as binary Al-M (M = Cr, Co, Ir, Mn, Pd, and Pt), ternary (Al-Cr-Cu, Al-Cr-Ni, and Al-Mn-Ni), and quaternary (Al-Cu-Li-Mg, and Al-Fe-V-Si) alloys (Table 5.7.2).

The phases with large hexagonal unit cells are believed to be constructed of icosahedral or icosahedral-related clusters. The structural model formulated for the hexagonal Al-Fe-V-Si phase [5.86] is believed to be constructed of Mackay icosahedra of (Fe + V) and (Al + Si). The Mackay icosahedra are also constructing clusters for the αPm3 AlMnSi and AlFeSi phases [5.136].

It had been suggested that the crystalline (hexagonal μ and λ) and quasiperiodic (decagonal and icosahedral) phases of Al_4Mn composition can be formed by different stacking of the same icosahedral clusters, possibly of Mackay icosahedron type [5.130]. However, it was found later that neither complete Mackay icosahedra, nor Bergman polyhedra are present, but different fragments of Mackay icoosahedra occur in the structure of the μ-phase [5.137].

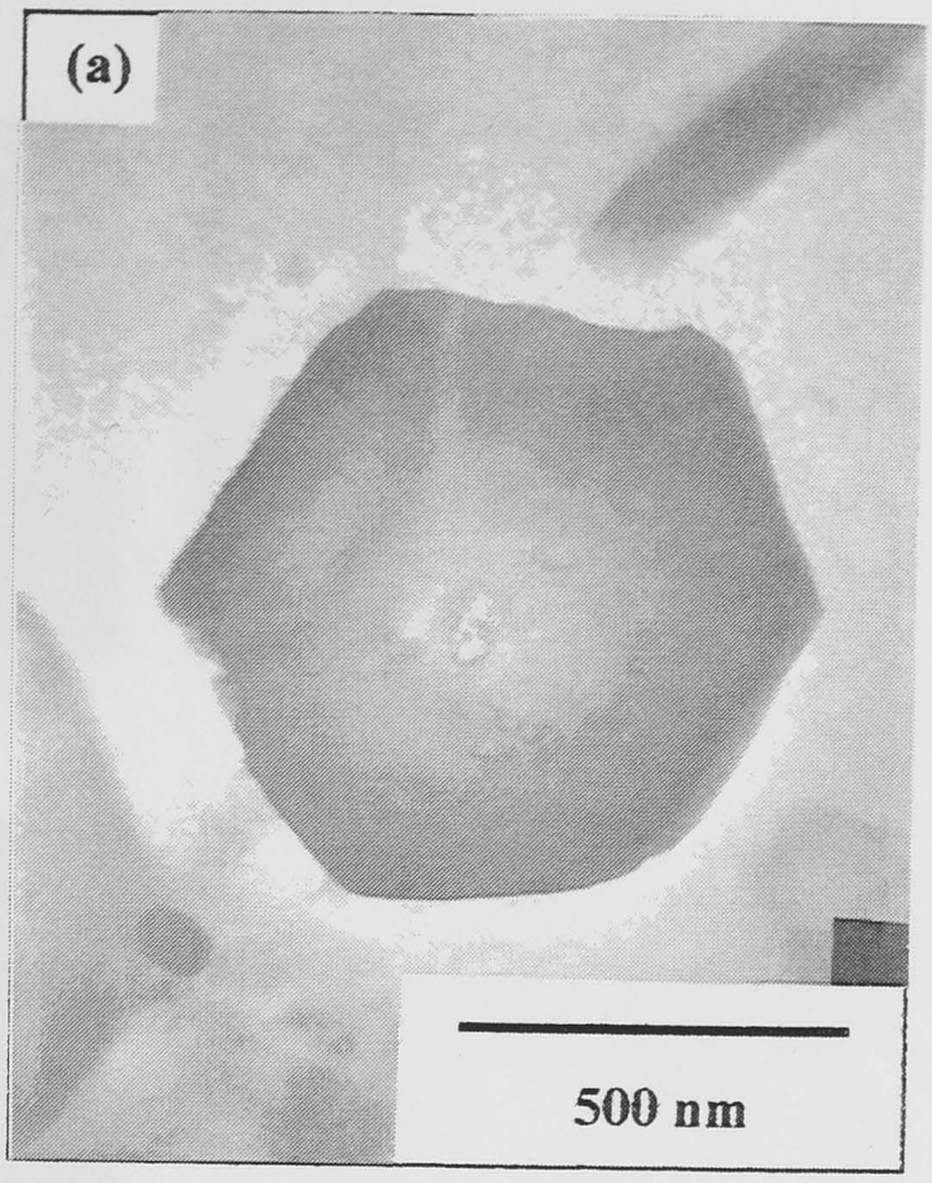
The structure of hexagonal $Al_{14.4}Cr_{3.4}Ni_{1.1}$ phase [5.138] is constructed in a different way from that of the hexagonal Al-Fe-V-Si phase [5.86]. The structure of the $Al_{14.4}Cr_{3.4}Ni_{1.1}$ phase is constructed with 12 icosahedral clusters. Each cluster consists of a transition metal (TM) at the centre and 11 Al atoms and one TM atom on the fivefold vertices of the icosahedron. Two clusters are linked along the *c* axis by sharing a triangular face to form a pair of clusters. Two pairs of clusters are linked with two trigonal anti-prisms, constructing a column along the *c* axis. Six columns form the unit cell of the crystal structure.

Table 5.7.2 Hexagonal phases in aluminium alloys.

Alloy system	Phase	Lattice parameter (nm)			Reference
		a	*c*	*c/a*	
Al-Co	Al_5Co_2	0.7658	0.7604	0.99	5.139
Al-Cr	ε-Al_4Cr	2.01	2.48	1.23	5.140
	μ-Al_4Cr	2.00	2.47	1.24	5.141
Al-Ir	Al_4Ir (M) ❄	1.231	2.623	2.12	5.142 & 5.143
	Al-Ir (S) ☆	0.31	0.52	1.67	5.143
Al-Mn	$Al_{10}Mn_3$	0.7543	0.7898	1.05	5.144
	λ-Al_4Mn	2.84	1.24	0.44	5.53, 5.73,
	"	"	"	"	5.134, 5.135
	"	"	"	"	& 5.145
	μ-Al_4Mn	1.995	2.452	1.23	5.73, 5.130,
	"	"	"	"	5.134, 5.137,
	"	"	"	"	&5.146
Al-Pd	NR	1.229	2.647	2.15	5.142
Al-Pt	NR	"	"	"	5.142
Al-Cr-Cu	$Al_{67}Cr_{15}Cu_{0.5}$	1.282	1.271	0.99	5.147
Al-Cr-Ni	$Al_6Cr_{0.5}$ $Ni_{0.5}$	1.24	1.24	1.00	5.147
	ρ_2-$Al_{7.96}Cr_{1.87}Ni_{0.17}$	1.77	1.24	0.70	5.148
	ρ_3-$Al_{7.96}Cr_{1.87}Ni_{0.17}$	3.07	1.24	0.40	5.148
	$Al_{14.4}Cr_{3.4}Ni_{1.1}$	1.7674	1.2516	0.71	5.138
Al-Mn-Ni	$Al_4Mn_{0.5}Ni_{0.5}$	1.272	1.261	0.99	5.147
Al-Cu-Li-Mg	Z-$Al_{59}Cu_5Li_{26}Mg_{10}$	1.403	2*a*	2	5.149 & 5.150
Al-Fe-V-Si	NR	2.514	1.257	0.5	5.86
Al-Fe-V	Al_x(Fe, V), x = 5-6	2.59	1.30	0.5	Present study
Al-Fe-V-Si	$(Al, Si)_5(Fe, V)$	2.52	1.24	0.5	Present study

Note: (M) ❄ = metastable

(S) ☆ = stable



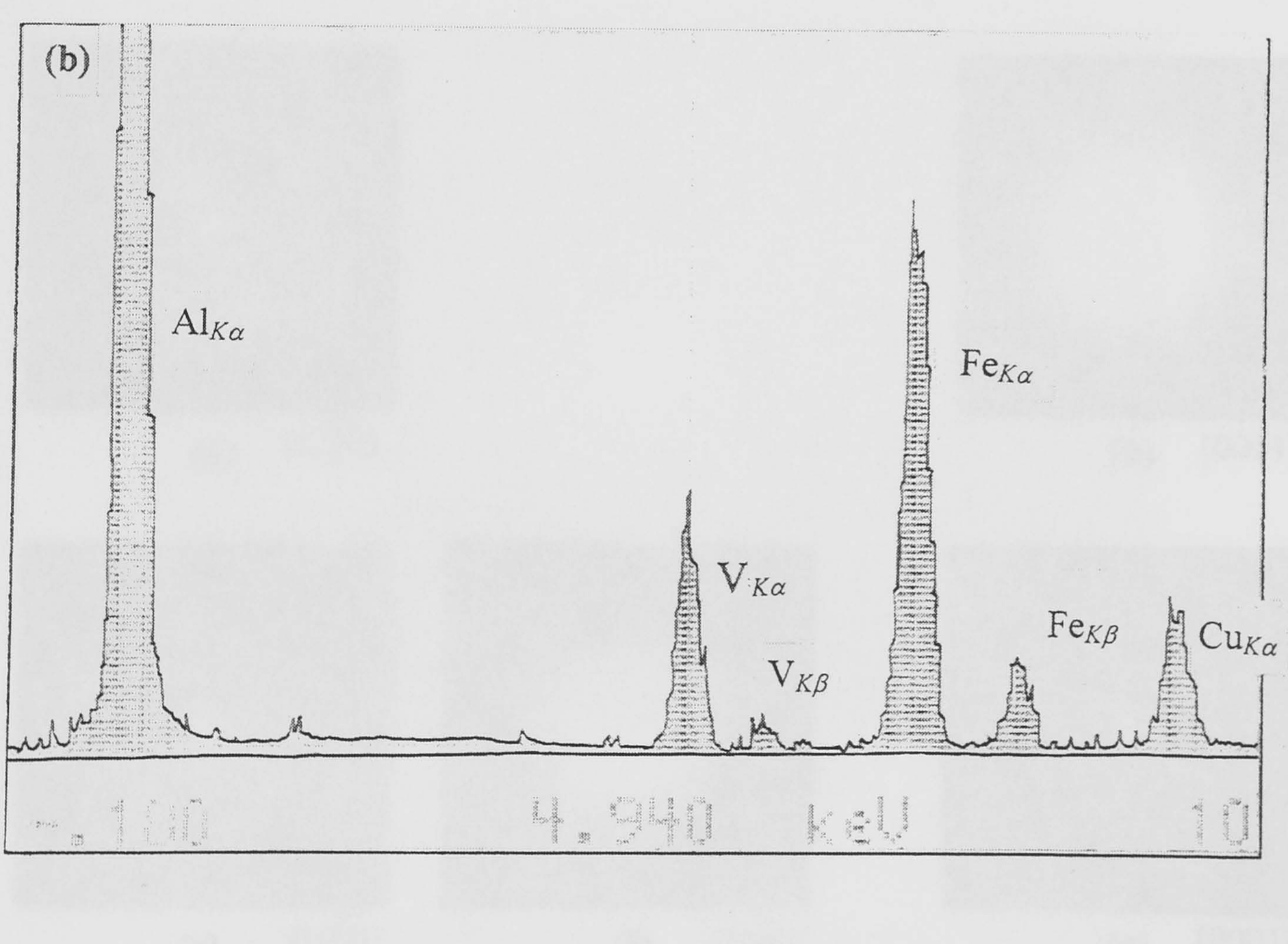
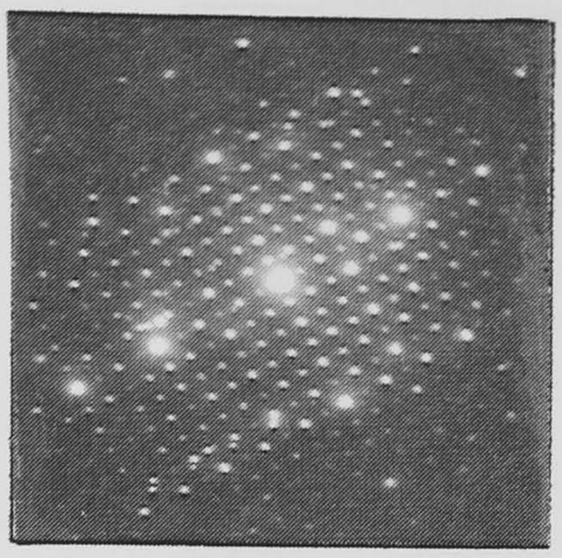
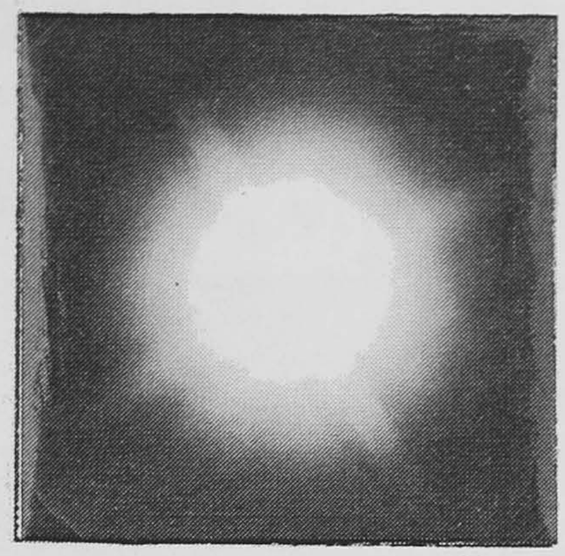


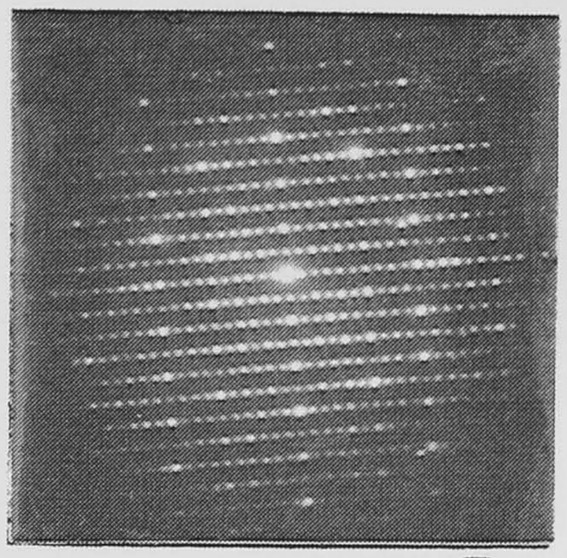
Fig. 5.7.1.4 Identification of a H-Al_x(Fe, V) particle; (a) bright field TEM image taken with an electron beam parallel to [0001] zone axis , (b) EDS spectrum.



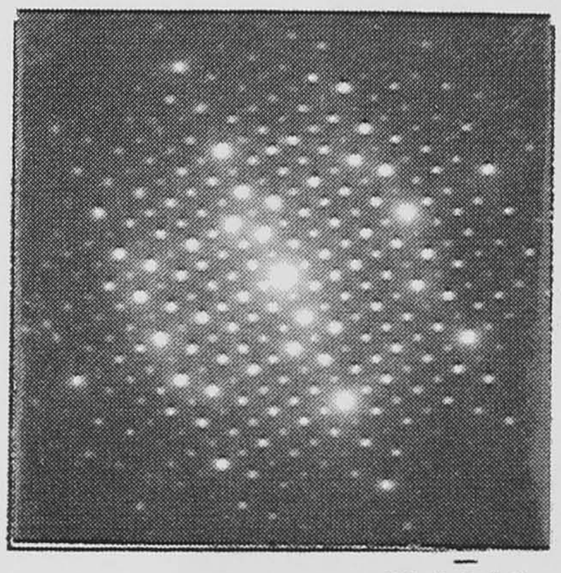
(a) [2$\bar{1}$30]



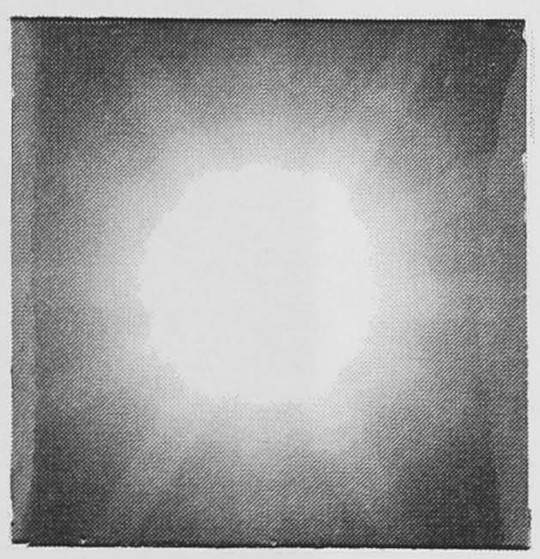
(b) [2$\bar{1}$30]



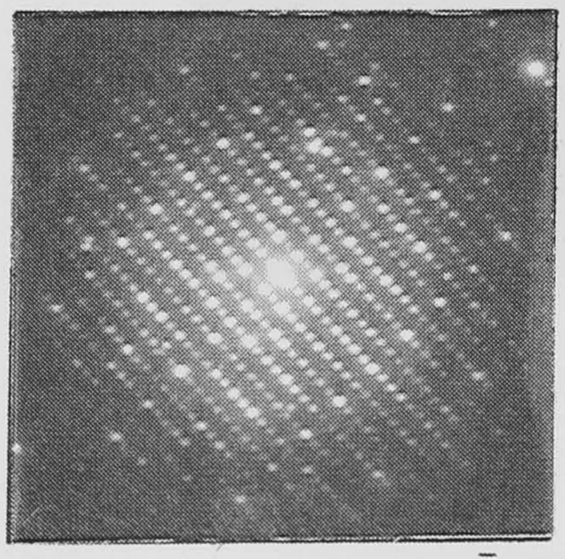
(c) [11$\bar{2}$0]



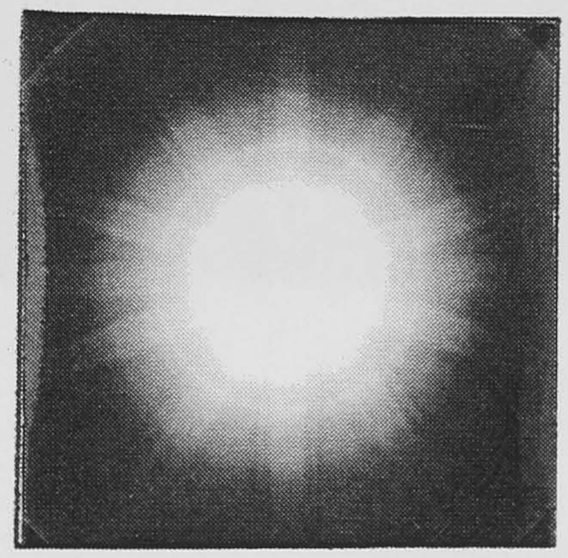
(d) [12$\bar{3}$0]



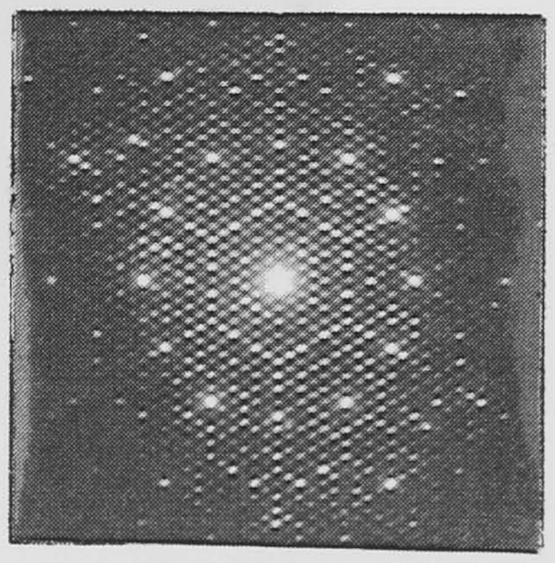
(h) [0001]



(e) [10$\bar{1}$0]

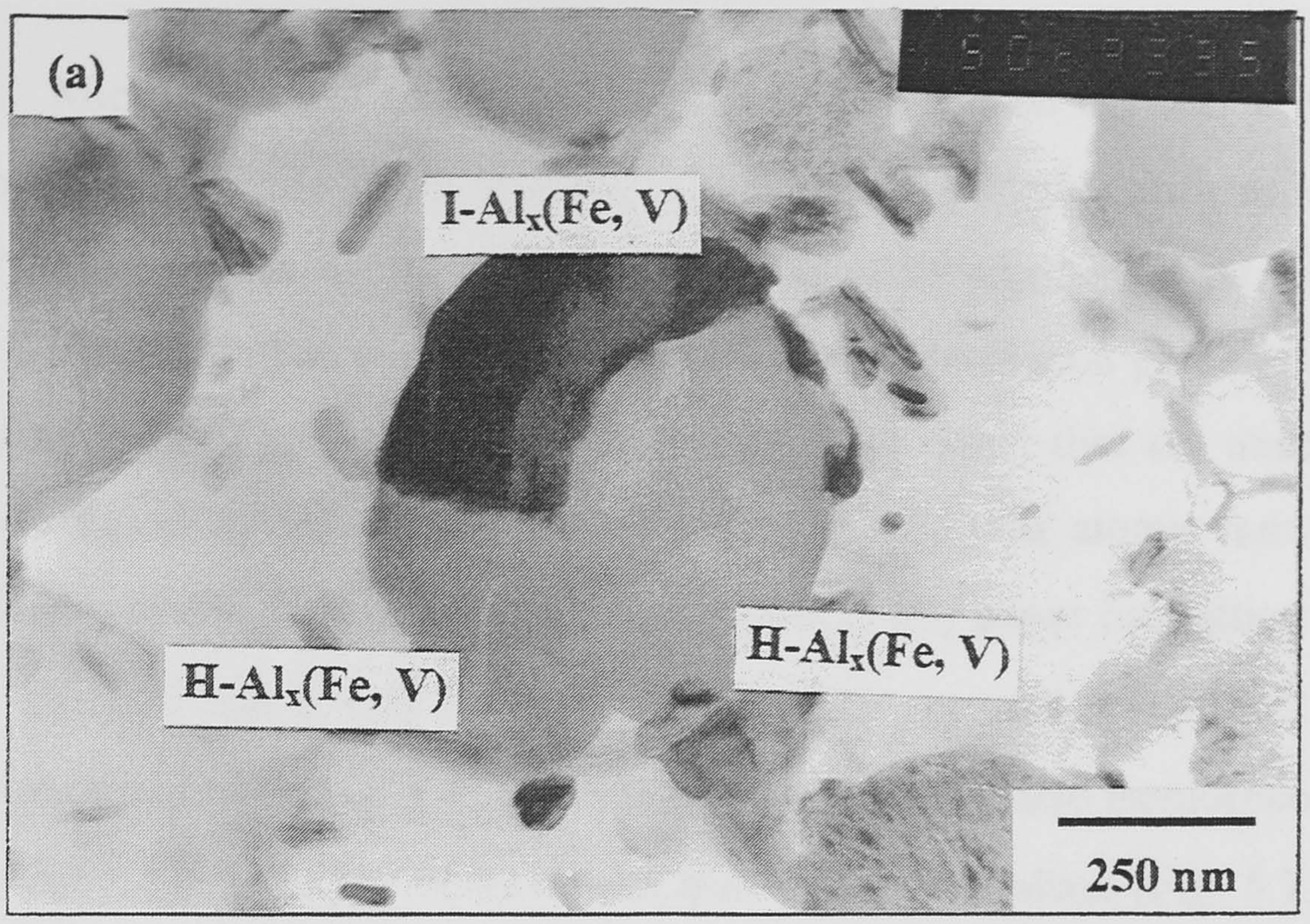


(f) [10$\bar{1}$0]



(g) [0001]

Fig. 5.7.1.5 Selected area electron diffraction patterns and convergent beam electron diffraction patterns (whole pattern) of the H-Al_x(Fe, V) phase.



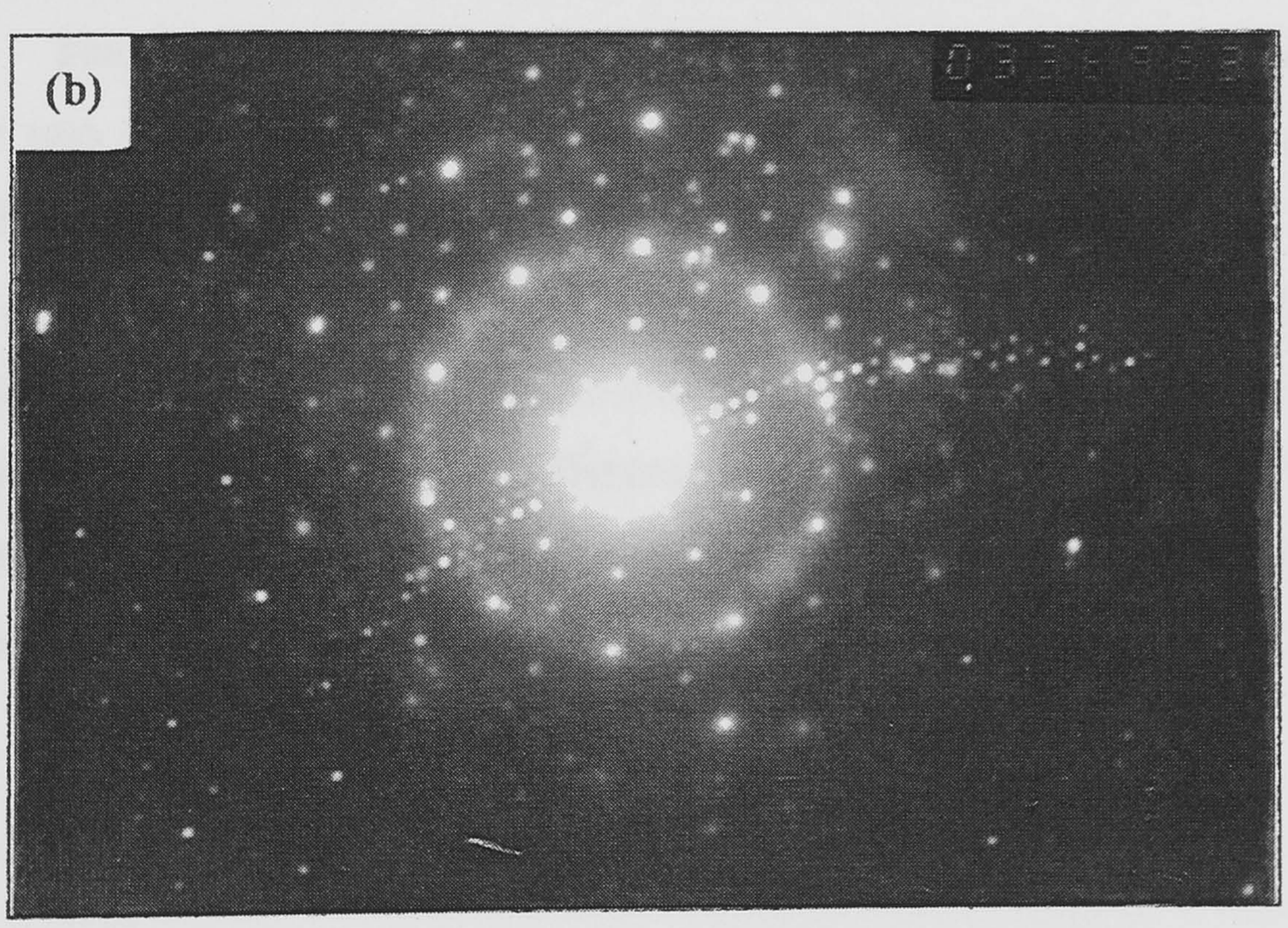


Fig. 5.7.1.6 Bright field TEM image and electron diffraction pattern of H-Al$_x$(Fe, V) and I-Al$_x$(Fe, V) phases: (a) an I-Al$_x$(Fe, V) particle adjacent to two H-Al$_x$(Fe, V) particles, (b) the SADP taken with the electron beam parallel to the fivefold axis of the I-Al$_x$(Fe, V) particle.

(5) H-Alx(Fe, V) phase

Microstructures of RS-Al-Fe-V alloy heat-treated at 550 °C for 2 hours exhibited some knife blade-shaped, vanadium-rich particles with aspect ratio of 3:1. These particles were frequently observed to be adjacent to $Al_{13}Fe_4$ particles (Fig. 5.7.1.7 (a)). The composition of the knife blade-shaped particles determined by using EDS (Fig. 5.7.1.7 (c) was $Al_{46}(V, Fe)_7$. Note that the atomic ratio of Al:(V + Fe) in the $Al_{46}(V, Fe)_7$ phase is very close to the atomic ratio of Al:V in the $Al_{45}V_7$ phase. The monoclinic $Al_{45}V_7$ or α'(VAl) phase has lattice parameters of a = 2.5605 nm, b = 0.76218 nm, c = 1.1082 nm, and β = 128.92 [5.151]. The space group of this phase is $C2/m$. The α'(VAl) phase is also isomorphous with the θ (Cr-Al) [5.152]. Indexing of SADPs of the $Al_{46}(V, Fe)_7$ phase (Fig. 5.7.1.7 (b)) by using lattice parameters of the $Al_{45}V_7$ phase was successful. This suggests that the $Al_{46}(V, Fe)_7$ phase has the same structure as the $Al_{45}V_7$ phase. The knife blade-shaped particle is therefore designated here as the $Al_{45}(V, Fe)_7$ phase.

The juxtaposition of $Al_{45}(V, Fe)_7$ and $Al_{13}Fe_4$ phases may indicate that these two phases result from decomposition of the crystalline Al-Fe-V phases which can be either unknown Al-Fe-V or H-Al_x(Fe, V) phases.

The EDS analyses showed that the $Al_{45}(V, Fe)_7$ phase contained 9.37 at. % V and 3.78 at. % Fe while the $Al_{13}Fe_4$ phase contained 21.49 at. % Fe and an insignificant amount of V. The difference in vanadium content in these two phases may relate to the difference in diffusion rate of Fe and V from the original Al-Fe-V phases to $Al_{45}(V, Fe)_7$ and $Al_{13}Fe_4$ phases during decomposition.

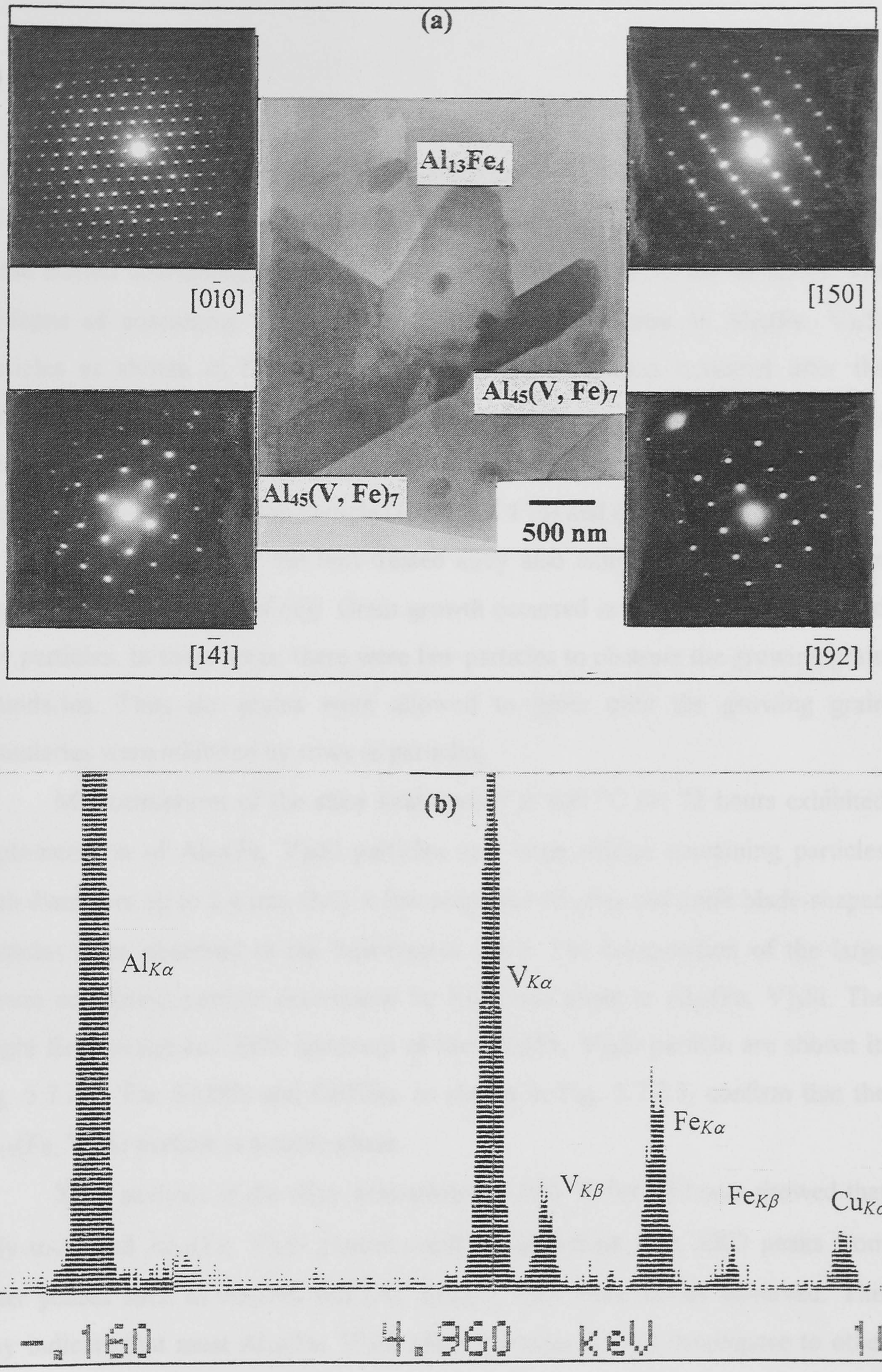


Fig. 5.7.1.7 Identification of the $Al_{45}(V, Fe)_7$ phase: (a) bright field TEM image and electron diffraction patterns, (b) EDS spectrum. Note that two $Al_{45}(V, Fe)_7$ particles are adjacent to an $Al_{13}Fe_4$ particle.

5.7.2 RS-Al-Fe-V-Si Alloy

(1) $Al_{13}(Fe, V)_3Si$ Phase

Coarsening of the $Al_{13}(Fe, V)_3Si$ phase particles was hardly observed in the RS-Al-Fe-V-Si alloys heat-treated at 500 °C, even after heating for 72 hours. The phase started coarsening when the alloy was heated at 550 °C for 48 hours. The evidence of coarsening could be seen as an agglomeration of $Al_{13}(Fe, V)_3Si$ particles as shown in Fig. 5.7.2.1 (a). The agglomeration occurred after the particles with small inter-particle distances had coarsened until their boundaries met one another. With further heating, the boundaries of agglomerated particles dissolved and formed a large particle (Fig. 5.7.2.1 (b) and (c)).

Microstructures of the heat-treated alloy also exhibited evidence of grain growth (Fig.5.7.2.1 (b) and (d)). Grain growth occurred in the areas that contained few particles. In these areas, there were few particles to obstruct the growing grain boundaries. Thus the grains were allowed to grow until the growing grain boundaries were inhibited by rows of particles.

Microstructures of the alloy heat-treated at 600 °C for 72 hours exhibited agglomeration of $Al_{13}(Fe, V)_3Si$ particles and large silicon containing particles with diameters up to 2.4 μm. Only a few plate-like $Al_{13}Fe_4$ and knife blade-shaped particles were observed in the heat-treated alloy. The composition of the large silicon containing particle determined by EDS was close to $Al_{13}(Fe, V)_3Si$. The bright field image and EDS spectrum of the $Al_{13}(Fe, V)_3Si$ particle are shown in Fig. 5.7.2.2. The SADPs and CBEDs, as shown in Fig. 5.7.2.3, confirm that the $Al_{13}(Fe, V)_3Si$ particle is a cubic phase.

XRD analysis of the alloy heat-treated at 600 °C for 72 hours showed that only α-Al and $Al_{13}(Fe, V)_3Si$ phases could be identified. The XRD peaks from other phases such as $Al_{13}Fe_4$ and $(Al, Si)_{45}(V, Fe)_7$ were hardly observed. This may indicate that most $Al_{13}(Fe, V)_3Si$ phase particles do not decompose to other phases during heating for 72 hours at temperatures up to 600 °C.

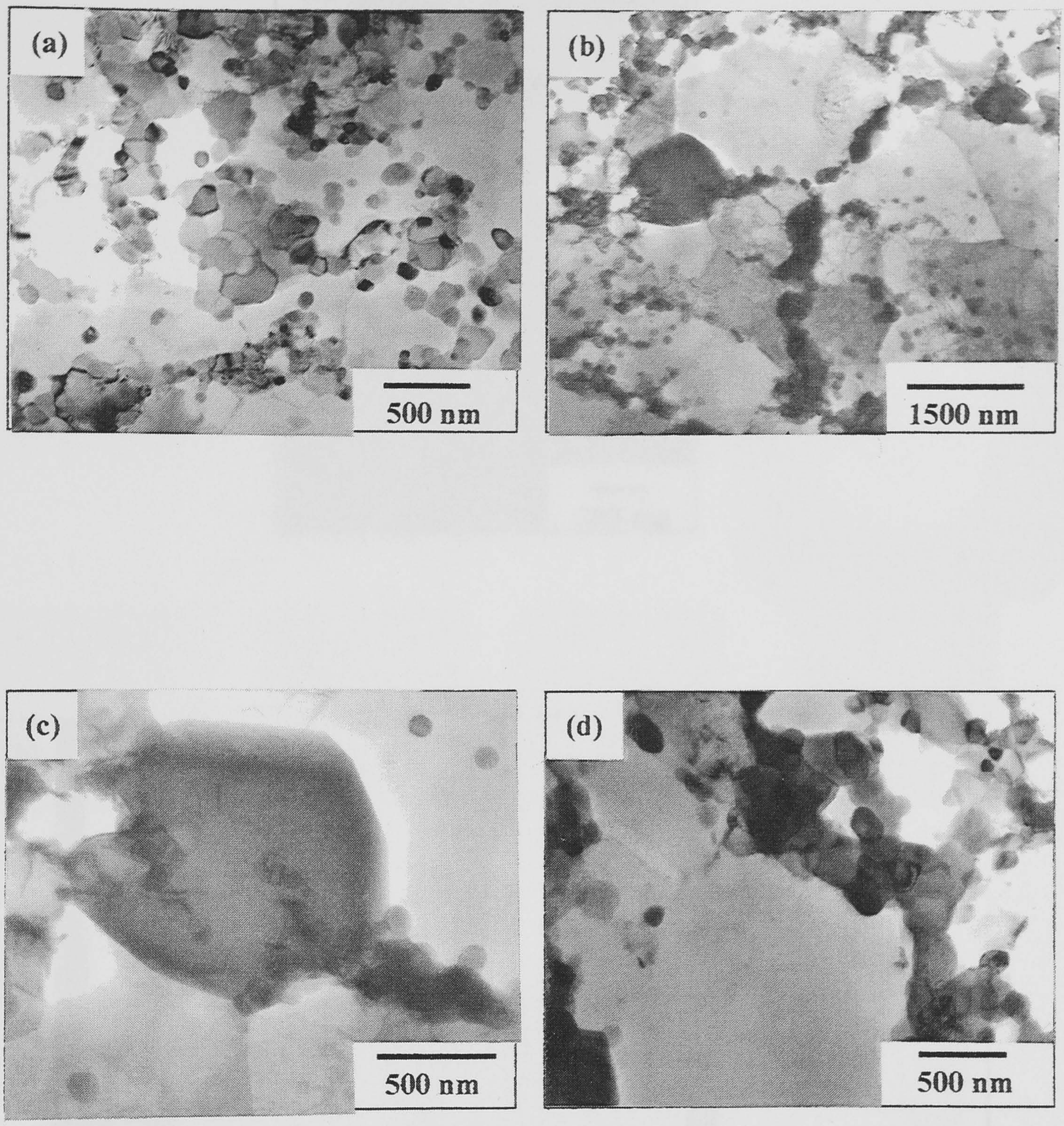


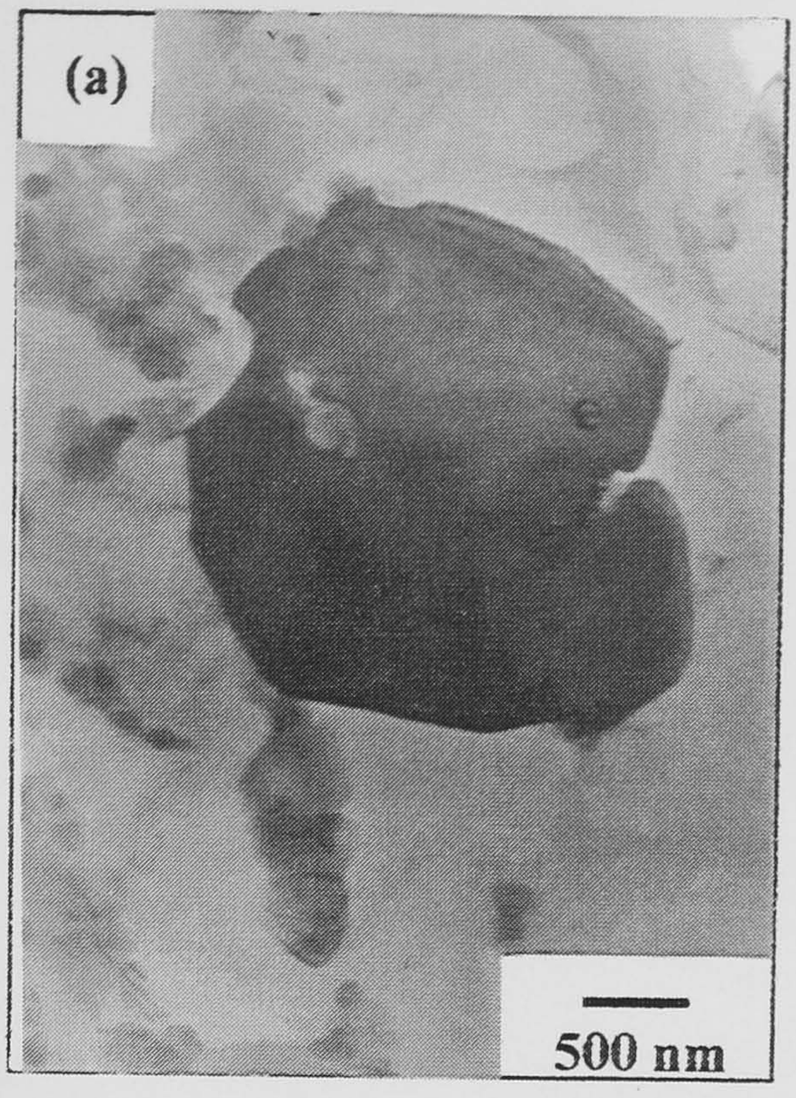
Fig. 5.7.2.1 Microstructures of the heated RS-Al-Fe-V-Si alloy:

(a) agglomeration of the $Al_{13}(Fe, V)_3Si$ particles,

(b) coarsening of the $Al_{13}(Fe, V)_3Si$ particles at grain boundaries,

(c) high magnification of (b) showing the formation of a large $Al_{13}(Fe, V)_3Si$ particle from fine spherical $Al_{13}(Fe, V)_3Si$ particles,

(d) evidence of grain growth.



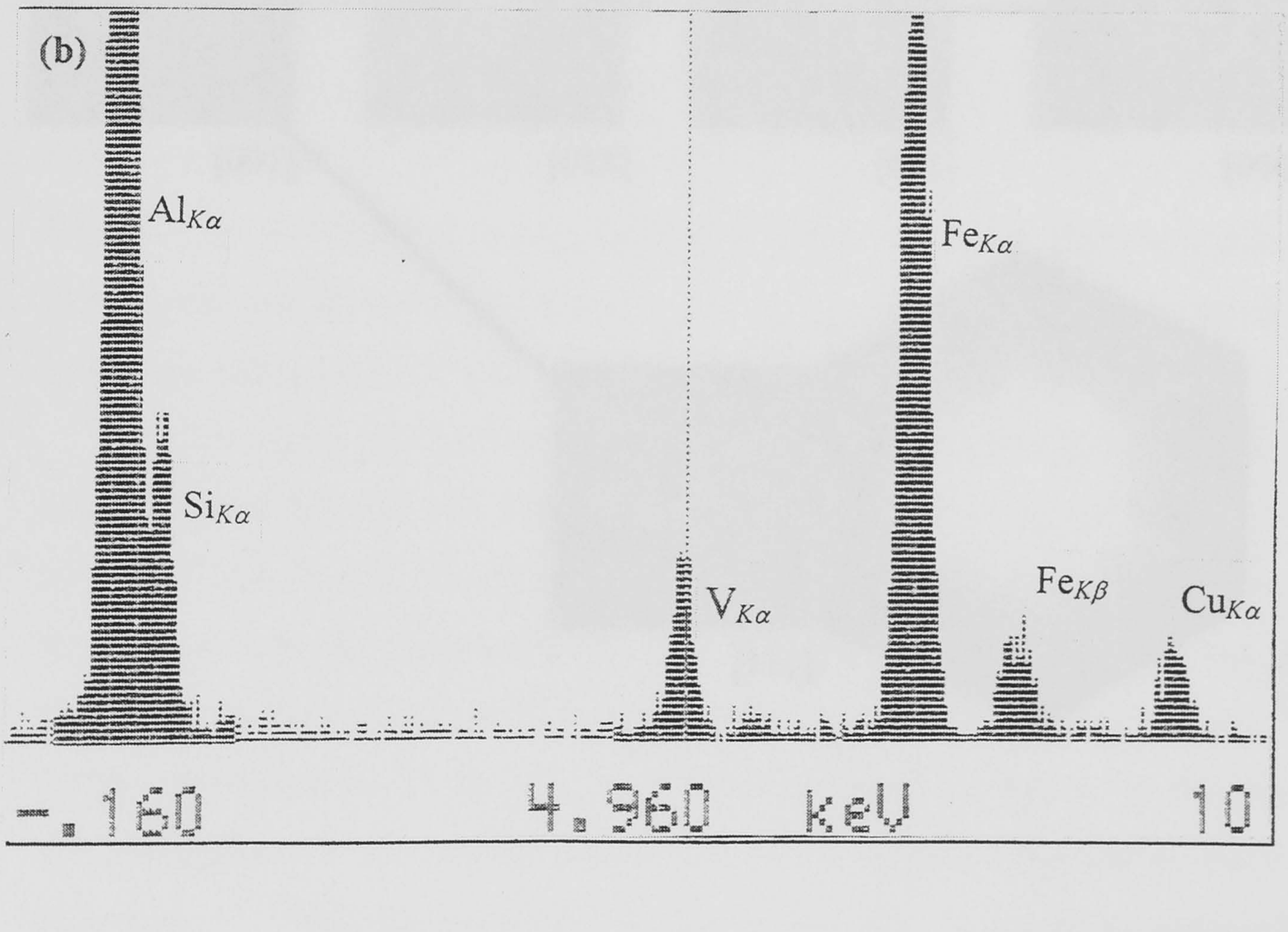


Fig. 5.7.2.2 Identification of the $Al_{13}(Fe, V)_3Si$ particle:
(a) a bright field TEM image, (b) EDS spectrum.

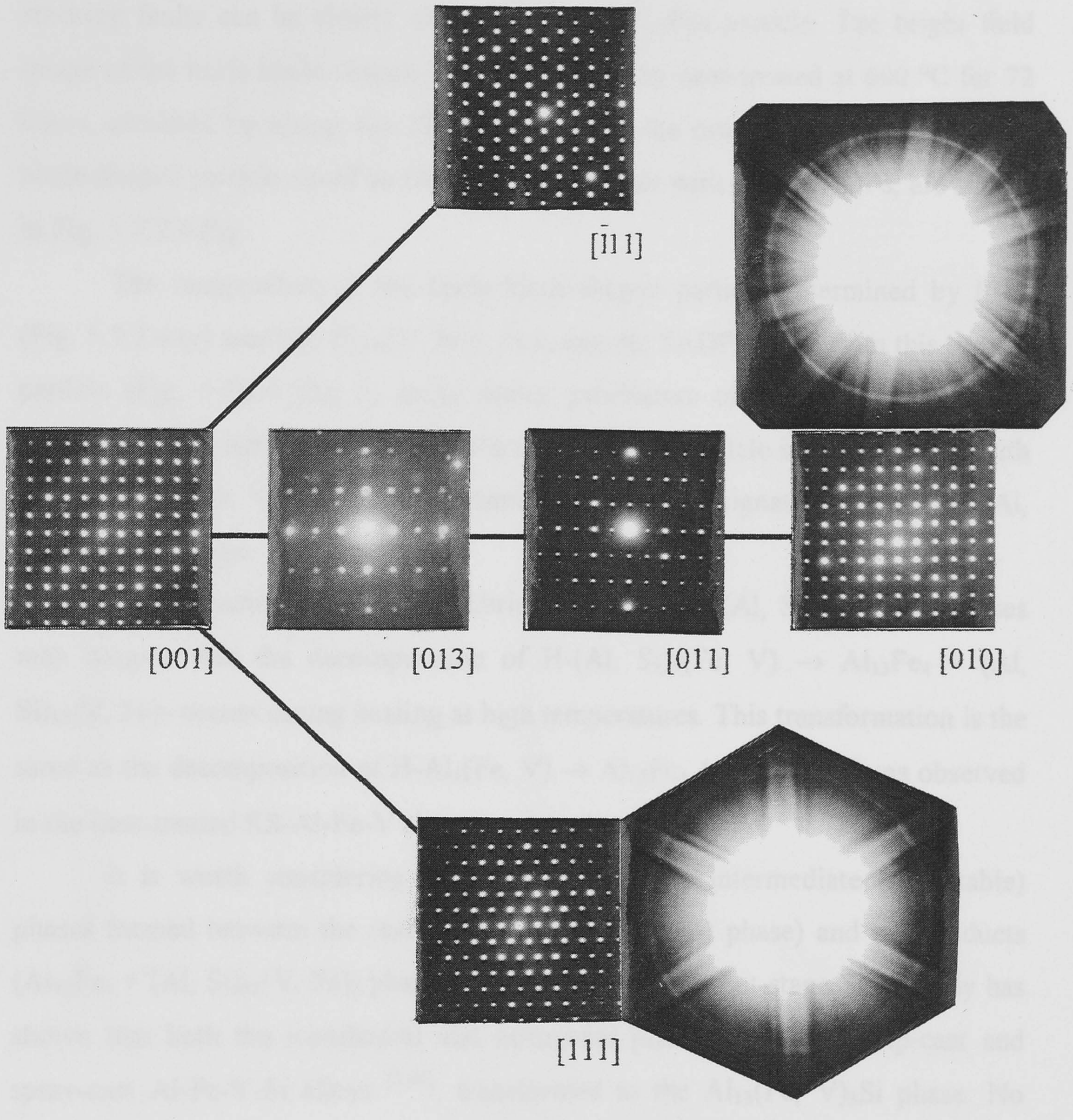


Fig. 5.7.2.3 Electron diffraction patterns of the $Al_{13}(Fe, V)_3Si$ phase.

(2) H-$(Al, Si)_5(Fe, V)$ phase

In microstructures of the RS-Al-Fe-V-Si alloy heat-treated at 500 °C for 48 hours, an $Al_{13}Fe_4$ particle was observed to be adjacent to a spherical $Al_{13}(Fe, V)_3Si$ particle and a knife blade-shaped particle (Fig.5.7.2.4 (a)). Typical micro-twins or stacking faults can be clearly observed in the $Al_{13}Fe_4$ particle. The bright field image of the knife blade-shaped particle in the alloy heat-treated at 600 °C for 72 hours, obtained by tilting the TEM specimen to the orientation where the knife blade-shaped particle could be clearly seen, together with some SADPs, are shown in Fig. 5.7.2.4 (b).

The composition of the knife blade-shaped particle determined by EDS (Fig. 5.7.2.4 (c) was $(Al, Si)_{46}(V, Fe)_7$. Indexing the SADPs taken from this type of particle (Fig. 5.7.2.4 (b)) by using lattice parameters of the $Al_{45}V_7$ phase was successful. This indicates that the knife blade-shaped particle is isomorphous with the $Al_{45}V_7$ phase. The knife blade-shaped particle is designated here as the $(Al, Si)_{45}(V, Fe)_7$ phase.

The coexistence of two equilibrium $Al_{13}Fe_4$ and $(Al, Si)_{45}(V, Fe)_7$ phases may suggest that the decomposition of H-$(Al, Si)_5(Fe, V) \rightarrow Al_{13}Fe_4 + (Al, Si)_{45}(V, Fe)_7$ occurs during heating at high temperatures. This transformation is the same as the decomposition of H-$Al_x(Fe, V) \rightarrow Al_{13}Fe_4 + Al_{45}(V, Fe)_7$ as observed in the heat-treated RS-Al-Fe-V alloy.

It is worth considering here if there are any intermediate (metastable) phases formed between the reactant (H-$(Al, Si)_5(Fe, V)$ phase) and the products ($Al_{13}Fe_4 + (Al, Si)_{45}(V, Fe)_7$ phases). Recently, an *in situ* hot-stage TEM study has shown that both the icosahedral and hexagonal phases, found in strip-cast and spray-cast Al-Fe-V-Si alloys [5.86], transformed to the $Al_{13}(Fe, V)_3Si$ phase. No further transformation of the $Al_{13}(Fe, V)_3Si$ phase was investigated in that study. An investigation of the microstructural stability of rapidly solidified Al-Fe-V-Si alloy ribbon [5.84] has shown that the hexagonal θ-$Al_2(Fe, V, Si)$ phase appeared in the alloy microstructures after heating at 650 °C and band-shaped $(Al, Si)_{13}Fe_4$ dispersoids existed after the alloy was heated at the same temperature for 25 hours.

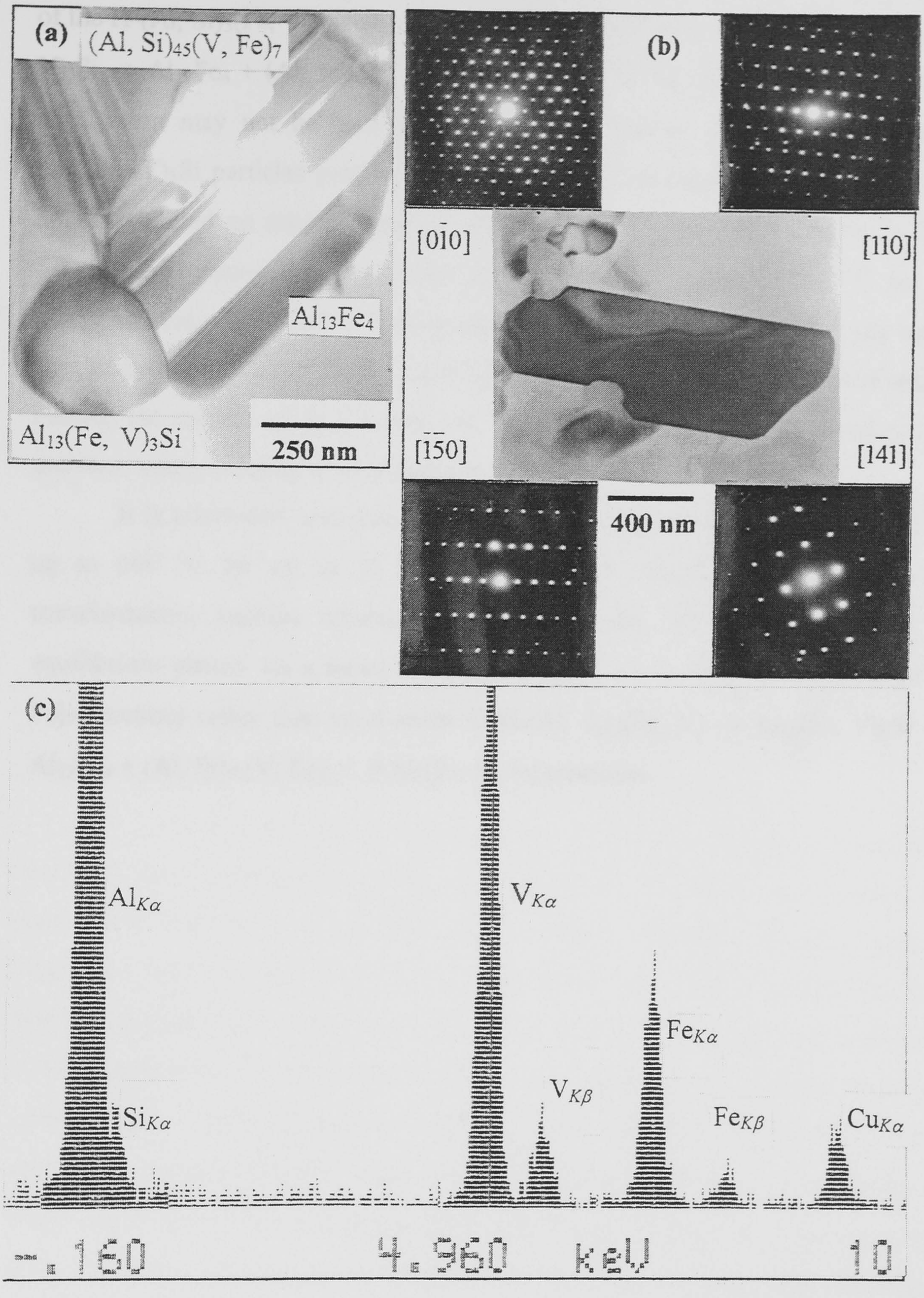


Fig. 5.7.2.4 Identification of the $(Al, Si)_{45}(V, Fe)_7$ phase; (a) bright field TEM image showing the coexistence of $(Al, Si)_{45}(V, Fe)_7$ phase with $Al_{13}Fe_4$ and $Al_{13}(Fe, V)_3Si$ phases, (b) typical morphology of $(Al, Si)_{45}(V, Fe)_7$ phase and SADPs, and (c) EDS spectrum.

From the information given above, one may imply that the decomposition of the H-$(Al, Si)_5(Fe, V)$ phase occurs via a series of H-$(Al, Si)_5(Fe, V) \rightarrow Al_{13}(Fe, V)_3Si \rightarrow Al_{13}Fe_4 + (Al, Si)_{45}(V, Fe)_7 + \theta\text{-}Al_2(Fe, V, Si)$ reactions. However, this implication may not be true for the following reasons. First, large coarsened $Al_{13}(Fe, V)_3Si$ particles present in the alloy after heat-treating at 600 °C for 72 hours exhibited no transformation reaction. Secondly, the stable $Al_{13}Fe_4 + (Al, Si)_{45}(V, Fe)_7$ phases already existed in the alloy after heating at 500 °C for 48 hours, whereas the $Al_{13}(Fe, V)_3Si$ particles in the alloy heat-treated at the same temperature for 72 hours hardly exhibited changes in terms of their size and shape. Finally, the number of $Al_{13}Fe_4$ and $(Al, Si)_{45}(V, Fe)_7$ phases was observed not to increase with increasing temperatures and times.

It is concluded here that when the alloy is heat-treated at temperatures of up to 600 °C for up to 72 hours, the $Al_{13}(Fe, V)_3Si$ particles exhibit no transformation reaction whereas the H-$(Al, Si)_5(Fe, V)$ phase transforms to equilibrium phases via a series of H-$(Al, Si)_5(Fe, V) \rightarrow Al_{13}Fe_4 + (Al, Si)_{45}(V, Fe)_7$ reactions rather than via a series of H-$(Al, Si)_5(Fe, V) \rightarrow Al_{13}(Fe, V)_3Si \rightarrow Al_{13}Fe_4 + (Al, Si)_{45}(V, Fe)_7 + \theta\text{-}Al_2(Fe, V, Si)$ reactions.

CHAPTER 6

CONCLUSIONS

It has been shown that the microstructural development in the as-atomised RS-Al-Fe-(V, Si) powder particles is particle size dependent. With regards to the powder particle size range investigated (0-65 μm), all RS-Al-Fe-(V, Si) powder particles with diameters ≤ 65 μm contain quasi-crystalline phases in the form of MI, GCMI or I phase particles. In fine powder particles, the MI particles are randomly oriented and distributed in the α-Al matrix resulting from planar growth of the solid/liquid interface. This type of microstructure is designated as zone A. In medium to coarse powder particles, the main microstructure morphology, designated as zone B, consists of microcellular α-Al with MI phase in the intercellular regions. In coarse powder particles, the microstructure, designated as zone C, consisting of either GCMI or I phase particles entrapped in coarse cellular/dendritic α-Al, is always observed in addition to zone B.

From knowledge of the powder microstructures mentioned above, the microstructural development in the as-atomised RS-Al-Fe-(V, Si) powders is proposed as follows. In an undercooled melt droplet, nucleation events of quasi-crystalline phases in the form of either MI phase (for most RS-Al-Fe-(V, Si) powder particles) or I phase (only for coarse RS-Al-Fe-V-Si powder particles) occur throughout the droplet. After nucleation, the quasi-crystalline phase particles grow further before interacting with the α-Al solid/liquid interfaces. The nucleation events of the α-Al phase, occurring after those of the quasi-crystalline phase particles, can be found either at the melt droplet surface or within the melt droplet. In fine melt droplets, the planar solid/liquid interface proceeds with high velocity and engulfs MI phase particles. This results in formation of zone A. In medium to coarse melt droplets, the microcellular solid/liquid interface proceeds with relatively low velocity and pushes the MI phase particles laterally. The MI phase particles are then entrapped in the intercellular regions, resulting in formation of zone B. In coarse melt droplets, either MI or I phase particles are allowed to grow resulting in formation of GCMI or globular I phase particles,

respectively. The coarse cellular/dendritic solid/liquid interface proceeding with a low velocity pushes the GCMI or globular I phase particles ahead of the interface prior to eventual particle entrapment. This results in formation of zone C.

The microstructures of the as-extruded alloys are related to the original powder microstructures. The microstructural inhomogeneity of the as-extruded alloy microstructures, observed as banded structures, is a replica of the microstructural inhomogeneity of the powder microstructures. The banded structure consists of two different areas. The first contains fine intermetallic particles distributed homogeneously in the matrix, designated as either band I or band I′ for RS-Al-Fe-V or RS-Al-Fe-V-Si alloys, respectively. The second contains fine and coarse intermetallic particles distributed unevenly in the matrix, designated as either band II or band II′ for RS-Al-Fe-V or RS-Al-Fe-V-Si alloys, respectively. Band I (or I′) results from the original zone A and zone B powder microstructures, whereas band II (or II′) results from zone C microstructures.

Intermetallic phases present in the as-extruded alloy microstructure are the products of phase transformation reactions occurring during consolidation. These reactions cannot be observed directly during consolidation, but can be deduced from thermal analysis study of the as-atomised powders. Phase transformation reaction series occurring during DSC scans of the as-atomised powders can be represented by the equations given below.

(1) RS-Al-Fe-V alloy

-Super-saturated solid solution $\rightarrow Al_6Fe$ (360 °C) $\rightarrow Al_{13}Fe_4$ (500 °C)

-Intercellular $Al_6Fe \rightarrow Al_{13}Fe_4$ (500 °C)

-MI $\rightarrow Al_{13}Fe_4 + Al_{45}(V, Fe)_7$ (500°C)

-GCMI-$Al_x(Fe, V) \rightarrow$ I-$Al_x(Fe, V)$ (450 °C)

(2) RS-Al-Fe-V-Si alloy

-Super-saturated solid solution + MI + GCMI-$(Al, Si)_x(Fe, V)$ + I-$(Al, Si)_x(Fe, V)$

$\rightarrow Al_{13}(Fe, V)_3Si$ (400 °C)

The mechanical properties such as 0.2 % CS and fracture toughness of both RS-Al-Fe-V and RS-Fe-V-Si alloys are excellent. The room temperature 0.2 % CS exceeds 300 MPa for RS-Al-Fe-V alloys and 400 MPa for RS-Al-Fe-V-Si alloys. The 250 °C 0.2 % CS exceeds 200 MPa for RS-Al-Fe-V alloys and 250 MPa for RS-Al-Fe-V-Si alloys. The fracture toughness measured for both RS-Al-Fe-V and RS-Fe-V-Si alloys is found to exceed 17 $MN/m^{3/2}$. The 0.2 % CS of the as-extruded alloys is inversely proportional to the particle size (D[v,0.5]) of the powder size fraction extruded. This is due to the as-extruded alloy microstructure being inherited from the original powder microstructure.

Metastable phases present in the as-extruded alloys, such as I-Al_x(Fe, V), H-Al_x(Fe, V), unknown Al-Fe-V, and H-(Al, Si)$_5$(Fe, V) phases, transform to stable phases during heat-treatment. Other stable phases such as $Al_{13}Fe_4$, Al_{45}(V, Fe)$_7$, and Al_{13}(Fe, V)$_3$Si coarsen during heat-treatment at high temperature. Phase transformation reactions can be represented by the equations given below.

(1) RS-Al-Fe-V Alloy

-I-Al_x(Fe, V) → H-Al_x(Fe, V) (550 °C/30 min.) → $Al_{13}Fe_4$ +Al_{45}(V, Fe)$_7$ (550 °C/2 hrs.)

-Unknown Al-Fe-V phase → $Al_{13}Fe_4$ +Al_{45}(V, Fe)$_7$ (500 °C/2 hrs.)

(2) RS-Al-Fe-V-Si Alloy

-H-(Al, Si)$_5$(Fe, V) → $Al_{13}Fe_4$ + (Al, Si)$_{45}$(V, Fe)$_7$ (500 °C/48 hrs.)

CHAPTER 7

SUGGESTIONS FOR FURTHER WORK

The microstructural development during processing of rapidly solidified Al-Fe-(V, Si) alloys has been studied in this thesis. However, the explanation for the microstructural development has been given in a qualitative way. Quantitative process/structure/property relationship facilitates alloy/process optimisation. For microstructural development in the as-stomised powder, some important parameters controlling solidification and formation of phases, such as undercooling and solidification velocity, are not known yet. It is perhaps impossible to accurately evaluate these parameters from the powder microstructure.

One possible way to determine these parameters is to compare the powder microstructure with the microstructure of the same alloy produced by techniques that facilitate measurement of undercooling and solidification velocity. Since a laser surface melting technique facilitates measurement of solidification velocity at high values, this technique may be employed for establishing a relationship between microstructure and solidification velocity for the RS-Al-Fe-(V, Si) alloys. By comparison of the RS-Al-Fe-(V, Si) powder microstructure with that of the laser surface melted Al-Fe-(V, Si) alloy processed under known solidification velocities, the velocity corresponding to the powder microstructure may be determined.

The value of undercooling, at which a particular phase can be formed, may be determined using techniques such as emulsification and fluxing of liquid metal droplets. These techniques facilitate accurate measurement of the degree of undercooling. Microstructural observation and phase identification of the alloy produced with known values of undercooling should give information about the value of undercooling at which a particular phase can be formed.

Since both RS-Al-Fe-V and RS-Al-Fe-V-Si alloys exhibit excellent strength and toughness, more mechanical and chemical tests such as creep rupture, fatigue, and corrosion resistance, need to be performed. In addition, as both alloys show potential for elevated temperature applications and in order to find suitable

processing techniques for these alloys, other metal forming processes such as plate rolling and tube extrusion need to be investigated.

Although several phase transformation reactions have been known, the mechanism and kinetics of the reactions have not yet investigated. An *in situ* hot-stage TEM study may provide useful information about the reactions.

Since several novel phases, such as GCMI, icosahedral, H-Al_x(Fe, V) and H-$(Al, Si)_5$(Fe, V), have been found in the RS-Al-Fe(V, Si) alloy and the crystal structure of these phases are not yet known, investigation of their structures would be worthwhile.

REFERENCES

(1) References to Chapter 1

1.1 Perepezko, J. H., *Mater. Sci. Eng.*, **65**, 125 (1984).

1.2 Kui, H.-W., Greer, A. L., and Turnbull, D. *Appl. Phys. Lett.*, **45**, 615 (1984).

1.3 Herlach, D. M., *Ann. Rev. Mater. Sci.*, **21**, 23 (1991).

1.4 Herlach, D. M., Cochrane, R. F., Egry, I., Fecht, H. J., and Greer, A. L. *Int. Mater. Rev.*, **38** (6), 273 (1993).

1.5 Savage, S. J., and Froes, F. H. *J. Metals.*, **36** (4), 20 (1984).

1.6 Kim, Y-W., Griffith, W. M., Froes, F. H. *J. Metals.*, **37** (8), 27 (1985).

1.7 Gummeson, P. U. *Powder Met.*, **15** (29), 67 (1972).

1.8 Lawley, A. (a) *Int. J. Powder Met. & Powder Tech.*, **13** (3), 169 (1977). (b) *Ann. Rev. Mater. Sci.*, **8**, 49 (1978).

1.9 Klar, E., and Fesko, J. W.: in Metals Handbook (9th ed.). American Society for Metals, Metals Park, Ohio, 25 (1984).

1.10 Dunkley, J. J. (a) *Powder Met.*, **29** (1), 10 (1986). (b) *Met. Mater.*, **6** (6), 361 (1990).

1.11 Davies, H. A. *Powder Met.*, **33** (3), 223 (1990).

1.12 Ward-Close, C. M., and Froes, F. H. *J. Metals.*, **46** (1), 28 (1994).

1.13 Waldman, J.: in Rapidly solidified powder aluminum alloys. (Fine, M. E., and Starke, Jr., A. E., eds.), ASTM-STP 890, Philadelphia, PA, 39 (1986).

1.14 Froes, F. H. *Mater. Sci. Eng.*, **A184**, 119 (1994).

1.15 Quist, W. E., and Lewis, R. E.: in Rapidly solidified powder aluminum alloys. (Fine, M. E., and Starke, Jr., A. E., eds.), ASTM-STP 890, Philadelphia, PA, 7 (1986).

1.16 Das, S. K., and Davis, L. A. *Mater. Sci. Eng.*, **98**, 1 (1988).

1.17 Froes, F. H., and Pickens, J. R. *J. Metals.*, **36** (1), 14 (1984).

1.18 Suryarayana, C., Froes, F. H., Krishnamurthy, S., and Kim, Y-W. *Int. J. Powder Met.*, **26** (2), 117 (1990).

(2) References to Chapter 2

2.1 Kurz, W., Trivedi, R. *Mater. Sci. Eng.*, **A179/A180**, 46 (1994).

2.2 Boettinger, W. J., and Coriell, S. R.: in Science and technology of the undercooled melt; rapid solidification materials and technologies. (Sahm, P. R., Jones, H., and Adam, C. M., eds.), Martinus Nijhoff Publishers, Dordrecht, pp. 81 (1986).

2.3 Turnbull, D., and Cech, R. E. *J. Appl. Phys.*, **21**, 805 (1950)

2.4 Cohen, M., Kear, B. H., and Mehrabian, R.: in Proceedings of the 2nd international conference on rapid solidification processing: principles and technologies II. (Cohen, M., Kear, B. H., and Mehrabian, R., eds.). Claitors Publishing Division, Baton Rouge, pp. 1 (1980).

2.5 Verhoeven, J. D. Fundamentals of physical metallurgy. John Wiley & Sons, Toronto, (1975).

2.6 Perepezko, J. H. *Mater. Sci. Eng.*, **65**, 125 (1984)

2.7 Perepezko, J. H.: in Science and technology of the undercooled melt; rapid solidification materials and technologies. (Sahm, P. R., Jones, H., and Adam, C. M., eds.), Martinus Nijhoff Publishers, Dordrecht, pp. 29 (1986).

2.8 Feuerbacher, B. *Mater. Sci. Rep.*, *4*, 1 (1989).

2.9 Battezzati, L., Antonione, C., Baricco, M., and Riontino, G.: in Proceedings of the 2nd European conference on advanced materials and processes (Clyne, T. W., and Withers, P. J., eds.), Vol. 1, The Institute of Materials, London, pp. 43, (1992).

2.10 Hirth, J. P. *Metall. Trans. A.*, **9A**, 401, (1978).

2.11 Mueller, B. A., and Perepezko, J. H. *Metall. Trans. A.*, **18A**, 1143, (1987).

2.12 Trivedi, R., and Kurz, W. *Acta Metall. Mater.*, **42** (1), 15 (1994).

2.13 Langer, J. S., and Muller-Krumbhaar, H. *J. Cryst. Growth.*, **42**, 11 (1977).

2.14 Trivedi, R. *J. Cryst. Growth.*, **48**, 93 (1980).

2.15 Kurz, W., and Fisher, D. J. *Acta Metall.*, **29**, 11 (1981).

2.16 Lipton, J., Glicksman, M. E., and Kurz, W. *Mater. Sci. Eng.*, **65**, 57 (1984).

2.17 Trivedi, R. *J. Cryst. Growth.*, **73**, 289 (1985).

2.18 Kurz, W., and Trivedi, R. *Acta Metall. Mater.*, **38** (1), 1 (1990).

2.19 Trivedi, R., Lipton, J., and Kurz, W. *Acta Metall.*, **35** (4), 965 (1987).

2.20 Lipton, J., Glicksman, M. E., and Kurz, W. *Metall. Trans. A.*, **18A**, 341, (1987).

2.21 Wu, Y., Piccone, T. J., Shiohara, Y., and Flemings, M. C. *ibid.* 915.

2.22 Herlach, D. M. *Mater. Sci. Eng.*, **R12** (4-5), 177 (1994).

2.23 Trivedi, R., and Kurz, W. *Int. Mater. Rev.*, **39**(2), 49 (1994).

2.24 Baker, J. C., and Cahn, J. W. in Solidification, ASM, Metals Park, OH, 23 (1971).

2.25 Aziz, M. J. *J. Appl. Phys.*, **53**, 1158 (1982).

2.26 Aziz, M. J., and Kaplan, T. *Acta Metall.*, **36**, 2335 (1988).

2.27 Trivedi, R. *Mater. Sci. Eng.*, **A178**, 129 (1994).

2.28 Suzuki, M., Piccone, T. J., Flemings, M. C., and Brody, H. D. *Metall. Trans. A.*, **22A**, 2761 (1991).

2.29 Eckler, K., Cochrane, R. F., Herlach, D. M., and Feuerbacher, B. *Mater. Sci. Eng.*, **A133**, 702 (1991).

2.30 Barth, M., Eckler, K., Herlach, D. M., and Alexander, H. *ibid.*, 790.

2.31 Loser, W., and Herlach, D. M. *Metall. Trans. A.*, **23A**, 1585 (1992).

2.32 Wei, B., Herlach, D. M., Sommer, F., and Kurz, W. *Mater. Sci. Eng.*, **A181/A182**, 1150 (1994).

2.33 Herlach, D. M. *Mater. Sci. Eng.*, **A179/A180**, 147 (1994).

2.34 DiVenuti, A. G., and Ando, T. *Metall. Mater. Trans. A.*, **29A**, 3047 (1998).

2.35 Eshelman, M. A., Seetharaman, V., and Trivedi, R. *Acta Metall.*, **36** (4), 1165 (1988).

2.36 Mao, X., Li, J., and Fu, H. *Mater. Sci. Eng.*, **A183**, 233 (1994).

2.37 Trivedi, R., Sekhar, J. A., and Seetharaman, V. *Metall. Trans. A.*, **20A**, 769 (1989).

2.38 Ludwig, A., and Kurz, W. *Acta Mater.*, **44** (9), 3643 (1996).

2.39 Hunt, J. D., *Acta Metall. Mater.*, **38** (3), 411 (1990).

2.40 *Idem. Acta Metall. Mater.*, **39** (9), 2117 (1991).

2.41 Lu, Shu-Zu., and Hunt, J. D. *J. Cryst. Growth.*, **123**, 17 (1992).

2.42 Lu, Shu-Zu., Hunt, J. D., Gilgien, P., and Kurz, W. *Acta Metall. Mater.*, **42** (5), 1653 (1994).

2.43 Boettinger, W. J., Shechtman, D., Schaefer, R. J., Biancaniello, F. S. *Metall. Trans. A.*, **15A**, 55 (1984).

2.44 Carrard, M., Gremaud, M., Zimmermann, M., and Kurz, W. *Acta Metall. Mater.*, **40** (5), 983 (1992).

2.45 Kurz, W., and Trivedi, R. *Metall. Mater. Trans. A.*, **27A**, 625 (1996).

2.46 Mullins, W. W., and Sekerka, R. F. *J. Appl. Phys.*, **35**, 444 (1964).

2.47 Trivedi, R., and Kurz, W. *Acta Metall.*, **34** (8), 1663 (1986).

2.48 Jackson, K. A., and Hunt, J. D. *Trans. Met. Soc. AIME.*, 236, 1129 (1966).

2.49 Trivedi, R., Magnin, P., and Kurz, W. *Acta Metall.*, **35** (4), 971 (1987).

2.50 Kurz, W., and Trivedi, R. *Metall. Trans. A.*, **22A**., 3051 (1991).

2.51 Zryd, A., Gremaud, M., and Kurz, W. *Mater. Sci. Eng.*, **A181/A182**, 1392 (1994).

2.52 Juarez-Islas, J. A., and Jones, H. *Acta Metall.*, **35** (2), 499 (1987).

2.53 Zimmermann, Z., Carrard, M., and Kurz, W. *Acta Metall.*, **37** (12), 3305 (1989).

2.54 Gill, S. C., Zimmermann, M., and Kurz, W. *Acta Metall. Mater.*, **40** (11), 2895 (1992).

2.55 Gill, S. C., and Kurz, W.: (a) *Acta Metall. Mater.*, **41** (12), 3563 (1993).
(b) *Acta Metall. Mater.*, **43** (1), 139 (1995).

2.56 Pierantoni, M., Gremaud, M., Magnin, P., Stoll, D., and Kurz, W. *Acta Metall. Mater.*, **40** (7), 1637 (1992).

2.57 Wei, B., Herlach, D. M., and Sommer, F. *J. Mater. Sci. Lett.*, **12**, 1774 (1993).

2.58 Jones, H. *Phil. Mag. B.*, **61** (4), 487 (1990).

2.59 Aziz, M. J. *J. Appl. Phys.*, **53**, 1158 (1982).

2.60 Jones, H. Rapid solidification of metals and alloys., The Institute of Metallurgist, London, (1982).

2.61 Martin, J., Doherty, R. D., and Cantor, B. Stability of microstructure in metallic systems., Cambridge University Press., Cambridge, Chapter 3 (1997).

2.62 Anantharaman, T. R.: in Metallic glasses; production, properties and applications. (Anantharaman, T. R., ed.), Trans Tech Publications, Netherlands, pp. 1 (1984).

2.63 Shiflet, G. J., He, Y., Poon, S. J., Dougherty, G. M., and Chen, H.: in Science and technology of rapid solidification and processing. (Otooni, M. A., ed.) Kluwer Academic Publishers, Netherlands, pp. 53 (1995).

2.64 Inoue, A., Ohtera, K., Tsai, A. P., and Matsumoto, T. *Jpn. J. Appl. Phys.*, **27** (4), L479 (1988).

2.65 Inoue, A., Ohtera, K., Tao, Z., and Matsumoto, T. *ibid.*, L1583.

2.66 Inoue, A., Ohtera, K., Kita, K., and Matsumoto, T. *ibid.*, L1796.

2.67 Tsai, A-P., Inoue, A., and Masumoto, T. *J. Mater. Sci. Lett.*, 7, 805 (1988).

2.68 Inoue, A., Kita, K., Ohtera, K., Kimura, H., and Masumoto, T. *ibid.*, 1287.

2.69 Inoue, A., Zhang, T., and Masumoto, T. *Mater. Trans. JIM.*, **30** (12), 965 (1989)

2.70 Inoue, A., Horio, Y., Kim, Y. H., and Masumoto, T. *Mater. Trans. JIM.*, **33** (7), 669 (1992).

2.71 Higashi, K., Uoya, A., Mukai, T., Tanimura, S., Inoue, A., Masumoto, T., and Ohtera, K. *Mater. Sci. Eng.*, **A181/A182**, 1068 (1994).

2.72 Kim, Y. H., Choi, G. S., Kim, I. G., and Inoue, A. *Mater. Trans. JIM.*, **37** (9), 1471 (1996).

2.73 Shechtman, D., Blech, I., Gratias, D., and Cahn, J. W. *Phys. Rev. Lett.*, **53** (20), 1951 (1984).

2.74 Suryanarayana, C., and Jones, H. *Int. J. Rapid Solidn.*, **3**, 253 (1987).

2.75 Goldman, A. I., and Widom, M., *Annu. Rev. Phys. Chem.*, **42**, 685 (1991).

2.76 Kelton, K. F. *Int. Mater. Rev.*, **38** (3), 105 (1993).

2.77 Kelton, K. F.: in Intermetallic compounds: principles and practice (Vol. 1). (Westbrook, J. H., and Fleischer, R. L., eds.), John Wiley & Sons, Chichester, pp. 453 (1995).

2.78 Steurer, W.: in Physical metallurgy (vol. 1)., (Cahn, R. W., and Haasen, P., eds.), Elsevier Scince B. V., Amsterdam, Appendix to Chapter 4 (1996).

2.79 Bendersky, L. *Phys. Rev. Lett.*, **55** (14), 1461 (1985).

2.80 Fung, K. K., Yang, C. Y., Zhou, Y. Q., Zhao, J. G., Zhan, W. S., and Shen, B. G., *Phys. Rev. Lett.*, **56** (19), 2060 (1986).

2.81 Wang, N., and Kuo, K. H. *Mater. Sci. Forum.*, **22-24**, 141 (1987).

2.82 Wang, N., Chen, H., and Kuo, K. H. *Phys. Rev. Lett.*, **59** (9), 1010 (1987).

2.83 Cao, W., Ye, H. Q., and Kuo, K. H. *Phys. Stat. Sol. A.*, **107**, 511 (1988).

2.84 Wang, N., Fung, K. K., and Kuo, K. H. *Appl. Phys. Lett.*, **52** (25), 2120 (1988).

2.85 Mai, Z. H., Xu, L., Wang, N., Kuo, K. H., Jin, Z. C., and Cheng, G. *Phys. Rev. B.*, **40** (18), 12183 (1989).

2.86 Wang, N., and Kuo, K. H. *Phil. Mag. Lett.*, **61** (2), 63 (1990).

2.87 Ishimasa, T., Nissen, H. –U., and Fukano, Y. *Phys. Rev. Lett.*, **55** (5), 511 (1985).

2.88 Chen, H., Li, D. X., and Kuo, K. H. *Phys. Rev. Lett.*, **60** (16), 1645 (1988).

2.89 Kuo, K. H., Feng, Y. C., and Chen, H. *Phys. Rev. Lett.*, **61** (15), 1740 (1988).

2.90 Aragon, J. L., Reyes-Gasga, J., Jose-Yacaman, M., Torres, M., and Pastor, G. *Phil. Mag. Lett.*, **62** (5), 337 (1990).

2.91 He, L. X., Li, X. Z., Zhang, Z., and Kuo, K. H. *Phys. Rev. Lett.*, **61** (9), 1116 (1988).

2.92 Tsai, A. P., Sato, A., Yamamoto, A., Inoue, A., and Masumoto, T. *Jpn. J Appl. Phys.*, **31**, L970 (1992).

2.93 Tsai, A. P., Matsumoto, T., and Yamamoto, A. *Phil. Mag. Lett.*, **66** (4), 203 (1992).

2.94 Li, X. Z., and Kuo, K. H. *J. Mater. Res.*, **8** (10), 2499 (1993).

2.95 Tsai, A. P., Inoue, A., and Masumoto, T. *Bull. Jpn. Inst. Met.*, **28**, 707 (1989).

2.96 Inoue, A., and Tsai, A. P. *Bull. Jpn. Inst. Met.*, **29**, 782 (1990).

2.97 Tsai, A. P. *MRS Bulletin*, **X**, 43 (1997).

2.98 Chen, H. S., Chen, C. H., Inoue, A., and Krause, J. T. *Phys. Rev. B.*, **32** (4), 1940 (1985).

2.99 Inoue, A., Tsai A. P., Kimura, H. M., and Masumoto, T. *J. Mater. Sci.*, **23**, 429 (1988).

2.100 Goldman, A. I., and Kelton, R. F. *Rev. Modern Phys.*, **65** (1), 213 (1993).

2.101 Suryanarayana, C. *Int. Mater. Rev.*, **40** (2), 41 (1995).

2.102 Boettinger, W. J., Bendersky, L., and Early, J. G. *Metall. Trans. A.*, **17A**, 781 (1986).

2.103 Levi, C. G., and Mehrabian, R. *Metall. Trans. A.*, **13A**, 221 (1982).

2.104 Levi, C. G., and Mehrabian, R. *Metall. Trans. A.*, **13A**, 13 (1982).

2.105 Marshall, G. J.: in Aluminum technology '86 (Sheppard, T., ed.), The Institute of Metals, London, pp. 679 (1986).

2.106 Premkumar, M. K., Lawley, A., and Koczak, M. J. *Metall. Trans. A.*, **23A**, 3219 (1992).

2.107 Jones, H. *Mater. Sci. Eng.*, **5**, 1 (1969/70).

2.108 Boettinger, W. J. *Mater. Sci. Eng.*, **98**, 123 (1988).

2.109 Zaidai, M. A. (a) *Mater. Sci. Eng.*, **98**, 221 (1988).
(b) in Aluminum technology '86 (Sheppard, T., ed.), The Institute of Metals, London, pp. 839 (1986).

2.110 Marshall, G. J., and Sheppard, T. *Met. Sci.*, **18**, 561 (1984).

2.111 Anantharaman, T. R., and Suryanarayana, C. *J. Mater. Sci.*, **6**, 1111 (1971).

2.112 Grant, N. J. *J. Metals.*, **35**, 20 (1983).

2.113 Sheppard, T., and Zaidai, M. A. *Int. J. Rapid Solidn.*, **2**, 199 (1986).

2.114 Ioannidis, E. K., and Sheppard, T. *Mater. Sci. Tech.*, **6**, 528 (1990).

2.115 Miyazawa, Y., and Pound, G. M. *J. Cryst. Growth.*, **23**, 45 (1974).

2.116 Hollomon, J. H., and Turnbull, D. *Progr. Met. Phys.*, **4**, 333 (1953).

2.117 Saunders, N. and Tsakiropoulos, P. *Mater. Sci. Tech.*, **4**, 157 (1988).

2.118 Chowdhury, A. J. S., and Sheppard, T. *Mater. Sci. Tech.*, **6**, 535 (1990).

2.119 Ioannidis, E. K., Marshall, G. J., and Sheppard, T. *J. Mater. Sci.*, **23**, 1486 (1988).

2.120 Dashwood, R. J., and Sheppard, T. *Mater. Sci. Tech.*, **9**, 483, (1993).

2.121 Liu, P., Dunlop, G. L., and Arnberg, L. *Mater. Sci. Eng.*, **98**, 437, (1988).

2.122 Parkinson, R. D., and Sheppard, T. *Powder Met.*, **29**(2), 135 (1986).

2.123 Zaidai, M. A., and Sheppard, T.: in High strength powder metallurgy aluminium alloys. (Hildeman, G. J., and Kozack, M. J., eds.), The Met. Soc. AIME., Pennsylvania, pp. 367 (1986).

2.124 Bendersky, L. A., Biancaniello, F. S., Ridder, S. D., and Shapiro, A. J. *Mater. Sci. Eng.*, **A134**, 1098 (1991).

2.125 Köster, U., and Schünemann, U.: in Rapidly solidified alloys: processes, structures, properties, applications. (Liebermann, H. H., ed.), Marcel Dekker, New York, pp. 303 (1993).

2.126 Lilienfeld, D. A., Nastasi, M., Johnson, H. H., Ast, D. G., and Mayer, J. W. *Phys. Rev. Lett.*, **55** (15), 1587 (1985).

2.127 Inoue, A., Bizen, Y., and Masumoto, T. *Metall. Trans. A.*, **19A**, 383 (1988).

2.128 Tsai, A. P., Inoue, A., Bizen, Y., and Masumoto, T. *Acta Metall.*, **37** (5), 1443 (1989).

2.129 Tsai, A. P., Inoue, A., and Masumoto, T. *Jpn. J. Appl. Phys.*, **26** (12), L1994 (1987).

2.130 Poon, S. J., Drehman, A. J., and Lawless, K. R. *Phys. Rev. Lett.*, **55** (21), 2324 (1987).

2.131 Drehman, A. J., Pelton, A. R., and Noack, M. A. *J. Mater. Res.*, **1** (6), 741 (1986)

2.132 Shen, Y., Poon, S. J., Shiflet, G. J. *Phys. Rev. B.*, **34** (5), 3516 (1986).

2.133 Chattopadhyay, K., and Mukhopadhyay, N. K. *Mater. Sci. Forum.*, **22-24**, 639 (1987).

2.134 Köster, U., and Schuhmacher, B. *Mater. Sci. Eng.*, **99**, 417 (1988).

2.135 Abis, S., Mengucci, P., and Riontino, G. *Mater. Sci. Eng.*,

A134, 1175 (1991).

2.136 Blank, E. *Z. Metallkunde.*, **63**, 315 (1972).

2.137 Furrer, P., and Warlimont, H. *Z. Metallkunde.*, **64**, 236 (1973).

2.138 Adam, C. M.: in Rapidly solidified amorphous and crystalline alloys. (Kear, B. H., Giessen, B. C., and Cohen, M., eds.), Elsevier Science Publishing, New York, pp. 411 (1982).

2.139 Polmear, I. J., Couper, M. J., and Bannister, M. J. *Mater. Forum.*, **12**, 54 (1988).

2.140 Ryum, N. *J. Mater. Sci.*, **10**, 2075 (1975).

2.141 Shechtman, D., Schaefer, R. J., and Biancaniello, F. S. *Metall. Trans. A.*, **15A**, 1987 (1984).

2.142 Chang, C. P., and Loretto, M. H. *Scripta Metall.*, **21**, 113 (1987).

2.143 *Idem. Acta Metall.*, **36** (4), 805 (1988).

2.144 *Idem. Phil. Mag. A.*, **57** (4), 593 (1988).

2.145 Sastry, G. V. S., and Suryanarayana, C. *Mater. Sci. Eng.*, **47**, 193 (1981).

2.146 Bi, Y. J., and Loretto, M. H. *Int. J. Rapid Solidn.*, **5**, 163 (1990).

2.147 Jacob, M. H., Doggett, A. G., and Stowell, M. J. *Fizika 2 Suppl.*, **2**, 18.1 (1970).

2.148 Ioannidis, E. K., and Sheppard, T. *J. Mater. Sci.*, **25**, 3965 (1990).

2.149 Ramakrishnan, K. N., McShane, H. B., Sheppard, T., and Ioannidis, E. K. *Mater. Sci. Tech.*, **8**, 709 (1992).

2.150 Lifshitz, I. M., and Slyozov, V. V. *J. Phys. Chem. Solids.*, **19** (1/2), 35 (1961).

2.151 Wagner, C. *Z. Electrochem.*, **65** (7/8), 581 (1961).

2.152 Boyd, J. D., and Nicholson, R. B. *Acta Metall.*, **19**, 1379 (1971).

2.153 Sheppard, T., McShane, H. B., Zaidai, M. A., Tan, G. H. *J. Mech. Work. Tech.*, **8**, 43 (1983).

2.154 Marshall, G. J., Ioannidis, E. K., and Sheppard, T. *Powder Met.*, **29** (1), 57 (1986).

2.155 Sheppard, T. *Int. J. Powder Tech.*, **3**, 254 (1974).

2.156 Chare, P.J. M., and Sheppard, T. *Int. J. Powder Met.& Powder Tech.*, **10**(3), 203 (1974).

2.157 Tan, G. H. Ph.D. Thesis, University of London, 1984.

2.158 Sheppard, T., and Castle, A. F. *Met. Tech.*, **4**(10), 454 (1976).

2.159 Castle, A. F., and Sheppard, T. *Met. Tech.*, **4**(10), 465 (1976).

2.160 Sheppard, T., and Chare, P. J. M. *Powder Met.*, **18**, 1 (1975).

2.161 McShane, H., Tutcher, M. G., and Sheppard, T. *Powder Met.*, **21**(2), 47 (1978).

2.162 McShane, H. B. Ph.D. Thesis, University of London, 1978.

2.163 Sheppard, T. *Met. Tech.*, **8** (4), 130 (1981).

2.164 Honeycombe, R. W. K. The plastic deformation of metals, Arnold, Surrey, chapter 11, (1977).

2.165 Jackson, A. Ph.D. Thesis, University of London, 1992.

2.166 Humphreys, F. J., and Hatherly, M. Recrystallization and related annealing phenomena, Pergamon, Oxford, chapter 11 (1995).

2.167 McQueen, H. J., and Jonas, J. J.: in Treatise on materials science and technology (vol. 6): plastic deformation of materials. (Arsenault, R. J., ed.). Academic Press, New York, pp.393, (1975).

2.168 McQueen, H. J., Wong, W. A., and Jonas, J. J. *Can. J. Phys.*, **45**,1225 (1967).

2.169 Jonas, J. J., Sellars, C. M., and Tegart, W. J. McG. *Metall. Rev.*, **14**, 1 (1969).

2.170 McQueen, H. J. *Metall. Trans. A.*, **8A**, 807 (1977).

2.171 McQueen, H. J., Evangelista, E., and Kassner, M. E. *Z. Metallkunde.*, **82**, 336 (1991).

2.172 Derby, B. *Acta Metall. Mater.*, **39**(5), 955 (1991).

2.173 Sellars, C. M. *J. Sheffield Univ. Metall. Soc.*, **8**, 43 (1969).

2.174 Roberts, W., and Ahlblom, B. *Acta Metall.*, **26**, 801 (1978).

2.175 Roberts, W., Boden, H., and Ahlblom, B. *Met. Sci.*, **13**, 195 (1979).

2.176 Sellars, C. M. *Metals Forum.*, **4**, 75 (1981).

2.177 Gawne, D. T., and Higgins, G. T. *J. Mater. Sci.*, **6**, 403 (1971).

2.178 Koster, U. *Met. Sci.*, **8**, 151 (1974).

2.179 Kamma, C., and Hornbogen, E. *J. Mater. Sci.*, **11**, 2340 (1976).

2.180 Humphreys, F. J. *Acta Metall.*, **25**, 1323 (1977).

2.181 Porter, J. R., and Humphreys, F. J. *J. Mater. Sci.*, **13**, 83 (1979).

2.182 Humphreys, F. J. *ibid.*, 136.

2.183 Jones, A. R., Ralph, B., and Hansen, N. *ibid.*, 149.

2.184 Gardner, K. J., and Grimes, R., *ibid.*, 216.

2.185 Chan, H. M., and Humphreys, F. J. *Met. Sci.*, **18**, 527 (1984).

2.186 Sheppard, T., and Tutcher, M. G. *Met. Sci.*, **14**, 579, (1980).

2.187 Sheppard, T., and Parson, N. C., and Zaidi, M. A. *Met. Sci.*, **17**, 481, (1983).

2.188 Mcqueen, H. J., Evangelista, E., Bowles, J., and Crawford, G. *Met. Sci.*, **18**, 395 (1984).

2.189 Mcqueen, H. J., Evangelista, E., and Ryan, N. D.: in Recrystallization '90. (Chandra, T., ed.), TMS, Pennsylvania, 89 (1990).

2.191 Byrne, J. G. Recovery, recrystallization, and grain growth, Macmillan, New York, (1965).

2.192 Zaidai, M. A., and Sheppard, T. *Met. Sci.*, **17**, 219 (1983).

2.193 Wong, W. A., McQueen, H. J., and Jonas, J. J., *J. Inst. Metals.*, **95**, 129 (1967).

2.194 Castle, A. F., and Sheppard, T. *Met. Tech.*, **3**, 433 (1976).

2.195 Sheppard, T., and McShane, H. *Powder Met.*, **19** (3), 126, (1976).

2.196 McShane, H. B., and Sheppard, T. *Powder Met.*, **27** (2), 101 (1984).

2.197 Mukhopadhyay, A. K., Flower, H. M., and Sheppard, T. *Mater. Sci. Tech.*, **6**, 461 (1990).

2.198 Sheppard, T., Tutcher, M. G. and Flower, H. M. *Met. Sci.*, **13**, 473 (1979).

2.199 Tutcher, M. G. Ph.D. Thesis, University of London, (1979).

2.200 Sheppard, T., and Tutcher, M. G. *Met. Tech.*, **8**, 319, (1981).

2.201 Tan, G. H., and Sheppard, T. *Powder Met.*, **29** (2), 143 (1986).

2.202 Sheppard, T., Zaidai, M. A., and Tan, G. H., *Met. Sci.*, **17**, 563 (1983).

2.203 Ramakrishnan, K. N., McShane, H. B., and Sheppard, T. *Mater. Sci. Tech.*, **9**, 104 (1993).

2.204 Zaidi, M. A., Robinson, J. S., and Sheppard, T. *Mater. Sci. Tech.*, **1**, 737 (1985)

2.205 Dashwood, R. J., and Sheppard, T. *Mater. Sci. Tech.*, **8**, 455, (1992).

2.206 Dashwood, D. J., and Sheppard, T. *Mater. Sci. Tech.*, **9**, 678, (1993).

2.207 Ramakrishnan, K. N., McShane, H. B., and Sheppard, T. *Z. Metallkunde.*, **85**, 260, (1994).

(3) References to Chapter 3

3.1 Duwez, P., Willens, R. H., and Klement, Jr., W. *J. Appl. Phys.*, **31**, 1136 (1960).

3.2 Luo, H. L., and Duwez, P. *Appl. Phys. Lett.*, **2** (1), 21 (1963).

3.3 Duwez, P., and Willens, R. H. *Trans. AIME.*, **227**, 362 (1963).

3.4 Duwez, P., Willens, R. H., and Crewdson, R. C. *J. Appl. Phys.*, **36** (7), 2267 (1965).

3.5 Jha, S. C., and Sanders, Jr., T. H. in High strength powder metallurgy aluminium alloys (Hildeman, G. J., and Koczak, M. J., eds.) The Met. Soc. AIME., 243 (1986).

3.6 Weins, W. N., Winholtz, R. A., and Vidal, K. E. *ibid.*, 255.

3.7 Ramakrishnan, K. N., McShane, H. B., and Sheppard, T. *Int. J. Powder Met.*, **31** (4), 325 (1993).

3.8 Ramakrishnan, K. H. Ph.D. Thesis, University of London, 1993.

3.9 Chowdhury, A. J. S., and Sheppard, T. *Mater. Sci. Tech.*, **6**, 535 (1990).

3.10 Vasudevan, V. K., and Fraser, H. L. *Mater. Sci. Eng.*, **98**, 131 (1988).

3.11 Premkumar, M. K., Koczak, M. J., and Lawley, A. *ibid.* ref. No. 3.5(a), 265.

3.12 Ezz, S., Koczak, M. J., Lawley, A., and Premkumar, M. K. *ibid.*, 287.

3.13 Mahajan, Y. R., Kim, Y-W., and Froes, F. H. *ibid.*, 333.

3.14 Thursfield, G., and Stowell, M. J. *J. Mater. Sci.*, **9**, 1644 (1974).

3.15 Okazaki, K., and Skinner, D. J. *Scripta Metall.*, **18**, 911 (1984).

3.16 Becker, J., Fischer, G., Schäfer, R., Chen, D. L., Weiss, B., and Stickler, R. *Z. Metallkd.*, **83**, 548 (1992).

3.17 Dashwood, R. Report to Brite Euram Breu-0356-C, 1992.

3.18 Jones, H. *Mater. Sci. Eng.*, **5**(1), 1 (1969/70).

3.19 De Sanctis, M., Woodfield, A. P., and Loretto, M. H. *Int. J. Rapid Solidn.*, **4**, 53 (1988).

3.20 Jacobs, M. H., Doggett, A. G., and Stowell, M. J. *J. Mater. Sci.*, **9**, 1631 (1874).

3.21 Dermarkar, S. in Rapidly solidified powder aluminum alloys. (Fine, M. E., and Starke, Jr., A. E., eds.), ASTM-STP 890, Philadelphia, PA, 154 (1986).

3.22 Boettinger, W. J., Bendersky, L., and Early, J. G. *Metall. Trans. A.*, **17A**, 781 (1986).

3.23 Ackermann, L., Dermarkar, S., and Faure, J. F. in Aluminium technology '86. (Sheppard, T., ed.), The Institute of Metals, London, 698 (1986).

3.24 Chu, M. G., and Granger, D. A. *Metall. Trans. A.*, **21A**, 205 (1990).

3.25 Jacobs, M. H., Doggett, A. G., and Stowell, M. J. *J. Mater. Sci.*, **9**, 1631 (1974).

3.26 Chare, P. J. M., and Sheppard, T. *Powder met.*, **16**, 437 (1973).

3.27 Tonejc, A., and Bonefačić, A. *J. Appl. Phys.*, **40**, 419 (1969).

3.28 Tonejc, A. *Metall. Trans.*, **2**, 437 (1971).

3.29 Young, R. M. K., and Clyne, T. W. *Scripta Metall.*, **15**, 1211 (1981).

3.30 Thomas, R. W., Cama, H., Evans, P. V., and Hunt, J. D. in Solidification processing 1997: proceedings of the 4th decennial international conference on solidification processing. (Beech, J., and Jones, H., eds.), The Department of Engineering Materials, University of Sheffield, Sheffield, 559 (1997).

3.31 Adam, C. McL., and Hogan, L. M. *J. Austral. Inst. Met.*, **17** (2), 81 (1972).

3.32 Liang, D., and Jones, H. *Z. Metallkd.*, **83**, 224 (1992).

3.33 Hughes, I. R., and Jones, H. *J. Mater. Sci.*, **11**, 1781 (1976).

3.34 Liang, D., and Jones, H. *Mater. Sci. Eng.*, **A173**, 109 (1993).

3.35 Gilgien, P., Zryd, A., and Kurz, W. *Acta Metall. Mater.*, **43** (9), 3477 (1995).

3.36 Murray, J. L. *Mater. Res. Soc. Symp. Proc.*, **19**, 249 (1983).

3.37 Jones, H. *Mater. Sci. Eng.*, **A179/A180**, 1 (1994).

3.38 Shechtman, D., and Swartzendruber, L. J. *Mater. Res. Soc. Symp. Proc.*, **19**, 265 (1983).

3.39 Shechtman, D., Blech, I., Gratias, D., and Cahn, J. W. *Phys. Rev. Lett.*, **53**, 1951 (1984).

3.40 Adam, C. M., Ramanan, V. R. V., and Skinner, D. J. in Undercooled alloy phases. (Collings, E. W., and Koch, C. C., eds.), The Metallurgical Society, Pennsylvania, 59 (1986).

3.41 Carrard, M., Gremaud, M., and Pierantoni, M. *Scripta Metall. Mater.*, **25**, 925 (1991).

3.42 Dunlap, R. A., Lloyd, D. J., Christie, I. A., Stroink, G., and Stadnik, Z. M.

J. Phys. F: Met. Phys., **18**, 1329 (1988).

3.43 Gopal, E. S. R., Baranidharan, S., and Sekhar, J. A. *Mater. Sci. Eng.*, **99**, 413 (1988).

3.44 Zhang, X. D., and Loretto, M. H. *Phil. Mag. B.*, **64** (6), 697 (1991).

3.45 Cotton, J. D., and Kaufman, M. J. *Metall. Trans. A.*, **22A**, 927 (1991).

3.46 Shurer, P. J., Koopmans, B., van de Woude, F., and Bronsveld, P. *Solid State Commun.*, **59**, 619 (1986).

3.47 Fung, K. K., Yang, C. Y., Zhou, Y. Q., Zhao, J. G., Zhan, W. S., and Shen, B. G. *Phys. Rev. Lett.*, **56** (19), 2060 (1986).

3.48 Zou, X. D., Fung, K. K., and Kuo, K. H. *Phys. Rev. B.*, **35** (9), 4526 (1987).

3.49 Kuo, K. H. *Mater. Sci. Forum.*, **22-24**, 131 (1987).

3.50 Kim, D. H., and Cantor, B. *Phil. Mag. A.*, **69** (1), 45 (1994).

3.51 Kim, Young-Won, and Froes, F. H. *Mater. Sci. Eng.*, **98**, 207 (1988).

3.52 Mondolfo, L. F. Aluminum alloys: structure and properties, Butterworths, London, 392 (1976).

3.53 Moss, M. *Acta Metall.*, **16**, 321 (1968).

3.54 Inoue, A., Arnberg, L., Lehtinen, B., Oguchi, M., and Masumoto, T. *Metall. Trans. A.*, **17A**, 1657 (1986).

3.55 Rao, K. V., Fidler, J., and Chen, H. S. *Europhys. Lett.*, **1** (12), 647 (1986).

3.56 Skinner, D. J., Ramanan, V. R. V., Zedalis, M. S., and Kim, N. J. *Mater. Sci. Eng.*, **99**, 407 (1988).

3.57 Zedalis, M. S., Ramanan, V. R. V., and Skinner, D. J. in Thermal analysis in in metallurgy. (Shull, R. D., and Joshi, A., eds.) The Minerals, Metals and Materials Society, Pennsylvania, 279 (1992).

3.58 Ramanan, V. R. V., Skinner, D. J., and Zedalis, M. S. *Mater. Sci. Eng.*, **A134**, 912 (1991).

3.59 Skinner, D. J., and Okazaki, K. *Scripta Metall.*, **18**, 905 (1984).

3.60 Skinner, D. J., Okazaki, K., and Adam, C. M. in Rapidly solidified powder aluminum alloys. (Fine, M. E., and Starke, Jr., E. A., Eds.) ASTM-STP 890, Philadelphia, PA, 211 (1986).

3.61 Inoue, A., Kimura, H., Sasamori, K., and Masumoto, T. *Mater. Trans. JIM.*, **36** (10), 1219 (1995).

3.62 *Idem*, *Int. J. Rapid Solidification.*, **11**, 103 (1996).

3.63 *Idem*, *Mater. Trans. JIM.*, **37** (6), 1287 (1996).

3.64 Hono, K., Zhang, Y., Sakurai, T., and Inoue, A. *Mater. Sci. Eng.*,

A250, 152 (1998).

3.65 Humphreys, E. S., Warren, P. J., and Cerezo, A. *ibid.*, 158.

3.66 Bye, R. L., Kim, N. J., Skinner, D. J., Raybould, D., and Brown, A. M., in Processing of structural metals by rapid solidification. (Froes, F. H., and Savage, S. J., eds.), ASM International, 283 (1987).

3.67 Skinner, D. J., Bye, R. L., Raybould, D., Brown, A. M., Zedalis, M. S. *ibid.*, 291.

3.68 Zedalis, M., Raybould, D., Skinner, D. J., and Das, S. K. *ibid.*, 347.

3.69 Gilman, P. S., and Das, S. K., in Proceedings of international conference on PM aerospace materials (A metal powder report conference, Luzern, November 2-4, 1987), MPR Publishing Services, Shrewsbury, 27.1 (1988).

3.70 Gilman, P. *Metals and Materials*, **6**, 504 (1990).

3.71 Skinner, D. J.:in Dispersion strengthened aluminum alloys. (Kim, Y-W., and Griffith, W. M., eds.), The Minerals, Metals and Materials Society, pp. 181 (1988).

3.72 M. A. Rodriguez, and D. J. Skinner, *J. Mater. Sci. Lett.*, **9**, 1292 (1990).

3.73 Kim, N. J. *Int. J. Rapid Solidification*, **6**, 175 (1991).

3.74 Skinner, D. J., R. L. Bye, D. Raybould and A. M. Brown, *Scripta Met.*, **20**, 867 (1986).

3.75 Wilkes, D. M. J., and Jones, H.: in Science and technology of rapid solidification processing. (Otooni, M. A., ed.), Kluwer Academic Publishers, Netherlands, pp. 157 (1995).

3.76 Franck, R. E., and Hawk, J. A. *Scripta Met.*, **23**, 113 (1989).

3.77 Park, W. J., Ahn, S., and Kim, N. J. *Mat. Sci. Eng.*, **A189**, 291 (1994).

3.78 Tang, Y. L., Guan, S. K., Shao, D. S., Shen, N. F., and Hu, H. Q. *J. Mater. Sci. Lett.*, **12**, 1749 (1993).

3.79 Srivastava, A. K., and Ranganathan, S. *Scripta Met.*, **27**, 1241 (1992).

3.80 Wang, J. Q., Hao, Y. Y., Chang, X. C., and Hu, Z. Q. *Int. J. Non-Equilibrium Processing*, **10**, 83 (1997).

3.81 Wang, J. Q., Tseng, M-K., Chen, X-F., Chang, B-J., and Xianyu, Z. *Mat. Sci. Eng.*, **A179/180**, 412 (1994).

3.82 Das, S. K., and Froes, F. H. in Rapidly solidified alloys: processes, structures, properties, applications. (Liebermann, H. H., ed.), Marcel Dekker, New York, 39 (1993).

3.83 Hariprasad, S., Sastry, S. M. L., Jerina, K. L., and Lederich, R. J.

Metall. Trans. A., **24A**, 865 (1993).

3.84 Hariprasad, S., Sastry, S. M. L., and Jerinal, K. L. *J. Mater. Sci.*, **31**, 921 (1996).

3.85 Srivastava, A. K., Ojha, S. N., and Ranganathan, S. *Metall. Mater. Trans. A.*, **29A**, 2205 (1998).

3.86 Amateau, M. F., Eden, T. J., Galbraith, J. M., Fodran, E. J., and Kaufman, M. J. in The third pacific rim international conference on advanced materials and processing (PRICM 3). (Imam, M. A., DeNale, R., Hanada, S., Zhong, Z., and Lee, D. N., eds.), The Minerals, Metals and Materials Society, Pennsylvania, 1645 (1998).

(4) References to Chapter 4

4.1 Dashwood, R. J. Ph.D. Thesis, University of London (1990).

4.2 Tan, M. J. Ph.D. Thesis, University of London (1989).

(5) References to Chapter 5

5.1 Doroszkowski, A.: in Paint and surface coating; theory and practice. (Lambourne, R., ed.), Ellis Horwood, Chichester, pp. 271 (1987).

5.2 Jones, H. *Mater. Sci. Eng.*, **5** (1), 1 (1969/70).

5.3 Boettinger, W. J., Bendersky, L., and Early, J. G., *Metall. Trans. A.*, **17A**, 781 (1986).

5.4 Ramakrishnan, K. N. Ph.D. Thesis, University of London, (1993).

5.5 Levi, C. G., and Mehrabian, R. *Metall. Trans. A.*, **13A**, 13 (1982).

5.6 Chu, M. G., and Granger, D. A. *Metall. Trans. A.*, **21A**, 205 (1990).

5.7 Boettinger, W. J., Bendersky, L. A., Schaefer, R. J., and Biancaniello, F. S. *Metall. Trans. A.*, **19A**, 1101 (1988).

5.8 Field, R. D., Zindel, J. W., and Fraser, H. L. *Scripta Metall.*, **20**, 415 (1986).

5.9 Asthana, R., Rohatgi, P. K., and Tewari, S. N.: in Microstructure formation during solidification of metal matrix composites. (Rohatgi, P. K., ed.), The Minerals, Metal & Materials Society, TMS, Warrendale, Pa, pp. 11 (1993).

5.10 Shangguan, D., Ahuja, S., and Stefanescu, D. M. *Metall. Trans. A.*, **23A**, 669 (1992).

5.11 (a) Juretzko, F. R., Dhindaw, B. K., Stefanescu, D. M., Sen, S., and Curreri, P. A. *Metall. Mater. Trans. A.*, **29A**, 1691 (1998).

(b) Stefanescu, D. M., Juretzko, F. R., Dhindaw, B. K., Catalina, A., Sen, S., and Curreri, P. A. *Metall. Mater. Trans. A.*, **29A**, 1697 (1998).

5.12 Omenyi, S. N., Smith, R. P., and Neumann, A. W. *J. Colloid Interface Sci.*, **75** (1), 117 (1980).

5.13 Zubko, A. M., Lobanov, V. G., and Nikonova, V. V. *Sov. Phys. Crystallogr.*, **18** (2), 239 (1973).

5.14 (a) Briant, C. L. *Faraday Soc. (Discussion).*, **61**, 25 (1976).

(b) Briant, C. L., and Burton, J. J. *Phys. Stat. Sol. (b).*, **85**, 393 (1978).

5.15 (a) Steinhardt, P. J., Nelson, D. R., and Ronchetti, M. *Phys. Rev. B.*, **28** (2), 784 (1983).

(b) Sachdev, S., and Nelson, D. R. *Phys. Rev. B.*, **32** (7), 4592 (1985).

5.16 Frank, F. C., and Kasper, J. S. *Acta Cryst.*, **11**, 184 (1958).

5.17 Urban, K., Mayer, J., Rapp, M., Wilkens, M., Csanady, A., and Fidler, J. *J. de Phys. Colloque C3.*, **47**, 465 (1986).

5.18 Bendersky, L. A., and Ridder, S. D. *J. Mater. Res.*, **1** (3) 405 (1986).

5.19 Bendersky, L. A., and Biancaniello, F. S., and Schaefer, R. J. *J. Mater. Res.*, **2** (4), 427 (1987).

5.20 Bendersky, L. A., Kaufman, M. J., Boettinger, W. J., and Biancaniello, F. S. *Mater. Sci. Eng.*, **98**, 213 (1988).

5.21 Bendersky, L. A., McAlister, A. J., and Biancaniello, F. S. *Metall. Trans. A.*, **19A**, 2893 (1988).

5.22 Kurz, W., Trivedi, R. *Mater. Sci. Eng.*, **A179/A180**, 46 (1994).

5.22 Kurz, W., and Trivedi, R. *Acta Metall. Mater.*, **38** (1), 1 (1990).

5.23 Gill, S. C., and Kurz, W.: (a) *Acta Metall. Mater.*, **41** (12), 3563 (1993).

(b) *Acta Metall. Mater.*, **43** (1), 139 (1995).

5.24 Boettinger, W. J., Coriell, S. R., and Sekerka, R. F. *Mater. Sci. Eng.*, **65**, 27 (1984).

5.25 Boettinger, W. J., Bendersky, L., and Early, J. G. *Metall. Trans. A.*, **17A**, 781 (1986).

5.26 (a) Gremaud, M., Carrard, M., and Kurz, W. *Acta Metall. Mater.*, **38**, 2587 (1990).

(b) Gremaud, M., Carrard, M., and Kurz, W. *Acta Metall. Mater.*, **39**, 1431 (1991).

5.27 Jones, H. *Mater. Lett.*, **6**, 181 (1988).

5.28 Jones, H. *Phil. Mag. B.*, **61** (4), 487 (1990).

5.29 Marshall, G. J.: in Aluminum technology '86. (Sheppard, T., ed.), The Institute of Metals, London, pp. 679 (1986).

5.30 Zaidi, M. A. (a) *Mater. Sci. Eng.*, **98**, 221 (1988).

(b) in Aluminum technology '86. (Sheppard, T., ed.), The Institute of Metals, London, pp. 839 (1986).

5.31 Sheppard, T., and Zaidi, M. A. *Int. J. Rapid Solidn.*, **2**, 199 (1986).

5.32 Ioannidis, E. K., and Sheppard, T. *Mater. Sci. Tech.*, **6**, 528 (1990).

5.33 Liu, P., Dunlop, G. L., and Arnberg, L. *Mater. Sci. Eng.*, **98**, 437, (1988).

5.34 Trivedi, R., Sekhar, J. A., and Seetharaman, V. *Metall. Trans. A.*, **20A**, 769 (1989).

5.35 Trivedi, R., and Kurz, W. *Acta Metall.*, **34** (8), 1663 (1986).

5.36 Mullins, W. W., and Sekerka, R. F. *J. Appl. Phys.*, **35**, 444 (1964).

5.37 Adam. C. M., Ramanan, V. R. V., and Skinner, D. J.: in Undercooled alloy phases. (Collings, E. W., and Koch, C. C., eds.), The Metallurgical Society, Pennsylvania, 59 (1987).

5.38 Young, R. M. K., and Clyne, T. W. *Scripta Metall.*, **15**, 1211 (1981).

5.39 Hughes, I. R., and Jones, H. *J. Mater. Sci.*, **11**, 1781 (1976).

5.40 Grant, N. J. *J. Metals.*, **35**, 20 (1983).

5.41 Rai, G., Lavernia, E., and Grant, N. J. *J. Met.*, **37**, 22 (1985)

5.42 Couper, M. J., and Singer, R. F.: in High strength powder metallurgy aluminum alloys II. (Hildeman, G. J., and Koczak, M. J., eds.), The Metallurgical Society, Pennsylvania, pp. 199 (1985).

5.43 Wang, W., Liu, D., and Grant, N. J. *Scripta Metall.*, **21**, 1279 (1987).

5.44 Cahn, J. W., Shechtman, D., and Gratias, D. *J. Mater. Res.*, **1** (1), 13, (1985).

5.45 Elser, V. *Phys. Rev. B.*, **32** (8), 4892 (1985).

5.46 Bancel, P. A., Heiney, P. A., Stephens, P. W., Goldman, A. I., and Horn, P. M. Phys. Rev. Lett., 54 (22), 2422 (1985).

5.47 Audier, M., and Guyot, P. *Phil. Mag. B.*, **53** (1), L43 (1986).

5.48 Ramanan, V. R. V., Skinner, D. J., and Zedalis, M. S. *Mater. Sci. Eng.*,

A134, 912 (1991).

5.49 Zedalis, M. S., Ramanan, V. R. V., and Skinner, D. J. in Thermal analysis in in metallurgy. (Shull, R. D., and Joshi, A., eds.) The Minerals, Metals and Materials Society, Pennsylvania, pp. 279 (1992).

5.50 Carrard, M., Gremaud, M., and Pierantoni, M. *Scripta Metall. Mater.*, **25**, 925 (1991).

5.51 Zindel, J. W., Kurath, P., and Fraser, H. L.: in High strength powder metallurgy aluminum alloys II. (Hildeman, G. J., and Koczak, M. J., eds.), The Metallurgical Society, Pennsylvania, pp. 213 (1985).

5.52 Bendersky, L. *Phys. Rev. Lett.*, **55** (14), 1461 (1985).

5.53 Bendersky, L., Schaefer, R. J., Biancaniello, F. S., Boettinger, W. J., Kaufman, M. J., and Shechtman, D. *Scripta Metall.*, **19**, 909 (1985).

5.54 Schaefer, R. J., and Bendersky, L. *Scripta Metall.*, **20**, 745 (1985).

5.55 Gillessen, F., and Herlach, D. M. *Mater. Sci. Eng.*, **A134**, 1220 (1991).

5.56 Kelton, K. F. *Int. Mater. Rev.*, **38** (3), 105 (1993).

5.57 Boettinger, W. J., Bendersky, L., and Early, J. G. *Metall. Trans. A.*, **17A**, 781 (1986).

5.58 Thomas, R. W., Cama, H., Evans, P. V., and Hunt, J. D.: in Solidification processing 1997: proceedings of the 4th decennial international conference on solidification processing. (Beech, J., and Jones, H., eds.), The Department of Engineering Materials, University of Sheffield, Sheffield, 559 (1997).

5.59 Adam, C. McL., and Hogan, L. M. *J. Austral. Inst. Met.*, **17** (2), 81 (1972).

5.60 Liang, D., and Jones, H. *Z. Metallkd.*, **83**, 224 (1992).

5.61 Hughes, I. R., and Jones, H. *J. Mater. Sci.*, **11**, 1781 (1976).

5.62 Burden, M. H., and Jones, H. *Metallography.*, **3**, 307 (1970).

5.63 Cullity, B. D. Elements of X-ray diffraction. Addison-Wesley Publishing Company, Massachusetts, (1978).

5.64 Jones, H. *Scripta Metall.*, **17**, 97 (1983).

5.65 Tonejc, A., and Bonefačić, A. *J. Appl. Phys.*, **40**, 419 (1969).

5.66 Jones, H. Rapid solidification of metals and alloys., The Institute of Metallurgist, London, (1982).

5.67 Mueller, B. A., and Perepezko, J. H. *Metall. Trans. A.*, **18A**, 1143, (1987).

5.68 Suzuki, T., Toyoda, S., Umeda, T., and Kimura, Y. *J. Crystal Growth.*, 38, 123 (1977).

5.69 Wu, Y., Piccone, Y., Shiohara, Y., and Flemings, M. C. *Metall. Trans. A.*, **18A**, 915 (1987).

5.70 Lipton, J., Kurz, W., and Trivedi, R. *Acta Metall.*, **35** (4), 957 (1987).

5.71 Tang, Y., and Shen, N. *Mater. Trans. JIM.*, **34** (7), 627 (1993).

5.72 Fontaine, A., Dixmier, J., and Guinier, A. *Fizika 2 Suppl.*, **2**, 23.1 (1970)

5.73 Murray, J. L., McAlister, A. J., Schaefer, R. J., Bendersky, L. A., Biancaniello, F. S., and Moffat, D. L. *Metall. Trans. A.*, **18A**, 385 (1987).

5.74 Skinner, D. J., Ramanan, V. R. V., Zedalis, M. S., and Kim, N. J. *Mater. Sci. Eng.*, **99**, 407 (1988).

5.75 Skinner, D. J.:in Dispersion strengthened aluminum alloys. (Kim, Y-W., and Griffith, W. M., eds.), The Minerals, Metals and Materials Society, pp. 181 (1988).

5.76 Polmear, I. J., Couper, M. J., and Bannister, M. J. *Mater. Forum.*, **12**, 54 (1988).

5.77 Dunlap, R. A., and Dini, K. *Can. J. Phys.*, **63**, 1267 (1985).

5.78 Young, R. M. K., and Tweed, J. H. *Mater. Sci. Eng.*, **A134**, 1153 (1991).

5.79 Gilman, P. S., and Das, S. K., in Proceedings of international conference on PM aerospace materials (A metal powder report conference, Luzern, November 2-4, 1987), MPR Publishing Services, Shrewsbury, pp. 27.1 (1988).

5.80 Skinner, D. J., R. L. Bye, D. Raybould and A. M. Brown, *Scripta Met.*, **20**, 867 (1986).

5.81 Wilkes, D. M. J., and Jones, H.: in Science and technology of rapid solidification processing. (Otooni, M. A., ed.), Kluwer Academic Publishers, Netherlands, pp. 157 (1995).

5.82 Park, W. J., Ahn, S., and Kim, N. J. *Mat. Sci. Eng.*, **A189**, 291 (1994).

5.83 Hariprasad, S., Sastry, S. M. L., and Jerinal, K. L. *J. Mater. Sci.*, **31**, 921 (1996).

5.84 Wang, J. Q., Tseng, M-K., Chen, X-F., Chang, B-J., and Xianyu, Z. *Mat. Sci. Eng.*, **A179/180**, 412 (1994).

5.85 McShane, H. B., and Sheppard, T. *Powder Met.*, **27** (2), 101 (1984).

5.86 Koh, H. J., Park, W. J., and Kim, N. J. *Mater. Trans. JIM.*, **39** (9), 982 (1998).

5.87 Tonejc, A., and Bonefačić, A. *Fizika 2 Suppl.*, **2**, 20.1 (1970).

5.88 Jacobs, M. H., Doggett, A. G., and Stowell, M. J. *J. Mater. Sci.*, **9**, 1631 (1874).

5.89 Skjerpe, P. *Metall. Trans. A.*, **18A**, 189 (1987).

5.90 Gilgien, P., Zryd, A., and Kurz, W. *Acta Metall. Mater.*, **43** (9), 3477 (1995).

5.91 Nicol, A. D. I. *Acta Cryst.*, **6**, 285 (1953).

5.92 Hollingsworth, E. H., Frank, G. R., and Willett, R. E. *Trans. Met. Soc. AIME.*, **224**, 188 (1962).

5.93 Walford, L. K. *Acta Cryst.*, **18**, 287 (1965).

5.94 Black, P. J., Edwards, O. S., and Forsyth, J. B., *Acta Cryst.*, **14** 993 (1961).

5.95 Shechtman, D., Blech, I., Gratias, D., and Cahn, J. W. *Phys. Rev. Lett.*, **53** (20), 1951 (1984).

5.96 Suryanarayana, C., and Jones, H. *Int. J. Rapid Solidn.*, **3**, 253 (1987).

5.97 Goldman, A. I., and Widom, M., *Annu. Rev. Phys. Chem.*, **42**, 685 (1991).

5.98 Kelton, K. F. *Int. Mater. Rev.*, **38** (3), 105 (1993).

5.99 Kelton, K. F.: in Intermetallic compounds: principles and practice (Vol. 1). (Westbrook, J. H., and Fleischer, R. L., eds.), John Wiley & Sons, Chichester, pp. 453 (1995).

5.100 Steurer, W.: in Physical metallurgy (vol. 1), (Cahn, R. W., and Haasen, P., eds.), Elsevier Scince B. V., Amsterdam, Appendix to Chapter 4 (1996).

5.101 Kim, N. J. *Int. J. Rapid Solidification*, **6**, 175 (1991).

5.102 Hahn, G. T., and Rosenfield, A. R. *Metall. Trans. A.*, **6A**, 653 (1975).

5.103 Dashwood, R. J. Ph.D. Thesis, University of London, 1990.

5.104 Chattopadhyay, K., and Mukhopadhyay, N. K. *Mater. Sci. Forum.*, **22-24**, 639 (1987).

5.105 Köster, U., and Schuhmacher, B. *Mater. Sci. Eng.*, **99**, 417 (1988).

5.106 Gilman, P. S., and Das, S. K., in Proceedings of international conference on PM aerospace materials (A metal powder report conference, Luzern, November 2-4, 1987), MPR Publishing Services, Shrewsbury,

27.1 (1988).

5.107 Skinner, D. J., R. L. Bye, D. Raybould and A. M. Brown, *Scripta Met.*, **20**, 867 (1986).

5.108 Wilkes, D. M. J., and Jones, H.: in Science and technology of rapid solidification processing. (Otooni, M. A., ed.), Kluwer Academic Publishers, Netherlands, pp. 157 (1995).

5.109 Black, P. J. *Acta Cryst.*, **8**, 43 (1955).

5.110 Black, P. J. *Acta Cryst.*, **8**, 175 (1955).

5.111 Mulazimoglu, M. H., Zaluska, A., Gruzleski, J. E., and Paray, F. *Metall. Mater. Trans. A.*, **27A**, 929 (1996).

5.112 Adam, C. McL., and Hogan, L. M. *Acta Metall.*, **23**, 345 (1975).

5.113 Liu, P., Thorvaldsson, T., and Dunlop, G. L., *Mater. Sci. Tech.*, **2**, 1009 (1986).

5.114 Zolliker, P., Yvon, K., and Baerlocher, Ch. *J. Less-common Met.*, **115**, 65 (1986).

5.115 Noreus, D., and Kihlborg, L. *J. Less-common Met.*, **123**, 233 (1986).

5.116 Grin, J., Burkhardt, U., Ellner, M., and Perters, K. *Z. Kristallogr.*, **209**, 479 (1994).

5.117 Edshammar, L. –E. *Acta Chem. Scand.*, **18**, 2294 (1964).

5.118 *Idem. ibid.* **19**, 2124 (1965).

5.119 Hudd, R. C., and Taylor, W. H. *Acta Cryst.* 15, 441 (1962).

5.120 Rajasekharan, T., Sarah, N., and Schubert, K. *Z. Metallkde.*, **73**, 526 (1982).

5.121 Fung, K. K., Yang, C. Y., Zhou, Y. Q., Zhao, G. J., Zhan, W. S., and Shen, B. G. *Phys. Rev. Lett.*, **56**, 2060 (1986).

5.122 Fung, K. K., Yang, Zou, X. D., and Yang, C. Y. *Phil. Mag. Lett.*, **55**(1), 27 (1987).

5.123 Zou, X. D., Fung, K. K., and Kuo, K. H. *Phys. Rev. B.*, **35**(9), 4526 (1987).

5.124 Kim, D. H., and Cantor, B. *Phil. Mag. A.*, **69** (1), 45 (1994).

5.125 Ellner, M. *Acta Cryst.* **B51**, 31 (1995).

5.126 Daulton, T. L., Kelton, K. F., and Gibbons, P. C. *Phil. Mag. B.*, **63** (3), 687 (1991).

5.127 Jiang, W. J., Hei, Z. K., Guo, Y. X, and Kuo, K. H. *Phil. Mag. A.*, **52** (6) L53 (1985).

5.128 Kuo, K. H. *Mater. Sci. Forum.*, **22-24**, 131 (1987).

5.129 Dunlap, R. A., and Dini, K. *Can. J. Phys.*, **63**, 1267 (1985).

5.130 Bendersky, L. *J. Microscopy.*, **146** (3), 303 (1987).

5.131 Le Lann, A. *Phase Transitions*, **16-17**, 143 (1989).

5.132 Le Lann, A. *Phil. Mag. B.*, **62**, 577 (1990).

5.134 Calvayrac, Y., Devaud-Rzepski, J., Bessiere, M., Lefebvre, S., Quivy, A., and Gratias, D. *Phil. Mag. B.*, **59** (4), 439 (1989).

5.135 Audier, M., and Guyot, P.*J. De Phys.*, **47**, C3, 405 (1986).

5.136 Guyot, P., and Audier, M. *Phil. Mag. B.*, **51** (1), L15 (1985).

5.137 Shoemaker, C. B. *Phys. Rev. B.*, **38** (12), 8511 (1988).

5.138 Sato, A., Yamamoto, A., Li, X. Z., Hiraga, K., Haibach, T., and Steurer, W. *Acta Cryst.*, **C53**, 1531 (1997).

5.139 Grushko, B., Wittenberg, R., Bickmann, K., and Freiburg, C. *J. Alloys Comp.*, **233**, 279 (1996).

5.140 Bendersky, L. A., and Roth, R. S., Ramon, J. T., and Shechtman, D. *Metall. Trans. A.*, **22A**, 5 (1991).

5.141 Wen, K. Y., Chen, Y. L., and Kuo, K. H. *Metall. Trans. A.*, **23A**, 2437 (1992).

5.142 Ma, L., Wang, R., and Kuo, K. H. *Scripta Metall.*, **22**, 1791 (1988).

5.143 Wang, R., Ma, L., and Kuo, K. H. *J. Less-Common Met.*, **163**, 27 (1990).

5.144 Taylor, M. A. *Acta Cryst.*, **12**, 393 (1959).

5.145 Kreiner, G., and Franzen, H. F. *J. Alloys Comp.*, **261**, 83 (1997).

5.146 Shoemaker, C. B., Keszler, D. A., and Shoemaker, D. P. *Acta Cryst.* **B45**, 13 (1989).

5.147 Zhou, W. L., Li, X. Z., and Kuo, K. H. *Scripta Metall.*, **23**, 1571 (1989).

5.148 Rosell-Laclau, E., Durand-Charre, M., and Audier, M. *J. Alloys Comp.*, **233**, 246 (1996).

5.149 Audier, M., Janot, Ch., De Boissieu, M., and Dubost, B. *Phil. Mag. B.*, **60** (4), 437 (1989).

5.150 LeBail, A., Leblanc, M., and Audier, M. *Acta Cryst*, **B47**, 451 (1991).

5.151 Brown, P. *Acta Crystallogr.*, **12**, 995 (1959).

5.152 Cooper, M, J. *Acta Crystallogr.*, 13, 257 (1960).

APPENDIX

A1. Powder Particle Size Distribution

The size distribution of each powder size fraction of RS-Al-Fe-(V, Si) alloy powders was determined by using a Malvern Laser Particle Sizer. Three types of powder sizes or diameters included in Table 5.1.1 (page 69) are defined as given below.

The *equivalent volume mean diameter or De Broucker mean* ($D[4,3]$)

$$D[4,3] = (\sum_{1}^{M} n_i d_i^4) / (\sum_{1}^{M} n_i d_i^3) \qquad (1)$$

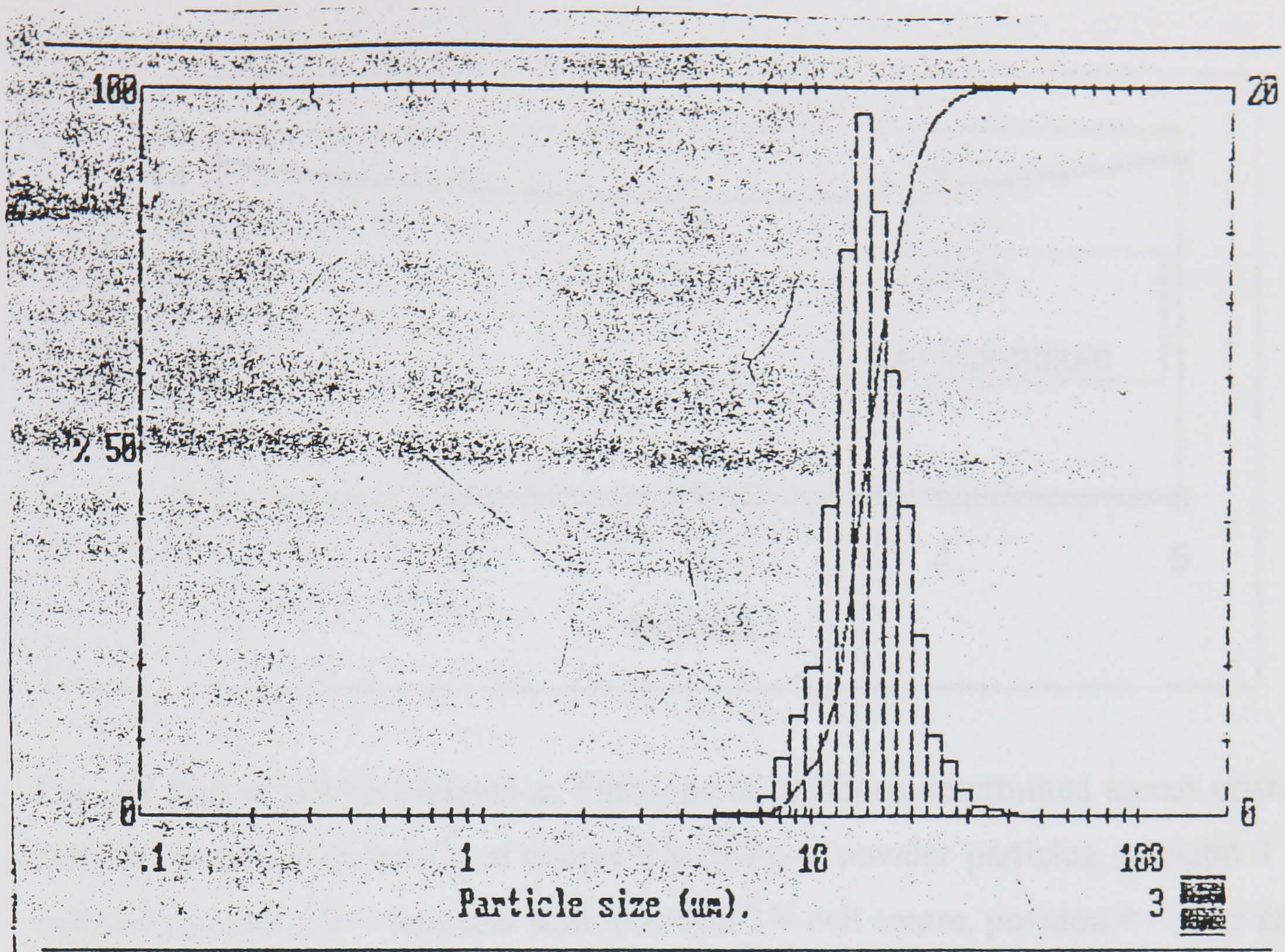
where d is diameter, n is number of powder particles, which have diameter = d.
The *De Broucker mean*, the average size based on unit weight of particle, shows where the mass of the system lies.

The *equivalent surface area diameter or Sauter mean diameter* ($D[3,2]$)

$$D[3,2] = (\sum_{1}^{M} n_i d_i^3) / (\sum_{1}^{M} n_i d_i^2) \qquad (2)$$

The *Sauter mean diameter* is the average size based on specific surface per unit volume.

The *volume median diameter* ($D[v,0.5]$ or D_{50} or $D_{0.5}$) is the value for which 50 percent of the particles (population) measured are less than the stated size.



High Under Size %	High Under Size %	High Under Size %	High Under Size %	High Under Size %	High Under Size %	Span 0.65
80.0 100	24.9 97.2	7.75 0.9	2.41 0.0	0.75 0.0	0.23 0.0	D[4,3] 15.14um
71.9 100	22.4 95.0	6.97 0.3	2.17 0.0	0.68 0.0	0.21 0.0	
64.7 100	20.1 90.0	6.27 0.2	1.95 0.0	0.61 0.0	0.19 0.0	D[3,2] 14.10um
58.2 100	18.1 81.5	5.64 0.1	1.75 0.0	0.55 0.0	0.17 0.0	
52.3 100	16.3 69.3	5.07 0.0	1.58 0.0	0.49 0.0	0.15 0.0	
47.1 99.9	14.6 52.7	4.56 0.0	1.42 0.0	0.44 0.0	0.14 0.0	D[v,0.9] 20.13um
42.3 99.9	13.2 33.4	4.10 0.0	1.28 0.0	0.40 0.0	0.12 0.0	
38.1 99.8	11.8 17.7	3.69 0.0	1.15 0.0	0.36 0.0	0.11 0.0	
34.2 99.7	10.7 9.3	3.32 0.0	1.03 0.0	0.32 0.0	0.10 0.0	D[v,0.1] 10.80um
30.8 99.4	9.58 5.2	2.98 0.0	0.93 0.0	0.29 0.0		
27.7 98.7	8.62 2.5	2.68 0.0	0.83 0.0	0.26 0.0		
Source = Data:tonosri Record No. = 10 Focal length = 45 mm Presentation = stnd		Beam length = 2.4 mm Residual = 1.770 % Obscuration = 0.2762 Volume distribution		Model indp Volume Conc. = 0.0606% Sp.S.A 0.4254 m^2/cc.		D[v,0.5] 14.43um Shape OFF

Fig. A1 Example of powder particle size distribution and a table of powder particle diameters of RS-Al-Fe-V powders with size fraction 11-18 μm

A2. Solute segregation in coarse cellular structures (zone C) of coarse RS-Al-Fe-(V,Si) powder particles determined by using EDS.

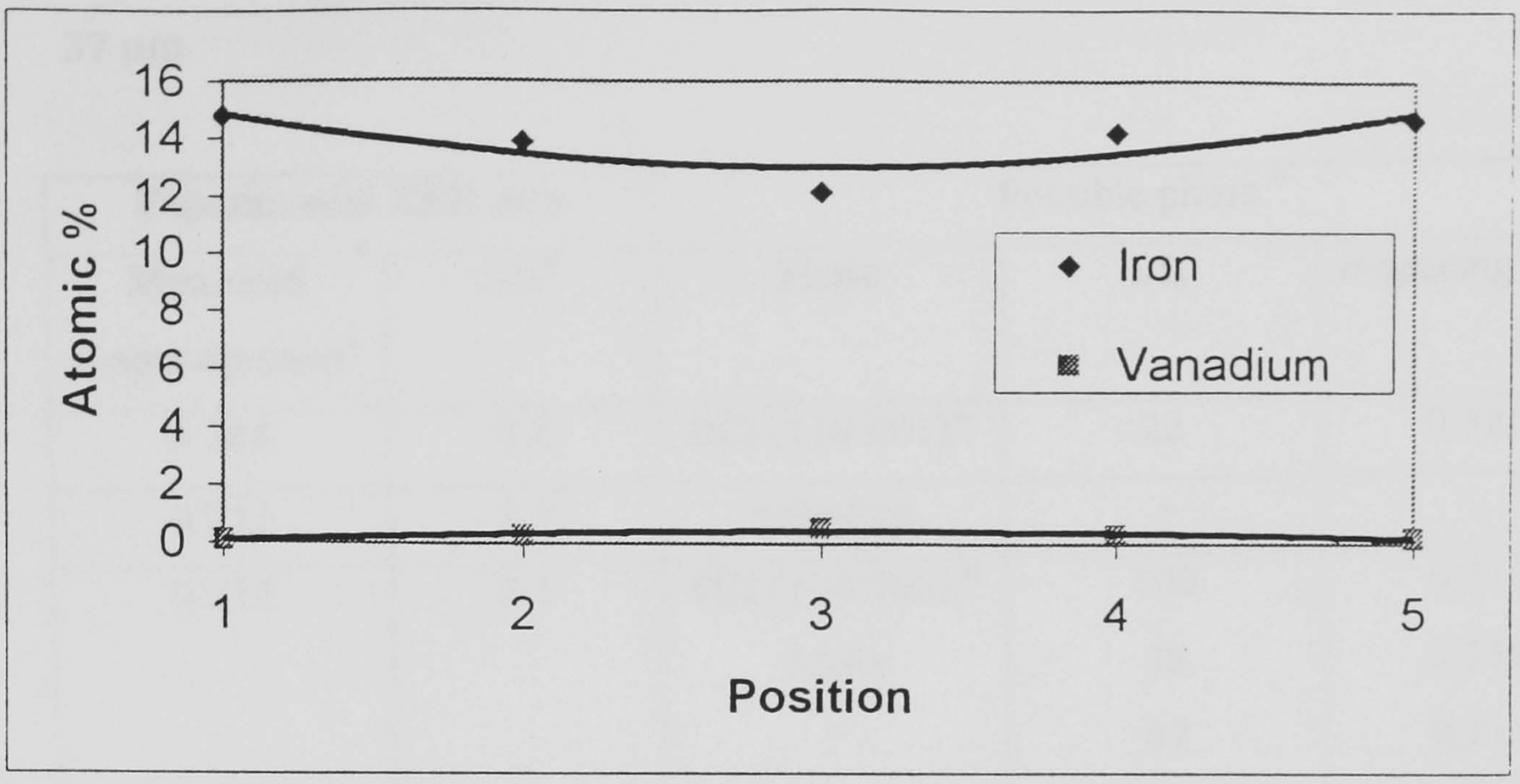


Fig. A2 Plot of solute contents as functions of positions determined across coarse cellular structures (zone C) of coarse RS-Al-Fe-V powder particles: position 1 = cell wall, position 2 = near cell wall, position 3 = cell centre, position 4 = near cell wall, and position 5 = cell wall, respectively.

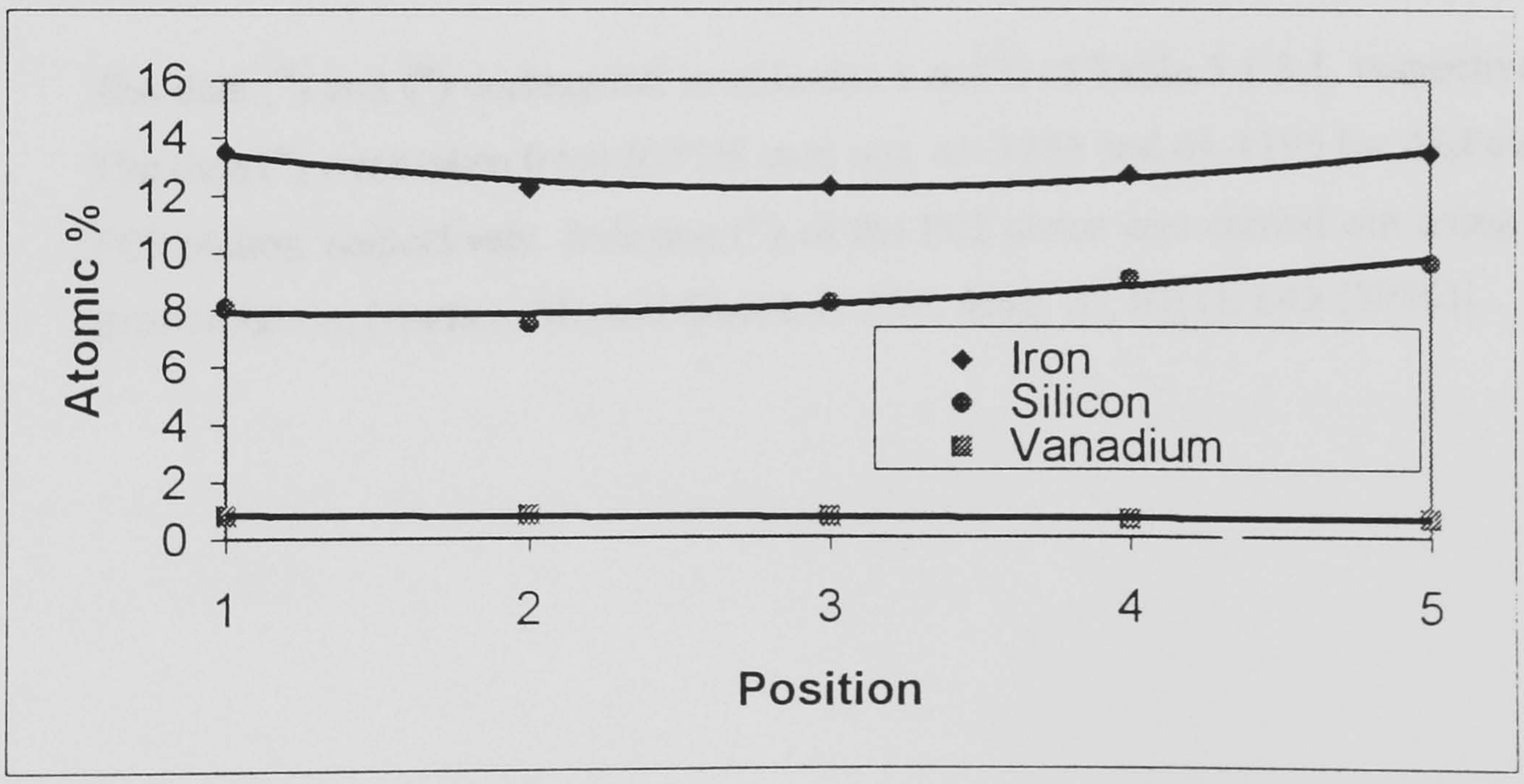


Fig. A3 Plot of solute contents as functions of positions determined across coarse cellular structures (zone C) of coarse RS-Al-Fe-V-Si powder particles: positions 1-5 are defined the same as in Fig. A2.

A3. Identification of phases in RS-Al-Fe-(V, Si) alloys using XRD

Table A3.1 Possible phases in RS-Al-Fe-V powder size fraction with $D[v,0.5]$ = 37 μm.

Experimental XRD data		Possible phase ✣		
Measured *d*-spacing (nm)✡	I/I_0 ✱	Phase	I/I_0	*d*-spacing (nm)
0.384	0.4	PCI (110 001)★	22	0.385
0.243	1.9	unknown	-	-
0.217	3.1	PCI (100 000)★	100	0.217
		Al_6Fe	38	0.218
		"	87	0.215
0.211	1.8	Al_6Fe	47	0.208
0.206	5.9	PCI (110 000)★	78	0.207
		Al_6Fe	100	0.207
0.150	0.4	PCI (111 000)★	11	0.150
		Al_6Fe	12	0.153
0.127	0.9	PCI (101 000)★	20	0.128

The data (✡) and (✱) correspond to columns 1 and 6 of Table 5.1.3.1, respectively. The data (✣) were taken from JCPDS card nos. 41-1285 and 44-1195 for Al_6Fe and PCI phases, respectively. Indexing (★) of the PCI phase was carried out using the prescription in [Audier, M., and Guyot, P. *Phil. Mag. B.*, **53**(1), L43 (1986)].

Table A3.2 Possible phases in RS-Al-Fe-V-Si powder size fraction with D[v,0.5] = 31 μm.

Experimental XRD data		Possible phase [+]		
Measured d-spacing (nm)[✡]	I/I_0[✱]	Phase	I/I_0	d-spacing (nm)
0.445	0.4	Silicide	50	0.450
0.400	1.3	Silicide	70	0.402
		PCI	22	0.385
0.343	0.2	Silicide	30	0.367
0.337	0.3	Silicide	30	0.340
		PCI	8	0.335
0.258	0.2	Silicide	10	0.284
0.247	0.6	Silicide	50	0.249
0.217	2.9	Silicide	90	0.218
		PCI	100	0.217
0.210	1.7	Silicide	60	0.211
		PCI(?)	78(?)	0.207(?)
0.149	0.2	Silicide	50	0.1494
0.127	1.1	Silicide	90	0.1273
		"	70	0.1267
		PCI	20	0.128

The data (✡) and (✱) correspond to columns 1 and 5 of Table 5.1.4.1, respectively. The data (+) were taken from JCPDS card nos. 6-669 and 44-1195 for silicide and PCI phases, respectively.

Table A3.3 Possible phases in heated RS-Al-Fe-V powder size fraction with $D[v,0.5] = 8\ \mu m$.

Experimental XRD data		Possible phase [+]		
Measured *d*-spacing (nm)[✡]	I/I_0[✱]	Phase	I/I_0	*d*-spacing (nm)
0.394	1.2	$Al_{13}Fe_4$	29	0.406
			35	0.404
			40	0.396
0.350	0.7	$Al_{13}Fe_4$	53	0.354
0.333	0.6	$Al_{13}Fe_4$	28	0.334
0.215	1.8	$Al_{13}Fe_4$	10	0.216
		$Al_{45}(V, Fe)_7$	37	0.218
		"	52	0.217
		"	29	0.216
0.209	4.0	$Al_{13}Fe_4$	75	0.210
		"	100	0.2095
		"	38	0.208
		$Al_{45}(V, Fe)_7$	40	0.2099
			58	0.2092
			92	0.2085
0.206	4.3	$Al_{13}Fe_4$	26	0.206
		"	85	0.205
		$Al_{45}(V, Fe)_7$	100	0.207

The data (✡) and (✱) correspond to columns 1 and 2 of Table 5.2.1.1, respectively.

The data (+) were taken from JCPDS card nos. 29-42 and 30-48 for $Al_{13}Fe_4$ and $Al_{45}(V, Fe)_7$ phases, respectively.

Table A3.4 Possible phases in the as-extruded Al-Fe-V alloys produced from the powder size fraction with $D[v,0.5]$ = 37 μm.

Experimental XRD data		Possible phase [+]		
Measured *d*-spacing (nm)[✡]	I/I_0[✱]	Phase	I/I_0	*d*-spacing (nm)
0.439	1.4	Al_6Fe	18	0.444
		"	14	0.431
0.396	2.0	$Al_{13}Fe_4$	35	0.404
		"	40	0.396
0.369	2.0	$Al_{13}Fe_4$	28	0.369
		"	32	0.367
0.350	1.7	$Al_{13}Fe_4$	53	0.354
0.326	0.3	Al_6Fe	10	0.325
0.244	2.8	$Al_{45}(V, Fe)_7$	20	0.249
		"	13	0.244
		unknown	-	-
0.224	1.0	Al_6Fe	65	0.227
		$Al_{45}(V, Fe)_7$	40	0.224
0.217	6.7	Al_6Fe	38	218
		$Al_{45}(V, Fe)_7$	37	0.218
		"	52	0.217
		I	100	0.217
0.215	4.0	Al_6Fe	87	0.215
		$Al_{45}(V, Fe)_7$	29	0.216
0.209	6.0	$Al_{13}Fe_4$	75	0.210
		"	100	0.2095
		"	38	0.208
		$Al_{45}(V, Fe)_7$	40	0.2099
		"	58	0.2092
		"	92	0.2085
0.206	11.6	Al_6Fe	100	0.207
		$Al_{13}Fe_4$	26	0.206
		"	85	0.205
		$Al_{45}(V, Fe)_7$	100	0.207
		I	78	0.207

The data (✡) and (✱) correspond to columns 1 and 6 of Table 5.3.1, respectively. The data (+) were taken from JCPDS card nos. 29-42, 30-48, 41-1285 and 44-1195 for $Al_{13}Fe_4$ and $Al_{45}(V, Fe)_7$, Al_6Fe, and I phases, respectively.

Table A3.5 Possible phase in the as-extruded Al-Fe-V-Si alloy produced from the powder size fraction with $D[v,0.5] = 31$ μm.

Experimental XRD data		Possible phase [+]		
Measured d-spacing (nm)[✡]	I/I_0[✱]	Phase	I/I_0	d-spacing (nm)
0.444	2.4	Silicide	50	0.450
0.397	9.7	Silicide	70	0.402
0.363	3.2	Silicide	30	0.366
0.336	2.8	Silicide	30	0.340
0.296	1.3	Silicide	10	0.300
0.281	1.4	Silicide	30	0.284
0.268	1.2	Silicide	10	0.271
0.247	3.9	Silicide	50	0.250
0.230	5.9	Silicide	10	0.236
0.223	2.8	Silicide	50	0.232
0.216	22.7	Silicide	90	0.218
0.210	9.7	Silicide	60	0.212
0.204	33.6	Silicide	100	0.206
0.199	4.9	Silicide	40	0.201
0.194	2.1	Silicide	10	0.196
0.186	2.0	Silicide	50	0.187

The data (✡) and (✱) correspond to columns 1 and 5 of Table 5.3.4, respectively.

The data (+) were taken from JCPDS card no. 6-669 for the silicide phase.

IBL
LONDON
UNIV.